SIXTH FRAMEWORK PROGRAMME

PRIORITY 4

Aeronautics and Space

Specifically Targeted Research Project

COINS

Cost effective Integral metallic Structure

3rd/Final Periodic Activity Report

Due date of deliverable: April 2010

Actual submission date: June 2010

Start date of project: 1st September 2006 Duration: 42 months

Prepared by: BAE SYSTEMS (Operations) Limited - Coordinator

Contract: AST5-CT 2006-030825 - COINS

Document reference sheet:

Reference:	**COINS/Activity 3/BAES/CJM 100125**
Date:	**January 2010**
Authors:	**Carla Murray, BAE Systems Advanced Technology Centre (ATC)**
Type:	**Final report**

COINS

Version: 1.0

COPYRIGHT AND CONFIDENTIALITY NOTICE

The work described in this document was performed as part of the COINS project (Cost Effective Integral Metallic Structure) which is funded under contract AST5-CT-030825 of the European Community. The project is a collaboration between BAE SYSTEMS (Operations) Ltd (prime partner), Airbus Deutschland GmbH, Alenia Aeronautica S.p.A, Dassault Aviation, Société Anonyme Belge de Constructions Aéronautiques, SHORT Brothers PLC, Alcan Centre de Recherches de Voreppe, Piaggio Aero Industries S.p.A, EADS CCR, EADS Deutschland GmbH Corporate Research Centre, GKSS Forschungszentrum Geesthacht GmbH, Cranfield University, Laboratory of Technology and Strength of Materials – University of Patras, Fundacion Fatronik, Airbus UK. The opinions, findings and conclusions expressed in this report are those of the authors alone and do not necessarily reflect those of the EC or any other organisation involved in the project.

No part of this publication may be reproduced or transmitted in any form or by any means, whether electronic, mechanical, photocopying or recording or otherwise; nor stored in any information retrieval system of any kind; nor used for tendering or manufacturing; nor communicated to any person, without the prior written permission of the COINS Project Steering Committee.

The contents of this document must be treated as confidential and protected as defined in the terms and conditions of the COINS Collaboration Agreement and shall not be distributed or reproduced without the formal approval of the COINS Project Steering Committee

© February 2010 COINS Project Steering Committee

All Rights Reserved

Revision table

Version	Date	Modified Pages	Modified Sections	Comments
1.0	January 2010			

Contents

Introduction 21

1 Work Package 1: FSW Process and Test Standards 21

1.1 Overview (BAE) 21

1.2 WP1.3: Testing Incorporating Residual Stress Effects 21

1.2.1 General 22

1.2.2 Weld Crack Growth Rates in the Absence of Residual Stress 23

1.2.3 Standard Tests for Welds Containing Residual Stress 24

1.2.4 Fatigue Crack Growth Test Recommendations 24

1.3 WP1.4 Revision of FSW Standards 24

1.4 WP1 References 24

2 Work Package 2: Design of Cost Effective IMS using FSW 25

2.1 Overview 25

2.2 Task 2.1 Design of welded IMS (Sabca) 26

2.3 Task 2.1 Design of IMS Incorporating FSW Using Existing and New Performance Data (Piaggio Aero) 26

2.4 Task 2.2 Design of Damage Tolerant welded structure 26

2.4.1 Task 2.2 Design of Damage Tolerant welded structure (Airbus Germany) 26

2.4.2 Task 2.2 and 2.5 Design of Damage Tolerance and long-term behaviour (Sabca) 26

2.4.3 Task 2.2 Design of Damage Tolerant Welded Structure (Piaggio Aero) 27

2.4.4 Task 2.2 Design of Damage Tolerant Welded Structure (ALCAN) 30

2.4.5 Task 2.2 Design of Damage Tolerant Welded Structures (Cranfield University) 31

2.4.6 Task 2.2 Design of Damage Tolerant Welded Structures (University of Patras) 33

2.4.7 Task 2.2 Design of Damage Tolerant Welded Structure (Airbus UK) 36

2.5 Task 2.3 Effect of Residual Stresses on Design 36

2.5.1 Task 2.3 Effect of Residual Stresses on Design (Airbus Germany) 36

2.6 Task 2.3 Effect of Residual Stresses on Design (EADS France) 36

2.6.1 Task 2.3 Effect of Residual Stresses on Design (GKSS) 45

2.6.2 WP2.3 Effect of Residual Stresses on Design (Cranfield University) 50

2.6.3 WP2.3 Effect of Residual Stresses on Design (University of Patras) 52

2.6.4 Fatigue testing of 2195 welded material with longitudinal weld 52
2.6.5 Mechanical behaviour of 2198 T8 before and after artificial ageing 56
2.6.6 M(T) Longitudinal weld – Crack towards weld 59
2.7 Task 2.4 Effects of Cracks in Structures 62
2.7.1 Task 2.4 Effects of Cracks in Structures (Airbus Germany) 62
2.7.2 WP 2.4 Effects of Cracks in Welded Structures (GKSS) 64
2.7.3 WP 2.4 Effects of Cracks in Welded Structures (University of Patras) 68
2.7.4 ESET test specimen 69
2.7.5 CT test specimen 72
2.7.6 WP 2.4 Effects of Cracks in Welded Structures (Cranfield University) 75
2.8 WP 2.5 Long Term Design Data 80
2.8.1 WP 2.5 Long Term Design Data (University of Patras) 80
2.8.2 Tensile test results 80
2.8.3 Fatigue Crack Propagation tests results 82
2.9 Task 2.6 Integrated Design Solutions 85
2.9.1 Task 2.6 Integrated Design Solutions for Integral Structure Containing Welds and Other Processes (BAE) 85
2.9.2 Task 2.6: Design of Cost-Effective IMS using FSW (Alenia Aeronautica) 95
2.9.3 Task 2.6 Integrated Design Solutions (Dassault Aviation) 96
2.9.4 Task 2.6 Integrated Solutions (Sabca) 98
2.9.5 Task 2.6 Integrated Design Solution for Integral Structure Containing Welds and Other Process (Piaggio Aero) 98
2.9.6 Task 2.6 Integrated Design Solution for Integral Structure Containing Welds and Other Process (Cranfield University) 99
3 Work Package 3: Development of New Applications for FSW 101
3.1 Task 3.1 Development of FSW Process for New Similar Alloys (Alenia Aeronautica) 101
3.1.1 Similar alloy welding: 2198 T8 102
3.1.2 Similar alloy welding: 2024 T3 102
3.1.3 Similar alloy welding: 7075 T6 103
3.1.4 Dissimilar alloy welding: 7075 T6 with 2024 T3 103
3.2 Task 3.1 Development of FSW Process for New Similar Alloys (EADS Germany) 103
3.3 Task 3.2 Testing of New Similar Alloys (EADS France) 109
3.4 Task 3.2 Testing of New Similar Alloys (EADS Germany) 114

3.5 Task 3.3 Development of FSW for New Dissimilar Alloys (Airbus Germany) 121
3.6 Task 3.3 Development of FSW for New Dissimilar Alloys (EADS Germany) 124
3.7 Task 3.4 Testing of new dissimilar alloys (EADS Germany) 124
3.8 Task 3.5 New Geometries (BAE) 124
3.8.1 Weld Joint Geometries 124
3.8.2 Conclusions and Recommendations 127
3.9 Task 3.5 New Geometries (Airbus Germany) 133
3.10 Task 3.5 New Applications, Geometries, fixtures, realisation, testing (Sabca) 143
3.11 Task 3.5 New Geometries (Piaggio Aero) 143
3.12 Task 3.5 New geometries (EADS Germany) 145
3.13 Task 3.5 New geometries (University of Patras) 147
3.13.1 Fatigue Testing of 2050 T3 T-Type samples 147
3.13.2 Fatigue testing of pre-corroded 2198 T8 FSW aluminum alloy with and without LoP defect 148
3.14 Workpackage 3: Development of New Applications for FSW (Airbus UK) 151
3.15 Task 3.6 Development of Fixtures for New Applications (BAE) 152
3.16 Task 3.7 Realisation of New Applications using Existing/New Data and New Geometries (BAE) 154
3.16.1 Fabrication of Subassembly A 154
3.16.2 Fabrication of Subassembly B 155
3.16.3 Fabrication of Subassembly C 155
3.16.4 Fabrication of Half-Section Assembly 155
3.16.5 Full-Section Assembly 156
3.16.6 Post Assembly Procedures and Surface Treatments 156
3.16.7 Results 156
3.16.8 Conclusions and Recommendations 156
3.17 Task 3.8 Testing and Evaluation of New Applications (Piaggio Aero) 159
3.18 Task 3.8 Testing and Evaluation of New Applications (EADS Germany) 164
3.19 Workpackage 3: ALCAN 164
4 Work Package 4: Repair Applications 165
4.1 WP 4.1 In-Production Repair Including Dissimilar Welds (University of Patras) 165
4.1.1 Testing of welded Joints 165

4.1.2 Tensile test results 166
4.1.3 Fatigue test results 167
4.2 Task 4.2 In Service (Airbus Germany) 168
4.3 Task 4.2 In service repair (Piaggio Aero) 173
4.4 Task 4.2 In service repair (University of Patras) 175
4.5 Task 4.2 In service repair (Airbus UK) 176
4.6 Task 4.3 FSW as a Repair Tool (BAE) 177
4.6.1 Non-Penetrating Surface Damage Repair 178
4.6.2 Planar Delamination in Thick Section Plate Repair 184
4.6.3 Weld Crack Repair 186
4.6.4 Unsupported Friction Stir Welding 188
4.6.5 Conclusions 191
4.7 Task 4.3 FSW as a repair tool (EADS Germany) 191
5 Work Package 5: Combination of FSW with other Production Processes 193
5.1 Task 5.1 Welding of large prefabricated part (Airbus Germany) 193
5.2 Task 5.1 Welding of large prefabricated part (Alenia Aeronautica) 201
5.3 Task 5.1 Combination with other production processes – prefabricated parts (Sabca) 202
5.4 Task 5.2 Combination of FSW with Stretch Forming (University of Patras) 202
5.4.1 FLD Coupons 202
5.4.2 Biaxial stretch forming model 205
5.5 Task 5.3 Creep-age forming (Dassault Aviation) 209
5.6 Workpackage 5: FSW with other production processes (Airbus UK) 216
6 Work Package 6: Improvements to the FSW Process 216
6.1 Overview 216
6.2 Task 6.1 Process Modelling (BAE) 217
6.2.1 The Thermal Model 218
6.2.2 Results and Discussions 218
6.2.3 Conclusions and Recommendations 220
6.3 WP6: Process Modelling (ALA) 223
6.4 Task 6.1 Process Modelling (SHORTS) 223
6.5 Task 6.1 Process Modelling (Alcan) 224
6.6 Task 6.1 Process Modelling (EADS France) 224

6.7 WP 6.1 Process Modelling, Data and Fundamental Understanding (University of Patras) 226
6.8 Task 6.2 Primary processing improvements (BAES) 230
6.9 Task 6.2 Primary processing improvements (AD) 230
6.10 Task 6.2 Primary processing improvements (EADS France) 230
6.11 Task 6.2 Primary processing improvements (EADS Germany) 230
6.12 Task 6.2 Primary processing improvements (GKSS) 235
6.13 Task 6.2 Primary processing improvements (Airbus UK) 235
6.14 Task 6.3: Post Weld Treatments (BAE Systems) 235
6.14.1 High-Power Beam Surface Melting 236
6.14.2 Laser Surface Melting 236
6.14.3 Laser Surface Alloying 237
6.14.4 Electron Beam Surface Melting 238
6.14.5 EBSM Concept Design 240
6.14.6 Summary 243
6.15 Task 6.3: Post Weld Treatments (Dassault) 249
6.16 Task 6.3: Post Weld Treatments (ALCAN) 249
6.17 Task 6.4 Process Monitoring Control (Airbus Germany) 249
6.18 Task 6.4 Process Monitoring Control (Fatronik) 249
6.19 WP6 Airbus Germany 254
7 Work Package 7 254
7.1 Task 7.3 Exploitation 254

Figure 1: Residual stresses in a FSW joint in 8mm thickness 2195 22

Figure 2: Design for new bulkhead test coupon..... 27

Figure 3: Residual Stress Distribution 28

Figure 4: Graph output of AFGROW (crack length vs. cycles) 30

Figure 5: Visual inspection of crack 30

Figure 6:Alternative positions of the crack retarder with respect to the weld in ESET samples of 2195 31

Figure 7: Positions of retarder straps in 2198 single (left) and double weld (right) configurations. 32

Figure 8: Comparison of fatigue crack growth rates plotted against crack length in mm in ESET samples of 2195 welds without retarder, and with 30 mm and 45 mm wide retarders. 32

Figure 9: da/dN Vs ΔK, 200 mm wide MT sample; centreline longitudinal weld, crack growth rates with retarder strap with those in sample without strap. Retarder sample tested at 20% greater nominal load to maintain same nominal stress level as sample without strap 33

Figure 10: Microhardness profile along the specimens length. The weld centre is located at x=0 34

Figure 11: Test specimen after failure 34

Figure 12: S-N curves of 2139T3 with the hole in the centre of the nugget and in the TMA 35

Figure 13: S-N curves of 2198T8 with the hole in the centre of the nugget and in the TMAZ..... 35

Figure 14: Seam position within CTW75 37

Figure 15: da/dN curves for welded and base material - R=0..... 38

Figure 16: da/dN curves for welded and base material - R=0.4..... 38

Figure 17: da/dN curves for welded and base material - R=0.7..... 39

Figure 18: Experimental da/dN curves and identified Forman's law for base material 39

Figure 19: Experimental da/dN curves and identified Forman's law for welded material..... 40

Figure 20: Simulated residual-stress-induced distortions on a CT specimen (magnified)..... 41

Figure 21: Computed RS-induced stress intensity factor as a function of the position into the sample thickness and crack length 42

Figure 22: Stress intensity factor as a function of crack length 43

Figure 23: Influence of residual stresses on Delta K 43

Figure 24: Influence of residual stresses on R-Ratio 44

Figure 25: Computed stress intensity factors with residual stress implicitly or explicitly taken into account 45

Figure 26: Examples of the ESET and CT samples containing FSW welds as indicated..... 45

Figure 27: Residual stresses parallel to the central FSW weld in 3 sizes of ESET samples..... 46

Figure 28: Residual stresses parallel to the FSW weld in 3 sizes of CT samples in 2195 aluminium alloy. 47

Figure 29: Residual stress field from 3.2 mm M(T) sample 750 X 300 mm with single central FSW longitudinal weld 2198 T8 49

Figure 30: Residual stress field from 3.2 mm M(T) sample 750 X 300 mm containing double weld. A central region of compressive stress between the tensile fields within the welds can clearly be seen . 49

Figure 31: Comparison of crack growth rates in FSW 2189 T8 sheets with 1.6 and 3.2 mm thicknesses and two sample lengths; there is little or no effect on crack growth rates 50

Figure 32: Comparison of fatigue crack growth rates in 3.2 mm 2198 T8 containing FSW with 3 weld orientations; longitudinal double weld, single central weld and a parallel (transverse) weld..... 50

Figure 33: ESET test sample and FE model for calculating crack opening stress 52

Figure 34: ESET test sample predicted & measured fatigue crack length Vs fatigue cycles growth ... 52

Figure 35: Dog-bone specimen geometry type 1 53

Figure 36: Dog-bone specimen geometry type 2 53

Figure 37: Comparative plot of the “Type 2” specimens..... 54

Figure 38: Comparative plot of the two types plate to plate welded specimens 55

Figure 39: Microhardness profile (0.3 mm from the surface) of specimens P2P9, P2P6. Note that P2P9 exhibits lower microhardness values than specimen P2P6..... 55

Figure 40: Microhardness profiles of the examined specimens. Note that P2E2 exhibits lower microhardness values than specimen P2E7 56

Figure 41: Picture of failed specimen 59

Figure 42: Comparative plot of 2139T3 parent material and respective welded plates: Improved fatigue crack propagation behaviour is observed in the welded plates. Differences diminish at high ΔK values 60

Figure 43: Comparative plot of 2198T8 parent material and respective welded plates..... 60

Figure 44: Sketch of biaxial coupon 62

Figure 45: Crack orientation in longitudinal (parallel to aluminium rolling direction) and circumferential direction ((perpendicular to rolling direction) 63

Figure 46: Differentiation of load ratio between upper and side shells of a fuselage 63

Figure 47: Pictures of the welded sample before manufacturing..... 64

Figure 48: Strain gauge map 64

Figure 49: The 6 axis fatigue test machine, (a) general view, (b) Detail of sample test area 65

Figure 50: The biaxial test sample showing the optical crack length measurement system and the clamps used to retard progress of secondary corner cracks initiated during fatigue cycling of the main crack..... 66

Figure 51: Crack paths followed by each of the four samples ..... **Error! Bookmark not defined.**

Figure 52: Fatigue crack propagation rates using estimated Walker equation constants (log-log diagram) 69

Figure 53: ESET type specimen geometry 70

Figure 54: ESET specimen - Residual stresses 70

Figure 55: ESET specimen – FE model 71

Figure 56: ESET specimen – Calculated SIFs and R_{eff} for R=0.1, Pmax=4330Nt 71

Figure 57: ESET specimen – Calculated SIFs and R_{eff} for R=0.6, Pmax=9730Nt 72

Figure 58: ESET specimen – Fatigue crack propagation for: (a) R=0.1, Pmax=4330Nt and (b) R=0.6, Pmax=9730Nt 72

Figure 59: CT type specimen geometry 73

Figure 60: CT specimen - Residual stress field 73

Figure 61: CT specimen – FE model 74

Figure 62: CT specimen – Calculated SIFs and R_{eff} 74

Figure 63: CT specimen – Fatigue crack propagation predictions 75

Figure 64:Crack deviation sample geometry & dimensions 75

Figure 65: Crack trajectories in samples with and without the weld line & the residual stresses, showing that residual stresses promote earlier crack deviation 76

Figure 66: Comparison of measured and calculated crack trajectories; prediction of the effects of hole distance h and effect of weld residual stress field 76

Figure 67: Dimensions of the biaxial test sample showing the locations of the strain gauges used in experimental stress analysis 77

Figure 68: Measured and calculated strains for load case 1 (*Fx:Fy* = 0:1) 79

Figure 69: Predicted and measured fatigue crack growth in the cruciform samples 79

Figure 70: Tensile specimens as part of the welded plates 81

Figure 71: Tensile specimens used. Arrows indicate the rolling direction 81

Figure 72: Bottom view of fractured specimen 82

Figure 73: Weld configurations tested 83

Figure 74: Comparative *plot of all tests performed* 84

Figure 75 Example fusion welded joint configurations 89

Figure 76 FSW butt joint configurations 90

Figure 77 Hybrid joint designs for thick to thin section corner joint 91

Figure 78 FSW tailored blank designs 91

Figure 79 Corner joint concepts using extrusion 92

Figure 80 Dissimilar alloy joint 92

Figure 81 Geometry of demonstrator half-section 93

Figure 82 Front nose cone example 94

Figure 83 Development of fully enclosed structure 95

Figure 84: Double-T IMS (wing spar) 2198/ 2196ext similar & dissimilar: 7475 + 2024 ext (butt joint) 96

Figure 85: Design of integrated metallic structure applied on FSWelded upper wing skin (Falcon upper wing) 97

Figure 86: showing the relative percent weight reduction in the wing obtained by using extrusions plus FSW with creep age forming (centre) and creep age forming only of extrusions (right) in comparison with the standard route of creep age forming of plates (left) 97

Figure 87: showing relative percent cost reduction obtained by using FSW of extrusions instead of plate for manufacture of Falcon upper wing 98

Figure 88: Examples of FSW lap joint in Al 2024-Al 7475 after fatigue testing by Piaggio 99

Figure 89: S- N curve obtained for coupons with friction stir welded lap joints in 2024/ 7475 alloys 99

Figure 90: Concept 1 Skin/stringer joint with FSW showing location of FSW and strain gauges 100

Figure 91: Finite element analysis showing out of plane displacements under in plane tension at a remote stress of 100 MPa for concept 1 sample. Maximum displacement = 1.1 mm at the stringer pad-up 100

Figure 92: Comparison of crack length Vs cycles data for experiments and for predicted curves for ther concept 1 design of skin- stringer joint with FSW. BM is base material data, FSW is using friction stir weld material data 101

Figure 93: ESAB Superstir F5A FSW machine used by EADS G 104

Figure 94: DeltaN Tool generation 4 mounted on the ESAB machine welding head 105

Figure 95: Pin geometry used in DeltaN tool 105

Figure 96: Macro section of 2050T8 DeltaN FSW, 15 mm thick, feed 200 mm/min, revs 500 1/min 106

Figure 97: Macro section of 2050T8 DeltaN FSW, 15 mm thick, feed 400 mm/min, revs 700 1/min 106

Figure 98: Vickers hardness testing results on DeltaN generation 4 weld on 2050 T8, welding speed 200 mm/min, 500 revs/min 107

Figure 99: Vickers hardness testing results on DeltaN generation 4 weld on 2050 T8, welding speed 400 mm/min, 700 revs/min 107

Figure 100: Vickers hardness testing results on DeltaN generation 3 welds on 2050 T3, welding speed 160 108

Figure 101: Vickers hardness testing results on DeltaN generation 3 welds on 2050 T3 & PWHT to T8, welding speed 160 mm/min, 450 revs/min 108

Figure 102: Fatigue crack growth curves in 2050 T8 base material and in the weld for various R ratios, T-L, CT specimens 111

Figure 103: Typical cross section for 7449 bobbin tool FSW 23mm thick plate 112

Figure 104: HV0.2 hardness profiles near the top (e/10), at mid thickness (5e/10) and near the bottom (9e/10) for as-welded TAF (30h and 400h after the welding operation) and post-welding T79 treated coupons. 113

Figure 105: S-N curve of 7449 T79 bobbin tool FSW 23 mm thick plate 114

Figure 106: FSWelded 7449T4-FSW-T7 by standard (left) and DeltaN (right) tool 116

Figure 107: FSWelded 2050T3-FSW-T8 by standard (left) and DeltaN (right) tool 116

Figure 108: Vickers hardness profile on standard tool FSWelded 7449T4 post weld heat treated T7 117

Figure 109: Vickers hardness profile on DeltaN tool FSWelded 7449T4 post weld heat treated T7. 117

Figure 110: Vickers hardness profile on 2050T3 alloy in as welded condition 118

Figure 111: Vickers hardness profile on alloy 2050T3 FSWelded and post weld heat treated to T8. 118

Figure 112: Fatigue test results and Woehler curve of DeltaN FSWelded 2050-T3-PWHT-T8 120

Figure 113: S-N data for Bobbin & DeltaN welding tools – 15mm thick 2050 alloy (Source: Cranfield Uni.) 121

Figure 114: Cylindrical pin tool for the dissimilar Ti/A1 FSW 121

Figure 115: Surface preparation of Ti before welding: left milling; right milling and steel shot blasting 122

Figure 116: Surface preparation of Ti before welding: left milling and pickling; right milling, steel shot blasting and pickling 122

Figure 117: FSW of 6013 and Ti6Al4V 123

Figure 118: Final results of the dissimilar welds 123

Figure 119: Micro-section of FS welded 6013 and TiAl6V4 124

Figure 120: Selected corner joint geometries 128

Figure 121: Photograph of typical dissimilar 7020/7056 weld 129

Figure 122: Rebated joint schematic and polished cross-section 129

Figure 123: Approaches investigated for tailored blank joint configuration 130

Figure 124: Cross-section of tailored-blank weld produced using square-edged anvil 131

Figure 125: Cross-section of tailored-blank weld produced using anvil with fillet radius 131

Figure 126: Cross-sections of tailored-blank weld produced using sacrificial insert material 132

Figure 127: Cross-section of double-sided weld 132
Figure 128: Interlocking joint welding sequence 133
Figure 129: Section through interlocking joint 133
Figure 130: Finite element model of a generic welded overlap joint 134
Figure 131: Finite element overall results of the overlap joint for the different directions, deformation magnified 15X 135
Figure 132: Detailed stress distributions around the joined area (S11, S22, S12 and S von Mises respectively) 136
Figure 133: Stress distributions along the overlap joint line 137
Figure 134: Pin length 137
Figure 135: Overlap welds, double passage 20-30 configuration and tripe passage 5-25-45 configuration 138
Figure 136: Overview of the fatigue results 139
Figure 137 : Fatigue comparison, effect of the pin length in single pass 140
Figure 138: Fatigue comparison, single pass with double pass without translation 140
Figure 139: Fatigue comparison, single pass with double pass with 4mm translation 141
Figure 140: Fatigue comparison, double pass configurations 141
Figure 141: Fatigue comparison, double pass 23-27 and 20-30 with triple pass configuration 142
Figure 142: Fatigue comparison, single, double and triple pass configuration, best results 142
Figure 143: Shear beam 144
Figure 144: Shear beam detail 145
Figure 145: Total view of the DeltaN tool welded 2050 alloy beam track 146
Figure 146: Detail view of the DeltaN tool weld top surface and its superb surface finish 146
Figure 147: Fatigue testing specimen types 147
Figure 148: Comparative plot of the LT and the TT welded sample 148
Figure 149: Comparison of the S-N curves derived for all test series performed 149
Figure 150: Specimen Fracture Types 150
Figure 151: Welded Laminated demonstrator 152
Figure 152: Tooling blocks and welding sequence 153
Figure 153: Demonstrator weld sequence and subassemblies 157
Figure 154: Schematic of the full assembly 158
Figure 155: Fully assembled and post weld treated final component 159
Figure 156: Welded wing spar test coupon 160

Figure 157: Failed shear beam test specimen 162
Figure 158: Modelled shear beam..... 162
Figure 159: Testing arrangements..... 163
Figure 160: Detail drawing of shear beam test specimen 163
Figure 161 :The fatigue crack started at Hi-Lok hole at 250,000 cycles 164
Figure 162: Weld types tested in WP4.1 by University of Patras..... 166
Figure 163: Indicative Stress displacement curves 167
Figure 164: Comparative S-N curves..... 167
Figure 165: Example of in-service damage of a fuselage due to impact with ground equipment 169
Figure 166: Example of repair of a fuselage panel with a riveted path. View from inside showing circumferential and horizontal stiffeners 169
Figure 167: Rivets distribution 170
Figure 168: Repair with friction stir weld in the less critical location..... 172
Figure 169: Repair with friction stir welds in the most critical locations 172
Figure 170: Fatigue test results on the riveted coupons performed at LTSM..... 173
Figure 171: An economical and rapid repair in service requires the Pax Door isn't disassembled so Pai and Eads-G decided to use Bobbin Tool..... 174
Figure 172: After repair the Pax Door repaired zone should be checked with a non destructive inspection (Liquid penetrant) and reinstalled..... 175
Figure 173: Fatigue Test Results 175
Figure 174: Repair weld over an in-service crack using a bobbin tool..... 177
Figure 175: Cross-sections of insert repair cases..... 179
Figure 176: Load displacement behaviour of insert repair with a singular edge weld 179
Figure 177: Cross-sections of strengthened weld repairs 180
Figure 178: Load displacement behaviour of insert repair with a three welds 181
Figure 179: Laminated insert repair..... 182
Figure 180: Load displacement behaviour of laminate insert repair..... 183
Figure 181: Load displacement behaviour of laminate insert repair with strengthening welds..... 184
Figure 182: Geometry used to simulate planar delamination 185
Figure 183: Simulation of tapered crack using partial thickness machined edge 186
Figure 184: Tapered crack repair indicating onset of weld defect..... 187
Figure 185: Crack repair sequence with insert..... 187
Figure 186: Maximum bending stress and deflection as functions of plate thickness (t) 189

Figure 187: Minimum bending stress and deflection as functions of plate length 190
Figure 188: Unsupported FSW showing suspension of material using edge support blocks 190
Figure 189: Weld produced using tool A indicating plastic deformation of rear face 191
Figure 190: View of the location of cracking next to rivet holes 192
Figure 191: Detailed view of a crack next to a rivet hole 192
Figure 192: Overview of the 6 different designs for the large test article 194
Figure 193: Examples of deformations of the unstiffened panel before welding design concept 3 ... 195
Figure 194: Distortion of a flat panel after FSW (concept 3) 196
Figure 195: Distortion of a stiffened panel after FSW (concept 1) 196
Figure 196: Welding of panel with bonded stiffeners (concept 2) 197
Figure 197: Example of large deformation caused from Laser welding of a stringer. In addition, in this particular case, the presence of gap between stringer and panel has led to a bad quality of LBW 197
Figure 198: Friction Stir Welding of concept 4 having LBW stringers (V534-H1504-006) 197
Figure 199: Distortions after FSW of the skin for the design concept 2 198
Figure 200: Distortions after FSW of the skin for the design concept 4 198
Figure 201: Distortions after FSW of the skin for the design concept 5 (dwg: V534-H1506-008) 199
Figure 202: Distortions after FSW of the skin for the design concept 6 (dwg: V534-H1506-010) 199
Figure 203: Picture showing the area of the defects identified in panel concept 6 200
Figure 204: Specimens extracted from test articles for weld assessment 200
Figure 205: Formability experimental set up, (a) Side view and (b) Top view 203
Figure 206: Developed FE model (a) Side view and (b) Top view 203
Figure 207: Deformed shape, (a) From the experiments and (b) from the mode 204
Figure 208: Predicted FLD curves, (a) For Parent Material, (b) For Transverse welded panel and (c) For lengthwise welded panel 205
Figure 209: Illustration of the stretch forming process 205
Figure 210: Technical drawings of the tool used (a) Front view, (b) Side view and (c) Top view ... 206
Figure 211: FE model for the stretch forming process 207
Figure 212: Local material properties 207
Figure 213: Deformed shapes of the metal sheet 208
Figure 214: Force displacement diagram 208
Figure 215: Creep-age forming testing matrix 210
Figure 216: Creep-age forming tests results 210

Figure 217: Mechanical properties after hot temperature elongation 212

Figure 218: Fatigue crack growth rate of 2196 T8 as welded condition..... 212

Figure 219: Fracture toughness of 2196 T8 in as welded condition 212

Figure 220: In salt spray exposure 213

Figure 221: Intergranular corrosion – according to ASTM G34 Standard (EXCO)..... 213

Figure 222: Intergranular corosion – according to AIR 9048 (Annex D Standard Method 1) 214

Figure 223: In sea cost atmosphere exposure. 215

Figure 224: Impact of peening processes on Fatigue Crack Growth rate of 2196 T8 FS Welded..... 216

Figure 225: Model geometry 221

Figure 226: Comparison of the through-thickness temperature differential for baseline weld and the weld with cooling applied to the tool body..... 222

Figure 227: Comparison of the through-thickness temperature differential for baseline weld and the weld with heating applied internally to the tool pin..... 222

Figure 228: Thermocouples location in 7449 plates 225

Figure 229: Forces and torque versus time during FSW of 23 mm thick 7449 TAF plates 225

Figure 230: Temperature versus time during FSW of 23 mm thick 2050 TAF plate 226

Figure 231: Diabolo-pin tool design 227

Figure 232: FSW FE model configuration for the Diabolo-pin tool case..... 228

Figure 233: Temperature measurement points for the case of Diabolo-pin tool 228

Figure 234: Comparison between temperature experimental measurements and FEA results – Diabolo-pin-tool (EADS-F) 229

Figure 235: Cut section and side view of DeltaN Tool gen1 231

Figure 236: Shoulder cup, shaft and bearing as the three main components of the DeltaN tool concept 231

Figure 237: DeltaN tool cross-section 232

Figure 238: DeltaN tool 232

Figure 239: Cut section view of Delta N tool generation 3 233

Figure 240: Top view of DeltaN tool generation 3 shoulder cup and tool case..... 233

Figure 241: DeltaN tool generation 4 tool case fixed at the lower end of the ESAB Superstir welding head..... 234

Figure 242: DeltaN tool generation 4 234

Figure 243: Surface appearance and cross-section of excimer laser surface melted AA2024 with treatment parameters of 10J/cm2, 9 pulses per unit area 243

Figure 244: Electrochemical reactivity following excimer laser surface melting of AA2024 at 10J/cm2, 9 pulses per unit area compared with the parent alloy: (a) cathodic polarisation curve and (b) anodic polarisation curves measured with a microelectrochemical cell with 0.1M NaCl solution at a scan rate of 1mV/s scan rate (Ag/AgCl reference electrode) 244

Figure 245: Schematic diagram of the pulsed, high power electron beam setup used for the treatment of specimens 244

Figure 246: The BAE Systems electron beam apparatus highlighting key components 245

Figure 247: Examples of uniform and non-uniform melt zone surface appearances and their associated etched microstructure cross-sections produced in electron beam surface melting of AA2024 at 20μs pulse duration, 6J, 1 pulse per unit area 245

Figure 248: Effect of scanning on beam path length 246

Figure 249: Set-up for scanning e-beam 246

Figure 250: Underside of processor showing rectangular aperture for scanning e-beam 247

Figure 251 Cross-section of elastomeric seal proposed by FTL 247

Figure 252: TWI sliding seal for e- beam processor 247

Figure 253: Cross-sectional view of curved workpiece and processor seals (half-view taken across narrow side of e-beam aperture) 248

Figure 254: Cross section of processor showing vacuum zones 248

Figure 255: Pin-to-backing distance 249

Figure 256: Concept for distance measurement using magnetic principles and exploratory results 250

Figure 257: FE simulation outputs: (a) self-inductance of the coil, (b) sensitivity of the circuit resonance frequency to variation of the distance from the shoulder to the backing 251

Figure 258: Experimental measurements obtained with the prototype device 251

Figure 259: Tool pin vibration (left) in order to reduce LOP (right) 252

Figure 260: Effect of pin vibration on LOP 253

Figure 261: Effect of vibration parameters on LOP 253

Figure 262: ANOVA (a) and maximum value (b) analysis of the effect of vibration parameters on LOP 254

Table 1: Open hole fatigue tests....33
Table 2: Parameters of Forman's fatigue law....37
Table 3: Samples types investigated on DESY synchrotron....48
Table 4: Fatigue testing of 2195 welded material with longitudinal weld....54
Table 5: Specimens failed at considerably lower cycles than expected....55
Table 6: Tests for determining Mechanical behaviour of 2198T8 before and after artificial ageing 57
Table 7: Fatigue Propagation test....58
Table 8: R-Curve test results....59
Table 9: Geometry of test samples and Summary of tests....60
Table 10: Paris Coefficients....61
Table 11: Test matrix for the biaxial tests....63
Table 12: Test Specimens (2198-T8 with a FS weld parallel to the x-axis)....78
Table 13: Tensile Test Results....80
Table 14: Weld configurations tested....83
Table 15: Tensile strength test results on 2050 T3 welds with T8 PWHT using standard and Delta N tools, with and without stretching before ageing to T8....109
Table 16: Testing matrix for 2050 Bobbin Tool Welds....110
Table 17: Testing matrix for 7449 Bobbin Tool welds....110
Table 18: Tensile properties of 7449 T79 bobbin tool FSW 23mm thick plate (average on 3 test specimens)....114
Table 19: Tensile test results of Standard and DeltaN FSWelded 2050 and 7449 alloys....119
Table 20: Welding parameters for the 6013T4/Ti6A14V....122
Table 21: COINS, overlap joints, test matrix with the different conditions tested....138
Table 22: COINS Fatigue results condensation of overlap joints....143
Table 23: Test Matrix and sketch of the specimen geometry....171
Table 24: Pin length as a percentage of the plate thickness....188
Table 25: FS Welded material characterisation testing matrix....211
Table 26: Geometry and welding parameters of the studied case, as provided by EADS-IW....227
Table 27: Pending issues for fully evaluation of the feasibility of the developed measuring device....251
Table 28: Identification of the PBD*....252
Table 29: Vibration conditions....252

Introduction

The overall objective of the COINS project is to *"Extend the application of integral metallic structure utilising friction stir welding by: advancing the state of the art of FSW technology; developing new geometries for FSW; and through innovations in design"*. A group of fifteen partners including end users, research organisations, Universities and a material supplier has been brought together to achieve this objective. The project ran for 42 months having been granted a 6-month extension. The extension was required due to slippages in the experimental programme caused by delayed material delivery earlier on in the project. This is the final project report and covers the last 18 months' activities.

During the lifetime of the project there have been 12 consortium meetings which have been technical reviews. In addition the first and second annual reviews with the EC Project Officer were held in conjunction with the scheduled technical reviews. In July 2009 the Co-ordinator held an overview meeting with the newly appointed EC Project Officer. There have been numerous additional collaborative meetings since the start of the project. At the technical meetings progress has been reported both by partner and by work package leader. Minutes and presentations from the meetings have been recorded.

This project has demonstrated a good level of partner co-operation and collaboration between individual industrial partners and between industrial and academic partners.

The overall technical progress in the programme has been good and part of the final technical reporting is the compilation of a Data Design Handbook cataloguing the project test results. It was agreed by the consortium that this would be a useful reference document for partners after the end of the project.

Technical reports by work package are given below.

1 Work Package 1: FSW Process and Test Standards

1.1 Overview (BAE)

It is essential in highly collaborative projects such as COINS to have consistency of data, both process and test. During the first year, process and test documents (deliverables D1 and D2) were produced, which provide guidance to all partners relating to the process data that needs to be recorded, and the test standards that are to be used. The COINS project will advance the understanding and application of FSW, and it is important that testing practices also evolve. The primary activity in WP1 during the second and final year has been testing to evaluate the effect of Residual Stress (RS) such that it can be accounted for in testing.

Tasks WP1.1 and WP1.2 were completed in the first year; Tasks 1.3 and 1.4 have been active during the second and final years of the project.

1.2 WP1.3: Testing Incorporating Residual Stress Effects

Most tests used for welds are based on tests designed for homogeneous material with no RS. Since RS is inherent in welded structures, it is important to establish what effect RS has on mechanical performance, particularly damage tolerance. The first year activities examined impact performance in

the presence of stress fields; during the second and final years fatigue crack growth rates have been examined.

Fatigue crack growths rate tests were conducted by CU on 1.6mm thickness AA2198 and 8.0mm thickness AA2195 material. The tests took into account the crack orientation, sample size and geometry, and are supported by RS measurements on comparable welds conducted by GKSS. All weld samples were produced by AUK. Detail results from this work are included in the following WP2 section due to synergies with the activities in that workpackage; below follows a discussion of the findings and recommendations to account for RS in testing.

1.2.1 General

While fatigue crack growth test standard of wrought and cast materials are well established (ASTM E647) and major variables identified, there is no specific test standard involving welds and RS surrounding them. In addition to RS, welds in their fusion (or nugget for FSW) contain regions of heterogeneous microstructure and significant modification of local static strength values. These local changes in themselves would be expected to influence fatigue crack growth rates in welded structures even in the absence of RS. The presence of residual stress modifies the crack growth rates further. A typical selection of RS fields around a FSW weld in 2195 8mm thickness from COINS deliverable D15 is shown in Figure 1.

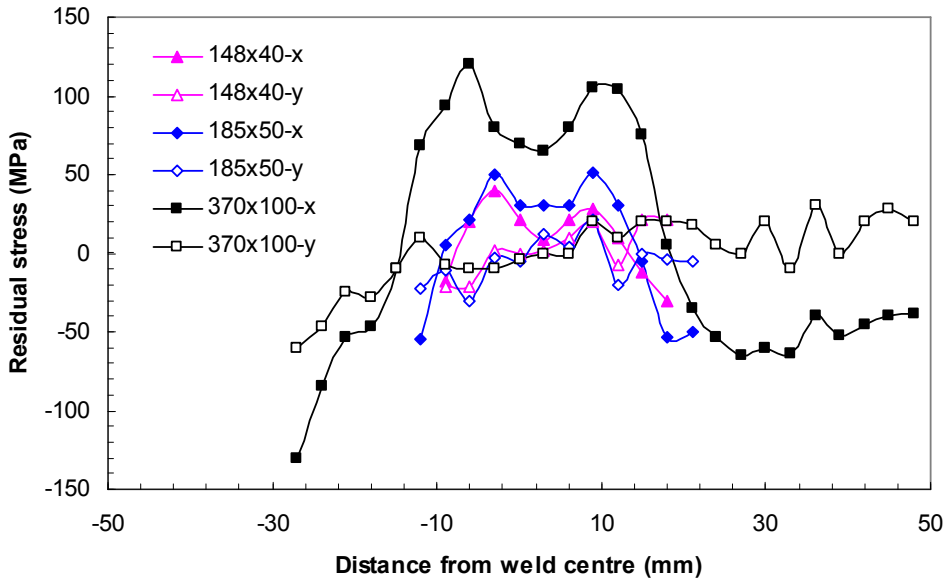

Figure 1: Residual stresses in a FSW joint in 8mm thickness 2195

This shows a double tensile peak located either side of the weld line in 3 different sizes of ESET sample with a single central longitudinal FSW joint. Note also the balancing compression stresses of up to 140MPa in the largest samples.

There is an emerging consensus on the process by which RS influence crack growth rates [1, 2]. The approach is to calculate the stress intensity factor associated with a crack tip in the RS stress field

($K_{residual}$). If the crack tip is in a compressive field this is negative, if in a tensile field it is positive. When combined with the externally applied maximum and minimum stress intensities, $K_{max, app}$ and $K_{min\ app}$, the crack opening and effective ΔK (ΔK_{eff}) will be changes; compressive RS closing and retarding the crack, tensile RS opening it up and accelerating the crack growth rates. Thus whether a crack is accelerated or retarded by a RS field will depend on where the crack tip is located in the RS field. If the crack tip is located within the weld and is propagating perpendicularly away from the weld, the tip will be in tension and accelerated growth will ensue. If the crack is located on the sample or structure edge, propagating towards the weld, it will be in a zone of compressive stress and growth rates will be reduced. The data shown in COINS deliverable D15 demonstrates the operation of this principle.

Noting that the RS field can extend into regions beyond the Heat Affected Zone (HAZ) into the parent plate material, if there are fatigue cracks growing in the parent plate adjacent to the weld, their growth rates will be changed even though their microstructure and properties have not been influenced by the weld.

The RS field caused by the weld, in addition to being determined by the weld process and the material characteristics, will be determined by the geometry of the component or structure being welded, and will be further modified by any post weld machining performed.

The RS and fatigue crack growth measurements made in the COINS project has confirmed previous studies that have shown large samples are required to realise the largest possible levels of RS in the weld (and thus representative of a welded structure). The largest samples for 8mm 2195 were 370x100mm with a longitudinal weld and had peak levels of RS in the weld of 120MPa. Larger samples may well have large stresses. Both modelling and experimental work demonstrates that stresses reduced with reducing sample size.

The work performed under WP1.3 and WP2.2 in the COINS project has established that even the smallest samples tested (40x150mm ESET and CT with external dimensions of 87x84mm) contained RS. In the case of the 40mm wide ESET, the peak longitudinal stress was <50MPa, and for the CT sample it was <80MPa. These stresses still significantly influenced the fatigue crack growth rates of parent plate material in comparison with growth rates measured on unwelded parent plate.

1.2.2 Weld Crack Growth Rates in the Absence of Residual Stress

It is well established (for instance [3]) that fatigue crack growth rates in the region less than ΔK=10MPa $m^{½}$ are subject to strong influences of microstructure, including grain size and second phase particle distributions. The influence is less in intermediate values of ΔK, say 10-30 MPa $m^{½}$, and reappears at large values of K_{max} (as opposed to ΔK). IF there were no RS present, a standard fatigue crack growth test could consist of propagating a crack parallel to the weld line, with the crack propagating on the weld line or along any plane parallel to the weld line put at a distance from it. Fatigue crack growth rates which are characteristic of the weld line put at a distance from it. Fatigue crack growth rates which are characteristic of the weld microstructure could be measured over the entire relevant range of ΔK values from threshold to final failure.

The work performed in COINS has established that smaller samples than the ones tested would be necessary to have RS approaching zero and obtain intrinsic crack growth properties of welded material, and it is recommended that this possibility be explored in future work. Such data would be

most valuable in providing standard fatigue crack growth data for welds in the absence of RS. This data would be used as input data in predictions of crack growth rates in welds with RS.

1.2.3 Standard Tests for Welds Containing Residual Stress

The validation trials which have taken place in WP1.3 and WP2.3 in COINS have demonstrated that although models to predict the effects of RS on fatigue crack growth rates are beginning to mature, they are still not sufficiently accurate to be used as the basis of design in welded structures. When they become accurate it will be possible to obtain intrinsic weld data from tests on stress free samples and then in conjunction with knowledge of the component or structure RS field, crack growth rates within the weld containing RS could be predicted.

In the meantime alternative approaches which are conservative must be employed. Unfortunately this will entail tests of samples of the recommended minimum size which contain full scale RS fields, in order to be conservative. The COINS work show samples should be at least 500x300mm in size. The COINS work has demonstrated that the crack tip location and orientation with respect to the weld and to the applied remote stress must be matched to that of the service situation if relevant crack behaviour is to be obtained.

For components and structural elements which are of size smaller that that required to create maximum RS fields, the test size and sample geometry should be matched to the application geometry and scale.

1.2.4 Fatigue Crack Growth Test Recommendations

- Fatigue crack growth tests as per ASTM 647 on samples machined from welded material, less the weld line. Comparison with tests on parent plate material to define intrinsic weld properties. Sample to be checked for freedom from RS
- Fatigue crack growth tests as per ASTM 647 on large scale welded samples containing full RS field. Crack tip located and orientated in same position & orientation as in the engineering application. Measurement of RS desirable

1.3 WP1.4 Revision of FSW Standards

Deliverable report D2, “Revised FSW Test Standard” has been updated to include the recommendations generated in WP1.3 and is identified as Issue 2. Reference should also be made to deliverable report D15, as this contains much of the supporting experimental data that was used to formulate the recommendations provided.

Information provided on tools and welding hardware (machines and fixtures), together with weld process information has been collected and will be made available to the partners as a future reference to the equipment and testing conducted within COINS.

1.4 WP1 References

[1] Glinka G. Effect of residual stresses on fatigue crack growth in steel weldments under constant and variable amplitude load. In: Fract. Mech., ASTM STP 677, American Society for Testing and Materials, 1979, pp. 198-214.

[2] Itoh YZ, Suruga S, Kashiwaya H. Prediction of fatigue crack growth rate in welding residual stress field, Eng Fract Mech, 33 (1989): 397-407.

[3] S Suresh "Fatigue of materials" chapter 6, Cambridge 1995.

2 Work Package 2: Design of Cost Effective IMS using FSW

In this Activity report, the work performed in the final 24-42 month period of Work Package 2 on "Design of cost effective integrated metallic structures using friction stir welding" is summarised. The work includes evaluation of the damage tolerance performance of novel designs of friction stir welded components designed by Piaggio and Airbus Germany, and evaluated by Piaggio, Cranfield University. The effects of residual stresses on fatigue crack growth have been studied and reported by Cranfield, University of Patras and by EADS France. A vital part of this activity has been the measurement of residual stress fields in friction stir welded samples by GKSS; the residual stress measurements in a wide range of samples are also reported. Successful retardation of propagating fatigue cracks by bonded crack retarders of aluminium adhesively bonded to the aluminium substrate is described. The use of samples containing offset open holes to study crack deviation and the effects of pad up geometry and residual stress fields on crack trajectory is reported. A wide range of material property tests on FSW samples has been performed, these include open hole fatigue tests, dogbone samples, stress life fatigue data, and specially constructed samples to study the influence of rolling direction on fatigue initiation and fatigue crack propagation. The influence of biaxial stress fields found in aircraft fuselages on fatigue crack growth rates in FSW samples is also reported. Finally detailed design studies of FSW structures are reported. These include studies of weight reduction and cost in FSW wing by Dassault, studies of weld configurations for repair of land vehicle structures by BAE Systems, and studies of fabricated beams and fuselages by SABCA and Airbus.

Overall objectives

- Design of IMS incorporating FSW for new applications using new and existing data
- Design of damage tolerant structure including welds with maximum residual strength using novel design features
- Incorporation of the effects of residual stresses and crack growth properties into designs
- Production of general design considerations for IMS using FSW

Tasks active in months 25-42

Task 2.2 Optimisation of design of DT welded IMS
Task 2.3 Effect of residual stresses on design
Task 2.4 Effect of cracks in structures
Task 2.5 Long term design data
Task 2.6 Integrated design solutions for integral structures containing welds

2.1 Overview

Work package 2 considers factors controlling the design of friction stir welded structures, exploring how the weld process influences the shapes which can be produced and how models to predict service performance particularly in fatigue can be developed and used to optimise the designs containing the welds. The work content consists of:

- Development of a series of demonstrator designs for FSW structures from which generic design principles for use with FSW structures can be extracted
- Measurement of quantitative FSW design data essential for structural design using this joining process
- Development of models for prediction of design related properties such as fatigue crack growth, fail safety and crack trajectory stability.

Many of the sub tasks undertaken by the participants are common to more than one of the 6 subtasks above. Consequently this progress report lists achievements and progress by partners under the various subtask headings

2.2 Task 2.1 Design of welded IMS (Sabca)

- designed: angle joint with only one weld at some distance of the point of maximum stress; design with highest stress capability

2.3 Task 2.1 Design of IMS Incorporating FSW Using Existing and New Performance Data (Piaggio Aero)

(Activity concluded in 1st year)

2.4 Task 2.2 Design of Damage Tolerant welded structure

The objectives of this subtask are to design manufacture and test novel concepts to increase the damage tolerance of friction stir welded integral aircraft structures. This task was due for completion by m18 with deliverable D3, a report on the activity due at that time. The parts of the work concerned with design development of damage tolerant (DT) concepts were completed by partners Airbus D, Airbus UK, SABCA, ALCAN, and Piaggio. The subtasks concerned with manufacture and test of samples, to be done by Cranfield and by LTSM (Patras) has been delayed because of late supply of material. The former has been reported in deliverable D3.1, the latter will be reported in D3.2.

2.4.1 Task 2.2 Design of Damage Tolerant welded structure (Airbus Germany)

The major task accomplished in this period was the manufacture of FSW coupons in 3.2 mm thick 2198 T8 for testing by Cranfield University in the programme to establish the effect of bonded crack retarders on fatigue crack growth rates in these alloys. Additional materials such as bonding film and doublers were also supplied to CU. The retarders were attached to the samples at CU.

2.4.2 Task 2.2 and 2.5 Design of Damage Tolerance and long-term behaviour (Sabca)

Joint geometry characteristics:

- Joint is not at the highest stress point
- Area with increased thickness; after machining of FSW “traces”, the local thickness will be slightly reduced, so that the neighbouring section might act as a crack stopping device

- Fully welded joint design (by comparison to some other corner joints)

2.4.3 Task 2.2 Design of Damage Tolerant Welded Structure (Piaggio Aero)

Pai analyzed Damage Tolerance capability of structures defined in the task 2.1 all results were included in D3.1 deliverable.

Following inputs of Alenia Pai designed a new bulkhead test coupon and analyzed the model by a FE model.

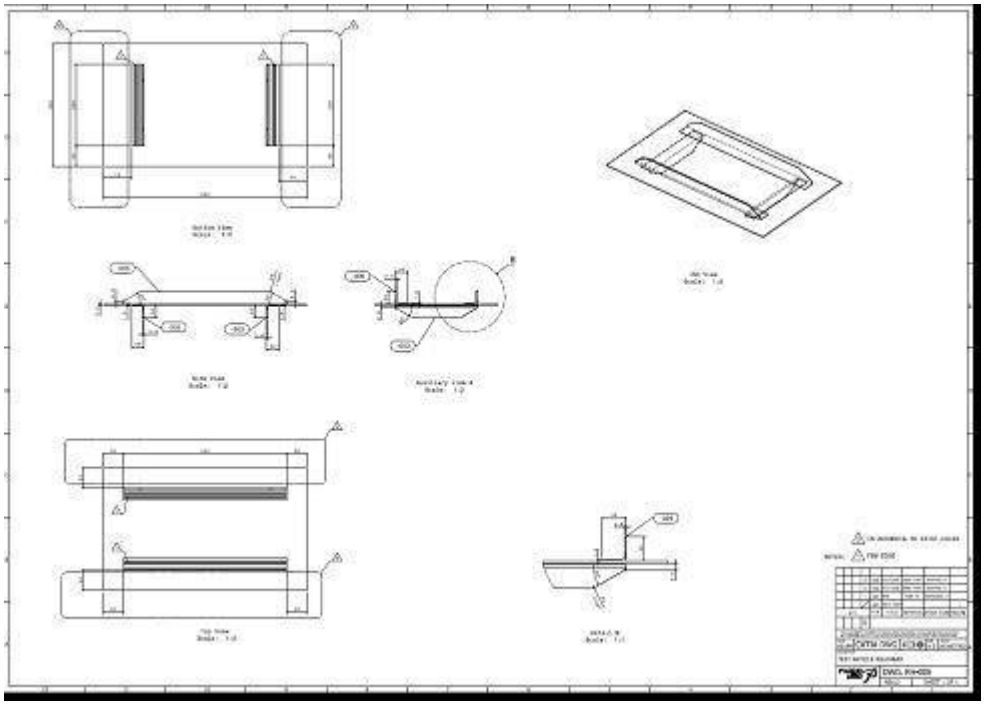

Figure 2: Design for new bulkhead test coupon

The scope of performed analysis was to verify fracture arrest capability of Friction Stir Welded stiffeners on a flat panel loaded along short sides and including a small initial crack.

The web is made of sheet Al 2056 (t= 3 mm), stiffener are extrusions Al 2024 .

Problems were encountered with the characterization of material Al 2056 so it was decided to use Al 2024 data.

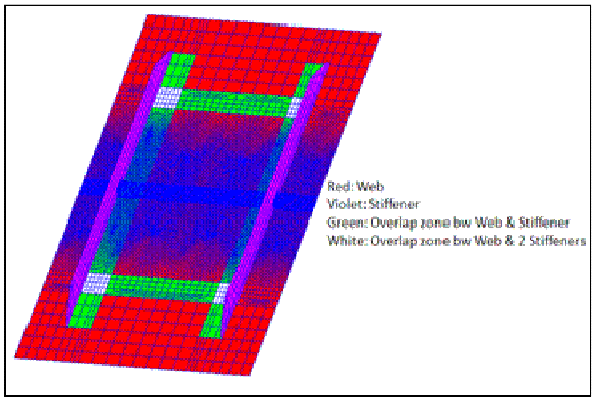

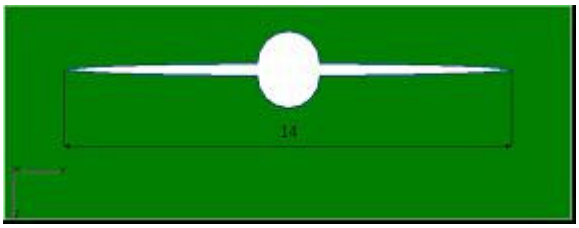

Residual Stresses due to welding have been taken into account. They have been introduced into the Heat Affected Zone (HAZ) by means of a "Stress Field Function" and are oriented in weld line direction.

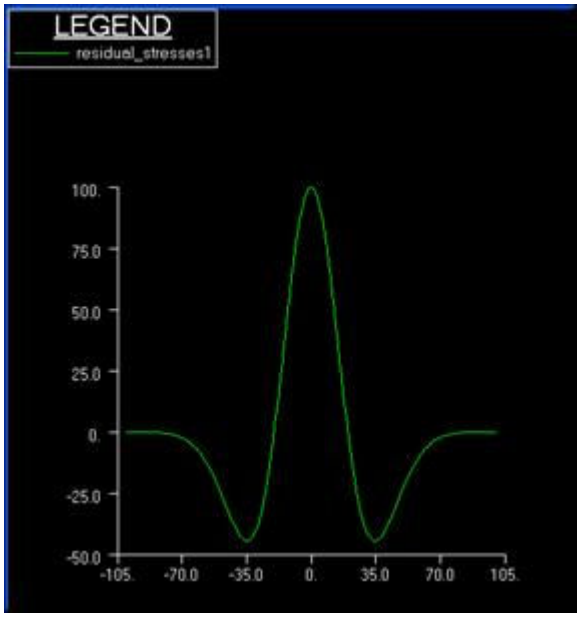

Figure 3: Residual Stress Distribution

Distribution law is:

$$\sigma_{res}(x) = \sigma_0 \cdot \left[1 - \left(\frac{x}{RL}\right)^2\right] \cdot e^{-0.5 \cdot \left(\frac{x}{RL}\right)^2}$$

σ_0 - the maximum residual stress (@ the centre of the weld seam) = 100 MPa
RL - half width of weld seam

Maximum residual stress value of 100 MPa has been read by experimental measurements.

Panel has been loaded with a cyclic tension load with a constant amplitude:
σ_{max} = 70 MPa; σ_{min} = 0 MPa, R = 0

Strain energy release rate for mode I, G_I, has been evaluated for each crack growth step by means of NASTRAN VCCT card, using an implicit non-linear solution (SOL 600).

Beta factors have been calculated from the well known expression:

$$\beta = \frac{K_I}{\sigma_{max} \cdot \sqrt{\pi \cdot a}}$$

Being the stress intensity factor for mode I, K_I, equal to:

$$K_I = \sqrt{G_I \cdot E}$$

Structure Life has been predicted by means of AFGROW, giving the calculated Beta values as user input.

Structure Life has been predicted by means of AFGROW, giving the calculated Beta values as user input.

The NASGRO equation has been used to calculate the crack growth rate:

$$\frac{da}{dN} = C \cdot \left[\frac{(1-f)}{(1-R)} \cdot \Delta K \right]^n \cdot \frac{\left(1 - \frac{\Delta K_{th}}{\Delta K}\right)^p}{\left(1 - \frac{K_{max}}{K_c}\right)^q}$$

Graph output of AFGROW is reported below (crack length vs. cycles).

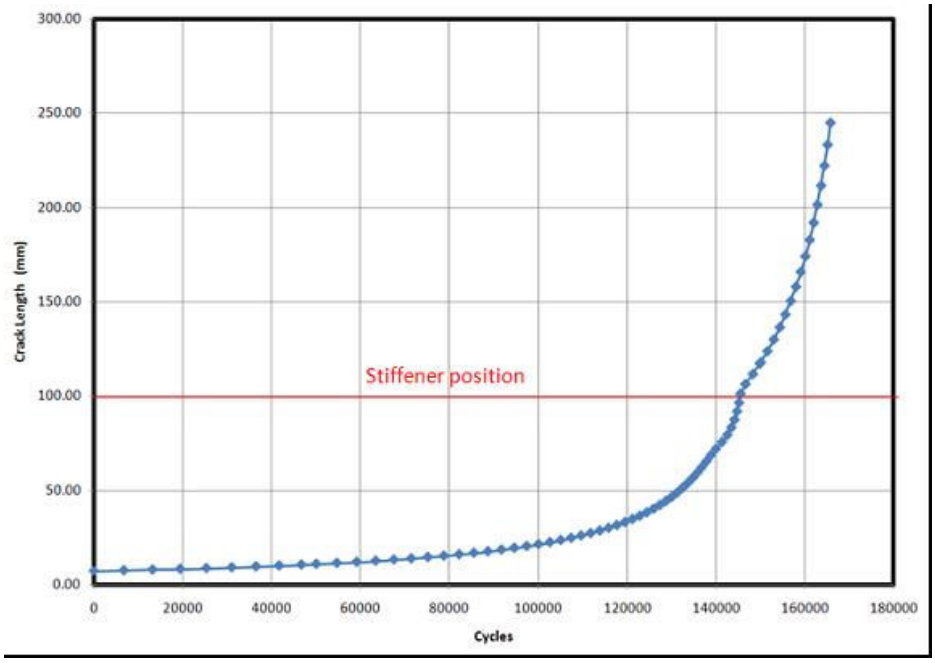

Figure 4: Graph output of AFGROW (crack length vs. cycles)

Analysis results will be validated from PAI by test on dedicated structures welded by Alenia.

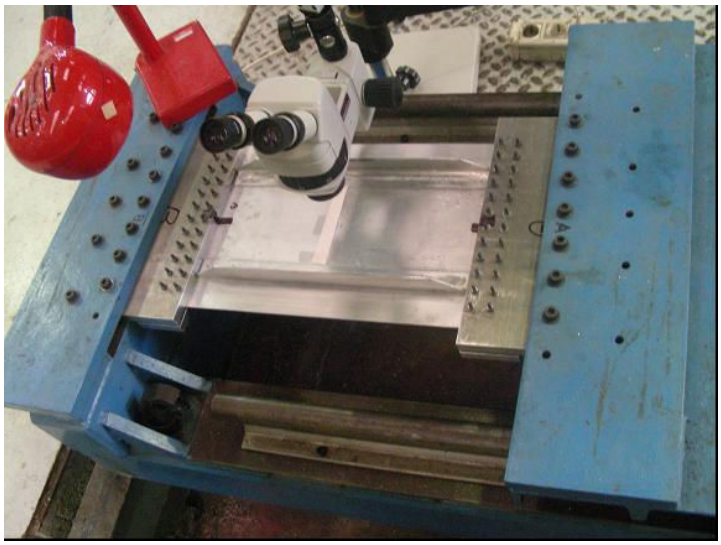

Figure 5: Visual inspection of crack

2.4.4 Task 2.2 Design of Damage Tolerant Welded Structure (ALCAN)

Crenellations and FSW added to damage tolerance panels in 2xxx alloys generate crack retardation (contribution to the deliverable D3.)

2.4.5 Task 2.2 Design of Damage Tolerant Welded Structures (Cranfield University)

In this period Cranfield has tested the crack retarder samples prepared by Airbus D. Fatigue crack growth rates have been measured and the effect of the retarders assessed.

Surface treatment was needed before adhesively bonding the strap to the sample surface. Airbus UK performed pickling, anodizing and priming for 10 ESE(T) samples. The bonded straps were of aluminium 2198, a similar alloy to the substrate. This would ensure that there were minimal residual stresses developed during the adhesive bonding elevated temperature cure cycle as stiffness and coefficient of thermal expansion of the two alloys would be very similar. There were two designs of straps: 45 x 3.2 x 382 mm; 30 x 3.2 x 382 mm. The thickness of the material for 2198-T8 strap was 3.2 mm; the stiffness ratio was 0.1 and 0.07 corresponding to the two different strap widths of 45 and 30 mm.
The stiffness ratio μ was defined as below:

$$\mu = \frac{E_{strap}A_{strap}}{E_{strap}A_{strap} + E_{smaple}A_{sample}} = 0.1$$

Where E_{strap} and E_{sample} are Young's modulus of the strap and substrate materials and A_{strap} and A_{sample} are the cross sectional areas of the strap and the sample.

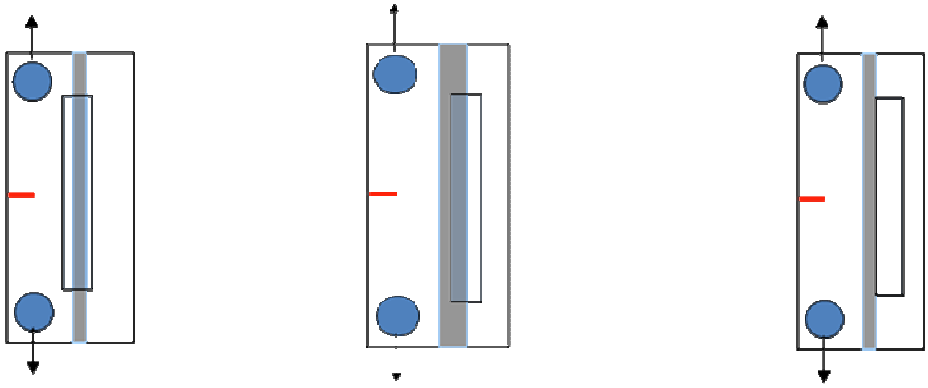

Figure 6:Alternative positions of the crack retarder with respect to the weld in ESET samples of 2195

Two sample types were used to evaluate the effects of the retarders, M(T); used for 3.2 mm thick samples of 2198 T8 alloy, and ESET; used for 8 mm thick samples of 2195 alloy. For the 2195 alloy the retarder was positioned over the welds in three different locations with respect to the welds as shown in Figure 6 Sample dimensions were 370 X 100 mm. For the 2198 M(T) samples in double and single weld configurations, the retarders were positioned as shown in Figure 7.

Figure 7: Positions of retarder straps in 2198 single (left) and double weld (right) configurations.

M(T) sample dimensions were 750 X 300 mm and 550 X 200 mm. The procedures used for bonding the strap to the sample were the same as for the 8 mm ESE(T) samples. The strap dimensions were 27 mm wide, 3.0 mm thick and with a length of 390 mm. The Stiffness Ratio μ was 0.2. The half notch length for all samples was 6.0 mm. Selected examples of fatigue crack growth results are shown in Figure 8 and Figure 9.

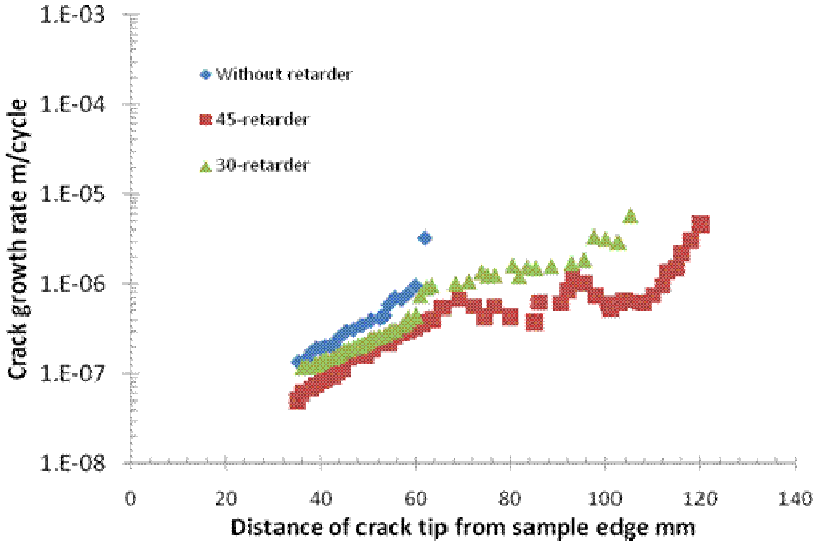

Figure 8: Comparison of fatigue crack growth rates plotted against crack length in mm in ESET samples of 2195 welds without retarder, and with 30 mm and 45 mm wide retarders.

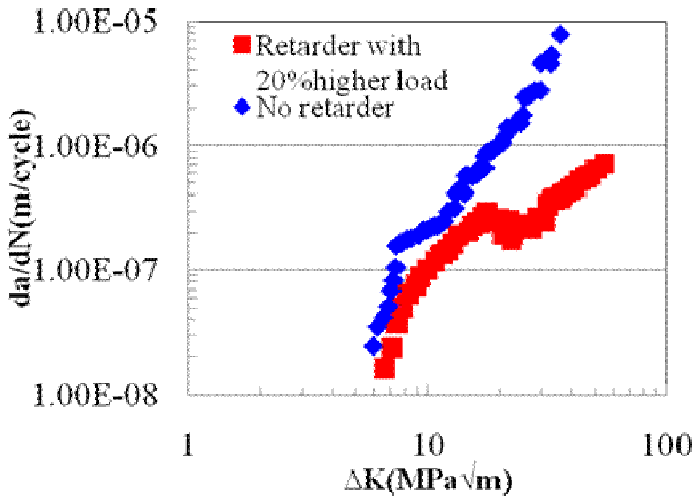

Figure 9: da/dN Vs ΔK, 200 mm wide MT sample; centreline longitudinal weld, crack growth rates with retarder strap with those in sample without strap. Retarder sample tested at 20% greater nominal load to maintain same nominal stress level as sample without strap

Figure 8 and Figure 9 both show that bonding the strap produces significantly reduced growth rates compared with both M(T) and ESET samples. There was little effect of small changes in strap location with respect to the weld.

2.4.6 Task 2.2 Design of Damage Tolerant Welded Structures (University of Patras)

Open hole fatigue tests

In this period the University of Patras conducted open hole endurance tests on samples of 2198 and 2139 containing FSW. The welds were transverse to the loading axis and the hole was placed at different locations with respect to the weld line, one set on the weld centreline and the other displaced laterally about 5 mm. It was concluded that FSW 2139 had slightly better fatigue performance than 2198, and that the hole position with respect to the weld line had no effect.

A total of 52 fatigue tests were carried out. The tests performed are summarized in Table 1 below. All tests were performed according to the ASTM E466 specification.

Tests	FSW location	Material	Number of coupons
kt = 2.5 R=0.1	Hole in TMAZ	2198 T8 FSW	13
kt = 2.5 R=0.1	Hole in the nugget	2198 T8 FSW	13
kt = 2.5 R=0.1	Hole in TMAZ	2139 T3 FSW	13
kt = 2.5 R=0.1	Hole in the nugget	2139T3 FSW	13

Table 1: Open hole fatigue tests

Two discrete cases for each material were tested: the hole being in the centre of the nugget and the hole being at a distance of 5mm from the weld centre. The distance of 5mm was chosen as the width of the weld was 10mm and therefore, the weld interface which is considered to be the weakest area of the weld is located at 5mm from the weld centre. This was also confirmed by microhardness measurements performed (Figure 10). Test results are presented in Figure 12 and Figure 13.

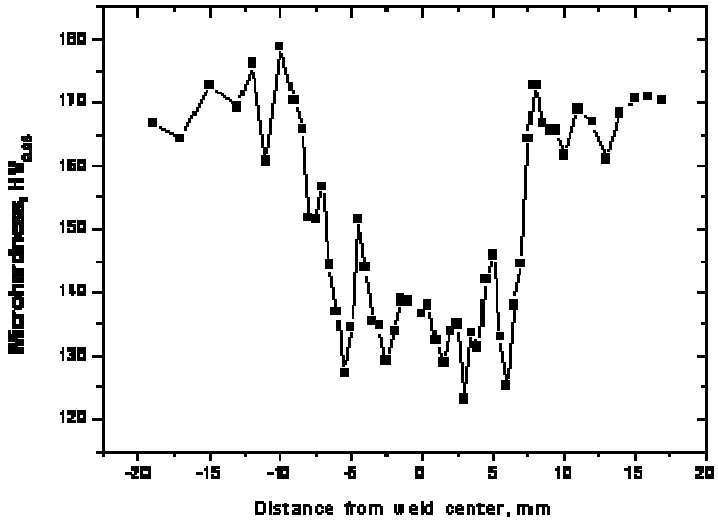

Figure 10: Microhardness profile along the specimens length. The weld centre is located at x=0

Figure 11: Test specimen after failure

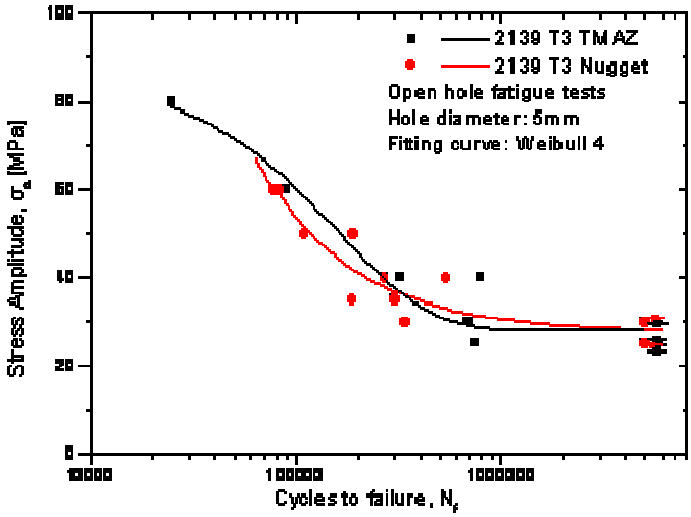

Figure 12: S-N curves of 2139T3 with the hole in the centre of the nugget and in the TMA

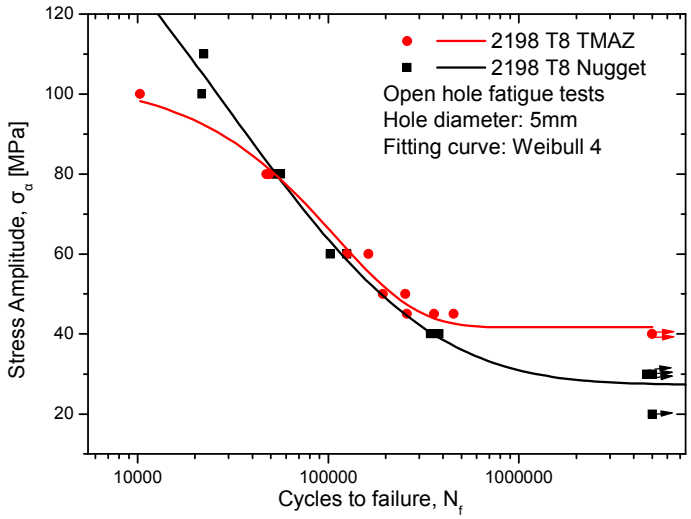

Figure 13: S-N curves of 2198T8 with the hole in the centre of the nugget and in the TMAZ

Main findings

- 2198 T8 exhibits a slightly improved fatigue behaviour compared to 2139 T3. This is more obvious in the case where the hole was on the TMAZ-nugget interface where a difference of about 15MPa stress amplitude was recorded for the fatigue limit. However, due to the limited number of tests, the figures can only be used as estimates.

- Comparing the fatigue behaviour according to the location of the holes, no significant differences are observed. This indicates a good weld quality, as the weld interface does not exhibit inferior behaviour with respect to the weld nugget.
- The fatigue behaviour in the high cycle fatigue region is almost identical, whereas in the case of 2198T8, the fatigue limit seems to be higher when the hole was in the TMAZ. The fatigue limit, however, cannot be precisely defined as a very limited number of tests were performed in the fatigue limit region.

2.4.7 Task 2.2 Design of Damage Tolerant Welded Structure (Airbus UK)

The major task accomplished in this period was the manufacture of FSW coupons in 3.2 mm thick 2198 T8 for testing by Cranfield University in the programme to establish the effect of bonded crack retarders on fatigue crack growth rates in these alloys. Additional materials such as bonding film and doublers were also supplied to CU. The retarders were attached to the samples at CU.

2.5 Task 2.3 Effect of Residual Stresses on Design

Task 2.3 aims to develop models to predict the fatigue crack growth behaviour of welded integral structures containing weld residual stresses.

2.5.1 Task 2.3 Effect of Residual Stresses on Design (Airbus Germany)

The effect of residual stresses on fatigue crack growth is investigated in collaboration with CU. The investigation is looking to crack growth in un-reinforced specimens as well as to crack growth in coupons having bonded crack retarders.

Contribution of AD was to weld the coupons out of Al-Li 2198 T8 and to deliver them to CU. Additional materials like doublers and bonding film was provided to CU. The coupons were bonded at CU.

2.6 Task 2.3 Effect of Residual Stresses on Design (EADS France)

During the final period of the Project (last 18 months), a simulation of crack growth taking into account residual stresses was performed (Task 2.3).

The objective of this work was to understand and predict the influence of a FSW seam on the crack growth behaviour.

The considered welding case was the 2050 T34 Al-Li alloy, welded in 14.8 mm thick using the Bobbin Tool technique in a butt configuration.

ABAQUS code was used for all calculations. Only the effect of residual stresses was investigated. The influence of metallurgy could not be taken into account in the simulation.

Fatigue crack growth tests have been performed on base and welded materials. Testing samples were CTW75 (largest possible samples considering the limited available welded material).

Tests have been performed with a crack parallel to the seam and located on the seam axis (Figure 14).

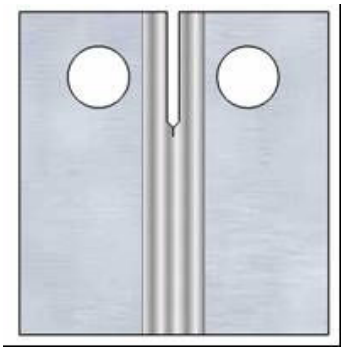

Figure 14: Seam position within CTW75

This choice was made for two reasons:

Cracks are far less prone to deviation when they are parallel to the seam.

A crack within and parallel to the seam advances in an homogeneous material (stress and micro-structure), which gives results easier to analyse.

Tests have been performed on base material and welded material for three R ratios: 0.1, 0.4 and 0.7.

For each R ratio, the da/dN curves for welded material and base material have been compared (Figure 15, Figure 16 and Figure 17).

Then, parameters of a modified Forman's law have been identified for both materials (Figure 18 and Figure 19).

The expression and parameter values of the modified Forman law are given hereafter.

$$\frac{da}{dN} = \frac{C \cdot \Delta K^m}{(1-R)^q K_c - \Delta K}$$

Material	*C*	*m*	*q*	K_c
Base	1.5 10-5	2.2	0.7	40
Welded	1.65 10-5	2.6	0.22	65

Table 2: Parameters of Forman's fatigue law

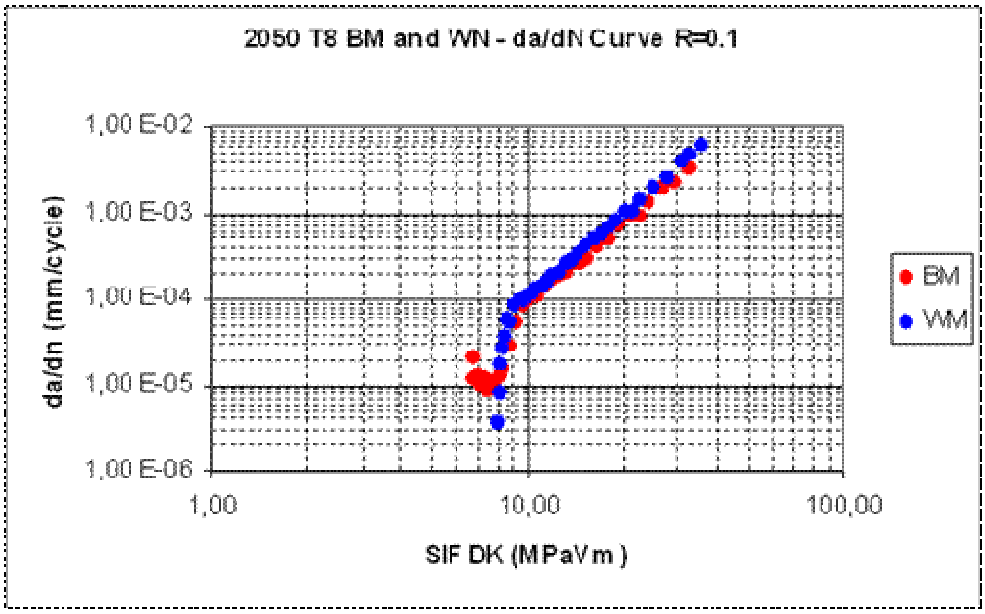

Figure 15: da/dN curves for welded and base material - R=0.

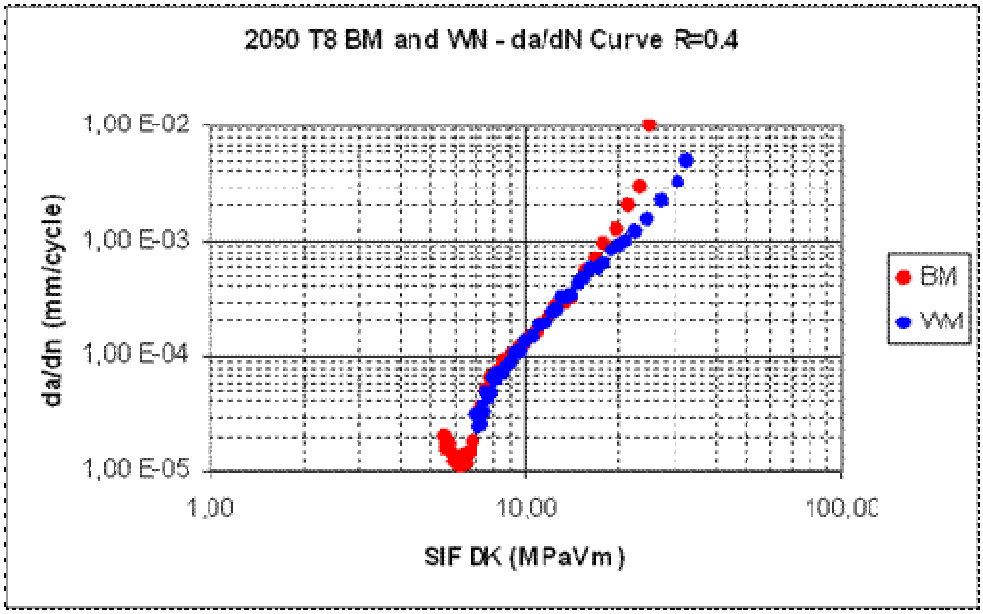

Figure 16: da/dN curves for welded and base material - R=0.4

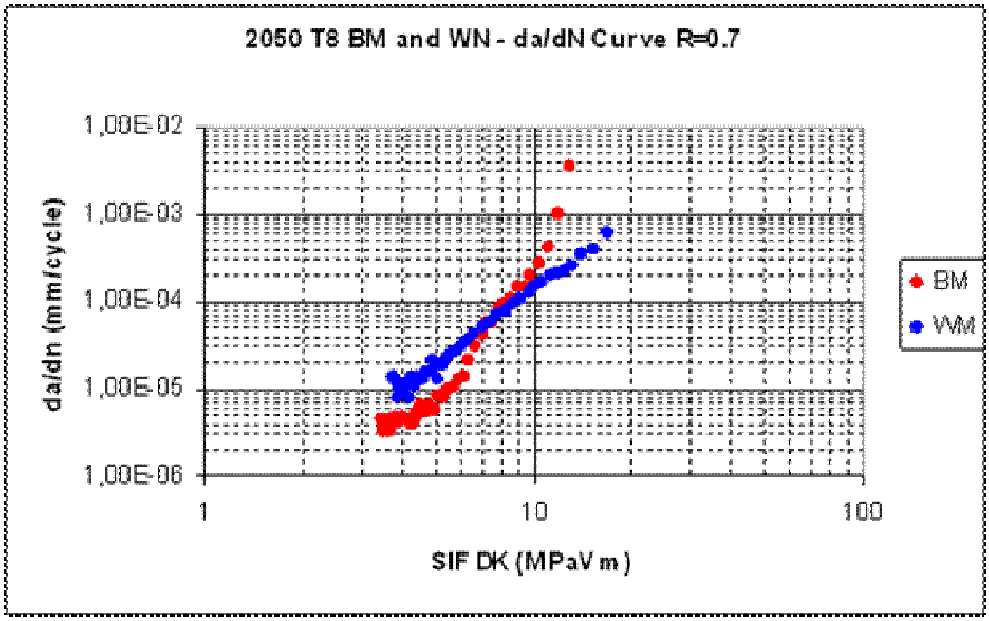

Figure 17: da/dN curves for welded and base material - R=0.7

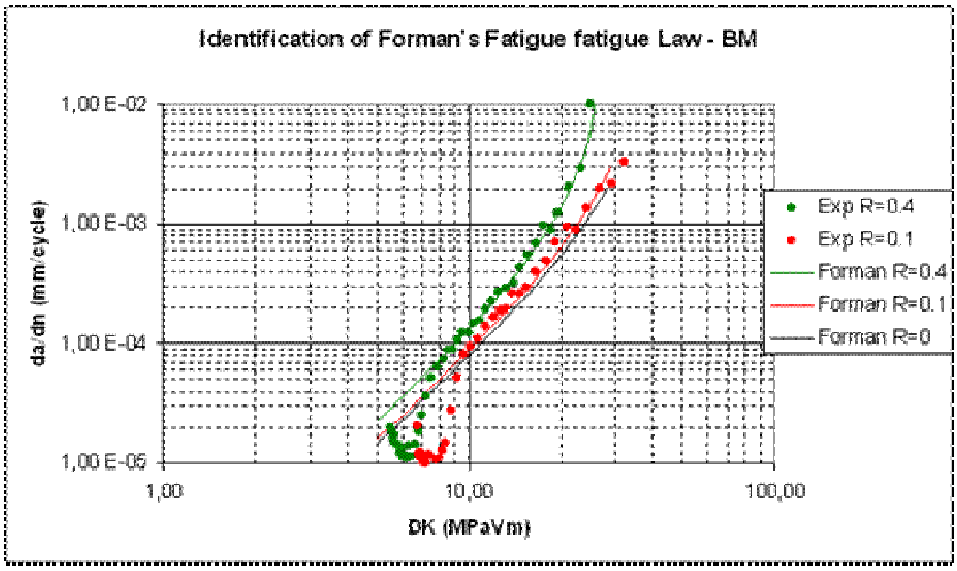

Figure 18: Experimental da/dN curves and identified Forman's law for base material

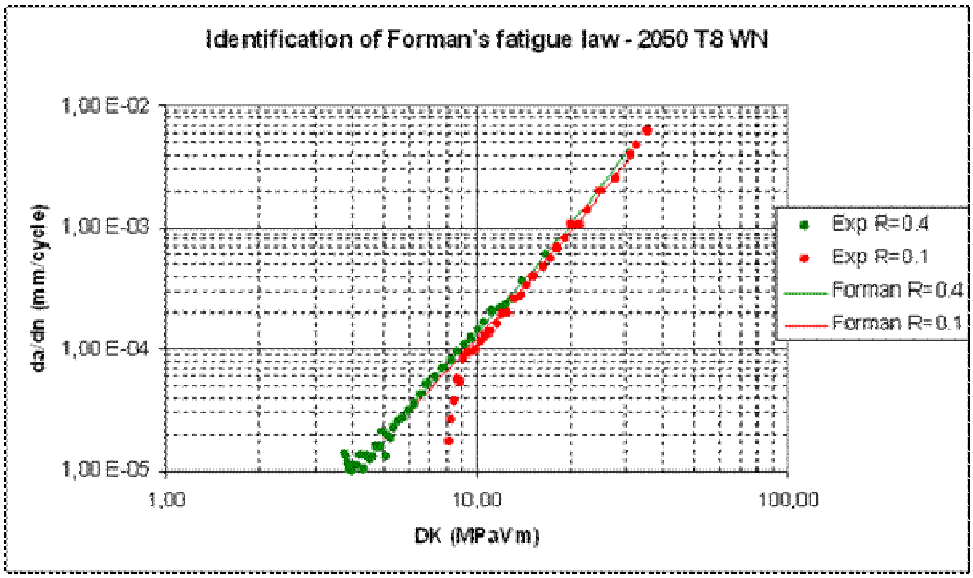

Figure 19: Experimental da/dN curves and identified Forman's law for welded material

Fatigue behaviours for base and welded materials seemed to be similar, at least for middle-range ΔK. This was true for R=0.1 and R=0.4. For R=0.7, da/dN curves were very different, with the base material exhibiting a rather low resistance even for middle range ΔK. Since this result was a bit surprising, added to the fact that the crack exhibited a significant amount of deviation, it has been decided not to consider this latter result (R=0.7) for the rest of the study.

Computed residual stresses have been introduced into a CTW75 model in order to compute stress-intensity factors as a function of crack length (Figure 20).

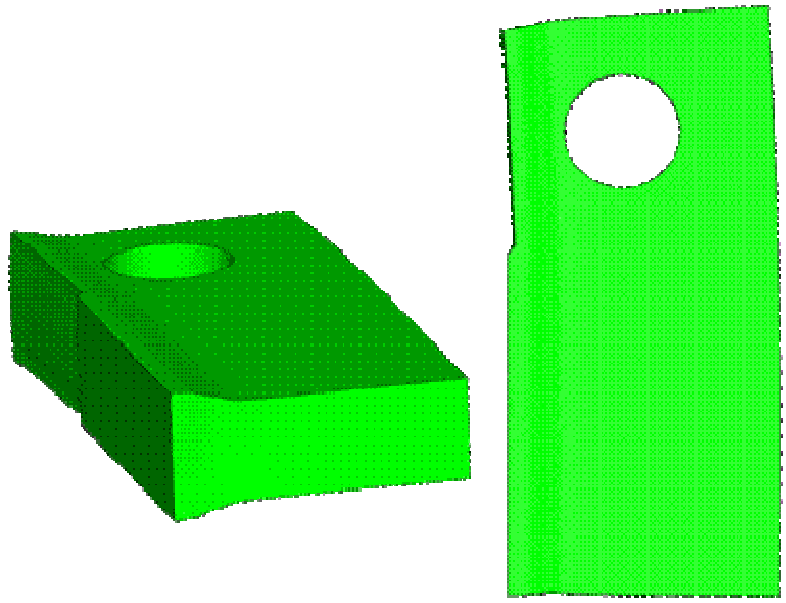

Figure 20: Simulated residual-stress-induced distortions on a CT specimen (magnified)

The objective was to compute the crack length "a" as a function of the number of cycles.

Two functions had to be known:

- da/dN as a function of ΔK and R (given by the Forman's law),
- K as a function of a (given by FE simulation).

When the residual stresses are implicitly considered (integrated within welded material fatigue law), ΔK and R are defined by the following relationships:

$$\Delta K = K_{\max} - K_{\min} = K^{Load}{}_{\max} - K_{\min}{}^{Load}$$

$$R = \frac{F_{\min}}{F_{\max}} = \frac{K_{\min}}{K_{\max}}$$

When the residual stresses are explicitly taken into account (by the use of base material fatigue law + the integration of residual stresses into the computation of stress intensity factors), ΔK and R are defined by the following relationships:

$$\Delta K = K^{Load}{}_{\max} + K^{Res} - K_{\min}{}^{Load} - K^{Res} = K^{Load}{}_{\max} - K_{\min}{}^{Load}$$

$$R = \frac{K_{\min}}{K_{\max}} = \frac{K_{\min}^{Load} + K^{Res}}{K_{\max}^{Load} + K^{Res}}$$

The difference between the two approaches lies into the R ratio, which is a correction of the apparent R ratio.

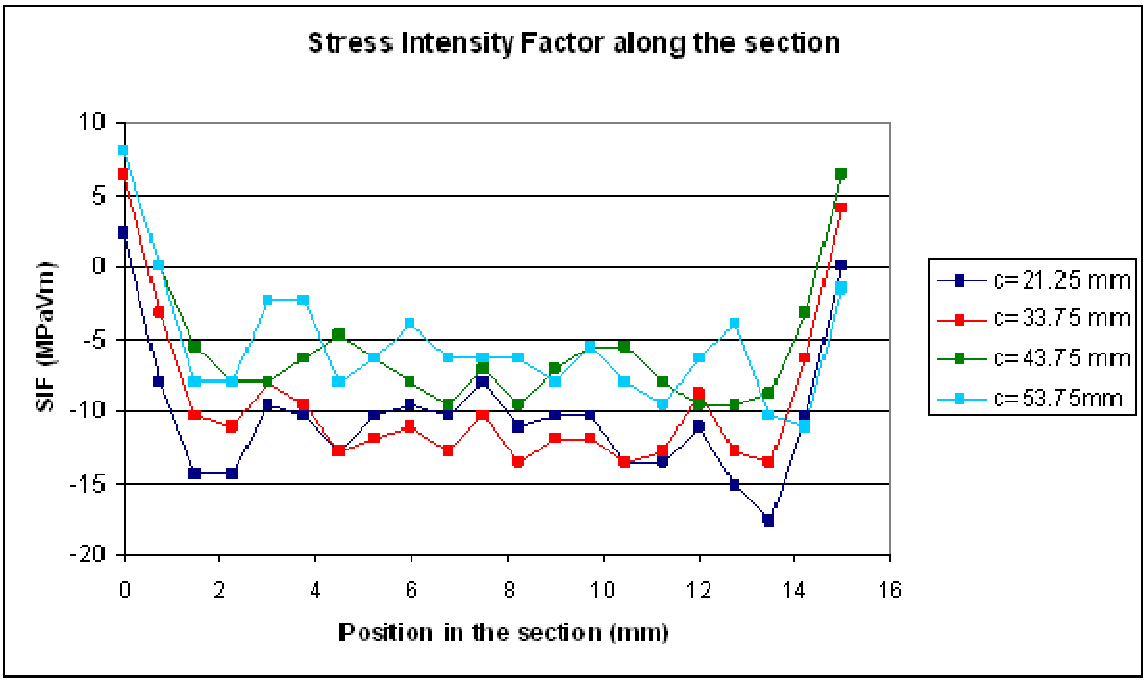

Figure 21: Computed RS-induced stress intensity factor as a function of the position into the sample thickness and crack length

Figure 21 presents the residual-stress-induced stress intensity factors as a function of crack length and position into the sample thickness.

The simulation of welding has been performed with 2050T34 material properties. To take into account the effect of thermal treatment (T34->T8), a 20% stress reduction has been applied before computing stress intensity factors. The stress-intensity factors have then been averaged along the sample thickness (excluding surface points) since only a 1D crack law is usable with the followed procedure.

Influences of residual stresses on stress intensity factors and R ratio are presented on Figure 23 and Figure 24. Delta K is not significantly impacted (only when K_{min} is negative; which is not physical so K_{min} is set to zero). R ratio is deeply impacted.

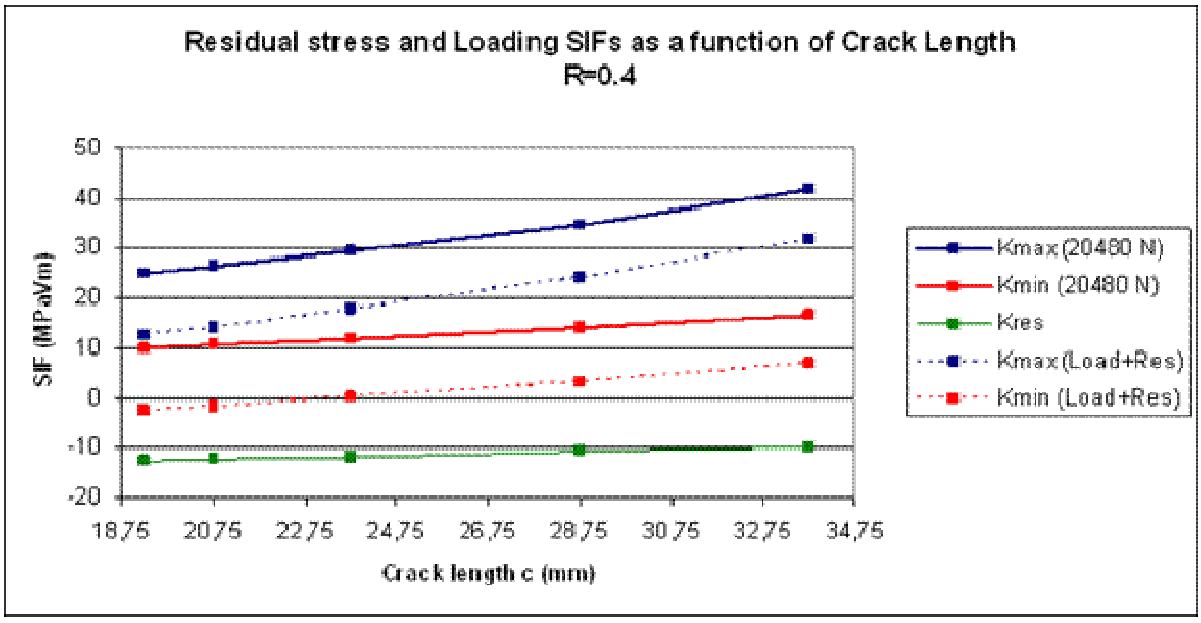

Figure 22: Stress intensity factor as a function of crack length

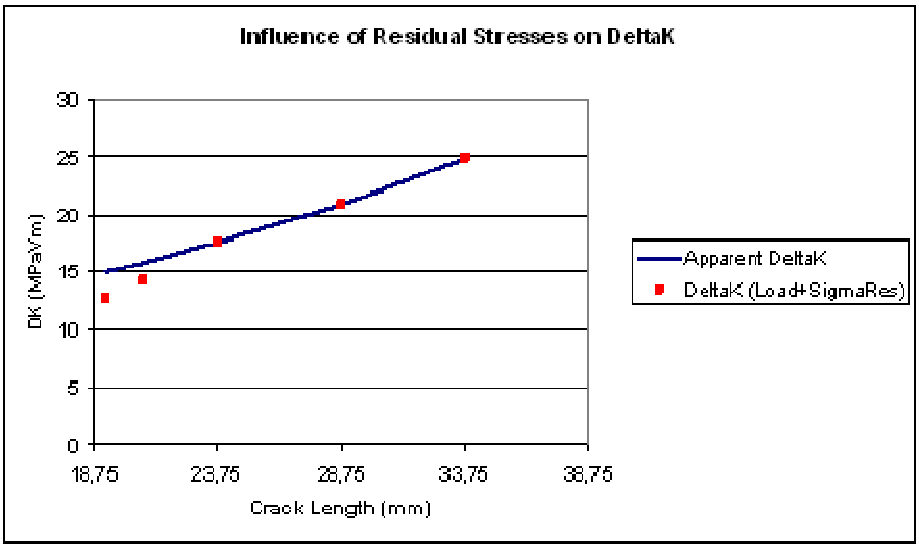

Figure 23: Influence of residual stresses on Delta K

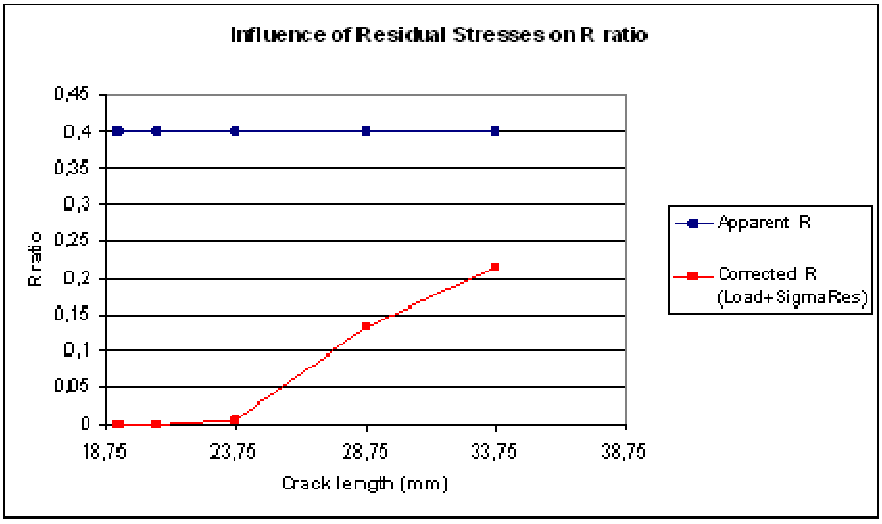

Figure 24: Influence of residual stresses on R-Ratio

A simulation of crack growth has been performed in order to compare explicit and implicit integration of residual stresses. Loading has been chosen so that applied deltaK are in the range of validity of the identified Forman's fatigue law. Figure 25 presents the results (crack length versus number of cycles). The blue curve was obtained with the fatigue properties of the welded material (implicit integration of residual stresses). The red curve was obtained with the fatigue properties of the base material and the explicit integration of residual stresses in the computation of stress intensity factors. A large difference between the two curves was observed. With the welded material properties (blue curve), the number of cycles for the same crack length was half the one for the base material + residual stresses. For a good agreement between the two curves, residual stresses had to be divided by 4 (red dashed curve).

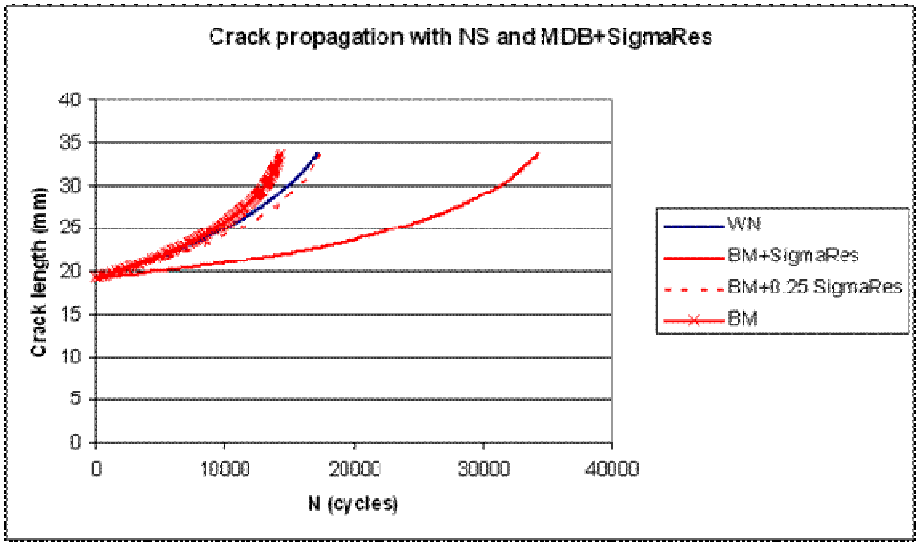

Figure 25: Computed stress intensity factors with residual stress implicitly or explicitly taken into account

2.6.1 Task 2.3 Effect of Residual Stresses on Design (GKSS)

In this period GKSS measured weld residual stresses in CT and ESET samples of 8 mm thick FSW 2195 using neutron diffraction. They have also measured residual stresses in samples of 2198 T8 of 3.2 mm thickness. Both plane coupons containing single & double welds and ones containing pad ups were measured. These measurements were made using synchrotron source radiation at DESY. Considerable difficulty was had in interpreting the latter set of results because of preferred grain orientation issues in the thinner samples.

8 mm thick 2195 samples

There were two samples geometries CT and ESET, and the generic shapes are shown in Figure 26 below.

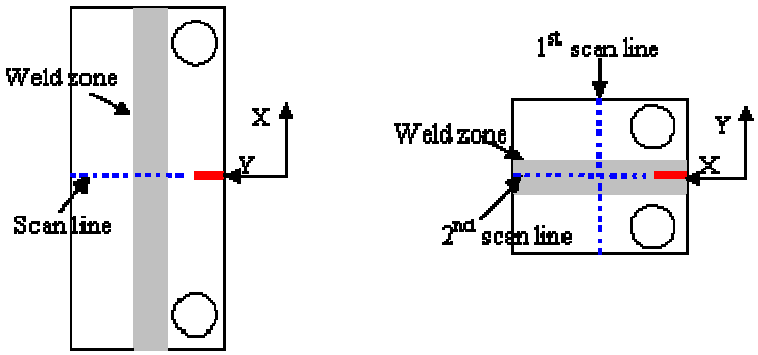

Figure 26: Examples of the ESET and CT samples containing FSW welds as indicated

Each geometry was in 3 different sizes. For ESET these were 148 X 40 mm, 185 X 50 mm and 370 X 100- mm. For CT samples the dimensions were 87.5 X 84 mm, 125 X 120 mm and 250 X 240 mm.

The residual stress measurements were carried out using the neutron diffractometer ARES-2. Neutrons of 0.164 nm wavelength were chosen with a Silicon (311) monochromator. Each specimen was scanned three times to measure the three independent strains in longitudinal (LD), normal (ND), and transverse (TD) directions. The gauge volume was defined by primary and secondary Cd slits with a height of 6 mm (ND/TD) or 3 mm (LD) and a width of 3 mm. These slits form a gauge volume with a nominal size of 3 mm × 3 mm × 6 mm (ND/TD) and 3 mm × 3 mm × 3 mm (LD). The gauge volume was placed at the middle of the sheet thickness. A gas filled DENEX area detector was used to measure the peak shift of the Aluminium (311) reflection at an angle of 84.4°. The (311) reflection is recommended because of its isotropic characteristics providing access to the macro stresses. The measured diffraction peaks were fitted with a Gaussian function. The approximation of a biaxial stress state was made for the calculation of stress-free lattice parameters and stresses.

Examples of the data generated for ESET samples and CT samples parallel to the weld is shown in Figure 27 and Figure 28.

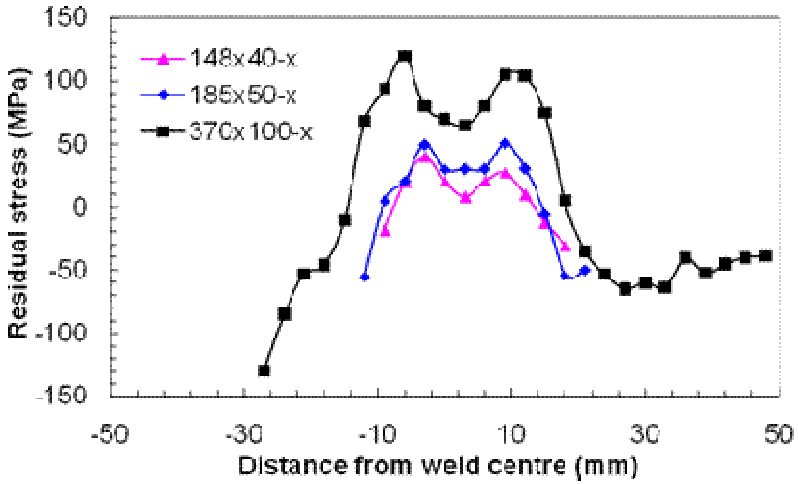

Figure 27: Residual stresses parallel to the central FSW weld in 3 sizes of ESET samples

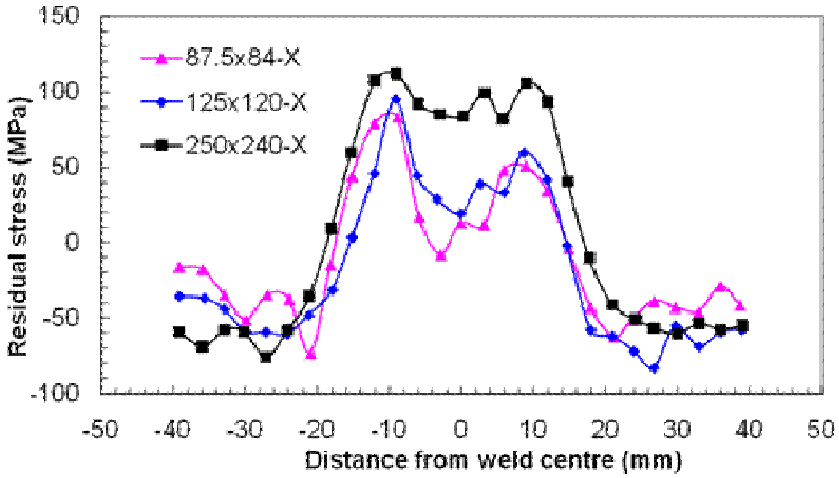

Figure 28: Residual stresses parallel to the FSW weld in 3 sizes of CT samples in 2195 aluminium alloy.

Residual stresses in 3.2 mm samples of 2198 T8 samples

The residual stress measurements were carried out at the GKSS high energy synchrotron beam line HARWII at DESY in Hamburg. A photon energy of 70 keV (wavelength: 0,177 Å) was chosen using a SiGe monochromator. The scans were performed perpendicular to the weld seam, if no other direction is stated. All specimens were scanned in transmission geometry. A Mar345 Image plate detector system and a Mar 555 flat panel detector were used to measure the Diffraction patterns (Debye-Scherrer rings).

Test samples

A wide range of test sample geometries, including 4 skin – stringer panel concepts were investigated. The complete list is shown in Table 3 below.

ScanName	Name	Dimensions [mm²]	Spatial Resolution [mm]
Cranfield			
FSW_coins01	2 pieces padded up welds	each 160 × 500	2
FSW_coins02	Single weld – 3 scans	300 × 750	1 / 3
FSW_coins03	Double weld – 3 scans	300 × 750	1 / 3
FSW_coins04	Single weld – 3 scans parallel to weld 1 and 3 BM 2 weld	100 × 300	2

Airbus Concepts			
FSW_airbus_01	Concept 1	Full panel	0.4 / 2
FSW_airbus_02	Concept 3	Full panel	0.4 / 2
COINS04_01	Concept 4	Full panel	0.5 / 2
COINS04_02	Concept 2	Full panel	0.5 / 2
COINS04_05	*Concept 1*	*Part 6*	*0.5 / 1 / 2*
COINS04_06	*Concept 1*	*Part 4*	*0.5 / 1 / 2*
COINS04_07	*Concept 3*	*Part 6*	*0.5 / 2*
COINS04_08	*Concept 3*	*Part 4*	*1 / 2*
Coins05_01	Concept 1	Part 3	1
Coins05_02	Concept 1	Part 3	1
COINS04_03	MTB1-1		0.5 / 3
Italic := data cannot be evaluated			

Table 3: Samples types investigated on DESY synchrotron

Items 02,03 and 04 were M(T) coupon samples containing either single central welds with a crack starter located on the weld centreline or a M(T) coupons with a double weld with the crack starter symmetrically placed between the welds. Items in italic in Table 3 resulted in data which could not be evaluated due to preferred orientation and coarse grain problems.

The data in non italic cannot be post processed in the conventional way. The solution was to integrate very large slices of the Debye-Scherrer rings to smooth the peaks in a statistical way. This leads to an inherent loss of information on the orientation of the measured strains and stresses.

A novel post processing schema and numerical code were developed and implemented to improve this issue. The steps of this procedure are:

- Automated fitting of the centre of the diffraction patterns
- Indexing of all available Aluminium (311) and Copper (220) reflexes
- Normalisation of the sample-detector-distance using the Copper reference
- Determination of the in-plain strain tensor components from a large number of permutations consisting of three Al (311) reflexes each
- Determination of the principal strain components in the in-plain strain tensor
- Derivation of the plain stress tensor from the mean principal in-plane strain values
- Calculation of the (LD) and (TD) stress values.

This approach provides a way to deal with textured material and large grain sizes. The statistical evaluation of reflexes that may be caused by single grains allows a transition from the 2nd and 3rd order residual stresses to the global 1st order values. This is archived without losing the information on stress orientation.

Examples of residual stresses obtained are shown in Figure 29 & Figure 30 below.

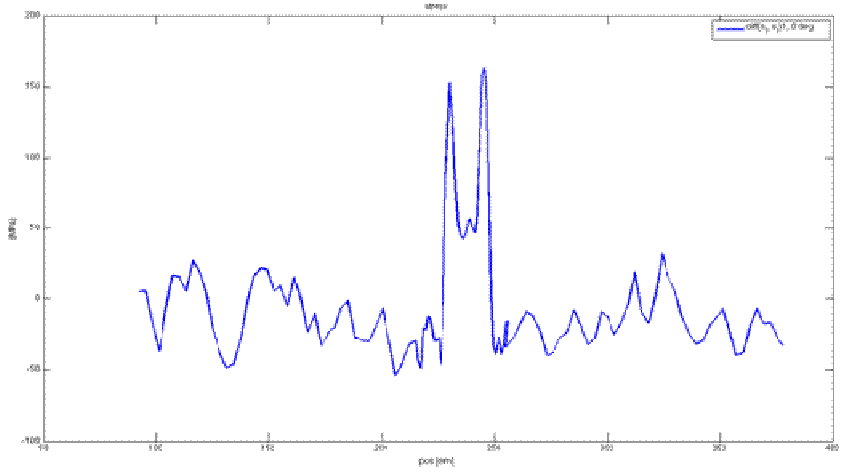

Figure 29: Residual stress field from 3.2 mm M(T) sample 750 X 300 mm with single central FSW longitudinal weld 2198 T8

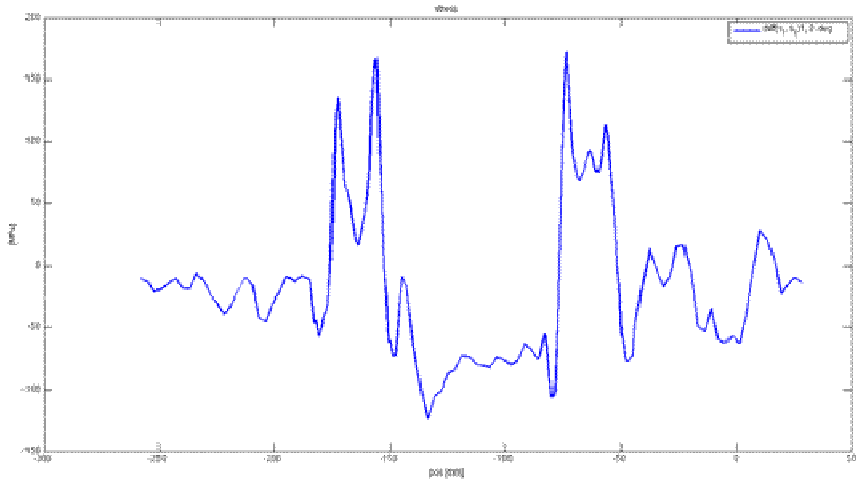

Figure 30: Residual stress field from 3.2 mm M(T) sample 750 X 300 mm containing double weld. A central region of compressive stress between the tensile fields within the welds can clearly be seen

2.6.2 WP2.3 Effect of Residual Stresses on Design (Cranfield University)

In this period Cranfield University has continued to measure and model the effects of residual stress on fatigue crack growth rates by conducting fatigue crack growth rates on 3.2 mm thick M(T) samples of 2198 T8 in a range of sizes containing single and double FSW welds; evaluating them in comparison with the 1.6 mm samples in this material measured earlier. Modelling & prediction of the effects of residual stress has continued by considering the response to compressive residual stress fields.

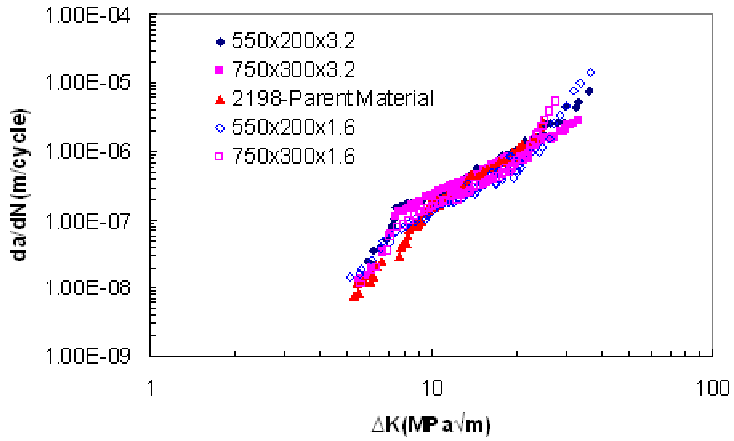

Figure 31: Comparison of crack growth rates in FSW 2189 T8 sheets with 1.6 and 3.2 mm thicknesses and two sample lengths; there is little or no effect on crack growth rates

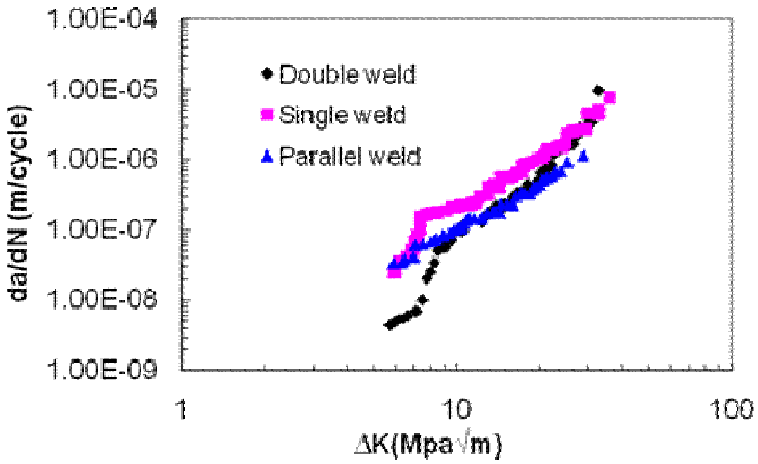

Figure 32: Comparison of fatigue crack growth rates in 3.2 mm 2198 T8 containing FSW with 3 weld orientations; longitudinal double weld, single central weld and a parallel (transverse) weld

Figure 31 shows that there is little or no effect of sample size or thickness on fatigue crack growth rates in 3.2 mm 2198 T8, implying that the residual stresses are similar in all of the samples. On the other hand, Figure 32 shows a comparison of single central weld with double weld and a transverse

weld in the same size of 3.2 mm thick 2198. The single weld with the crack starting in the tensile residual stresses has fastest growth rates, whereas the double weld with the crack starting in the compessive stress field between the welds has the slowest rates. At longer crack lengths these rates become identical with those in the transverse weld where the crack is propagating in the weld nugget throughout and will have reduced growth rates in the very ductile fine grained material there.

Modelling work

The crack closure method becomes necessary for predicting crack growth rates when there are compressive residual stresses, e.g. crack propagating towards a weld. For the crack closure approach, two methods have been used in this project to calculate the effective SIF range (ΔK_{eff}). The first is based on the Newman's crack-tip elastic-plastic analysis that results in a well-established correlation of crack opening stress (S_{op}) with the applied stress ratio (R). To account for welding residual tresses, the effective SIF ratio (R_{eff}) is used to replace the nominal applied R in the original Newman's equation. Using this equation can avoid FE modelling; hence it is interesting to investigate the application scope and accuracy of this analytical equation.

$$f = \frac{S_{op}}{S_{\max}} = A_0 + A_1 R + A_2 R^2 + A_3 R^3 \qquad (\mathrm{R} \geq 0)$$

$$f = \frac{S_{op}}{S_{\max}} = A_0 + A_1 R \qquad (-1 \leq \mathrm{R} < 0)$$

The expressions for the coefficients A_0, A_1, A_2, and A_3 can be found in [7]. Then the effective stress intensity factor range ΔK_{eff} is given by:

$$\Delta K_{eff} = \Delta K (1 - f) / (1 - R)$$

An alternative to the aforementioned analytical or empirical equations is numerical modelling of crack closure behaviour under combined residual stress and applied mechanical stress field. Crack opening stress (S_{op}) is determined by either the calculated crack opening displacement or a criterion based on crack tip stress changing from compressive to tensile. This modelling approach is time consuming and computational intensive, but it should give more quantitative results by considering more influential factors and their interactions. For example, it can model the material cyclic plasticity behaviour, e.g. cyclic strain hardening, and crack-tip constraint (e.g. 2D vs. 3D). Examples of the finite element meshes used are shown in Figure 33, and predicted and experimental crack length Vs cycles curves in Figure 34.

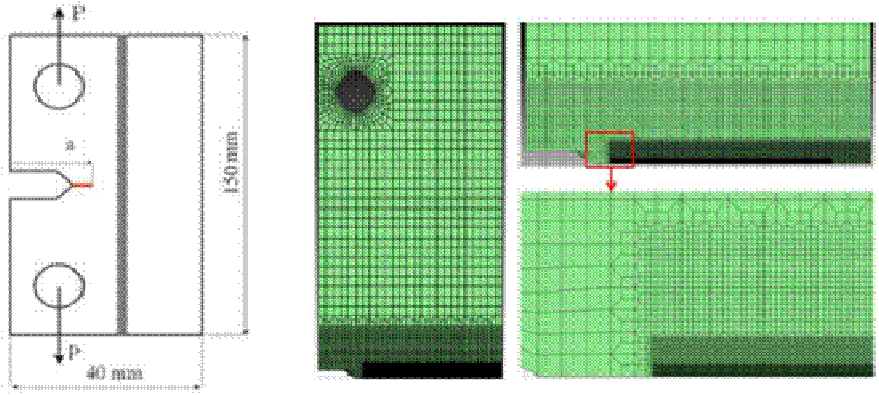

Figure 33: ESET test sample and FE model for calculating crack opening stress

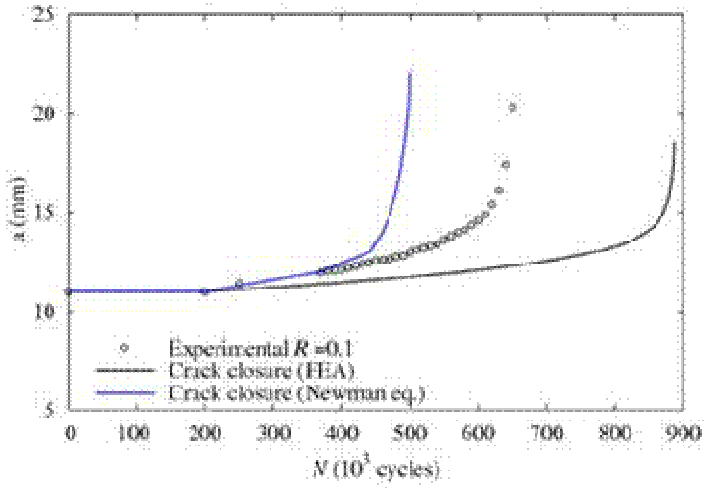

Figure 34: ESET test sample predicted & measured fatigue crack length Vs fatigue cycles growth

2.6.3 WP2.3 Effect of Residual Stresses on Design (University of Patras)

2.6.4 Fatigue testing of 2195 welded material with longitudinal weld

During the reporting period, the fatigue behaviour of 2195 material with two different weld configurations was evaluated. The two different specimen types tested were:

Type 1 specimens had a reduced cross section which consisted of the weld zone as well as non-welded material (Figure 35). The total width of the reduced section was 60mm, which consisted of 30mm weld zone and 50mm non-welded material.

Type 2 specimens had a reduced cross section which consisted only of the weld zone, the width of which was 30mm (Figure 36).

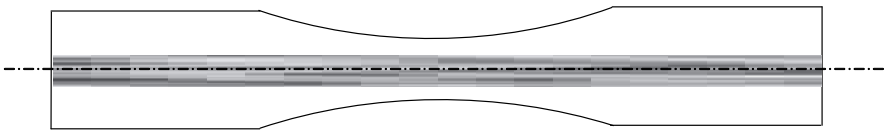

Figure 35: Dog-bone specimen geometry type 1

Figure 36: Dog-bone specimen geometry type 2

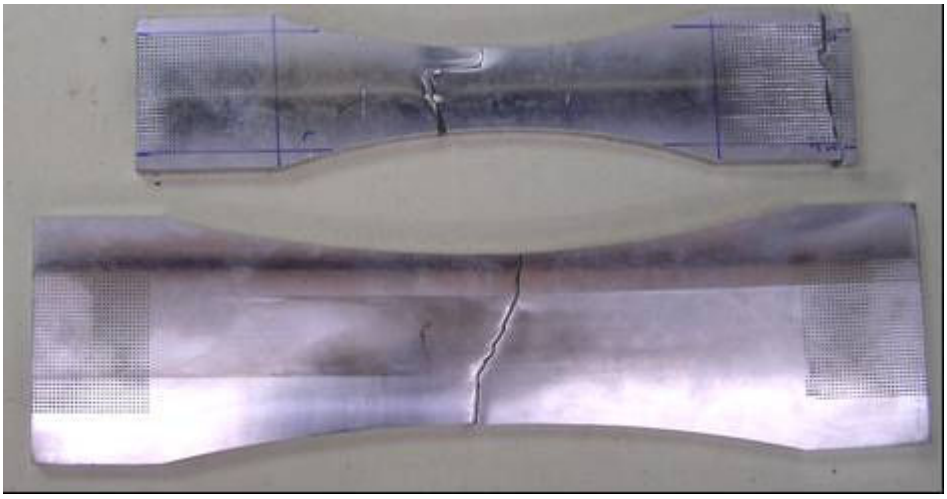

Figure 3.3. The two different specimen types tested

All tests were carried out according to the ASTM E466 specification at room temperature, with a frequency of 20Hz while the stress ratio was kept constant at R=0.1 The test specimens were machined symmetrically on both sides to the final thickness. All fatigue tests performed are summarized in Table 4. Test series 3* has been planned to be performed in addition to the COINS project in order to obtain a more global understanding of the fatigue behaviour. The test results are presented in the Figure 37 and Figure 38.

Test series	Material	Test sample	No. of samples	Sample size (mm)
1	2195	Dog-bone (plate to plate) type 1	12	420x80x10

2	2195	Dog-bone (plate to plate) type 2	12	200x30x10
3*	2195	Dog-bone (extrusion to plate) type 1	12	420x80x10
4	2195	Dog-bone (extrusion to plate) type 2	12	200x30x10

Table 4: Fatigue testing of 2195 welded material with longitudinal weld

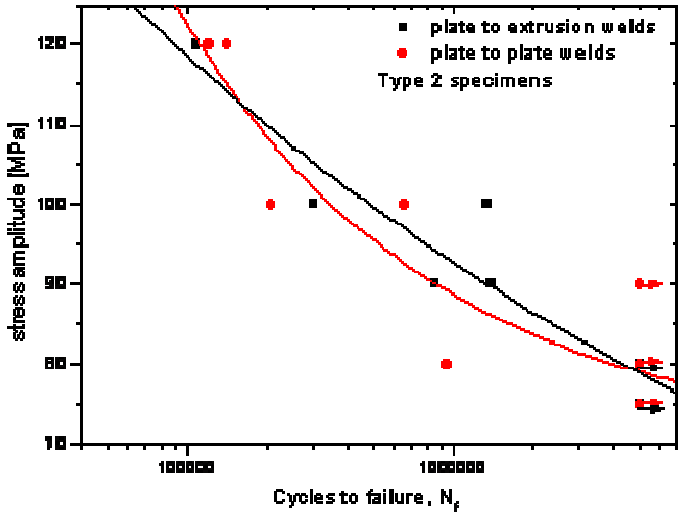

Figure 37: Comparative plot of the "Type 2" specimens

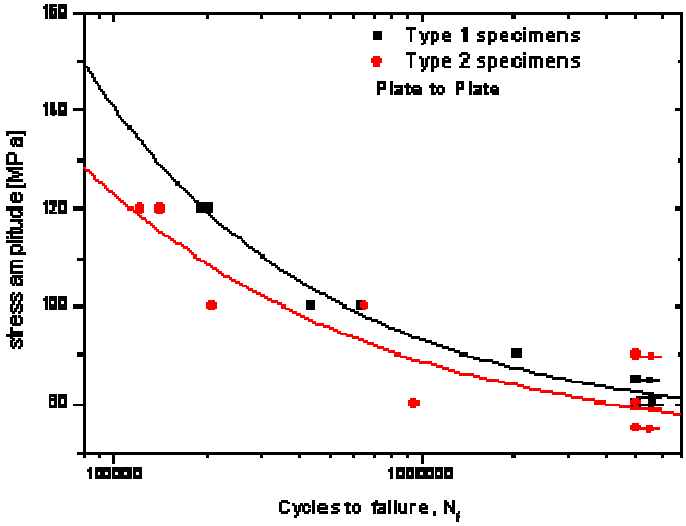

Figure 38: Comparative plot of the two types plate to plate welded specimens

From the fatigue tests performed on the "type 2" specimens (specimens of which reduced section consisted exclusively of the weld), a number of specimens failed at considerably lower cycles than expected according to the S-N curve. Fractographic investigation was performed on selected specimens in order to provide input for better understanding of the reasons which led to the early failures. Table 5 summarizes the specimens investigated:

Spec. Code	**σ_{max} MPa**	**σ_{min} MPa**	**Stress amplitude MPa**	**N_f cycles**
P2P6	200	20	90	255470
P2P9	200	20	90	5000000 (R.O)
P2E7	200	20	90	73316
P2E2	200	20	90	1394606

Table 5: Specimens failed at considerably lower cycles than expected

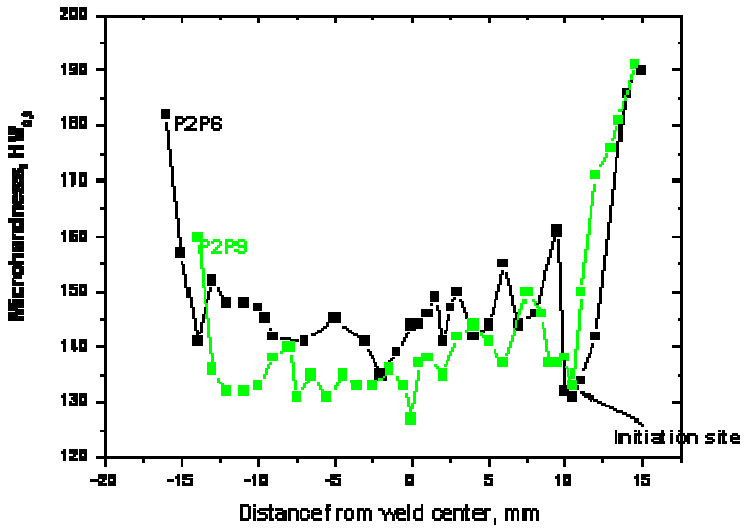

Figure 39: Microhardness profile (0.3 mm from the surface) of specimens P2P9, P2P6. Note that P2P9 exhibits lower microhardness values than specimen P2P6.

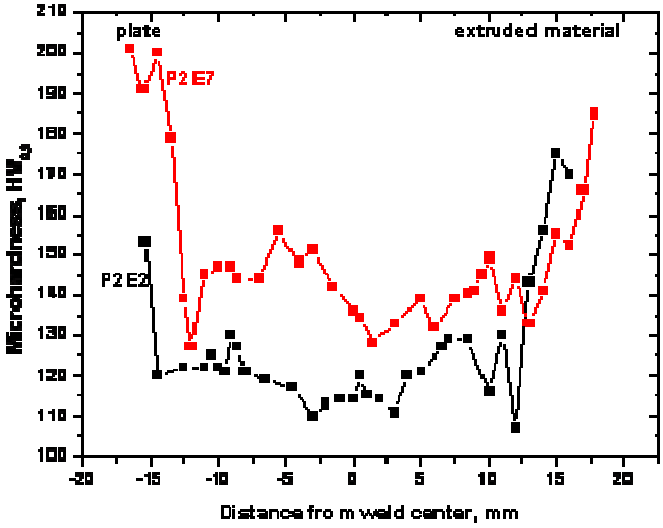

Figure 40: Microhardness profiles of the examined specimens. Note that P2E2 exhibits lower microhardness values than specimen P2E7

Main findings

- No considerable difference is observed in the fatigue behaviour of the material, with respect to the type of material welded (plate to plate or plate to extrusion). The welding process seems to diminish all material differences which could possibly lead to a different fatigue behaviour.
- Type 1 specimens (specimens of which the reduced cross section consisted of both, the weld zone and non-welded material) exhibit superior fatigue behaviour compared to the type 2 specimens. Smaller scatter between the test results has also been observed compared to the smaller specimens testing. These results are reasonable, as the minimum cross section of the large specimens consists of both, parent material and the weld nugget whereas the smaller specimens consist only of the weld nugget (parent 2195 exhibits superior fatigue behaviour than the respective welded material). This is in line with recent investigations which have shown that the fatigue behaviour of the same material may differ according to the microstructure.

2.6.5 Mechanical behaviour of 2198 T8 before and after artificial ageing

During the reporting period, the fatigue and fracture toughness behaviour of 2198 T8 material before and after additional artificial ageing of 1000 hours at 80ºC was assessed and compared. The respective tensile behaviour study was completed during the previous reporting period. The overall tests performed are summarized in the Table 6. FCG propagation tests on parent material were performed in addition to the planned work in the frame of the COINS project in order to compare fatigue propagation behaviour.

Material	Test sample	Test content	No. of samples	Test series
2198 T8 No ageing	Dog-bone	Tensile	3	1
	MT transv. weld, centre crack	FCG	2	3
	M(T) transv. weld, centre crack	R-curve	2	5
	MT transv. weld, crack at the interface	FCG	2	4
	M(T) transv. weld, crack at the interface	R-curve	2	6
2198 T8 Aged 1000h at 80°C	Dog-bone	Tensile	3	2
	MT transv. weld, centre crack	FCG	2	5
	M(T) transv. weld, centre crack	R-curve	2	7
	MT transv. weld, crack at the interface	FCG	2	6
	M(T) transv. weld, crack at the interface	R-curve	2	8

Table 6: Tests for determining Mechanical behaviour of 2198T8 before and after artificial ageing

R-curve and fatigue crack propagation specimens were machined according to the specifications ASTM E647-05 for the fatigue crack propagation specimens and ASTM E 561-05 for the R-curve specimens. All tests were performed at room temperature.

Fatigue crack propagation test results

The Paris coefficients according to the Paris equation $\frac{da}{dN} = C\Delta K^m$ have been calculated and presented in the Table 7.

Specimen Code	m	C	Crack location	Ageing
cbp3f13	1,68	7,56E-09	Centre	Non-Aged
cbp3f13	1,97	2,47E-09		
Mean Values	1,825	5,02E-09		
cbp3f5	1,78	6,29E-09	Interface	Non-Aged
cbp3f14	3,27	9,87E-11		
Mean Values	2,525	3,19E-09		
cbp3f3	1,16	1,49E-08	centre	Aged 1000H @ 80°C
Mean Values	1,16	1,49E-08		
cbp3f4	2,35	3,47E-10	Interface	Aged 1000H @ 80°C
cbp3f7	4,18	3,74E-12		
Mean Values	3,265	1,75E-10		

Table 7: Fatigue Propagation test

Main findings

- Fatigue propagation rate in the case where the crack propagates on the weld interface is higher than the respective rate of the weld nugget.
- It is necessary to underline that these statements are based on a limited number of tests. Additional testing would be recommended to provide confidence.
- In the present test series involving aged materials, 3 parameters influenced the observed behaviour simultaneously, namely the existence of the weld, the position of the crack and ageing of the material. Ageing of the specimens is expected to improve the fatigue behaviour of the material. The results of the tests involving weld and ageing lie close to that of the parent material. However, this is a weak conclusion as it is based on a single test.
- Testing of base material after ageing is recommended, for comparison with the respective parent material without ageing so as to quantify the effect of ageing.

	2198 T8		2198 T8 aged 1000h@80OC	
	Crack at interface	Crack in centre	Crack at interface	Crack in centre
Kmax [MPa√m]	151	202	153	200
Maximum physical crack size [mm]	86.7	89.6	88.7	88.6
Maximum effective crack size [mm]	114.4	129	116.8	122.8

Table 8: R-Curve test results

Discussion

The ASTM E561-98 specification requires for a set of data to be valid that the net stress (the ratio of the applied force divided by the remaining uncracked section) should be smaller than the yield stress of the material. It is well known that the local yield stress in a weld varies with respect to the distance from the weld centre. Therefore, it is not clear for the tests up to which data point should be considered to be in line with the above specification. In the results evaluation, two different values of the yield stress have been taken into account: The yield stress of the parent material and that of the weld, as evaluated from tensile tests performed. When the yield stress considered is that of the parent material (450MPa), then all data points are valid. The last valid data point when considering the yield stress of the welded material (320.83MPa and 288.01MPa for the aged and non-aged specimens respectively) has been marked on the respective plots.

Main findings

- Artificial ageing has no significant effect on the fracture toughness of 2198T8
- K_{max} is significantly lower when crack is on the weld interface

2.6.6 M(T) Longitudinal weld – Crack towards weld

During the reporting period, the FCG behaviour of FSW Aluminium 2198 T8 and 2139 T3, when a crack is propagating towards the weld zone was assessed. The results were compared to FCG behaviour of parent, non-welded material. In order to retain the symmetry of the test specimens, M(T) plates were produced with a double symmetrical weld, as shown in Figure 41.

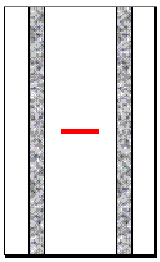

Configuration of test specimens

Figure 41: Picture of failed specimen

The number of tests and the geometry of the test samples are summarized in Table 9.

Test series	Material	Test content	No. of samples	Sample size (mm)
1	2139 T3	Parent material	2	800x400x5
2	2139 T3	Welded specimens	3	800x400x3.2
3	2198 T8	Parent material	2	800x400x5

4	2198 T8	Welded specimens	3	800x400x3.2

Table 9: Geometry of test samples and Summary of tests

Test Results

The test results are summarised in the comparative plots below.

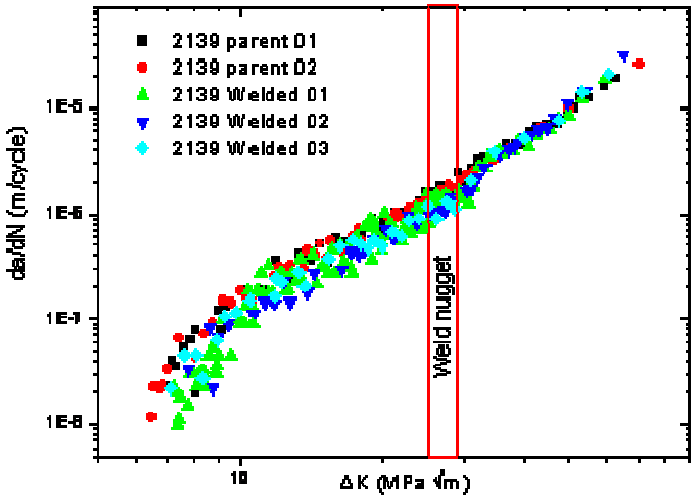

Figure 42: Comparative plot of 2139T3 parent material and respective welded plates: Improved fatigue crack propagation behaviour is observed in the welded plates. Differences diminish at high ΔK values

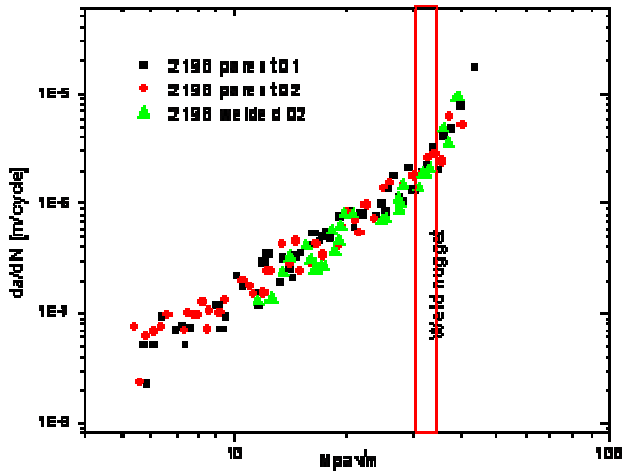

Figure 43: Comparative plot of 2198T8 parent material and respective welded plates

The Paris coefficients were calculated for all the above tests and are presented in Table 10. All coefficients were calculated for the region of ΔK between 20 and 30 MPa√m.

Specimen Code	m	C
2139-01	2.65	3.40E-10
2139-02	2.44	5.12E-10
Mean Values	2.545	4.26 E-10
welded 2139 -01	2.26	3.39E-09
welded 2139 -02	2.29	7.30E-10
welded 2139 -03	2.78	1.25E-10
Mean Values	2.44	1.415 E-9
2198-01	2.24	3.03E-10
2198-02	2.61	2.50E-10
Mean Values	2.54	2.765 E-10
welded 2198-03	1.61	4.88E-09

Table 10: Paris Coefficients

Discussion

The fatigue propagation behaviour in a friction stir weld is dominated by two parameters: The residual stress field in which the crack propagates and the microstructure and hardness of the material. In the case where the crack propagates perpendicular to the weld, such as in the current test series, both the residual stress field and the material microstructure of the material in which the crack propagates are constantly changing. In order to be able to better understand the fatigue crack propagation behaviour, these parameters have to be isolated and studied in parallel.

Main findings

- The fatigue crack propagation behaviour of the welded material was comparable to that of the parent, non-welded material. This indicated a weld of high quality with little effect on the fatigue crack propagation behaviour of the material. However, compared to the total propagation length, the zone which was affected by the weld was relatively small, therefore no significant effects were expected, especially since the crack met the weld zone at relatively high ΔK values.
- A retardation effect has been observed when the crack was propagating in the weld zone, although the propagation length was not sufficient to have a profound effect. This retardation effect has been reported previously by other researchers and has been attributed to the change of microstructure. As the crack meets a zone of lower yield stress, a larger plastic zone is expected to be formed which may account for the retardation observed. A similar but more profound effect was also recorded in other tests performed in the COINS project which are presented in the current deliverable in the respective chapter.

- The overall mean fatigue crack propagation rate of the welded specimens is slower than the respective rate of the parent material (C value), although the slope of the Paris region is comparable for all specimens (m value). This is consistent with the findings of similar published works.
- The above conclusion is week for the 2198 welded material, as only one successful test was performed.

2.7 Task 2.4 Effects of Cracks in Structures

The objective of the task is to study the behaviour of cracks in welded structures, particularly the phenomenon of crack deviation.

2.7.1 Task 2.4 Effects of Cracks in Structures (Airbus Germany)

2.7.1.1 Biaxial Tests

To investigate crack deviation under realistic load conditions a more complex test has been planned with the joint cooperation of CU and GKSS. The test consists of flat panel, about 860 x 860 mm, biaxially loaded. A biaxiality ratio of 1:1 represents loading on the top surface of the fuselage. A biaxiality ratio of 1:2 represents the stress situation on the side of the fuselage for a circumferential crack. A biaxiality ratio of 2:1 represents a longitudinal crack on the side of the fuselage. Cracks and welds with a longitudinal fuselage direction will be parallel to the rolling direction in the aluminium sheet. A sketch is given in Figure 44.

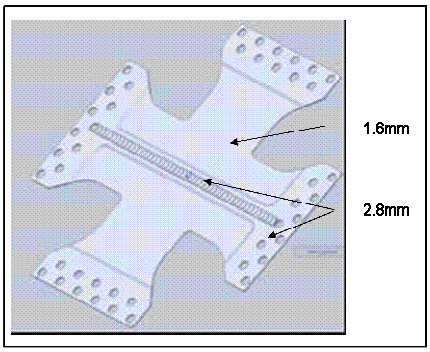

Figure 44: Sketch of biaxial coupon

Airbus Germany manufactured the sample in FSW in 2198 material, rough machined and GKSS finish machined the sample prior to testing it. Four samples in all were manufactured.

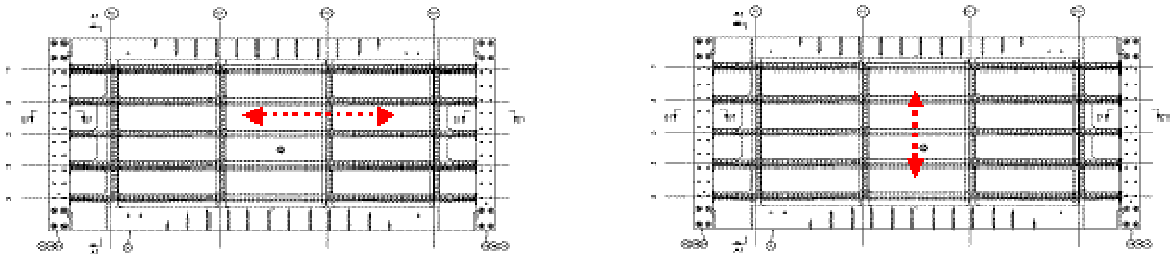

Figure 45: Crack orientation in longitudinal (parallel to aluminium rolling direction) and circumferential direction ((perpendicular to rolling direction)

In terms of longitudinal and circumferential loads the upper fuselage, under the effect of pressurization and bending loads, can be reproduced with a load ratio 1 to 1. A side panel subjected mainly to pressurization load can be represented by a load ration 1 to 2 (the higher load in circumferential direction).

Figure 46: Differentiation of load ratio between upper and side shells of a fuselage

The material of the investigation is Al-Li 2198T8, the weld will located in the geometrical centre of the specimen but in the retreating side of the weld. The minimum thickness is 1.6mm; in the area of the weld a local pad up having a width of 50mm increase the thickness to 2.8mm; same value for the area of the clamping. The test matrix is given in Table 11.

Tests	Crack location	Material orientation	Thickness	Pad-up thickness	Pad-up width	Biaxiality ratio	Coupons	Size [mm]
Design 1	TMAZ / Nugget	Weld orthogonal to rolling direction	1.6 mm	2.8 mm	25 mm	1 to 1	2	860x860
Design 2	TMAZ / Nugget	Weld parallel to rolling direction	1.6 mm	2.8 mm	25 mm	1 to 2	2	860x860

Table 11: Test matrix for the biaxial tests

The specimens have been welded by Airbus-D in Bremen and delivered to GKSS.

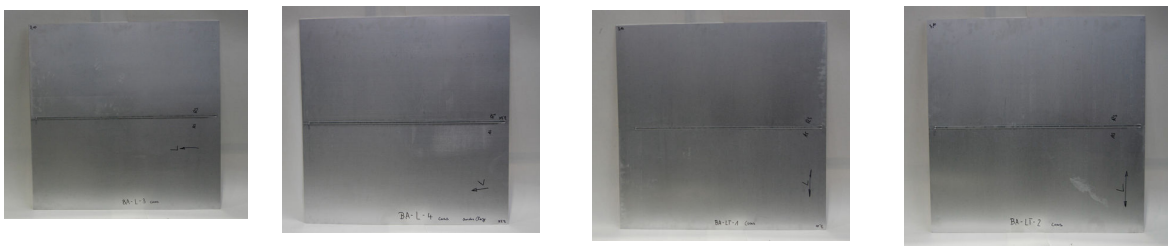

Figure 47: Pictures of the welded sample before manufacturing

The machining to the final geometry has been performed at GKSS.

The test setup, instrumentation including strain gauges map is shown Figure 48.

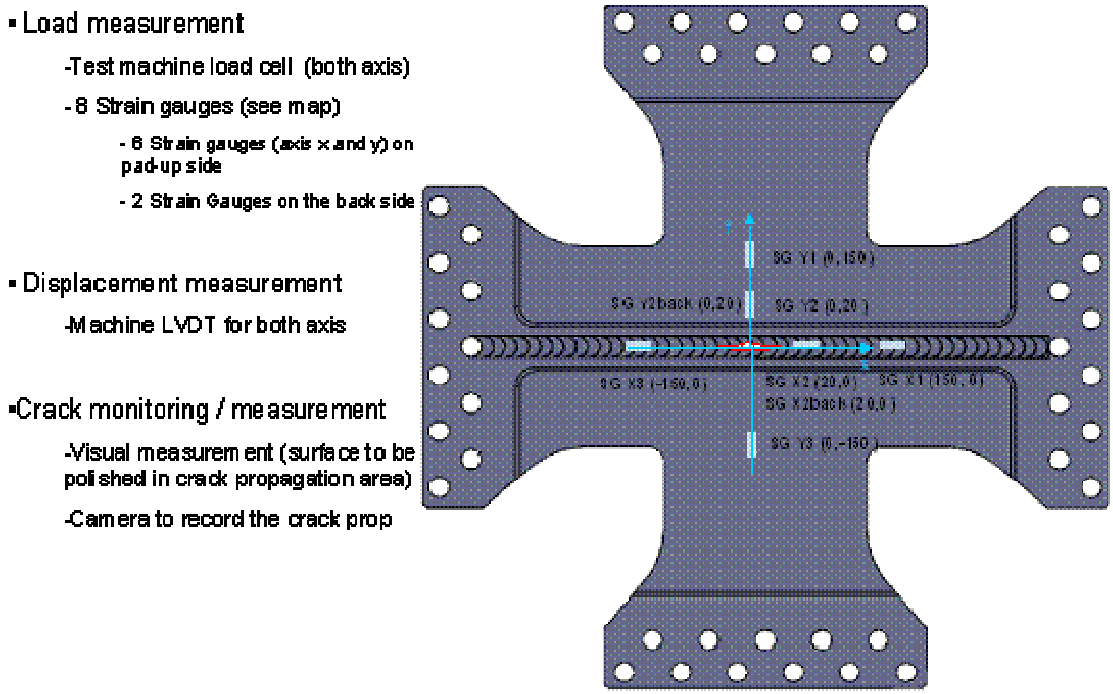

Figure 48: Strain gauge map

2.7.2 WP 2.4 Effects of Cracks in Welded Structures (GKSS)

GKSS performed biaxial fatigue tests on a six axis triaxial testing machine using 4 of the independent 1 MN actuators and controllers. The load control scheme always ensures that the centre of the sample always stays in the same place. The biaxial test sample has been manufactured using FSW by Airbus D out of 3.2 mm thick 2198 T8 alloy, and was final machined by GKSS prior to testing. The test rig is shown in Figure 49 and Figure 50.

Sample & test description

Four samples in all were manufactured. As explained at the beginning of this section, the samples represented loading in the fuselage for a crack at the fuselage side with a stress ratio of 1:2 for a longitudinal crack or 2:1 for a circumferential crack, or at the fuselage crown, with a stress ratio of 1:1 for both longitudinal and circumferential cracks. Longitudinal cracks will be parallel to the rolling direction of the sheet, circumferential cracks will be perpendicular to the rolling direction of the sheet.

All 4 samples had a crack starter, 40 mm long, located on the weld centreline, two of them with the weld perpendicular to the RD and 2 parallel to the RD. The direction perpendicular to the crack starter and weld was designated Y and the X direction was parallel to the weld and the crack starter.

Prior to testing in fatigue, samples were strain gauged and subjected to an experimental stress analysis. This was described earlier in the section on Cranfield University work on this topic. At the 40 kN maximum load using in the static and fatigue loading the remote measured strain orthogonal to the weld and crack was 1200-1300 με, corresponding to 85 MPa maximum stress. The FE analysis of the sample conducted by CU was broadly in agreement with the measured values of strains as described in the description of their work in this report.

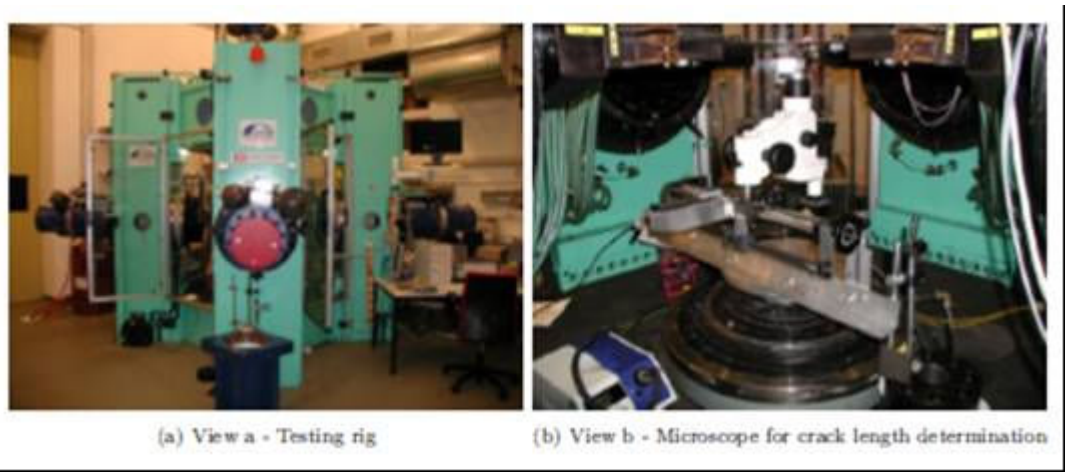

Figure 49: The 6 axis fatigue test machine, (a) general view, (b) Detail of sample test area

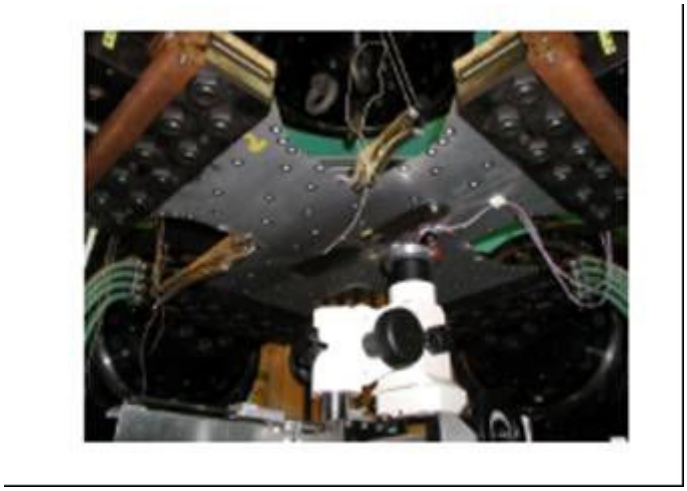

Figure 50: The biaxial test sample showing the optical crack length measurement system and the clamps used to retard progress of secondary corner cracks initiated during fatigue cycling of the main crack

Fatigue testing was conducted with the crack oriented parallel with the weld in the X direction. Loading in the X and Y axes was in phase, with R ratio of 0.1. On one of the tests the initial fatigue loading was with load ratio of 0.5:1, with the Y axis maximum load of 20 kN and the X axis 40 kN. This corresponded to a crack in a circumferential weld on the side of the fuselage. No crack growth was observed and the loading ratio was changed to 1:1, corresponding to the top of the fuselage. The other three tests had a load ratio of 1:1 from the outset with a maximum load on both axes of 40 kN. Cracks grew from the starting defect at these load levels.

Some difficulty was experienced in fatigue testing the samples. The FSW weld manufacturing process introduced significant out of plane distortion, causing bend stresses when the sample was loaded. Further out of plane bending occurred as a consequence of changes in thickness of the sample at the weld line (3.2 mm) compared with the main body of the sheet (1.6 mm). The samples also experienced secondary cracking at the corner radii during propagation of the primary weld crack. Propagation of the secondary cracks was retarded by crack stopping with hole drilling the tip (only partially effective in that the cracks re initiated after further cycling) and mechanical clamping (more successful- propagation of the crack was significantly retarded). In addition cracks in samples with the weld line oriented perpendicular to the sheet deviated from the weld line and ended with significant changes to their geometry, invalidating the assumptions on which their stress intensity calculations had been based.

Results

The paths followed by cracks in the 4 samples are shown in **Error! Reference source not found.** It can be seen that in samples with welds orthogonal to the sheet rolling direction there was crack deviation. In the samples with welds parallel to the rolling direction, there was much smaller crack deviation although at long crack lengths deviation of 1-2 mm occurred even in the parallel samples.

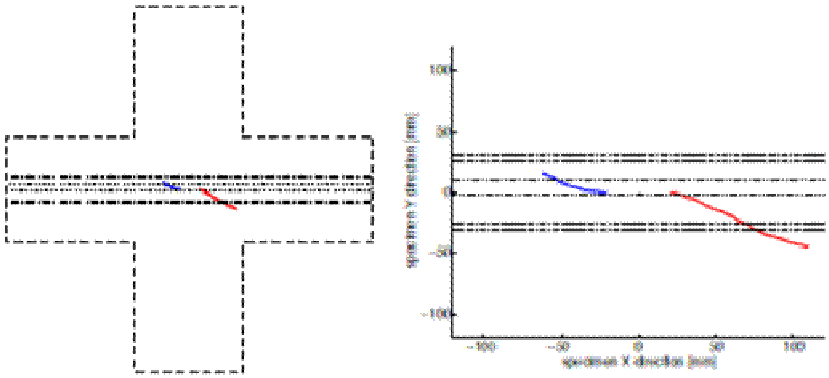

(a) crack path drawn on the specimen (b) detail of the crack path

Sample 1- weld orthogonal to rolling direction

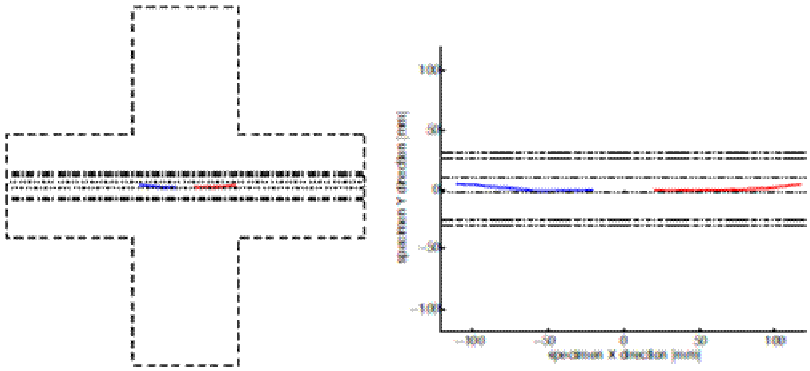

Sample 2 Weld parallel to rolling direction

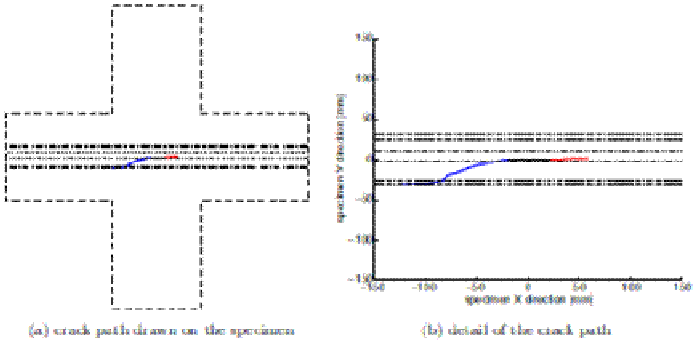

(a) crack path drawn on the specimen (b) detail of the crack path

Sample 3 Weld orthogonal to rolling direction

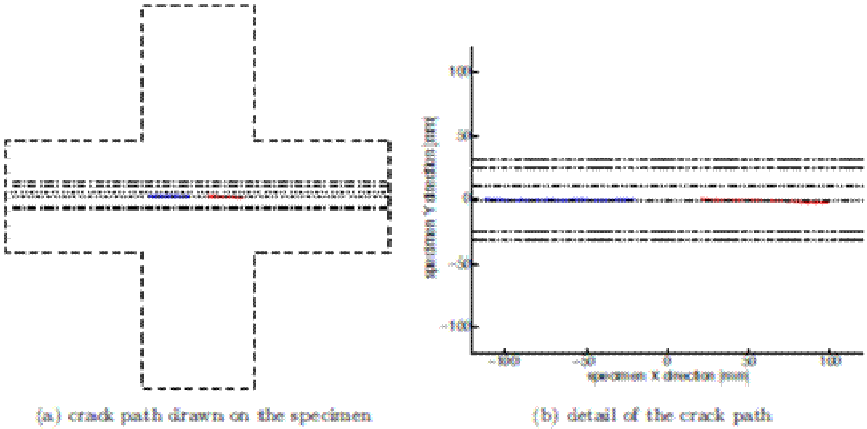

Sample 4 Weld parallel to rolling direction

Figure 51: Crack paths followed by each of the four samples

Average crack length Vs fatigue cycles curves for all the samples are shown in Figure 69 together with predicted values from the model developed by Cranfield University. It can be seen that the two samples with cracks and welds orthogonal to the rolling direction have shorter lives than the two samples with welds parallel to the rolling direction. The predicted growth rates are faster than experimental in all the samples.

2.7.3 WP 2.4 Effects of Cracks in Welded Structures (University of Patras)

University of Patras has continued the work on the development of software and methodology for prediction of fatigue crack growth rates in FSW samples, particularly looking at the effects of residual stress.

Numerical calculations of stress intensity factors under the influence of residual stresses (RS) are combined with a proper fatigue crack propagation rule for the prediction of crack behaviour under fatigue loading. It has been identified that the effective R ratio applied at the crack tip during fatigue loading is affected by the RS field. Thus, the fatigue crack propagation rule selected to be applied have to take into account the effect of R in the calculated crack propagation rates. For the present applications Walker rule to represent crack growth rate data was selected.

The Walker equation that has been used for fatigue crack propagation rate calculations is expressed in the form:

$$\frac{da}{dN} = \frac{A(\Delta K)^{\xi}}{(1-R)^{p}} \qquad (4.1)$$

For the determination of the constants A, ξ and p of equation (4.1) experimental measurements concerning fatigue crack growth at different stress ratios have been used. The following values have been estimated:

- A = 2.2×10-8
- ξ = 3.5
- p = 1.4

for da/dN in mm/circle and ΔK in $MPa\sqrt{m}$.

In Figure 52 the crack growth rates as a function of SIF are presented as calculated using equation (1) and as experimentally measured in a log-log diagram.

2.7.4 ESET test specimen

The basic geometrical characteristics of the ESET type of specimen are presented in Figure 53. The specimen is 8mm thick and is produced by FSW of two Al 2195-T8 plates. Elastic material properties E=72GPa and ν=0.3 have been used for the analysis and the calculations.

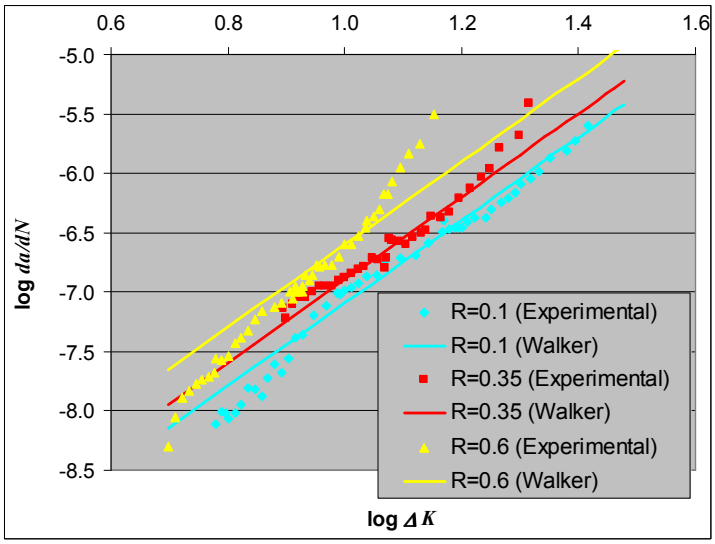

Figure 52: Fatigue crack propagation rates using estimated Walker equation constants (log-log diagram)

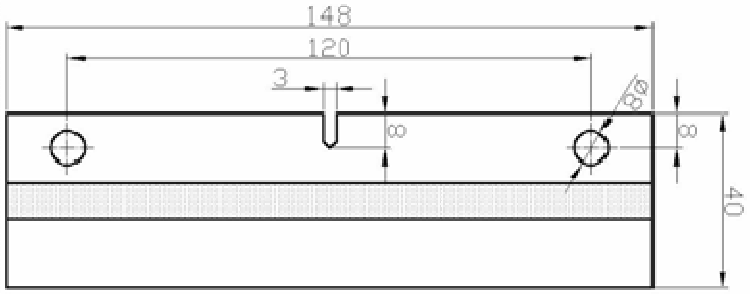

Figure 53: ESET type specimen geometry

Residual stresses developed due to FSW in the ESET specimen have been measured by GKSS in the frame of COINS Project. However, as the provided RS field is not self-equilibrated, residual stresses are re-distributed during the stress analysis of the specimen in order to come into equilibrium. In Figure 54 the measured and redistributed RS are presented. It has to be mentioned that as RS field if also affected by the existence of the crack, actual RS are difference near and away from the crack.

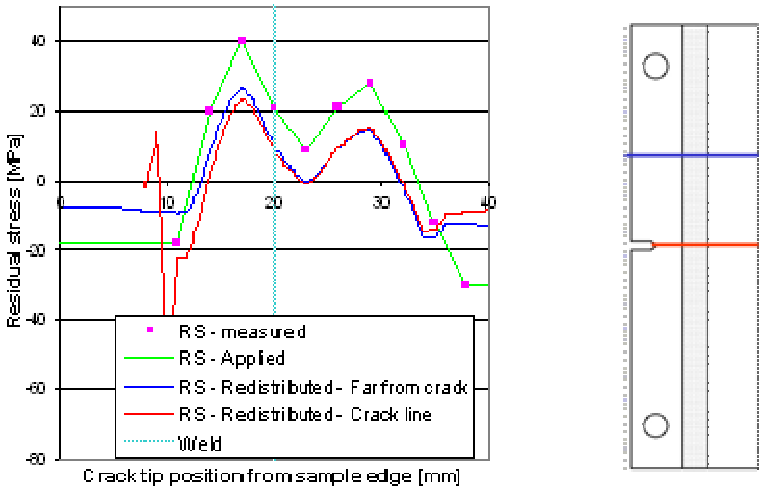

Figure 54: ESET specimen - Residual stresses

Two different external fatigue loadings have been applied to the ESET type of specimens, defined by the following values:

- P_{max} = 4330Nt, R=0.1 and
- P_{max} = 9730Nt, R=0.6

For the finite element analysis of the ESET type of specimens a three-dimensional FE model has been developed. 20-node structural solid element SOLID186 of ANSYS FE code has been used. Half of specimen geometry has to be modelled due to symmetry and proper symmetry conditions will be applied to the symmetry plane. As a result the FE model presented in Figure 55 has been built. The FE

model consists of 123901 nodes and 27473 elements. In the detail of Figure 55 the special and dense mesh in the area of crack front is presented, that is essential for the accurate calculation of SIFs.

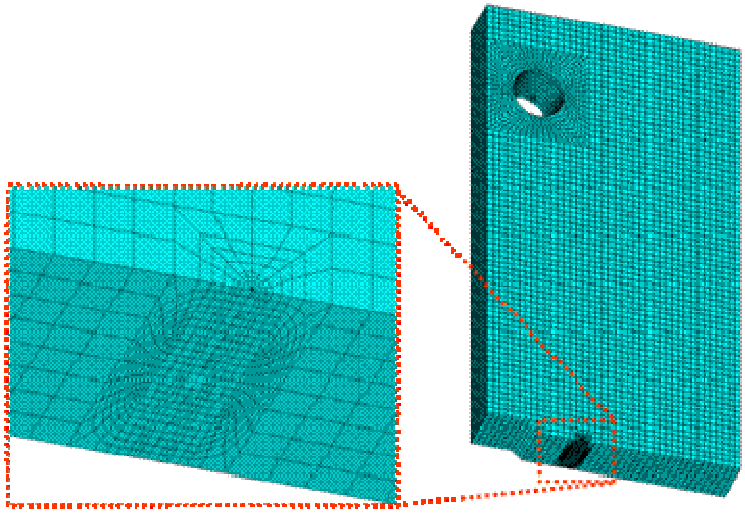

Figure 55: ESET specimen – FE model

Linear-elastic stress analysis is then conducted using the developed FE model. SIFs are calculated using the displacements of the nodes at the crack-tip area. Calculated SIFs vary through-the-thickness of the sample due to the plane-stress / plane strain effect. Thus, the average through-the-thickness value is used for crack propagation calculation. In Figure 56 and Figure 57 the calculated SIF and R_{eff} values for the two different external load cases (for R=0.1, P_{max}=4330Nt and R=0.6, P_{max}=9730Nt) are respectively presented. In Figure 58 the fatigue crack growth predictions for the two test cases are presented.

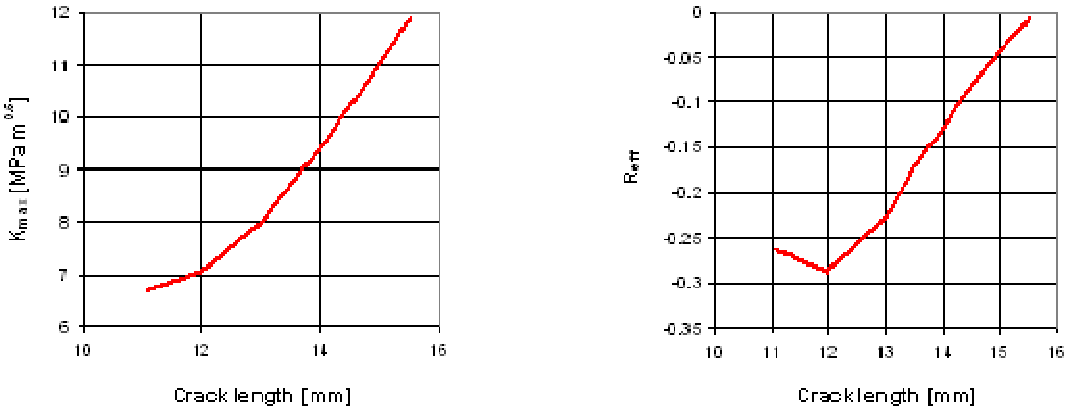

Figure 56: ESET specimen – Calculated SIFs and R_{eff} for R=0.1, Pmax=4330Nt

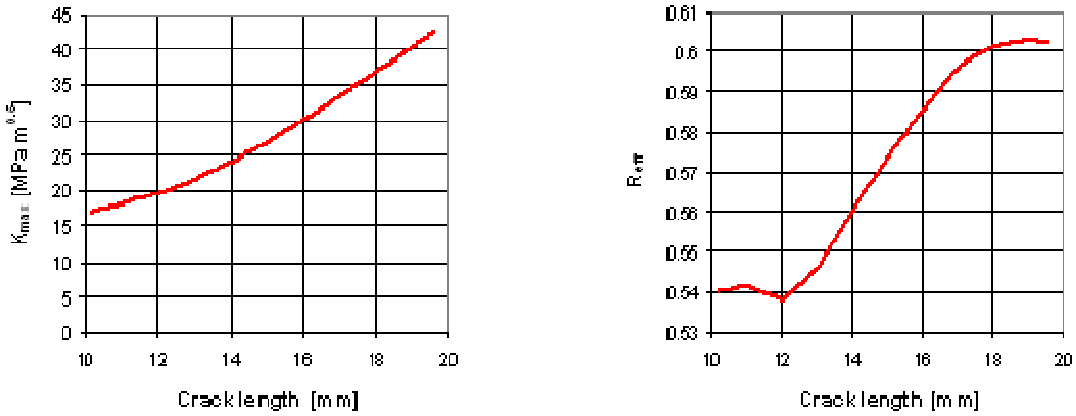

Figure 57: ESET specimen – Calculated SIFs and R_{eff} for R=0.6, Pmax=9730Nt

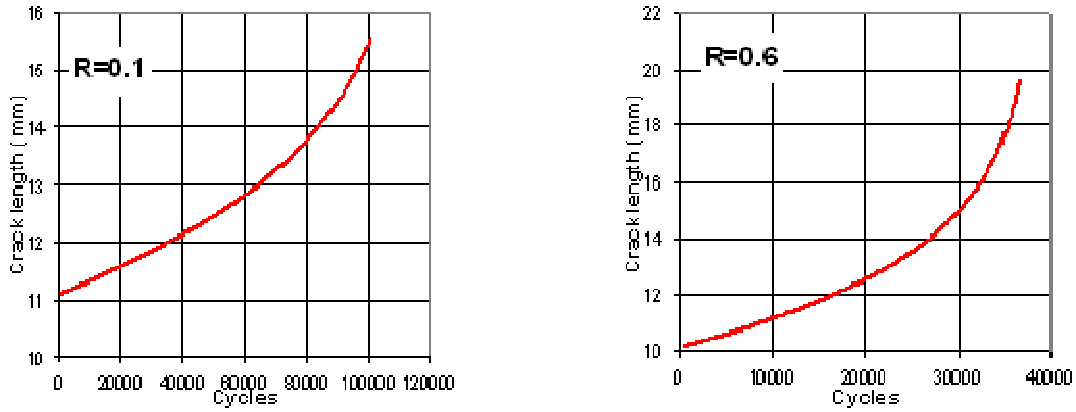

Figure 58: ESET specimen – Fatigue crack propagation for: (a) R=0.1, Pmax=4330Nt and (b) R=0.6, Pmax=9730Nt

2.7.5 CT test specimen

The basic geometrical characteristics of the CT type of specimen are presented in Figure 59. Specimen thickness is 8mm thick and is made of Al 2195-T8 with elastic material properties E=72GPa and ν=0.3. The RS field applied for this type of specimen is presented in Figure 60. External fatigue loading is applied during the specimen testing with P_{max} = 6450 Nt and load ratio R = 0.1.

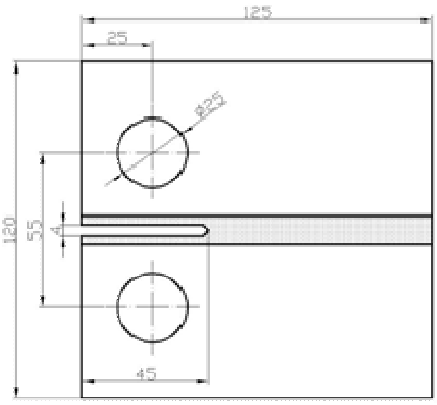

Figure 59: CT type specimen geometry

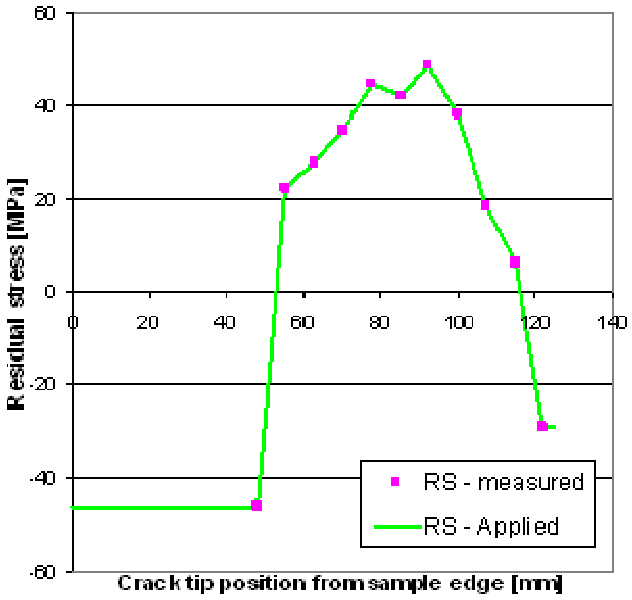

Figure 60: CT specimen - Residual stress field

For the finite element analysis of the CT type of specimen a three-dimensional FE model has been developed using the SOLID186 solid element of ANSYS FE code. Due to symmetry, only half of specimen geometry has been modelled and proper symmetry conditions have been applied. The FE model is presented in Figure 61. It consists of 54976 nodes and 11297 elements. In the detail of Figure 61 the special mesh in the area of crack front is presented.

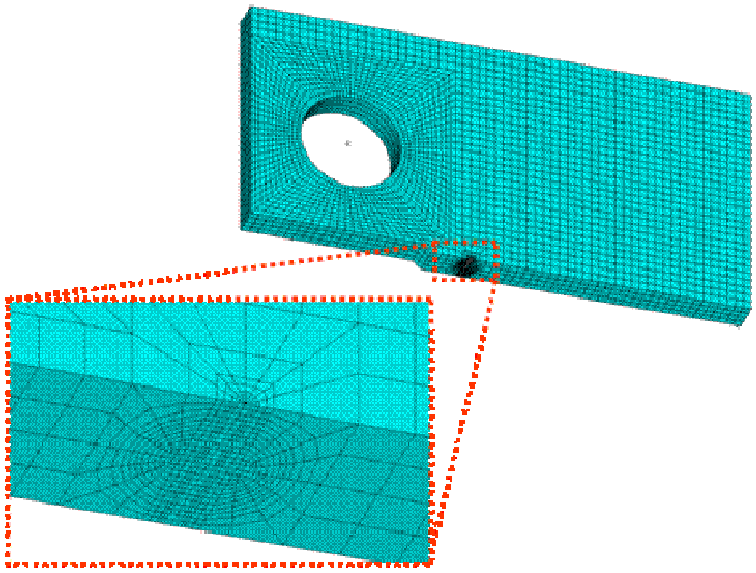

Figure 61: CT specimen – FE model

In Figure 62 the calculated SIF and R_{eff} values for the combination of the external load (P_{min}=645 Nt and P_{max}=6450 Nt) and RS are presented. In Figure 63 the fatigue crack growth predictions are presented.

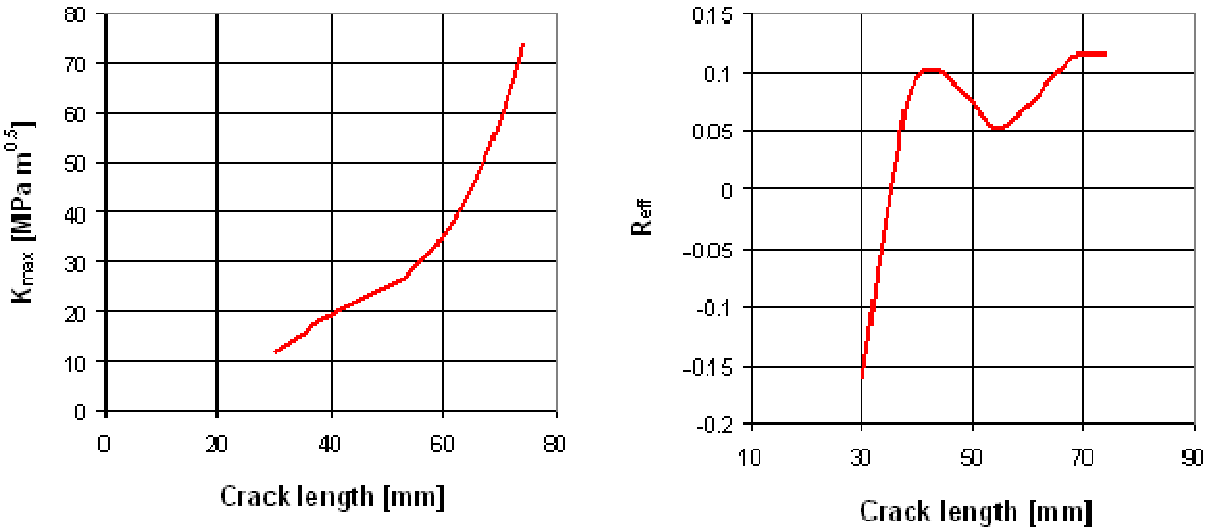

Figure 62: CT specimen – Calculated SIFs and R_{eff}

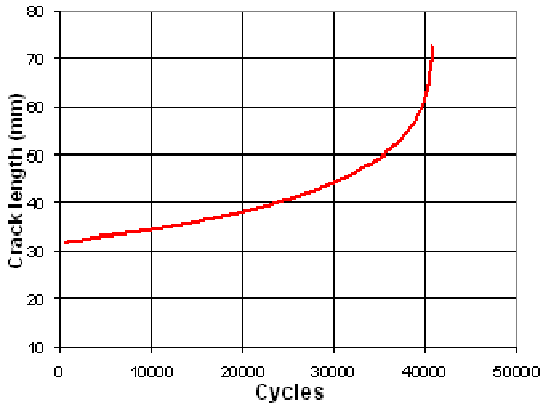

Figure 63: CT specimen – Fatigue crack propagation predictions

2.7.6 WP 2.4 Effects of Cracks in Welded Structures (Cranfield University)

In Task 2.4 in the final period Cranfield University tested crack deviation samples manufactured by Airbus D. A finite element stress analysis was conducted of the cruciform samples.

Testing of crack deviation samples

The geometry of the crack deviation samples is shown in Figure 64. The crack grows in the weld, parallel to the thicker pad up region, adjacent to an open hole which attracts the crack, modifying the stress intensity, introducing elements other than pure mode I.

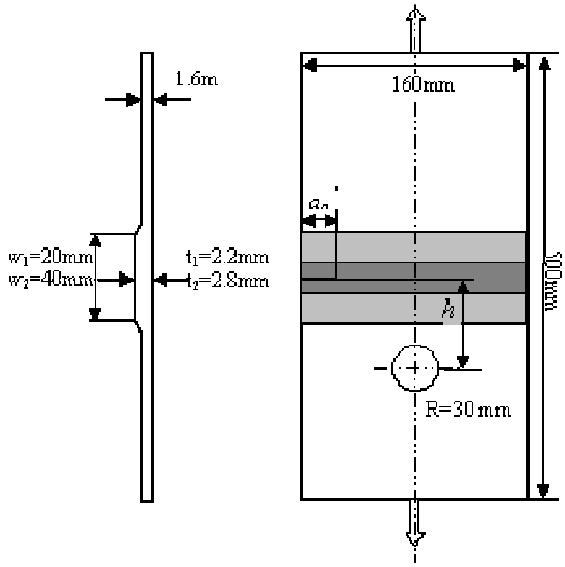

Figure 64:Crack deviation sample geometry & dimensions

Samples were tested in fatigue with the crack propagating initially along the weld centreline in the thicker padup. As it passed the open hole it began to deviate and the track tip trajectory was monitored during the fatigue process. It was found that the extent of crack deviation depended on the distance h from the hole centre to the crack plane. The behaviour of cracks with and without welds and with

different distances of the hole h from the crack plane were measured and compared. Typical results are shown in Figure 65, where crack paths with and without weld residual stresses are compared

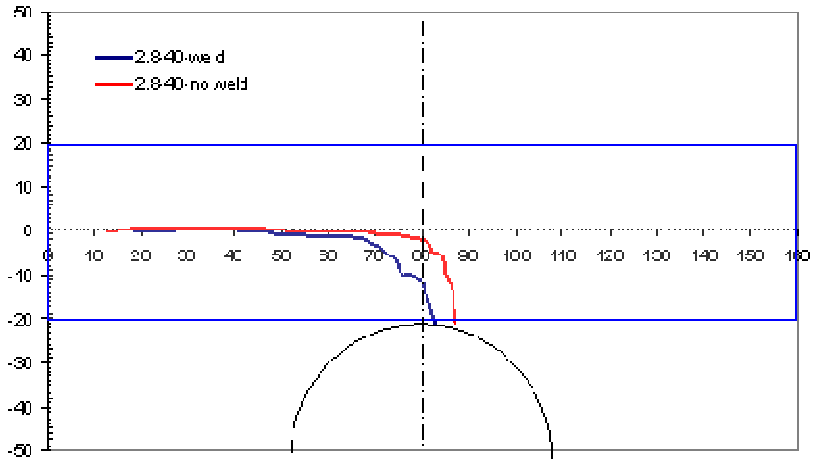

Figure 65: Crack trajectories in samples with and without the weld line & the residual stresses, showing that residual stresses promote earlier crack deviation

Tests were conducted to establish the role of pad up thickness on crack deviation behaviour, and it was found to have a negligible effect.

Finite element models reported in earlier work in the project were used to predict the crack trajectories for the effects of residual stress and the effect of the hole centre distance h. Using the maximum tangential stress criterion, successful predictions of crack trajectory were made, even though the analysis was a static one and was being used to predict the effects in a fatigue crack growth situation. A comparison of predicted and experimentally measured crack trajectories is shown in Figure 66 below.

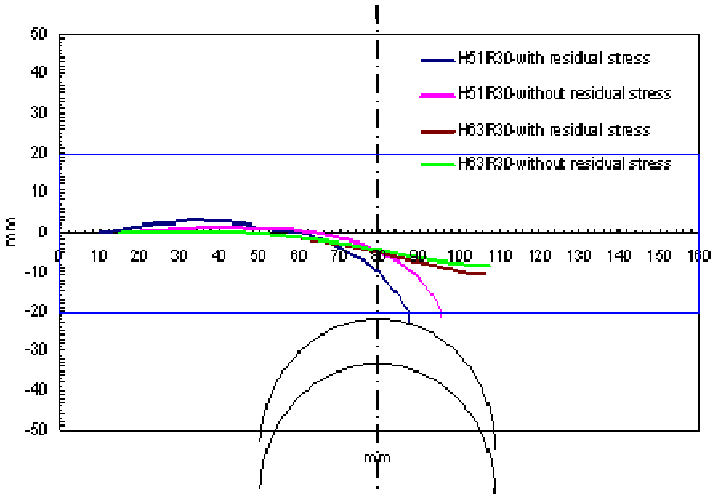

Figure 66: Comparison of measured and calculated crack trajectories; prediction of the effects of hole

distance h and effect of weld residual stress field

Cruciform sample subjected to Biaxial loading- FE analysis

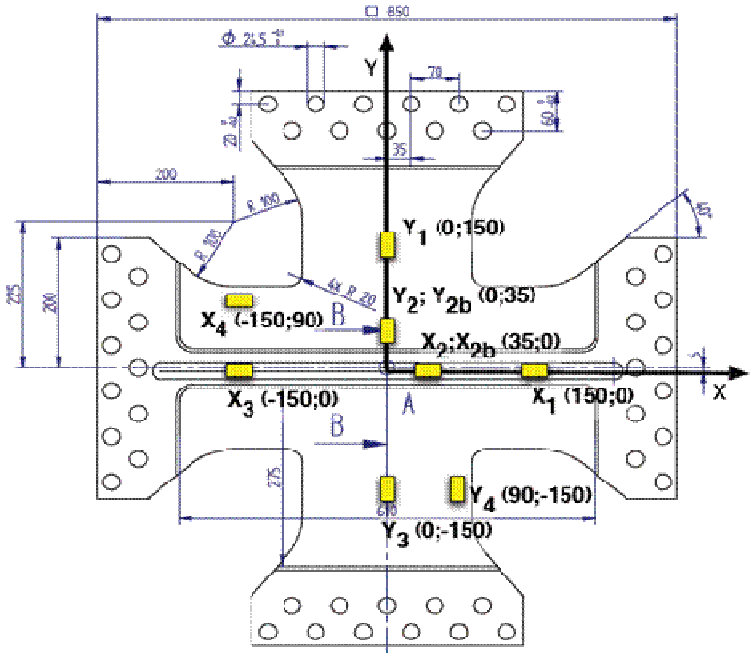

Figure 67: Dimensions of the biaxial test sample showing the locations of the strain gauges used in experimental stress analysis

In this work CU collaborated with GKSS and with Airbus D to establish theoretical and experimental stress analysis of the cruciform samples under biaxial loading. Fatigue life predictions were made of crack trajectories and lives under biaxial loading.

Specimen and test programme

Table 12 summarises the test sample orientations and test conditions. Figure 67 shows the test specimen with pad-up, weld and strain gauge positions.

Specimen No.	Weld orientation	Applied load P_x:P_y (kN)	Notes / Observations	No. of secondary cracks from the corners of loading arms junction
COI-BIAX1	Weld orthogonal to rolling direction	40:40	Load ratio was P_x = 40 kN, P_y = 20 kN in the first 80,000 cycles	0
COI-BIAX2	Weld parallel to	40:40		2

	rolling direction			
COI-BIAX3	Weld orthogonal to rolling direction	40:40		0
COI-BIAX4	Weld parallel to rolling direction	40:40	The shoulder side of specimen surface was machined up to 3.1 mm thick since this specimen was thicker than all the others in its welded state	2

Table 12: Test Specimens (2198-T8 with a FS weld parallel to the x-axis)

FE modelling and prediction

Prior to the manufacture of the specimens, CU performed a detailed FE modelling of the cruciform test articles in order to help selecting some design parameters of the specimen details.

Deformation and stress/strain analyses were performed using the FEM and comparisons were made with the strain gauge measurement. FE stress analyses were performed by using 3D solid elements with four elements in the thickness dimension in order to accurately model the secondary bending. The co-curvilinear thin shell elements are used for the same stress analysis. The calculated strains by the 3D solid and 2D shell elements are compared with the test measured strains. The 3D and 2D models agreed well in calculated strains and deformation, but discrepancy exists in the FE and measured strains on some strain gauge locations. Detailed strain comparisons are shown in Figure 68.

Life prediction

Based on the calculated *K* and material crack growth rates measured from welded M(T) specimens made of the same 2198 alloy with a transverse weld, fatigue crack growth life is predicted and presented in Figure 69. Comparison was made with the test results. Although all four test specimens are plotted in Figure 69, it is meaningful to compare the average life of the two specimens with nearly symmetric crack growth, i.e. COI-BIAX2 and COI-BIAX4.

Based on the comparison, the predicted life is shorter than the measured average life. There are three possible reasons for the underestimation of crack growth life.

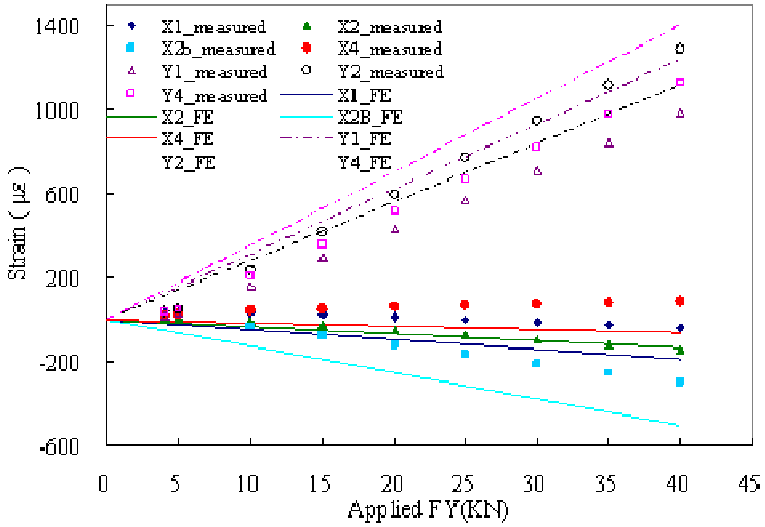

Figure 68: Measured and calculated strains for load case 1 (*Fx:Fy* = 0:1)

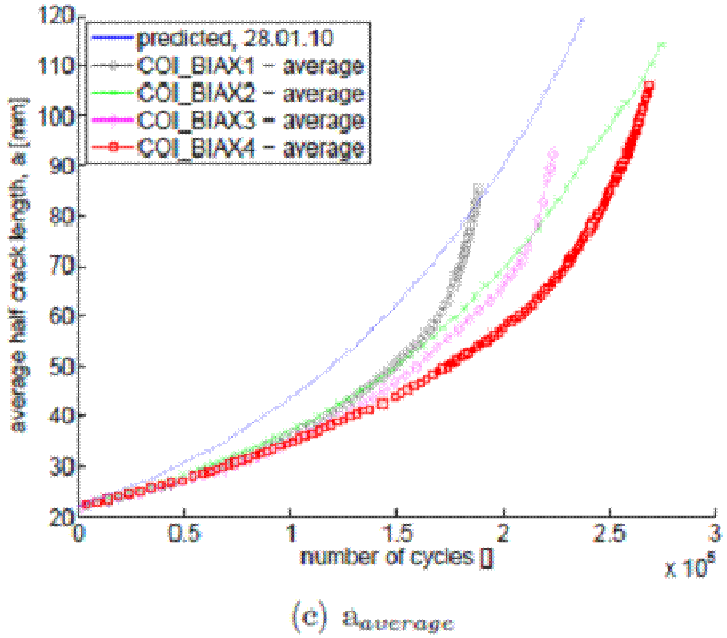

(c) $a_{average}$

Figure 69: Predicted and measured fatigue crack growth in the cruciform samples

2.8 WP 2.5 Long Term Design Data

Previous activity in years 1 & 2 in this task has been by Airbus D and Airbus UK and SABCA to produce samples for University of Patras to test. The following is a summary of the test work performed by Patras under this heading in the final period of the project.

2.8.1 WP 2.5 Long Term Design Data (University of Patras)

During the reporting period, the mechanical behaviour of friction stir welded 2050 T3 aluminium alloy was assessed. A total of 6 tensile and 16 Fatigue crack propagation tests were performed. All tests were performed at room temperature.

Specimen Code	Young Modulus [GPa]	Yield stress [MPa]	Tensile Strength [MPa]	Elongation to failure ε_{50} [%]
T1 (TT)	82.7	282.6	427.2	10.0
T2 (TT)	81.7	288.1	429.2	9.7
T3 (TT)	80.2	287.4	426.4	10.5
Mean Values	81.5	286.0	427.6	10.1
T4 (LT)	79.5	286.8	428.0	8.8
T5 (LT)	81.4	290.2	433.4	10.6
T6 (LT)	80.3	294.9	431.9	10.6
Mean values	80.4	290.6	431.1	10.0

Table 13: Tensile Test Results

2.8.2 Tensile test results

The configuration of the tensile test specimens are shown in the Figure 70 and Figure 71

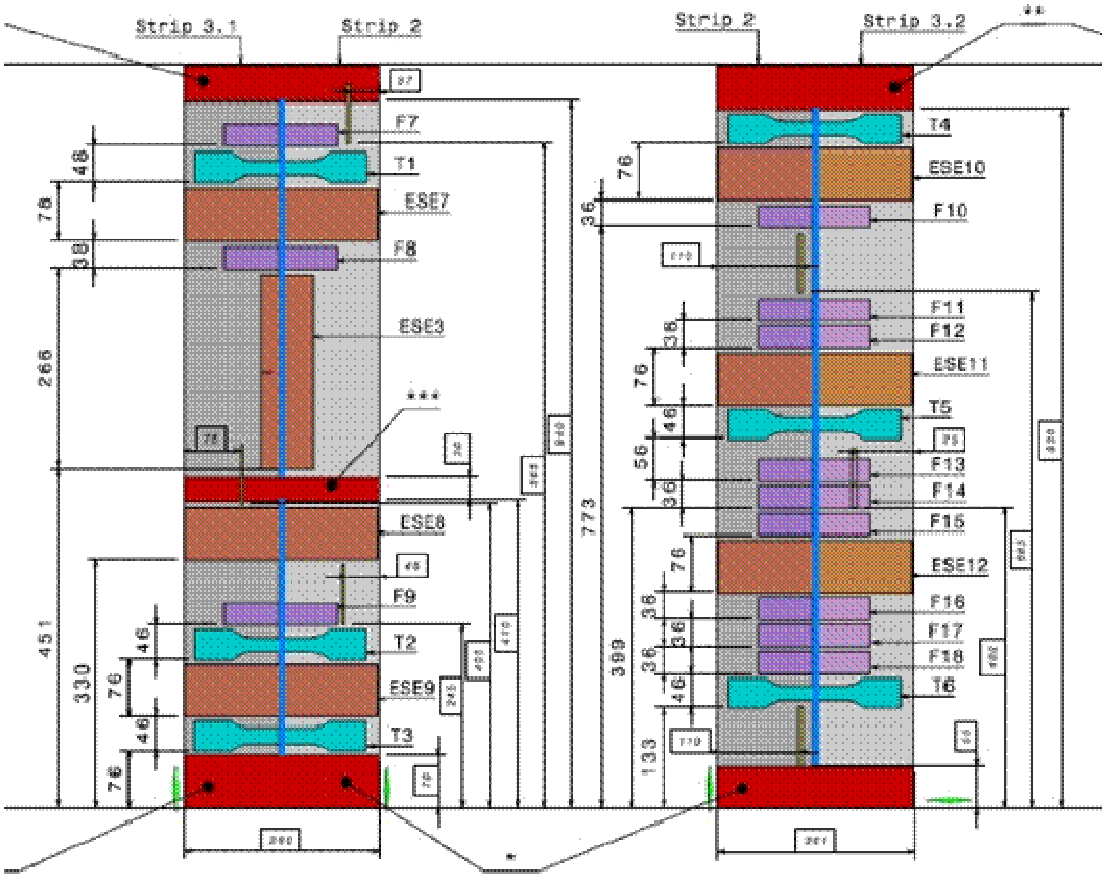

Figure 70: Tensile specimens as part of the welded plates

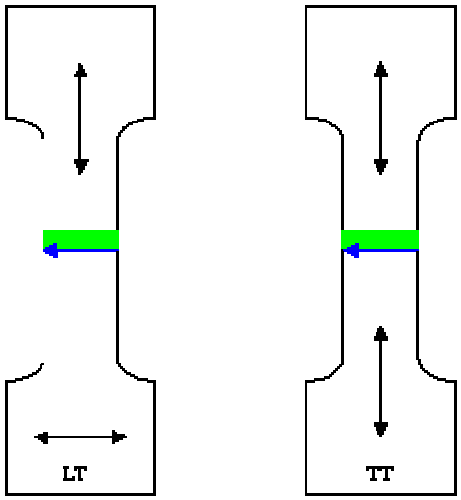

Figure 71: Tensile specimens used. Arrows indicate the rolling direction

Main findings

No significant differences are observed in the tensile behaviour of the welded specimens with respect to the rolling direction of the welded plates. The effects of the welding procedure seem to dominate on any differences which could have been expected due to the difference in the rolling direction of the plates.

No particular pattern was observed with respect to the fracture area with respect to the welding tool. Assuming that the welding tool rotated clockwise, Specimens T3 and T4 failed on the retreating side whereas specimens T1, T2, T5 and T6 failed on the advancing side of the weld. The fracture appearance was similar on all specimens.

Figure 72: Bottom view of fractured specimen

2.8.3 Fatigue Crack Propagation tests results

Four different weld configurations were tested, as summarized in the table and figure below. Four additional tests were performed on parent material.

Test sample	No. of samples	Rolling direction	Test series
C(T) geometry, reference material (non welded)	2	LT	1
C(T) geometry, reference material (non welded)	2	TT	2
ESE(T) geometry, crack parallel to the weld	3	TT	3
ESE(T) geometry, crack parallel to the weld	3	LT	4
ESE(T) geometry, crack perpendicular	3	TT	5

ESE(T) geometry, crack perpendicular	3	LT	6

Table 14: Weld configurations tested

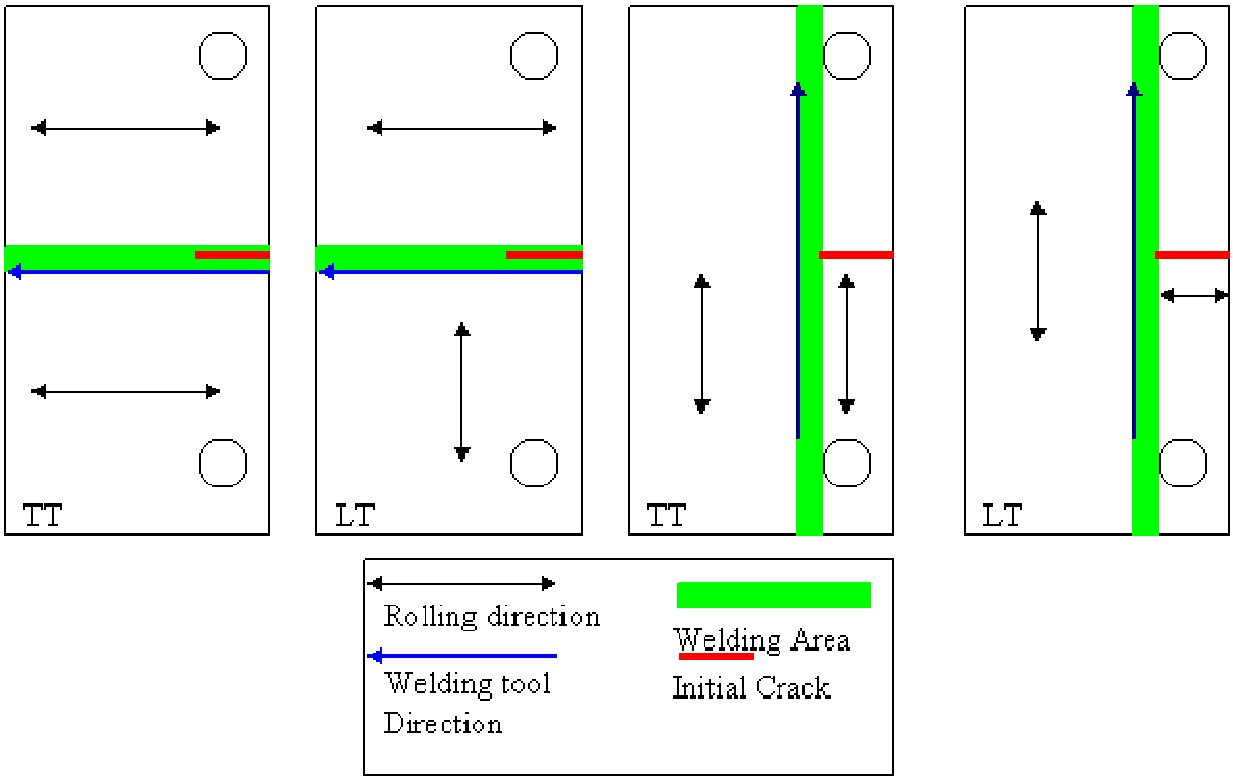

Figure 73: Weld configurations tested

Discussion

The reliability of the tests where the crack was propagating perpendicular to the weld is could not be proved in the current study. A macroscopic analysis of the fracture surfaces reveals uneven crack propagation throughout the specimen thickness. There was no consistency regarding the location of the non-uniform crack propagation area: some specimens had the fast fracture characteristics on the top side of the weld (shoulder of the weld tool) and others on the bottom side (note that all specimens were machined prior to the test to create a uniform surface). Therefore, the crack length measurements made cannot be of high confidence, as these were performed by optical means. Crack measurements by use of a DC-PD system would also give unreliable results, as the DC-PD calibration requires through-thickness cracking.

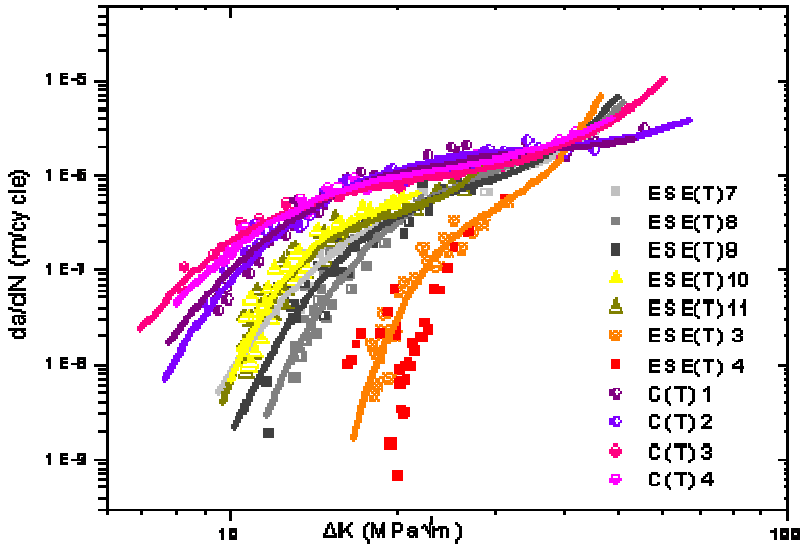

Figure 74: Comparative *plot of all tests performed*

During testing of ESE(T) 4 specimen, the crack growth rate was greatly reduced ($<1x10^{-9}$)as soon as the crack reached the weld zone. The crack continued to propagate after about 400000 fatigue cycles. The same behaviour was observed for specimen ESE(T)3, where the crack propagated up to the weld zone and then crack arrest was observed. The test was continued and the specimen failed in the grips after about $2x10^6$ cycles. In order to assess the fatigue crack propagation behaviour, the specimen was reduced in length by 30mm and new holes were opened for gripping. The initial crack length was then increased by 6mm so as to reduce the loads and avoid grip failure. The test was completed successfully, although the dimensions of the ASTM E647-05 specifications were not met.

Conclusions

- The fatigue propagation rate in the welded material is lower than the respective rate of the parent material up until the 3rd area (fast propagation area) of the da/dN – ΔK curve. The lower yield stress of the weld nugget causes an increase in the plastic zone ahead of the crack, which may be the reason for this behaviour.
- There is a much smaller linear (Paris) region in the da/dN – ΔK curves of the welded material. This may be caused by the residual stress distribution which was not taken into account in the calculation of ΔK.
- The fatigue crack propagation rate when the crack was propagating in the weld nugget was observed in the case where the welded plates had the same rolling direction, parallel to the crack propagation. An investigation of the material microstructure in the weld nugget would help to understand the observed difference in the crack propagation behaviour.

2.9 Task 2.6 Integrated Design Solutions

In this final period, the bulk of the activity has been with Dassault Aviation in design studies and cost evaluations of the Falcon 7X upper wing skin using a mixture of FSW followed by creep age forming. Additional test work has been performed by Cranfield University in stress analysis and testing of novel padup geometries developed by Airbus D. A small amount of completion work has been performed by SABCA on their FSW box beam and by Piaggio on testing of their FSW pressure bulkhead design.

2.9.1 Task 2.6 Integrated Design Solutions for Integral Structure Containing Welds and Other Processes (BAE)

BAE Systems is interested in the potential of FSW to replace Gas Metal Arc Welding (GMAW) as the primary welding method used in the land vehicle fabrication. In this workpackage, alternative joint concepts were developed in concert with BAE Systems' internal business units and took into account factors such as the access restrictions of FSW and tooling requirements. Some of these joint designs were implemented in Workpackage 3 and used on the BAE Systems technology demonstrator.

2.9.1.1 Existing Fusion Welded Joints

Some current GMAW joint designs used in the manufacture of land vehicles are shown in Figure 76 which highlight the range of joint types and thicknesses used. Common features of the configurations shown are the used of multiple filled weld passes and the limited penetration depth (relative to the material thickness) that is achieved. The latter will limit the load capacity of the joint, though solutions such as those shown in Figure 76b and Figure 76c use geometry to maximise the strength under particular loading configurations. Some use of edge preparation prior to welding has been applied, for example v-profiles appear to have been used in the joints depicted in Figure 76b and Figure 76d to improve penetration.

2.9.1.2 Joint Development for FSW

The design study examined several alternative joint configurations using FSW to replace the joints currently used with GMAW. For simplicity, two material thicknesses are identified and referenced as 'thick' and 'thin' section. These are defined as:

- 'Thick' section – material greater than 25mm thickness. A full penetration weld is not possible using FSW.
- 'Thin' section – material up to approximately 25mm thickness, in which a full penetration weld can be produced using FSW.

2.9.1.3 Butt Joints

Straight-edged butt joints are the standard welding configuration for FSW. All joint solutions that have been developed are essentially variations on the butt joint. Figure 77 presents three variations on the butt joint; (a) conventional square-edge full penetration butt, (b) double-sided square edged butt and (c) rebated butt joint. The double-sided and rebated butt joints would be used for joint thick-section material, in which it is not practicable to achieve a single-pass, full penetration weld. Offsetting the two welds to create the rebated butt joint has certain mechanical advantages. For

example, this joint geometry results in better performance in shear if loading is only expected from one side of the plate.

2.9.1.4 Corner Joints

Internal fillet welds are the Achilles heel of standard FSW processes due to the requirement for the tool to be normal to the component being welded. Consequently, particular attention was made towards the development of solutions for corner joints.

In Figure 77, concepts for a hybrid joint design using a combination of GMAW and FSW are shown. These are essentially GMAW joint configurations with simple modifications. FSW offers greater weld penetration compared to GMAW, which it would be anticipated would improve the overall joint strength compared to a GMAW only design. However, the inclusion of GMAW would limit the alloy selection to current alloys, which are principally older, lower strength alloy variants and mitigates one of the main advantages of FSW: the capability to used higher strength alloys. The internal GMAW fillet could be omitted if the design can tolerate leaving the internal joint open.

Figure 78 shows examples where, through a simple joint redesign, internal corner welds are avoided and FSW has been applied to produce tailored blank joints that removed the requirement for the inclusion of GMAW. The internal corner was of particular concern; by geometry it is a stress concentration point and from a processing perspective there is a potential risk for the formation of a root flaw that would act as an initiation site for a weld crack. To resolve this, a couple of potential solutions were investigated. Figure 78a shows how the backing anvil could be modified to have a shaped corner, which could be either rounded or chamfered. In such a situation, a small volume of plastic material would be forged into the profile during welding. An alternative solution is shown in Figure 78b, which uses a disposable bar, made from the same material as the parent which becomes consolidated into the weld. The disposable bar is machined back to the required profile as a post weld process to finish the joint.

The second feasible solution for corner joints using FSW is to move the weld away from the actual corner by utilising extruded material. Two examples are shown in Figure 79. By using extrusion to move the welds away from the corner they become standard butt joints. In the example shown, the joint is between thick and thin section but any combination of thick and thin sections are feasible. Figure 79b shows the same joint using rebated butt joints as an alternative to standard butt joints, which may be preferable depending on operational requirements

2.9.1.5 Dissimilar Alloy Welding

Depending on particular designs, the exclusive use of FSW may not be possible. A proposed solution that still allows higher strength alloys to be selected is to joint a strip of fusion weldable alloy to the high-strength variant. The fusion weldable alloy, which typically has a lower strength, can be made proportionally thicker than the high strength alloy, such that the structure is not weakened, and only a minimum weight penalty is incurred. An example of such a weld is shown in Figure 80.

Welding dissimilar alloys (of interest to BAE Systems) has been successfully demonstrated, as presented under Workpackage 3 in the second year activity report. The mechanical properties of the joint created were found to be similar to that of a weld in the lower strength alloy. GMAW processes can then be applied to finish the structure.

Alternatively, dissimilar alloy welds could be used to create a structure with different mechanical properties in different regions as dictated by the expected loading conditions on the vehicle in those regions

2.9.1.6 Technology Demonstrator

A scaled technology demonstrator was produced to demonstrate the application of FSW using new joint geometries and alloys (the production of the demonstrator is described under Workpackage 3). The component was a generalised cross-section of a land vehicle hull based on current BAE Systems platforms and incorporated five new and different joint designs, dissimilar alloy welds and extrusions alongside plate material. It should be noted; the technology demonstrator was not intended to present a single solution, but to incorporate a range of features that may, or may not, be used or considered for a production vehicle; in that respect the demonstrator is overly complex. The technology demonstrator is illustrated in Figure 81 and an overview is now discussed. The overall length of the component was 500mm.

- Eleven welds in total (per half-section), including butt, rebated butt, tailored blank, double-sided and inter-locking joints with both 45° and 90° angled joints
- Extruded (7449 aluminium alloy) use in corner joints
- Various material thicknesses
- Dissimilar alloy welds

Weld sequencing was a major consideration when designing the demonstrator. Designing a correct welding sequence not only assists in fit-up and assembly of the final product but assists in reduction of distortion. The demonstrator was designed to be made from three separate sub-assemblies not only to reduce distortion but for ease of manufacture.

The completed demonstrator component is shown in Figure 155 (Workpackage 3). Manufacture of the part, which included 24 welds in total, was conducted using modular tooling blocks. Each half-section was fabricated in three subassemblies prior to the final assembly which mated the two half-sections. The demonstrator component welds were then part ground and painted with undercoat and topcoat to exhibit standard finishing operations.

The successful fabrication of the finished article was attributed to careful consideration of a number of factors that included:

- Size, shape and position of welds within each sub-assembly
- Application of correct weld sequence
- Optimisation of correct welding parameters to minimise heat input and distortion
- Engineering good practice. Correct and accurate design of tooling blocks, including overhead and side clamping that allowed good fit-up of parts and sub-assemblies prior to welding
- The application of friction stir tack welding, where required, to the beginning and end of weld plates prior to the actual weld taking place

2.9.1.7 Closing the Structure

The manufacture of the demonstrator component highlights the ability to successfully construct a partially enclosed structure by the application of both good engineering practices and weld procedures. By applying what was learned from the demonstrator development, the progression from a partially enclosed to a fully enclosed structure could be realised by following a set of simple rules that are highlighted below.

- The overall design of the structure must incorporate smaller sub-assemblies to minimise distortion and aid final assembly
- Keep corner joint configurations as simple as possible by the design of extruded or machined sections and by minimising the number of welds per joint
- Maximise the use of single pass, square edge butt welds within corner joints and overall structural design
- Optimise welding parameters to minimise heat input
- Apply good engineering practices. These include simple, stiff, accurate modular tooling blocks. Sufficient overhead and side clamping. The use of tacking techniques to assist in accurate joint and final assembly.

Figure 82 shows an example of a more complex structure that could be made by applying the simple rule set developed above. Small sub-assemblies could again be designed that allowed two half shell components to be joined in final assembly. Figure 82a shows the two half shells exploded along the final joint line. The simplicity of the design also shows how the structure is self supporting with the top half located on top of the bottom half prior to final welding by a single pass square edge butt weld, rebated, or interlocking joint. Figure 82b shows the final assembly.

Figure 83 shows how a fully enclosed structure might develop. Figure 83a shows an exploded view (minus the right-hand-side body section for ease of viewing) of body assembly, front nose cone and rear door section. Figure 83b shows the assembly of the parts prior to final welding. It can be seen that the rear door locates into a rebate in the body section which allows for a single weld in a rebated joint configuration to be carried out. The front nose cone is also shown to locate into the body assembly by rebated joint which again allows for a similar weld to be carried around the circumference too complete the enclosed structure. Figure 83 c shows how the final assembly may look including doors.

2.9.1.8 Conclusions and Recommendations

- The joint design study identified numerous alternative joint configurations, utilising FSW, that have the potential to be applied to the manufacture of land vehicles
- Scaled examples of novel corner joint design have been successfully produced on specifically designed tooling blocks, demonstrating alternatives to more common fusion welded joints
- By optimising welding parameters heat input can be minimised, reducing the ‘heat affected zone’ and distortion levels
- It is essential that during the production of the welds and corner joints the individual weld pieces are clamped very securely into the tooling blocks either by side clamping, overhead clamping or a combination of both methods to negate separation of the joint during the

welding process. Friction stir tacking was demonstrated as a very successful procedure in assisting plate and sub-assembly alignment prior to welding

- By applying a simple set of rules fully enclosed structures can be designed and built by applying FSW techniques

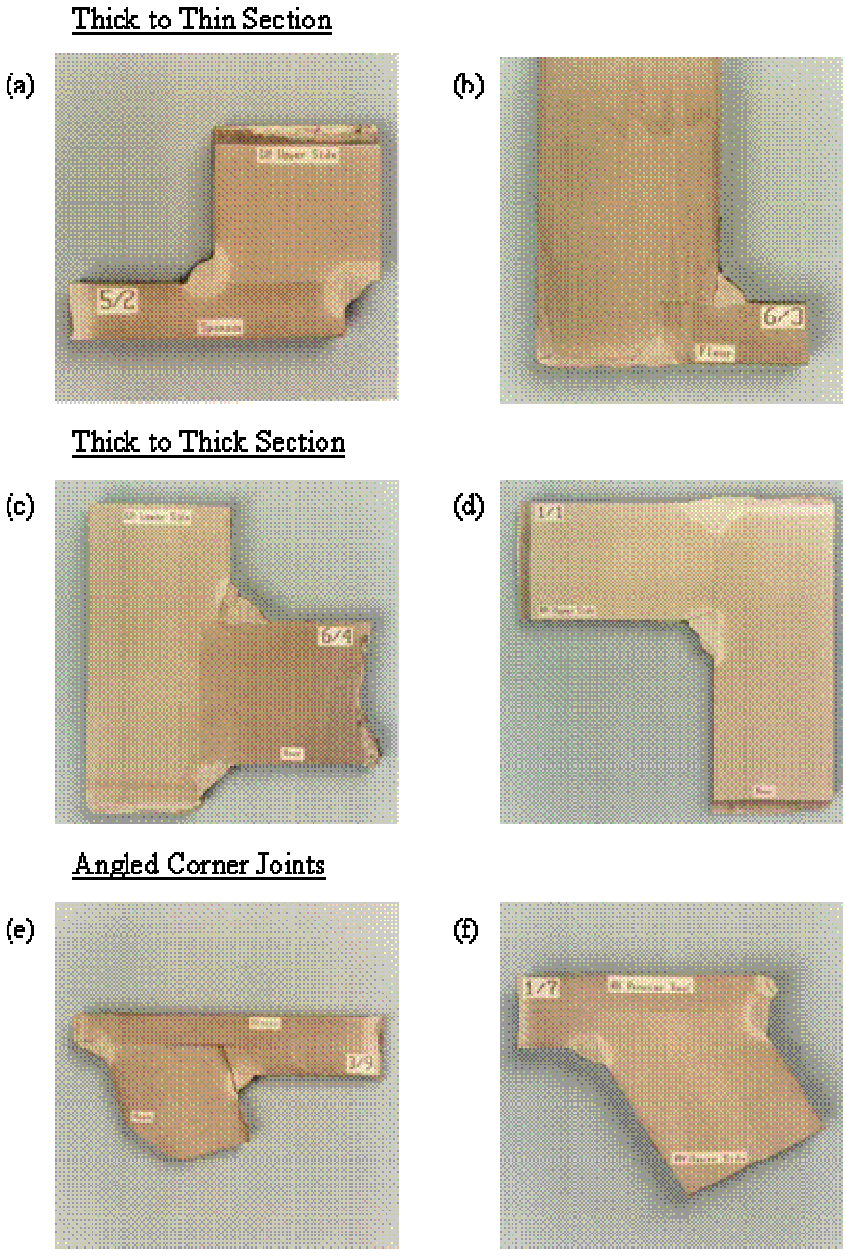

Figure 75 Example fusion welded joint configurations

(a) conventional straight-edged butt weld configuration

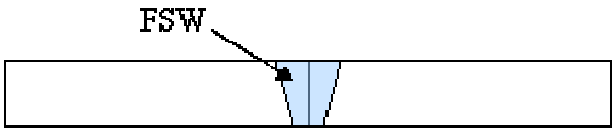

(b) double-sided, straight-edged butt weld configuration

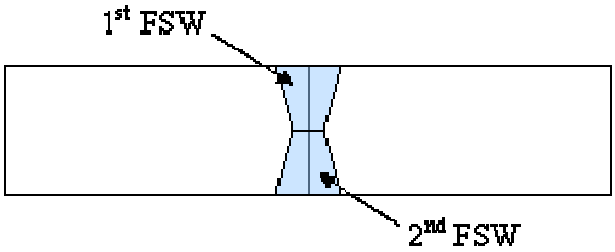

(c) rebated butt weld configuration

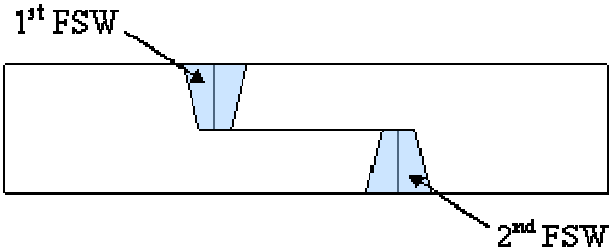

Figure 76 FSW butt joint configurations

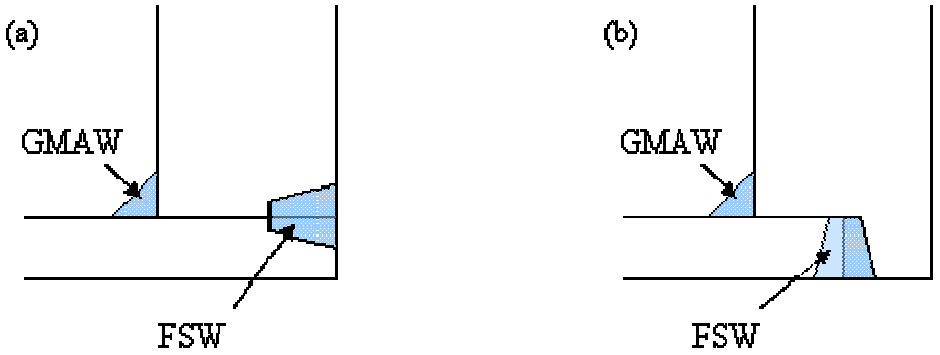

Figure 77 Hybrid joint designs for thick to thin section corner joint

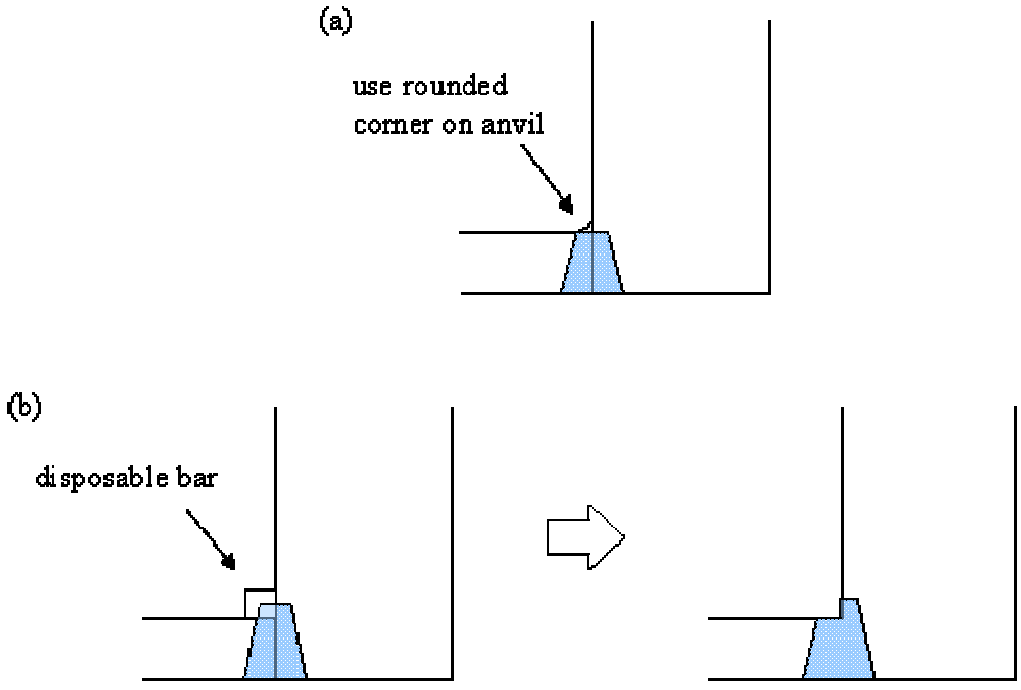

Figure 78 FSW tailored blank designs

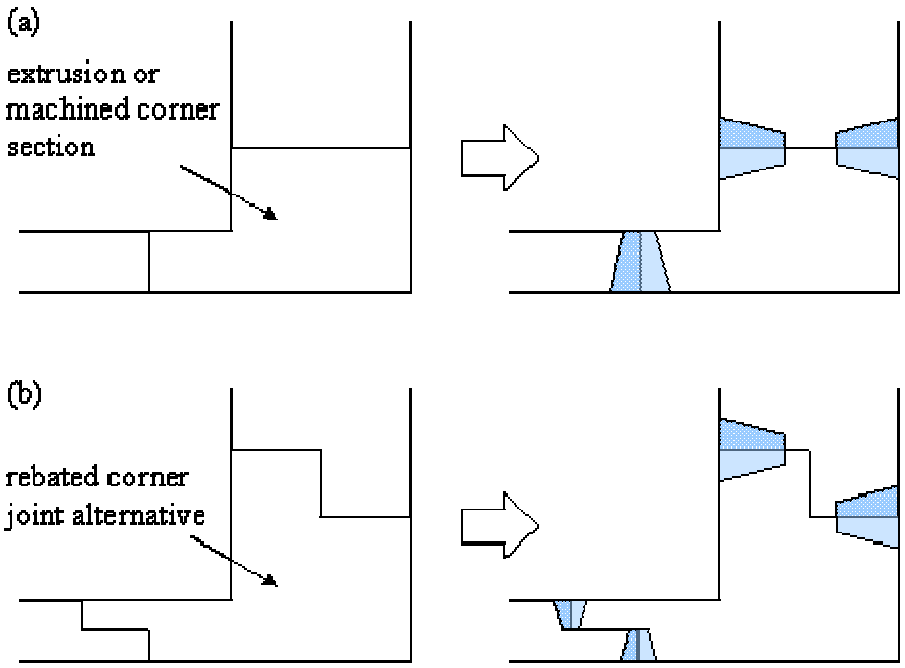

Figure 79 Corner joint concepts using extrusion

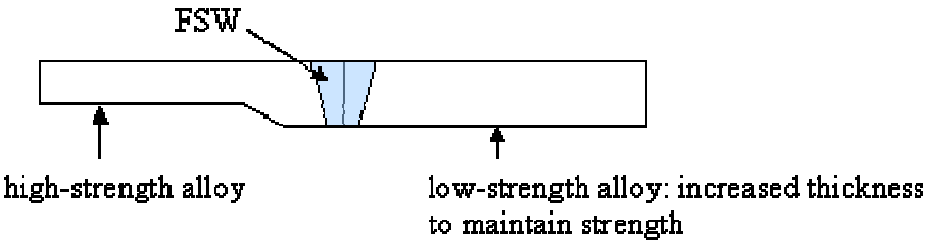

Figure 80 Dissimilar alloy joint

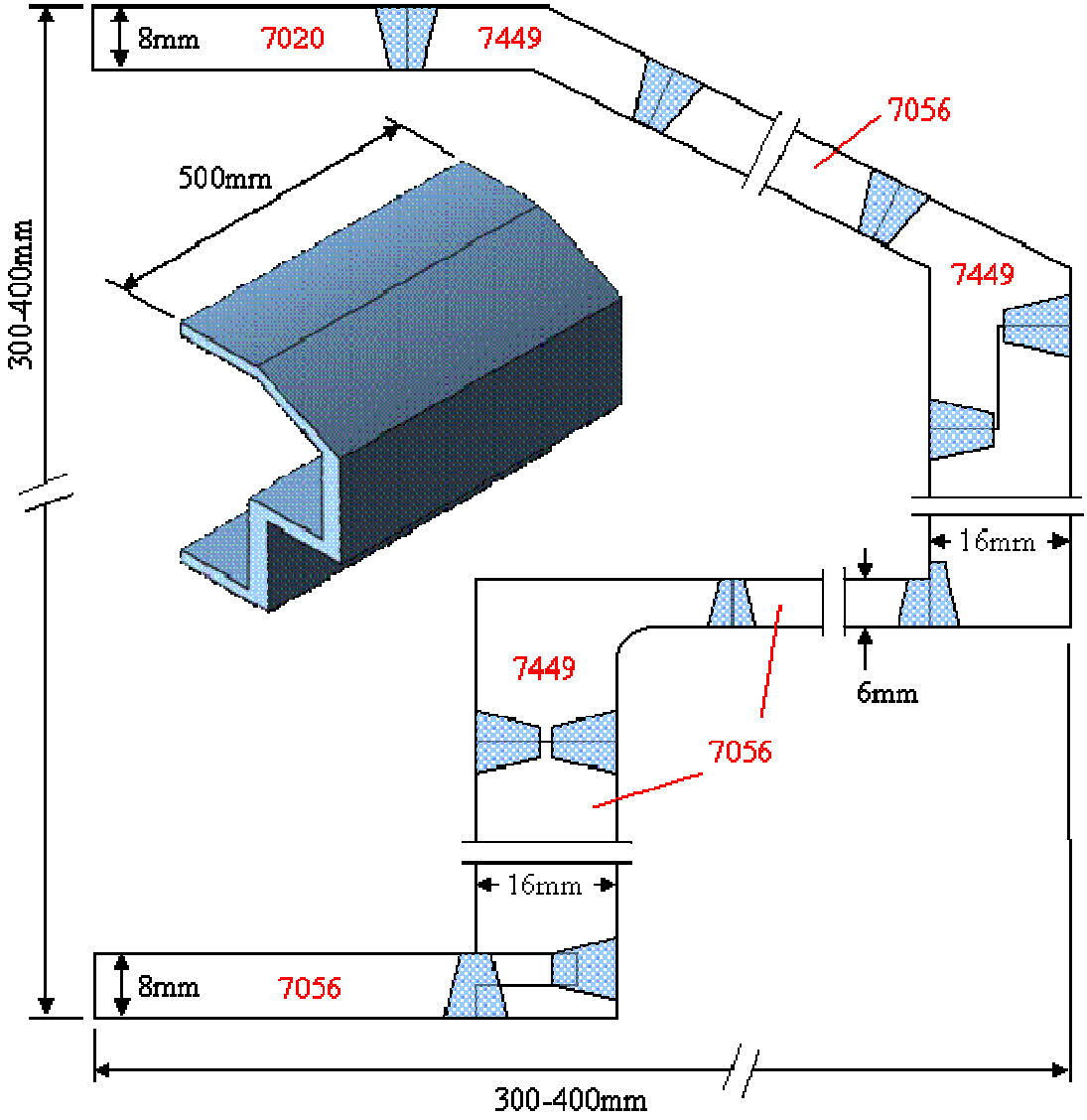

Figure 81 Geometry of demonstrator half-section

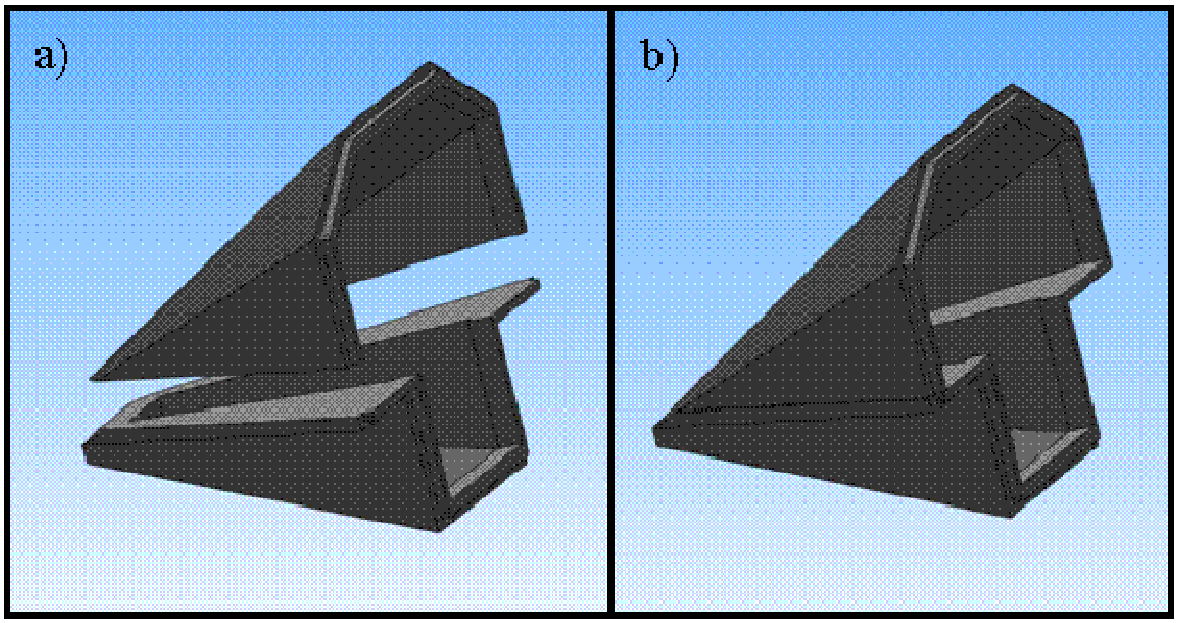

Figure 82 Front nose cone example

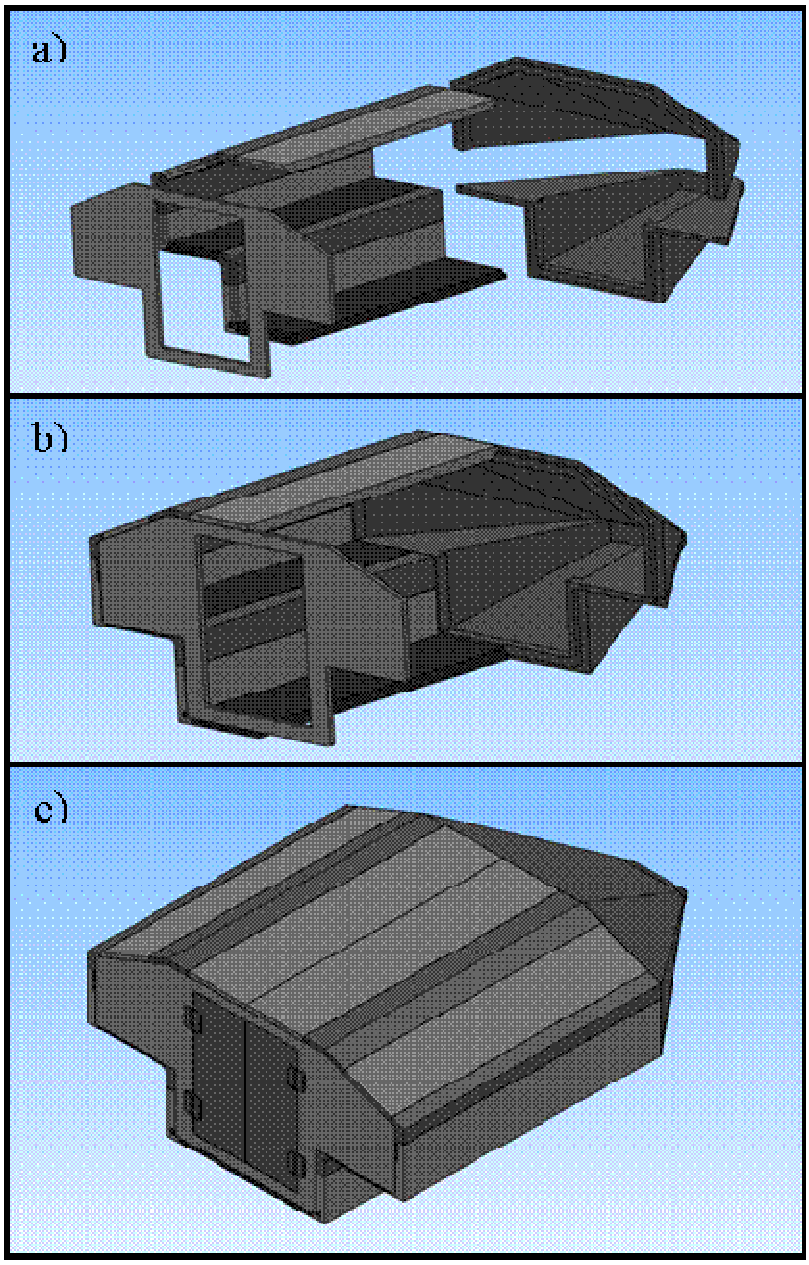

Figure 83 Development of fully enclosed structure

2.9.2 Task 2.6: Design of Cost-Effective IMS using FSW (Alenia Aeronautica)

Designed "I" beam structure incorporating FSW using existing and new performance data. This activity was made in collaboration with Piaggio. Validated 2-T manufacturing concept of Piaggio drawing.

Bulkhead panel:

1m x 1m approx, 2056 T3 +2024 T351 stiffeners welded by Lap joints
Review with Piaggio on shearweb design: T extruded substituted with L extruded.

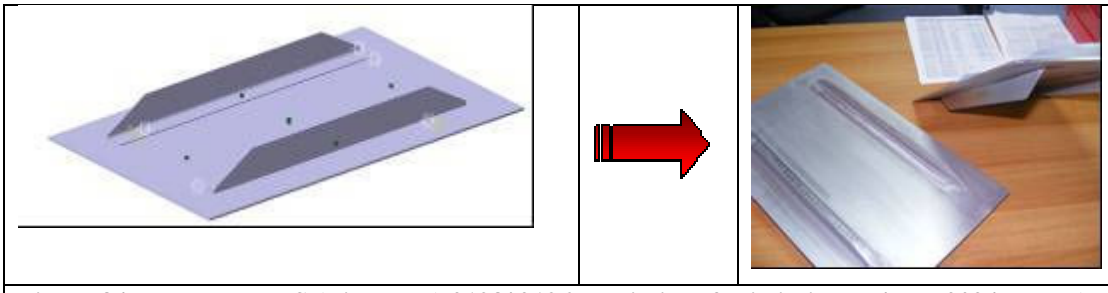

Figure 84: Double-T IMS (wing spar) 2198/ 2196ext similar & dissimilar: 7475 + 2024 ext (butt joint)

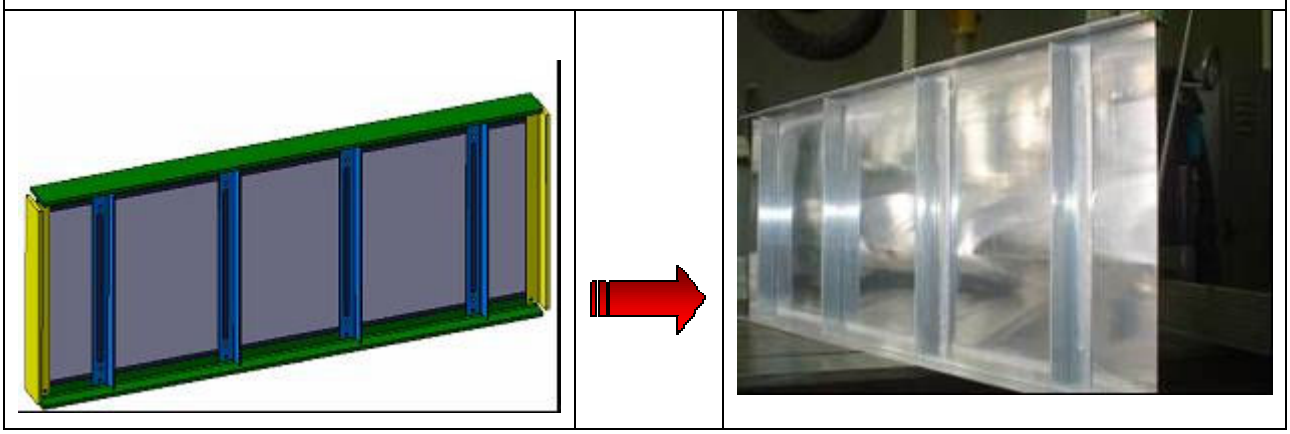

2.9.3 Task 2.6 Integrated Design Solutions (Dassault Aviation)

The DASSAULT-AVIATION contribution concerns the design of Falcon 7X upper wing skin based on extrusions assembled by Friction Stir Welding and formed by creep age forming in the objective of a reduction of the manufacturing cost.

To be compliant with the specificity of Falcon wing skin (wing root, profile break), the studied solution is based on (see Figure 85):

- Extrusions, taken into account the maximum available dimensions,
- Thick plates (wing root, wing tip), taken into account the optimized rolling direction,
- The mechanical properties of welded extrusions in longitudinal and transverse directions determined within task 5.3.

The weight of upper panel has been evaluated and compared with the current solution based on creep-age formed thick plates (see Figure 86). The manufacturing cost of upper panel has been evaluated and compared with the current solution based on creep-age formed thick plates (see Figure 87). The contribution for D15 deliverable has been done.

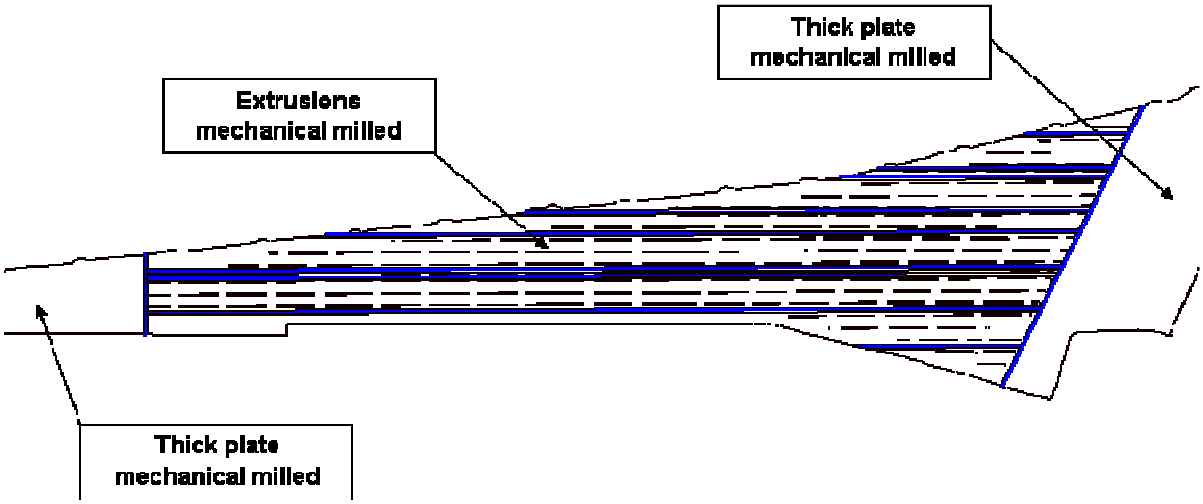

Figure 85: Design of integrated metallic structure applied on FSWelded upper wing skin (Falcon upper wing)

The weight evaluation is shown in Figure 86 and the cost evaluation in Figure 87.

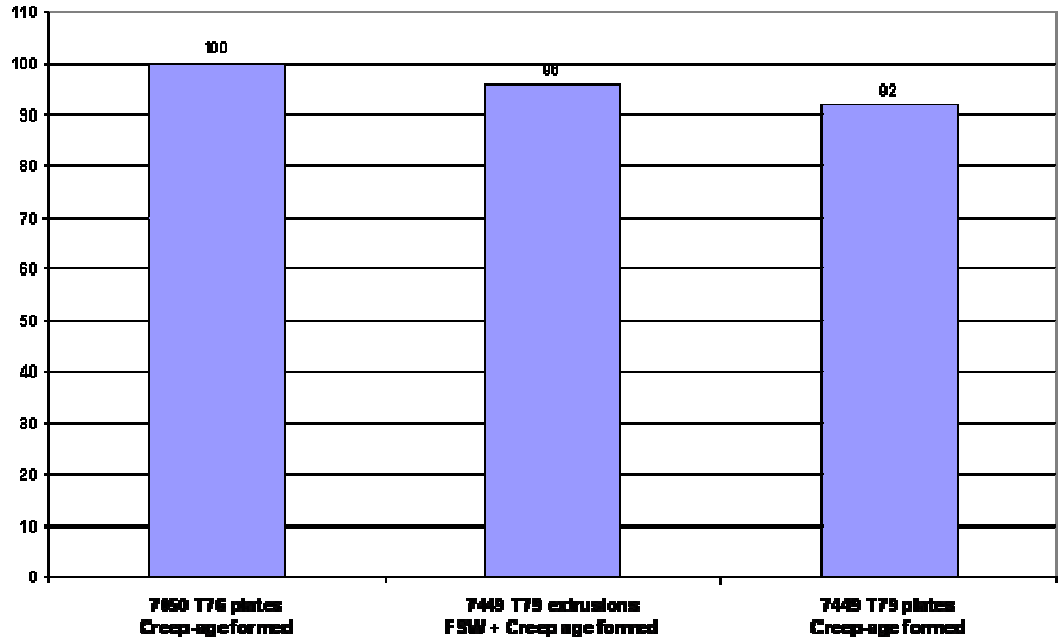

Figure 86: showing the relative percent weight reduction in the wing obtained by using extrusions plus FSW with creep age forming (centre) and creep age forming only of extrusions (right) in comparison with the standard route of creep age forming of plates (left)

The evaluations show that some weight reduction (5%) is possible by using the extrusions plus FSW route, but there are major cost savings associated with this of up to 30%

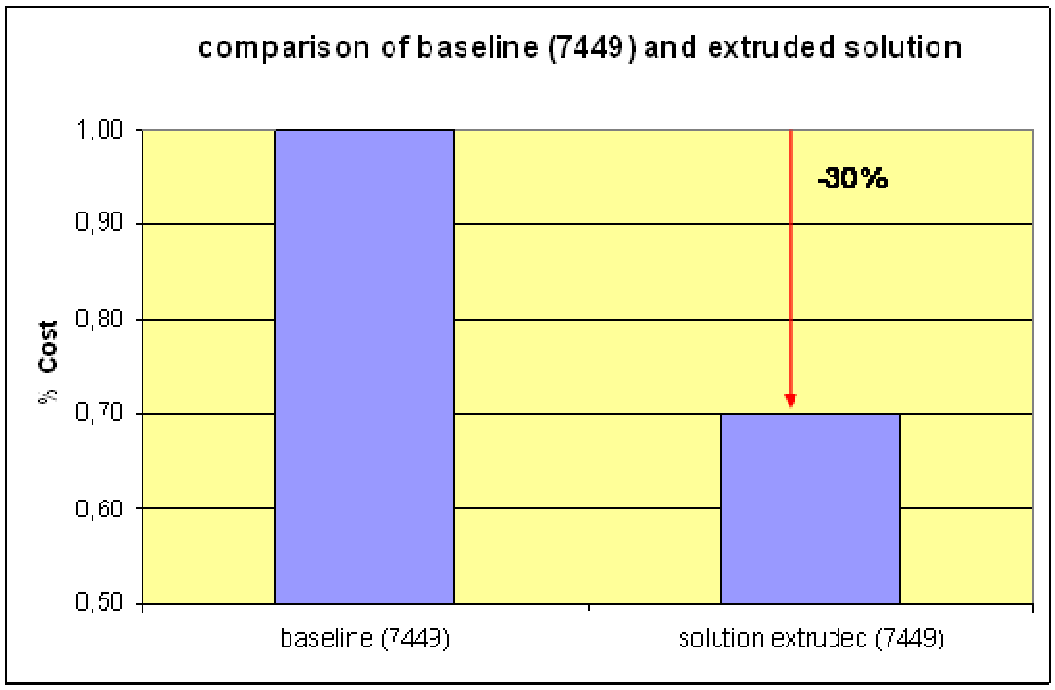

Figure 87: showing relative percent cost reduction obtained by using FSW of extrusions instead of plate for manufacture of Falcon upper wing

2.9.4 Task 2.6 Integrated Solutions (Sabca)

For the fabricated beam, in this period SABCA continued with their multipurpose integrated tooling concept. This included

- Backing bars enable also pre-assembly of specimen and PWHT clamping
- Stiffeners integrated in vertical walls also act as a guidance system for the backing bars withdrawal, as well as for some potential inside inspection, milling and repair systems

2.9.5 Task 2.6 Integrated Design Solution for Integral Structure Containing Welds and Other Process (Piaggio Aero)

Piaggio in task 2.6 was involved with Fatronik on the design of a small test coupon representative of the P1280 pressure bulkhead. The design of the test coupon was defined and the material\l delivered to Fatronik. Fatronik performed static tests and Piaggio performed fatigue tests of FSW welded lap joint. The results of the lap joint tests are as shown below.

Figure 88: Examples of FSW lap joint in Al 2024-Al 7475 after fatigue testing by Piaggio

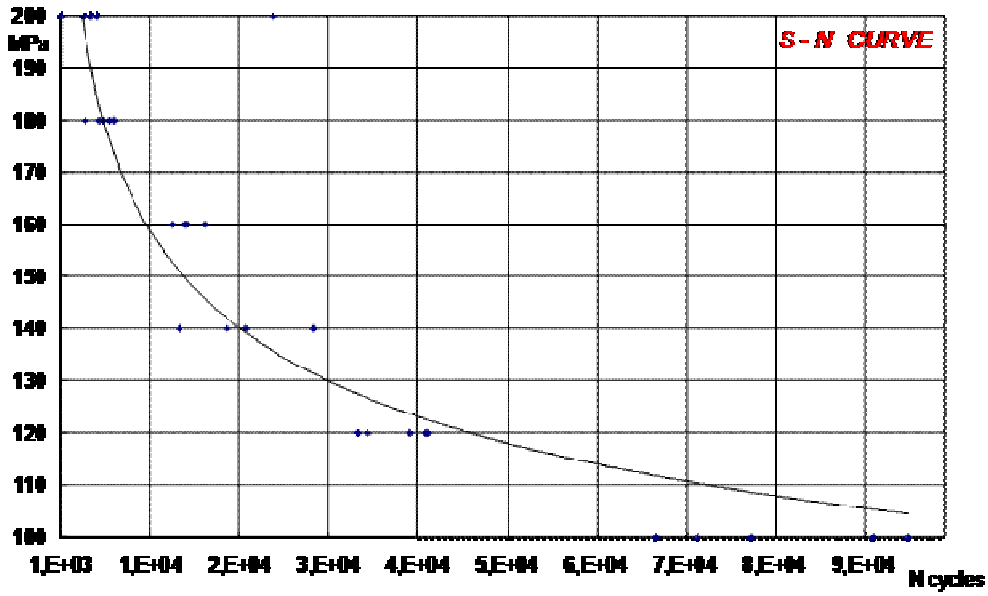

Figure 89: S- N curve obtained for coupons with friction stir welded lap joints in 2024/ 7475 alloys

2.9.6 Task 2.6 Integrated Design Solution for Integral Structure Containing Welds and Other Process (Cranfield University)

In this period Cranfield University has conducted finite element and experimental stress analysis of selected designs of skin-stringer panel joint from the 6 concepts originally developed by Airbus D in years 1 & 2 of this project. Stress intensity values for this sample geometry have been calculated for a range of crack lengths. Based on these and on the values of residual stresses for this joint design measured by GKSS, calculated predictions of fatigue life and crack length Vs fatigue cycles have been calculated. The predicted curves have been compared with those obtained during experimental fatigue testing for damage tolerance.

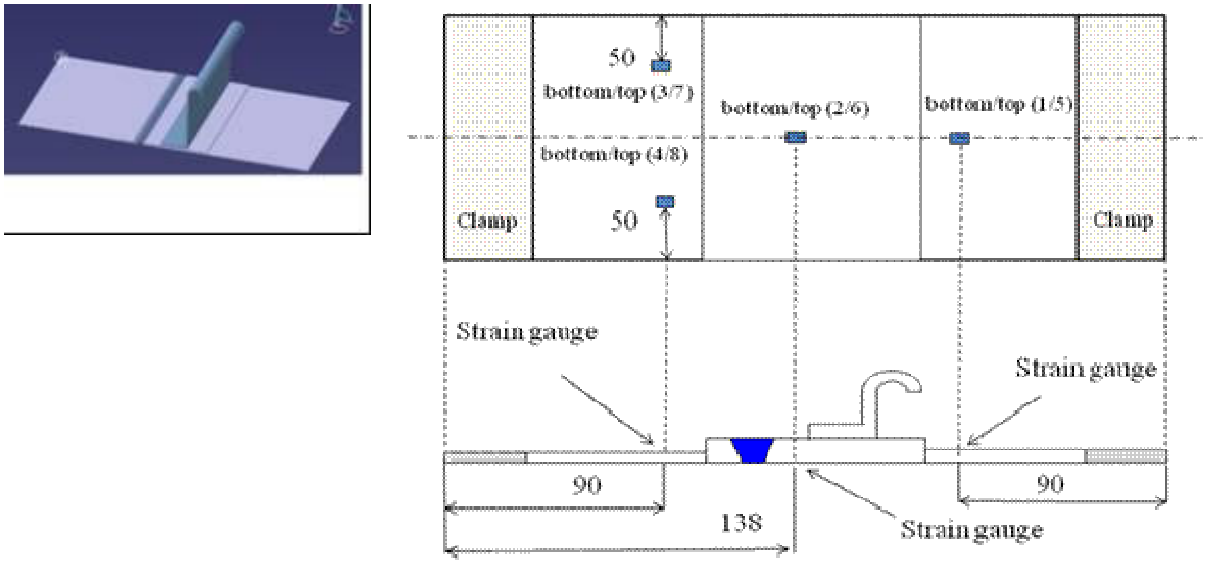

Figure 90: Concept 1 Skin/stringer joint with FSW showing location of FSW and strain gauges

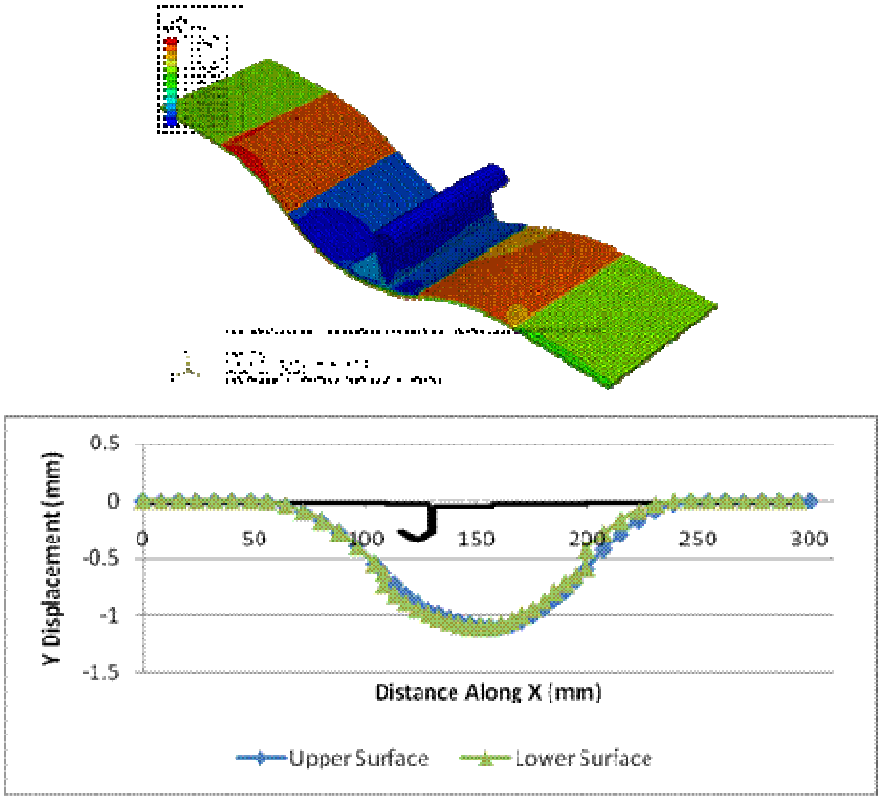

Figure 91: Finite element analysis showing out of plane displacements under in plane tension at a remote stress of 100 MPa for concept 1 sample. Maximum displacement = 1.1 mm at the stringer pad-up

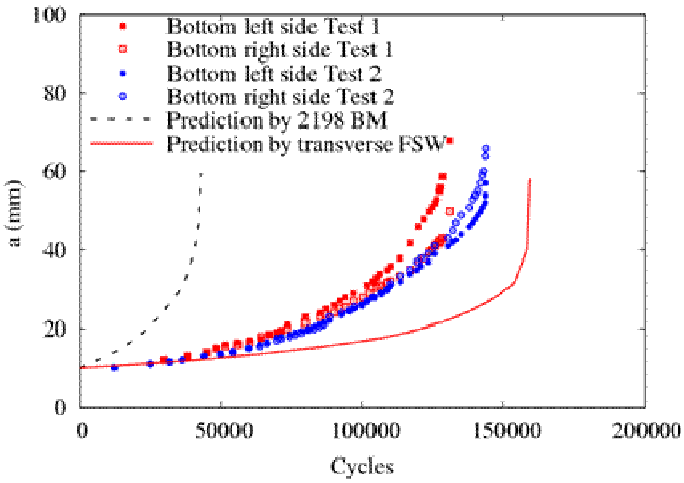

Figure 92: Comparison of crack length Vs cycles data for experiments and for predicted curves for ther concept 1 design of skin- stringer joint with FSW. BM is base material data, FSW is using friction stir weld material data

The experimental stress analysis was performed using strain gauges located at the positions shown in Figure 90. The values obtained experimentally during in plane loading of the sample were in good agreement- within a few % of strain with those of a finite element model of the joint. The asymmetric position of the pad up and the stiffener provoked significant out of plane bending as shown in Figure 91.

Finite element models were also used to calculate stress intensity factor values for the crack development in the joint design, with the crack centre on the line of the stringer. These values were then used together with material fatigue crack growth data gathered in Tasks 2.2 and 2.3 to predict the a Vs N behaviour of this geometry and compare it with experimentally measured values. Two sets of material data were used. One of these was base material or BM in Figure 92 This was data from unwelded sample. The other was from transverse weld data from FSW samples of this alloy. The two sets of material data gave very different lives- changed by a factor of between 3 and 4 on life. . The actual experimental data fell between these two extremes but closest to the transverse welded data, which was however slightly non conservative, whereas the BM data resulted in a conservative predication, which was however in significant error.

3 Work Package 3: Development of New Applications for FSW

3.1 Task 3.1 Development of FSW Process for New Similar Alloys (Alenia Aeronautica)

The Alenia contribution to WP3 consists in defining and developing the process for similar butt joint configuration with materials like 2198 T8, 7075 T6 and 2024 T3 between themselves (3.1-3.2). These results are been basics for the dissimilar butt joint configurations development of 2198 T8/ 2196 T8 and 2024 T3 / 7075 T6 (3.3-3.4), in order to produce and to test the “I shape” structure. The

parameters have been developed by Alenia using a standard tool and facility: Rigiva R100 (in Pomigliano Plant) and Colgar NC (in Torino Plant).

Alenia contribute is also the definition & process development for dissimilar lap joint between 2056 t3 (skin) and 2024 t351 extruded (stringer).

The preliminary tests made to find the best parameters are been visible inspection, bending test, micro/macro observations and tensile test.

For the characterisation program (process repeatability verification) of the 2024 t3 and 7075 t6, the welded proprieties through static tension, compression, shear, fatigue, stress corrosion, microhardness, intergranular and exfoliation corrosion.

For the characterisation program of 2198/2198 we have checked them with static tension, microhardness, and fatigue. The 2196 hasn't been tested because is identical to 2198 but extruded.

For dissimilar characterisation program of 2024 / 7075 we have used the same tests of theirs similar configurations.

The 2056/2024 test for lap joint characterisation has been performed with hoop stress (static and dynamic) and T-pull static (always static and dynamic), in order to manufacture the bulkhead panel.

3.1.1 Similar alloy welding: 2198 T8

AA 2198 T8 was used. The thickness welded is been 3.2 mm and the dimensions of each sheet before weld are been 200 mm x 300 mm (this last dimension is parallel to rolling). The welding tool had a shoulder of ϕ15 mm and an threaded pin of M5x2.4. These tests are preparatory to weld 2198 with 2196. We have evaluated the Joint quality with the bending tests. The micro observation shows that weld of "good-bend-specimen" don't present any defects. The table of tensile tests shows the best results: an yield 253-257MPa and an ultimate load 364-368 MPa. The approximate mean value is more than 90%.

3.1.2 Similar alloy welding: 2024 T3

The Alloy tested was AA 2024 with heat treatment T3. The dimension of sheets are 225 mm x 500 mm (this is parallel to rolling), with a thickness of 2.5 mm . The welding tool has a shoulder of ϕ10 mm and an frustum-conical pin of ϕ 4.2 mm. The trial planning for this material is been produced combining some process parameters. The welds manufactured with these parameters are been tested in order to identify the best solution. Afterwards Alenia has tested trough macro observation and bending test.

Bending test is regulated trough ASTM document:

- E 190 – 92: Standard Test Method for Guided Bend Test for Ductility of Welds.
- E 290 – 97a: Standard Test Methods for Bend Testing of Material for Ductility.

Macro observations are regulated trough ASTM document:

- E 3 – 01: Standard Guide for Preparation of Metallographic Specimens.

Last step, the specimens which have exceeded even the macro observation and bending test, have been tested by:

- Static Tension
- Static Compression
- Shear
- Fatigue

The instructions are in ASTM document:

- E 8 – 04: Standard Test Methods for Tension Testing of Metallic Materials.
- ASTM E9: "Standard Test Method of Compression Testing of Metallic Materials at Room Temperature
- ASTM B831: Standard Test Method for Shear Testing of Thin Aluminium Alloy Products
- ASTM E 466: Standard Practice for Conducting Force Controlled Constant Amplitude Axial Fatigue Test of Metallic Materials

3.1.3 Similar alloy welding: 7075 T6

The Alloy tested was an AA 7075 in heat treatment T6. The thickness welded is 2.5 mm and the dimension of each sheet before weld is 225 mm x 500 mm (this last dimension is parallel to rolling). The welding tool has a shoulder of ϕ10 mm and an frustum-conical pin of ϕ 4.2 mm.

In order to find the best solution of this parameters, the welds are been inspected with a first valuation: the visible control. After, we have tested with macro observation and bending test

At the end, those who have surpassed also the visible inspection and bending, are analysed by tensile test. The best parameter is characterized to 200 mm/min of travel speed, to 830 rpm of rotation speed and 1° of tilt angle.

3.1.4 Dissimilar alloy welding: 7075 T6 with 2024 T3

After the characterization of 7075 T6 and 2024 T3 welded with themselves, we have developed the dissimilar weld between 7075 and 2024. The tool used is the same of similar configuration.

The optimal process parameter used are been the same of 2024 t3: 800 rpm, 100 mm/min because those of 7075 T3 (800rpm, 200mm/min) are "colder" and so may not allow the weld.

Trying the weld of two sheet into different position configuration (advancing and retreating side, in an anticlockwise and clockwise verse) it was able to study the position of them. We have concluded that the 7075 must be located in advancing side.

The bending test results are good like also the macro observation test. For the mechanical properties the comparison must be made with the alloy least performing: the 2024. The mean value of 0.2% yield strength is 302 MPa (98 % of BM). The mean value of maximum tensile strength is 445 MPa. The efficiency compared to base material is 94%.

3.2 Task 3.1 Development of FSW Process for New Similar Alloys (EADS Germany)

Developments of welding parameters for welds up to 20 mm thick 2050 using the new DeltaN tool concept showing optimised heat generation - full characterisation of the welds.

EADS G welds were performed on the ESAB Superstir F5A FSW machine, shown in Figure 93.

Figure 93: ESAB Superstir F5A FSW machine used by EADS G

This 2-D machine is numerically controlled and the axes are electrically driven. Welds can be performed in force or position or combined controlled mode.

For the COINS Project, the machine was equipped with the DeltaN tool, shown Figure 94.

Figure 94: DeltaN Tool generation 4 mounted on the ESAB machine welding head

Next to the body the DeltaN tool consisted of a 4 flat threaded conical pin made out of MP159 alloy, shown in Figure 95.

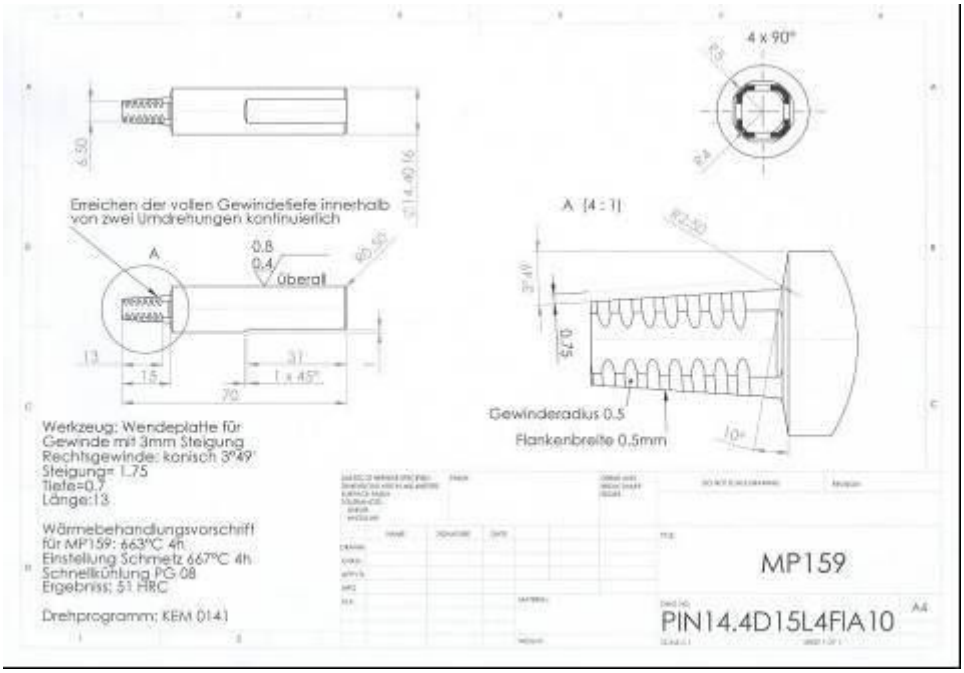

Figure 95: Pin geometry used in DeltaN tool

EADS G alloy of interest was also 15 mm thick 2050. This alloy was butt welded in T3 and T8 tempers. Further some welds were stretched by 3% before artificial ageing to T8 temper.

Basic characterisation of EADS G welds was done by macro sections, micro hardness measurements and tensile tests.

Welding parameters for welds up to 15 mm thick were developed using the new DeltaN tool concept with optimised heat generation.

The development of the DeltaN tool is one main activity in Work Package 6, which will not be reported here. This activity is running in parallel to the activities reported in the following.

Therefore the parameter study started using not the final DeltaN tool status and ended by using the fourth and final generation of DeltaN tool.

The recommended usable range of welding parameters for alloy 2050 T3 in 15 mm thickness, showing sufficient surface appearance from top side as well as no feature on root side is a welding speed between 200 and 400 mm/min, 500 to 700 rpm and a vertical down force of 32 kN.

The characterisation of the DeltaN generation 4 welds on 15 mm thick 2050T8 was done by macro sections, shown in Figure 96 and Figure 97.

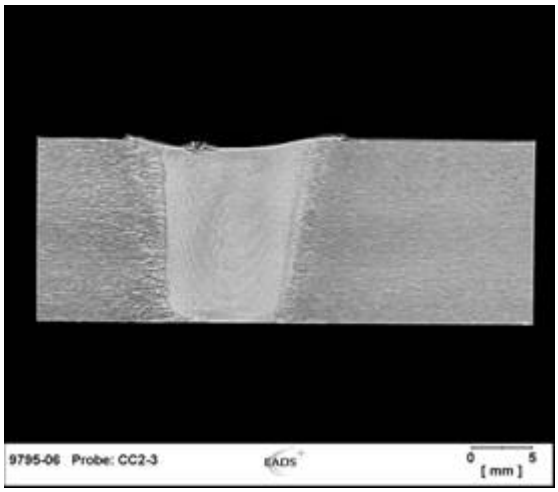

Figure 96: Macro section of 2050T8 DeltaN FSW, 15 mm thick, feed 200 mm/min, revs 500 1/min

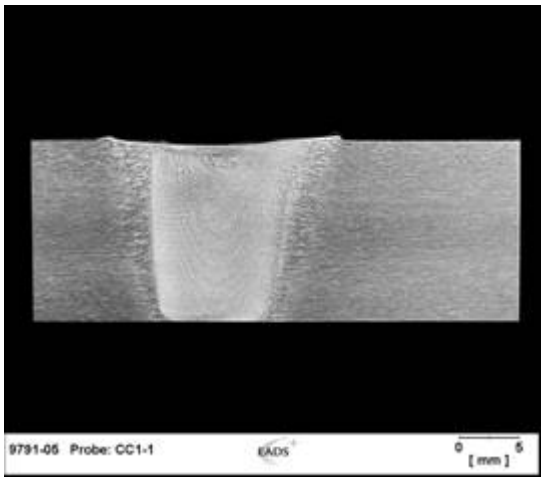

Figure 97: Macro section of 2050T8 DeltaN FSW, 15 mm thick, feed 400 mm/min, revs 700 1/min

In both cases the welds were tight and free of feature. The Dynamically Recrystallized Zone (DRZ) showed the typical nearly cylindrical shape of a DeltaN tool weld. This shape led to a reduction of distortion and was achieved by a non-rotating shoulder.

Next to the macro sections Vickers hardness testing was done. Results are presented in Figure 98 and Figure 99.

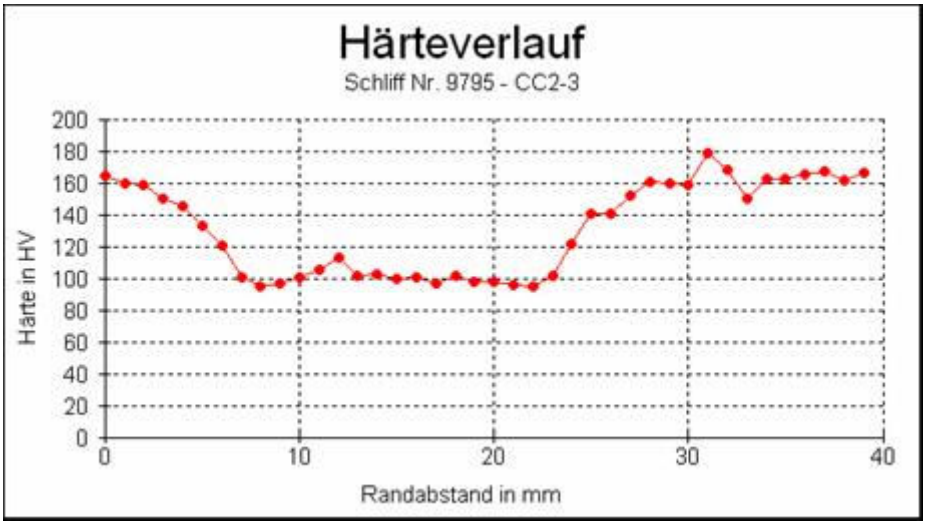

Figure 98: Vickers hardness testing results on DeltaN generation 4 weld on 2050 T8, welding speed 200 mm/min, 500 revs/min

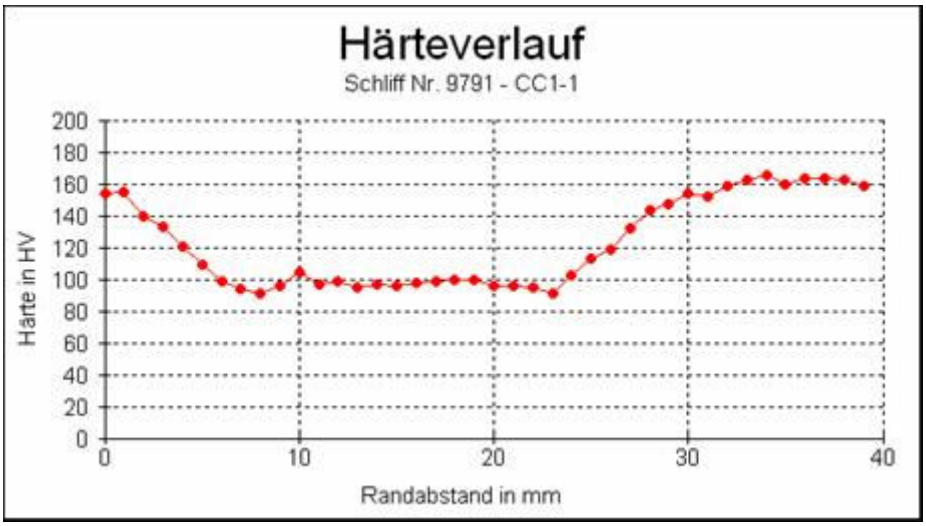

Figure 99: Vickers hardness testing results on DeltaN generation 4 weld on 2050 T8, welding speed 400 mm/min, 700 revs/min

The comparison of both hardness curves led to the conclusions that 2050 T8 had a severe loss of hardness of approximately 60HV after welding but the alloy further showed a very robust reaction on the FSW process heat impact. The softening or degradation of hardness did not depend on the heat input.

The welding speed did not matter.

Further welds were performed on 15 mm thick 2050 in T3 temper. After welding in T3, one specimen was artificially aged to T8 by applying 155°C heat treatment during 18 hours. Micro hardness results are shown in Figure 100 and Figure 101.

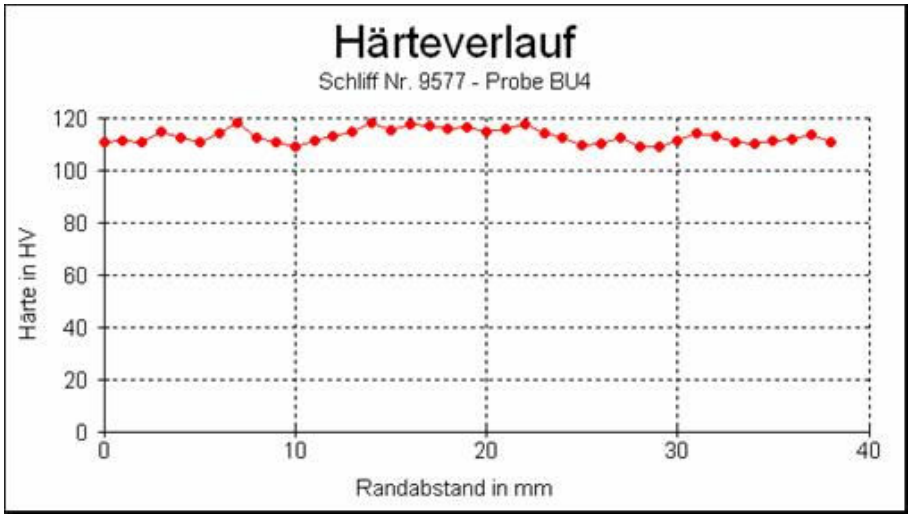

Figure 100: Vickers hardness testing results on DeltaN generation 3 welds on 2050 T3, welding speed 160 mm/min, 450 revs/min

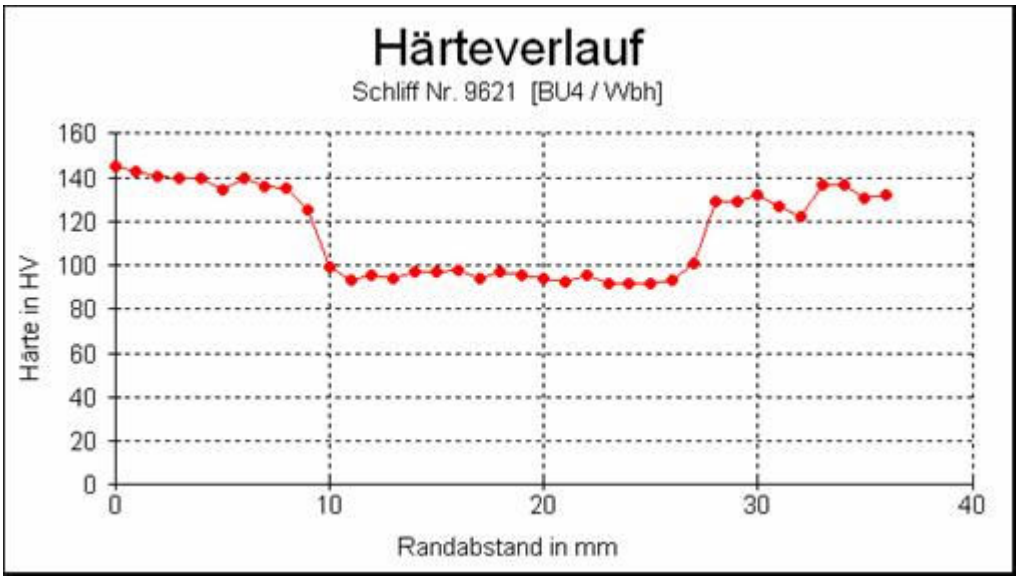

Figure 101: Vickers hardness testing results on DeltaN generation 3 welds on 2050 T3 & PWHT to T8, welding speed 160 mm/min, 450 revs/min

The hardness of the DRZ did not respond on the PWHT while the HAZ was aged.

This result was disappointing because the loss of hardness was severe and could not be overcome by simply ageing.

Literature says that one measure to strengthen the DRZ by ageing is to apply an additional stretching of the material for generating dislocations.

On tensile test specimens this procedure was done. The result was promising, as shown in Table 15.

Type of Weld	YS (MPa)	UTS (MPa)	El (%)
2050 Standard Tool	289-290	419	9,7-10,6
2050 DeltaN Tool	292-294	420-421	6,8-7,4
2050 Standard Tool (3% PWStretch)	466-466	497-498	6,5

Table 15: Tensile strength test results on 2050 T3 welds with T8 PWHT using standard and Delta N tools, with and without stretching before ageing to T8.

The results on one hand corresponded to the experiences that have been made by changing the welding parameters: The hardness and also the tensile test results did not depend on the tool technology as it does not depend on different levels of heat input. The tensile strength test of DeltaN tool welds led to same values as the standard tool welds.

On the other hand the effect of stretching between welding and ageing was significant. The strength of the weld reached base material properties in this case.

3.3 Task 3.2 Testing of New Similar Alloys (EADS France)

In this task during the final period, work carried out consisted in:

- Crack propagation tests on 2050 bobbin tool welds, which completed the full characterisation of these welds.
- Basic characterisation tests of 23 mm thick 7449 bobbin tool welds: metallographic investigation, tensile and fatigue testing.

Table 16 and Table 17 recall the different tests carried out and testing conditions.

Tests	Thermal state	Location	Direction	Number	Test specimens
Microhardness profiles / Macro and micro cross sections	T34 T8	BM& weld	-	-	Metallographic block (80x10x14.8)
DSC	T34 T8	BM& weld	-	8 8	Disks (∅5xH1.5)
Tensile tests	T8	BM&weld	L & LT	12 (4X3)	Cylinder-shaped (∅6x42 gauge except NZ/LT ∅10x60)

Fatigue endurance R=0.1 Kt=1	T8	weld	LT	10	Flat-shaped (3x14 gauge section)
Fatigue Crack Growth R=0.1, R=0.4 and R=0.7	T8	BM&NZ	T-L	6	CT W75 B

Table 16: Testing matrix for 2050 Bobbin Tool Welds

Test	Thermal state	Location	Direction	Number	Test specimens
Microhardness profiles / Macro and micro cross sections	TAF T79	BM& weld	-	-	Metallographic block (80x10x14.8)
Tension	T79	BM& weld	L & LT	12 (4X3)	Cylinder-shaped (∅6x42 gauge except NZ/LT ∅10x60 gauge)
Fatigue endurance R=0.1 Kt=1	T79	weld	LT	10	Cylinder -shaped (∅8 gauge section)

Table 17: Testing matrix for 7449 Bobbin Tool welds

Fatigue crack growth tests were performed in the T-L configuration at various R ratios with the crack located either in the 2050 base material or in the nugget in order to investigate the influence of the residual stresses on the propagation rate. The experimental results are displayed in Figure 102. It can be seen that the propagation rate is very similar in the base material and in the nugget zone and that the R ratio has a minor effect on the propagation rate, especially for a crack located in the nugget.

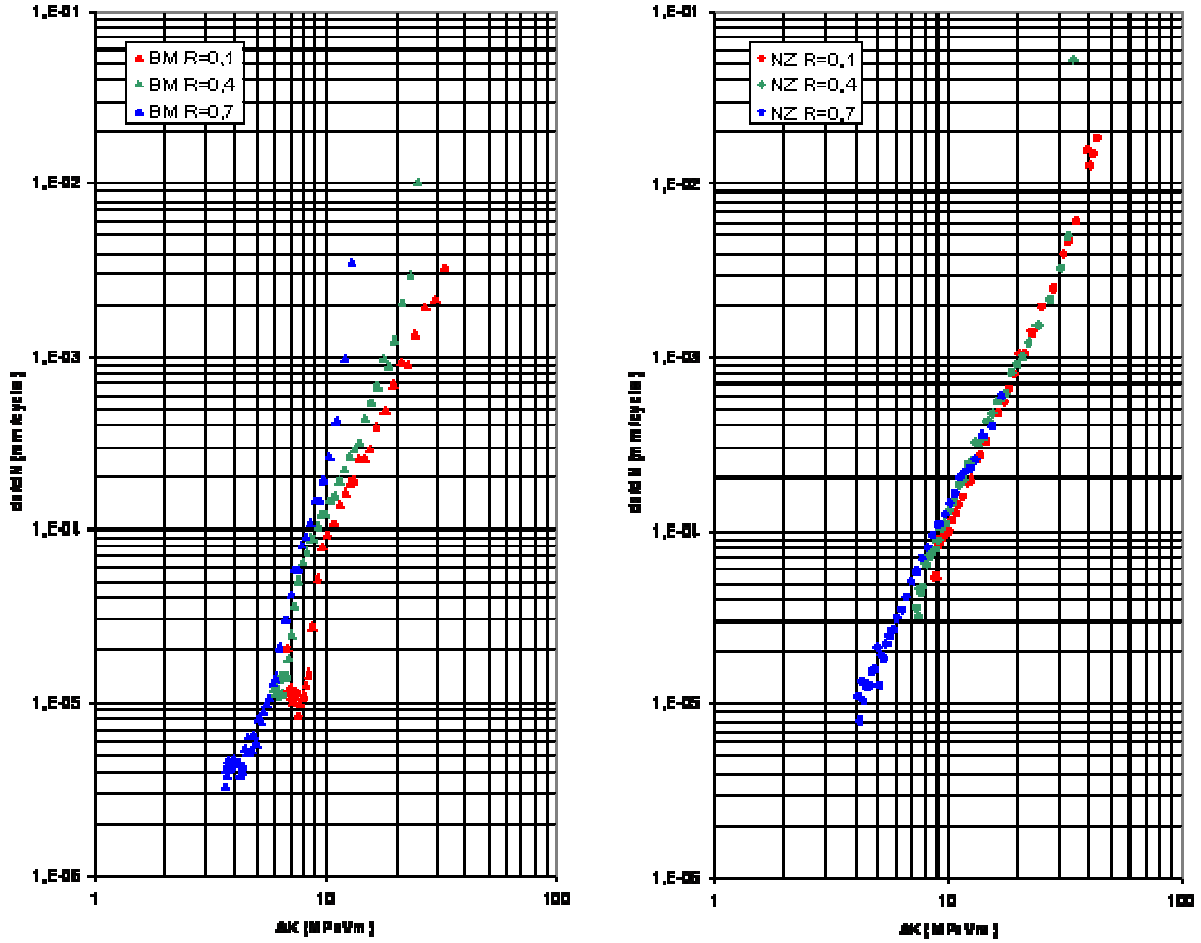

Figure 102: Fatigue crack growth curves in 2050 T8 base material and in the weld for various R ratios, T-L, CT specimens

Regarding the 23 mm thick 7449 bobbin tool welds, no defects were found in the various examined cross sections (Figure 103). Microhardness measurements were carried out on as welded coupons and after the T79 post-welding ageing (Figure 104). In the nugget zone of as welded specimens, the hardness is around 125HV 30h after the welding operation and around 135HV 400h after. The maximal temperature reached during the welding operation is probably high enough to solutionize the alloying elements and the cooling quick enough to prevent the formation of coarse precipitates. The heat condition is thus close to a W temper, and a natural ageing is noticed between 30h and 400h. After the artificial T79 ageing, the hardness in the nugget zone is close to that of the base metal (170HV vs. 180-200HV in the BM). In both HAZ, the hardness is quite low, roughly half that of the BM (90HV) with no significant effect of natural or artificial ageing. One can expect the formation of coarse precipitates that trap the alloying elements, during the welding operation. Such precipitates can be indirectly observed in Figure 103 through the grain boundary decoration. It is worthy of note that in the base material, the hardness at mid thickness is systematically lower than that near the surface.

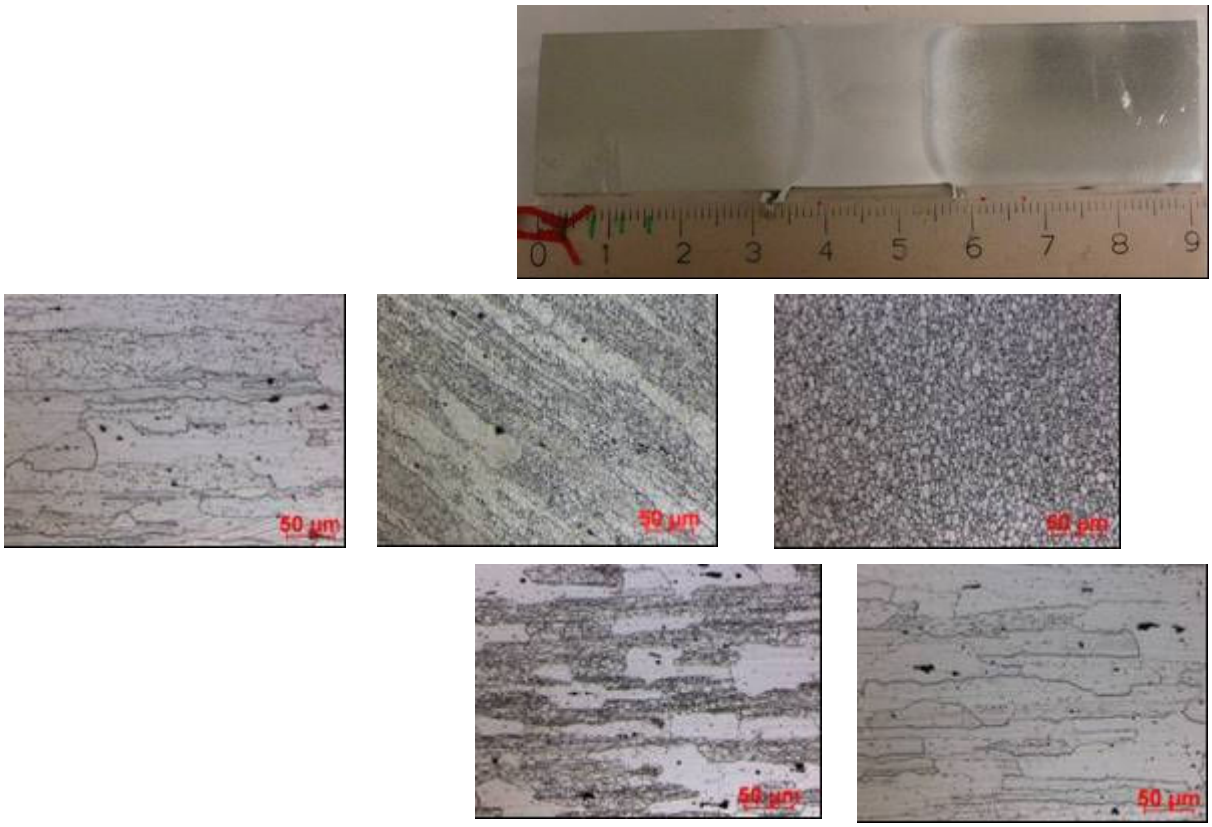

Figure 103: Typical cross section for 7449 bobbin tool FSW 23mm thick plate

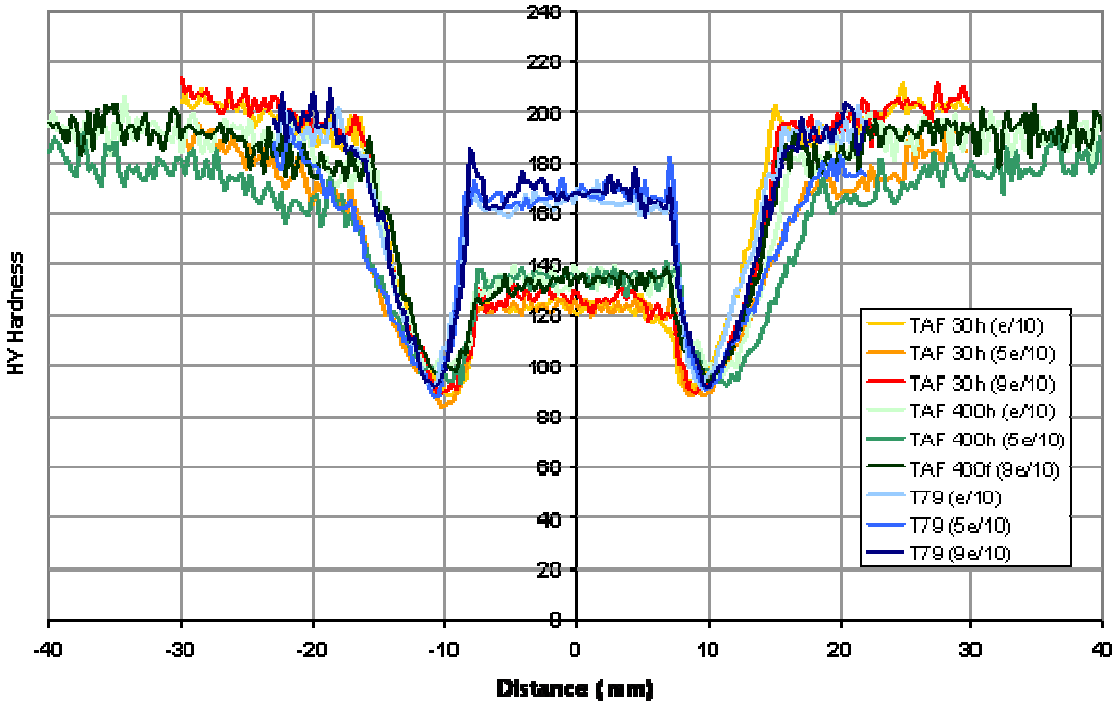

Figure 104: HV0.2 hardness profiles near the top (e/10), at mid thickness (5e/10) and near the bottom (9e/10) for as-welded TAF (30h and 400h after the welding operation) and post-welding T79 treated coupons.

Tensile specimens were machined out in the 7449 base metal and in the weld zone after the T79 ageing (test specimen in the nugget for L direction and across the weld for LT direction). The tensile properties are displayed in Table 18. For the L specimens, a mean reduction in YS and UTS of 13% is consistent with the 11% decrease in hardness between the nugget and the base material. For the LT specimens across the weld, a necking is observed in both HAZ and the fracture initiates in one of them. Compared to the base material, a reduction of 49% in YS and 38% in UTS is observed, consistent with the hardness reduction of 50% between the HAZ and the base material.

It is to be noticed a 62% joint efficiency for thick 7XXX FSW is a good result compared to the prior state of the art (usual joint efficiency about 50%).

	E (GPa)	Yield strength (MPa)	Ultimate Stress (MPa)	Elongation (%)
BM L	71	564 (ref.)	593 (ref.)	11.3
NZ L	72	484 (-14%)	524 (-12%)	7.2
BM LT	73	581 (ref.)	614 (ref.)	9.5

NZ LT	74	299 (-49%)	383 (-38%)	4.0

Table 18: Tensile properties of 7449 T79 bobbin tool FSW 23mm thick plate (average on 3 test specimens)

Fatigue tests on smooth (K_t=1.0) test specimens machined out across the 7449 weld in the LT direction have been carried at R=0.1. The S-N curve (Figure 105) displays a very high fatigue stress level, with a maximum stress of 250 MPa at 10^5 cycles which represent 84% of the tensile yield stress. Most of the ruptures take place outside the gauge part of the test specimens, which underlines the fact that the weld zone is relatively resistant to fatigue.

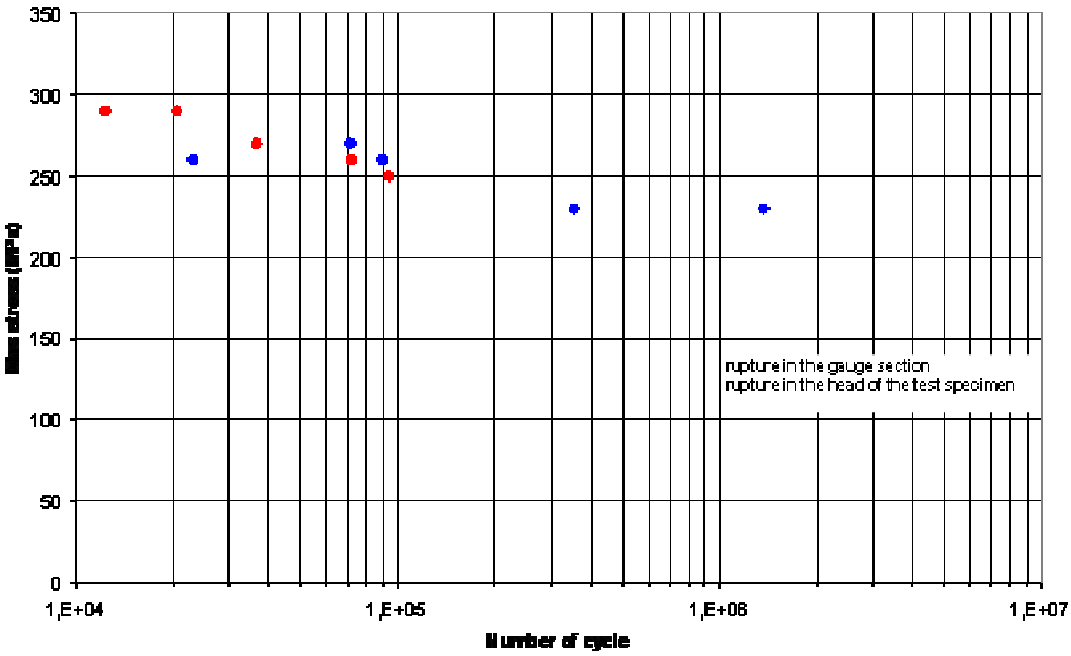

Figure 105: S-N curve of 7449 T79 bobbin tool FSW 23 mm thick plate

3.4 Task 3.2 Testing of New Similar Alloys (EADS Germany)

Testing of thick 2050 alloy welded with DeltaN tool.

Base materials of EADS G interest where the same: 2050 T3 and 7449 T4 from Alcan. The plates have been milled down to a 15 mm thickness for welding.

Most of the welds were performed with the DeltaN tool and further with a state-of-the-art standard tool also. Therefore some of the results are related to both tool concepts.

The standard tool had a shoulder diameter of 24 mm and a pin diameter of 10 mm with threads and 4 flats. The DeltaN tool shoulder diameter is not relevant and the pin was identical to the standard tool.

The FSW parameters where like follows:

- 2050 by Standard Tool: Fz of 29 KN, Revs 500 1/min and feed of 160 mm/min

- 2050 by DeltaN Tool: Fz of 15-25 KN, Revs 450 1/min and feed of 160 mm/min
- 7449 by Standard Tool: Fz of 32 KN, Revs 300 1/min and feed of 80 mm/min
- 7449 by DeltaN Tool: Fz of 28 KN, Revs 450 1/min and feed of 80 mm/min

2050 and 7449 alloys were welded respectively in T3 and T4 tempers and then aged to T8 and T7. As an additional scenario, a 3% stretch was applied on 2050ST (Standard Tool) tensile test specimens after welding and before ageing to T8 (see Table 19).

At EADS G, the welds were characterised as followed:

- Micro sections and micro hardness measurements,
- Tensile testing,
- Fatigue testing

The initial 15 mm thickness of tensile and fatigue specimens was machined by 2 mm on top and bottom sides.

On 7449 and 2050 alloys, welds have been performed by using standard and DeltaN tool. One advantage of the DeltaN tool concept is the smaller width and higher degree of vertical symmetry of the weld, as shown in Figure 106 and Figure 107. This leads to reduced shrinking and therefore to less distortion after welding.

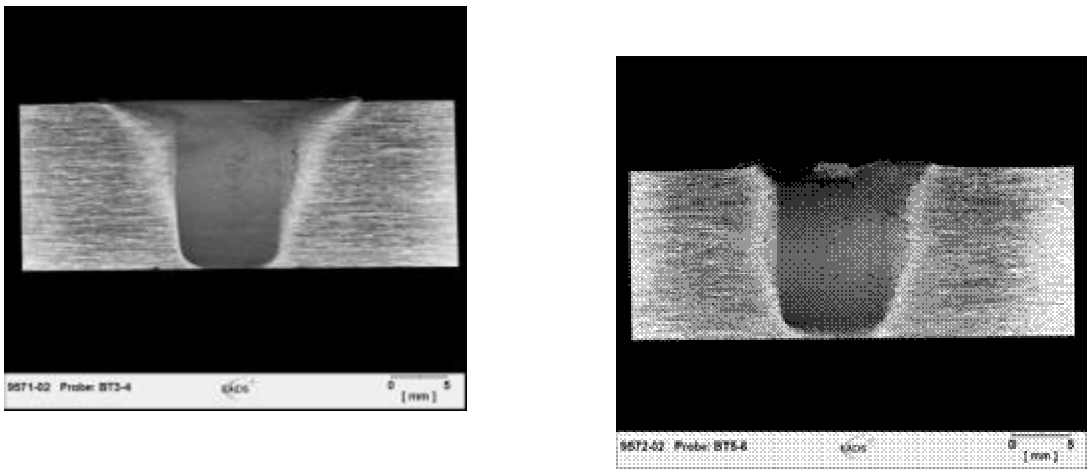

Figure 106: FSWelded 7449T4-FSW-T7 by standard (left) and DeltaN (right) tool

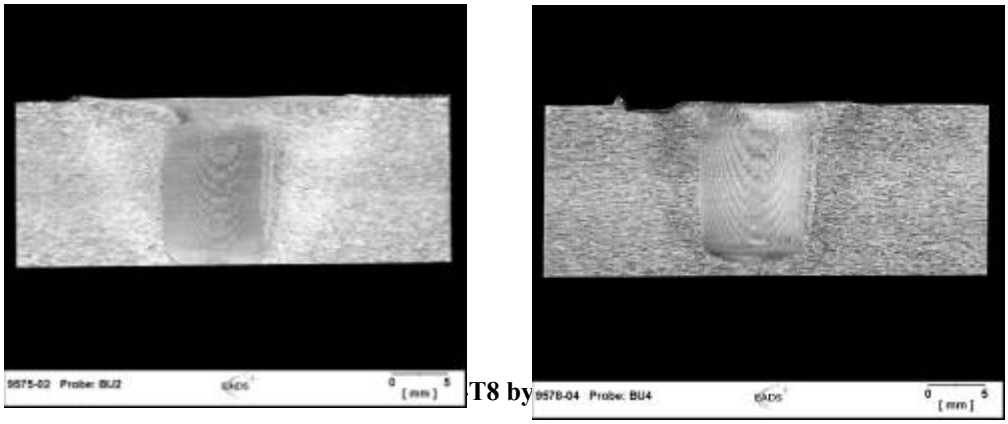

T8 by

On the above mentioned sections also Vickers hardness curves have been generated.

The hardness curve of 7449T4-FSW-T7 showed attractively high values in the Dynamically Recrystallized Zone (DRZ). This is the consequence of the post-weld treatment. Unfortunately the TMAZ and HAZ do not react on the extra heat input because the friction stir welding thermal cycle did not function as a solution heat treatment but as overageing (Figure 108).

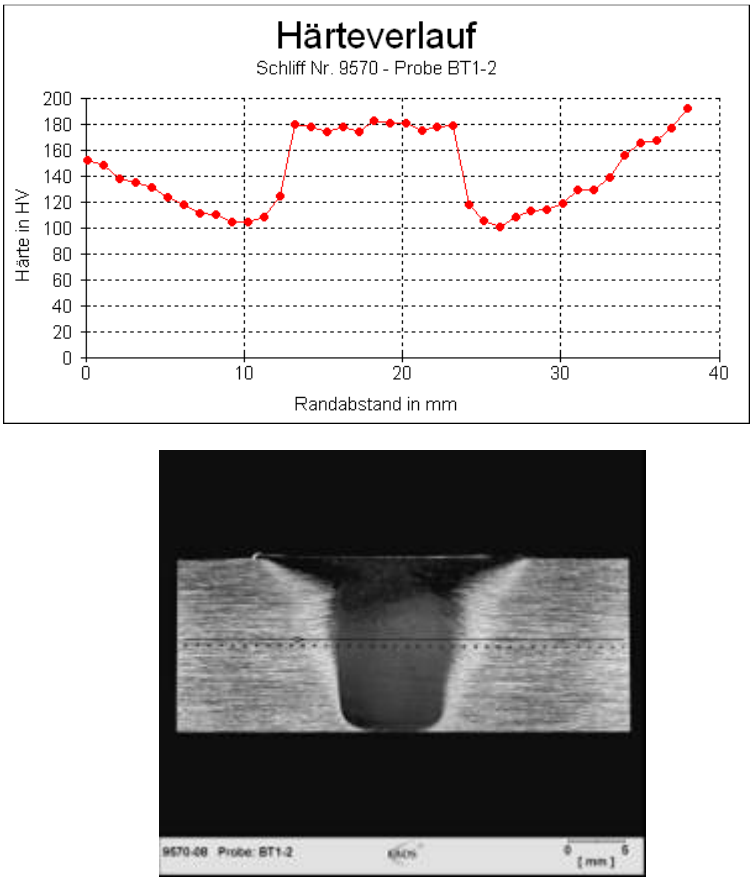

Figure 108: Vickers hardness profile on standard tool FSWelded 7449T4 post weld heat treated T7

Hardness measurements on the DeltaN tool weld on the same alloy showed similar results, see Figure 109.

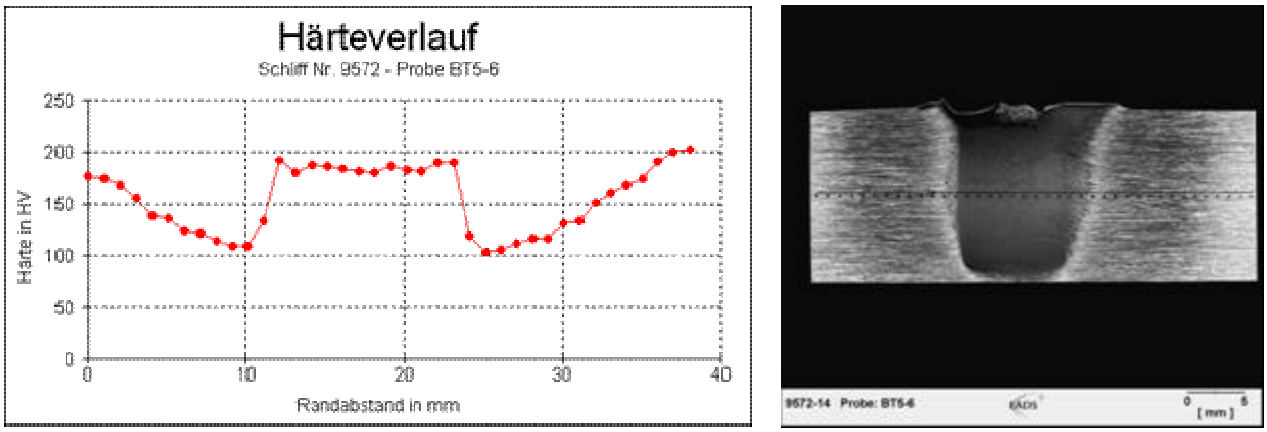

Figure 109: Vickers hardness profile on DeltaN tool FSWelded 7449T4 post weld heat treated T7

The 2050 welds have been hardness tested in two configurations.

A first measurement has been performed in T3 as welded temper condition, see Figure 110. The relatively low base material hardness was not influenced by the welding process.

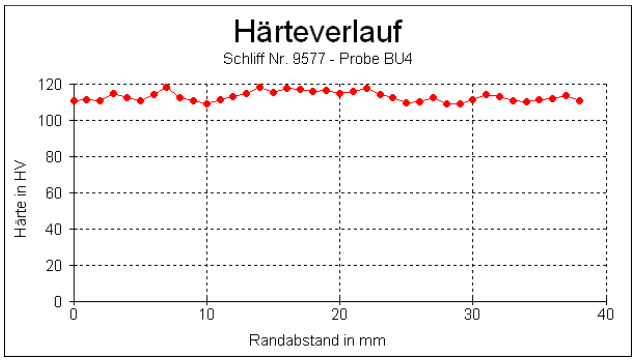

Figure 110: Vickers hardness profile on 2050T3 alloy in as welded condition

After a post welding heat treatment to T8, the hardness in the base material increased significantly whereas it decreased in the DRZ and TMAZ, as shown in Figure 111.

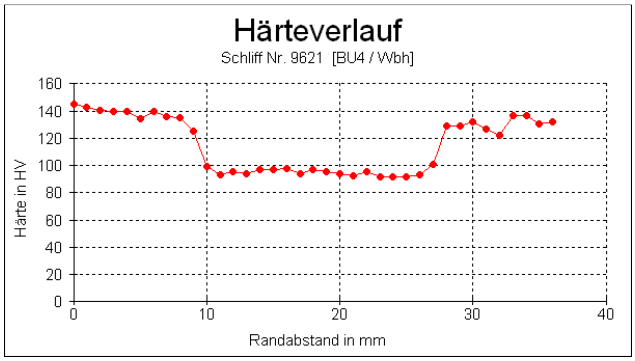

Figure 111: Vickers hardness profile on alloy 2050T3 FSWelded and post weld heat treated to T8

After performing an additional mechanical stretch of a few percent on the weld zone the strength in the DRZ and TMAZ can be increased significantly.

Static strength testing was performed on standard and DeltaN tool welds out of 2050 and 7449 alloys.

For each welding case described below two specimens were tested and therefore two values are mentioned.

Table 19 shows the tensile testing results. The ST cases are the standard tool welds, the DN cases the DeltaN welds.

Welding case	Yield Strength/ MPa	Tensile Strength/ MPa	Elongation/ %
2050ST	289-290	419-419	9.7-10.6

2050ST(3%PWStretch)	466-466	497-498	6.5-6.5
2050DN	292-294	420-421	6.8-7.4
7449ST	285-290	386-387	2.8-2.9
7449DN	309-312	408-409	2.4-2.4

Table 19: Tensile test results of Standard and DeltaN FSWelded 2050 and 7449 alloys

The conclusions of these tensile test results are the following:

- The measured values show nearly no scatter. This is an indicator for the robustness of the FSW process and its impact on the base material.
- The location of failure is generally in the thermo-mechanically affected zone (TMAZ)
- The DeltaN tool welds show no benefit for that tool concept. The results are equal to the standard tool weld test results.
- The weld efficiency as relation of the tensile strength welded joint to tensile strength of the base material is 80% for 2050 and 70% for 7449.
- The 3% post weld stretch on 2050FSW before ageing to T8 is of high relevance for the improvement of the tensile strength properties: the weld efficiency is lifted to 100%. From tensile strength and elongation point of view for welded application the 7449 alloy can be substituted by 2050 alloy.

The fatigue behaviour of a DeltaN tool similar 2050T3 FSWeld + post-weld-heat-treatment to T8 was determined and documented in a Woehler curve, shown in Figure 112.

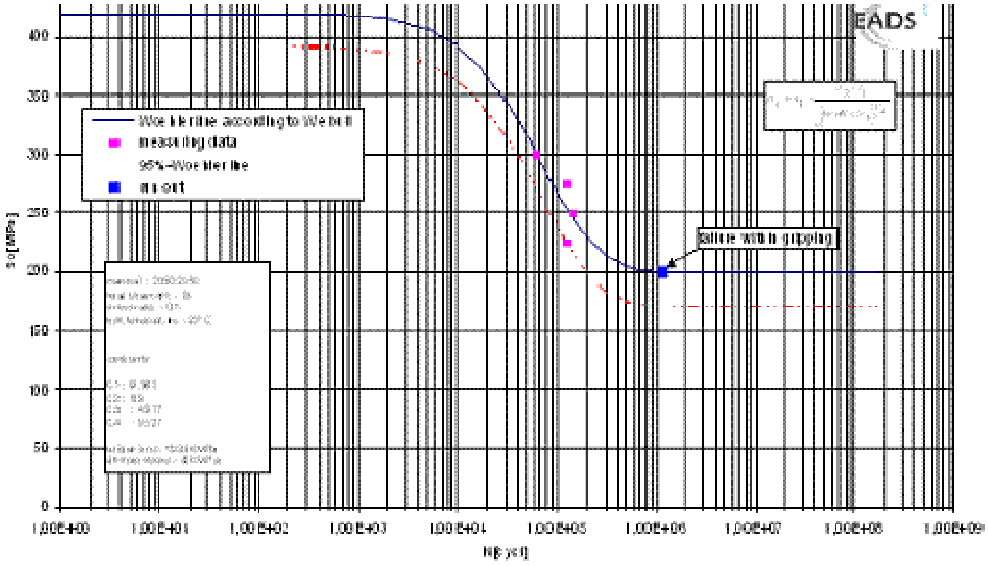

Figure 112: Fatigue test results and Woehler curve of DeltaN FSWelded 2050-T3-PWHT-T8

The result is typical for a 2050 FSWeld and does not show a benefit by using the DeltaN tool concept. A fatigue stress level of 200 MPa and a maximum stress of 275 MPa at 100000 cycles were determined.

The failure location is the TMAZ of the weld. Only the long run specimen for the 200 MPa stress level failed in the grips of the testing machine.

Considering the results scattering, Bobbin and DeltaN tools welds out of 2050 plate were found to show similar fatigue properties, as displayed in Figure 113.

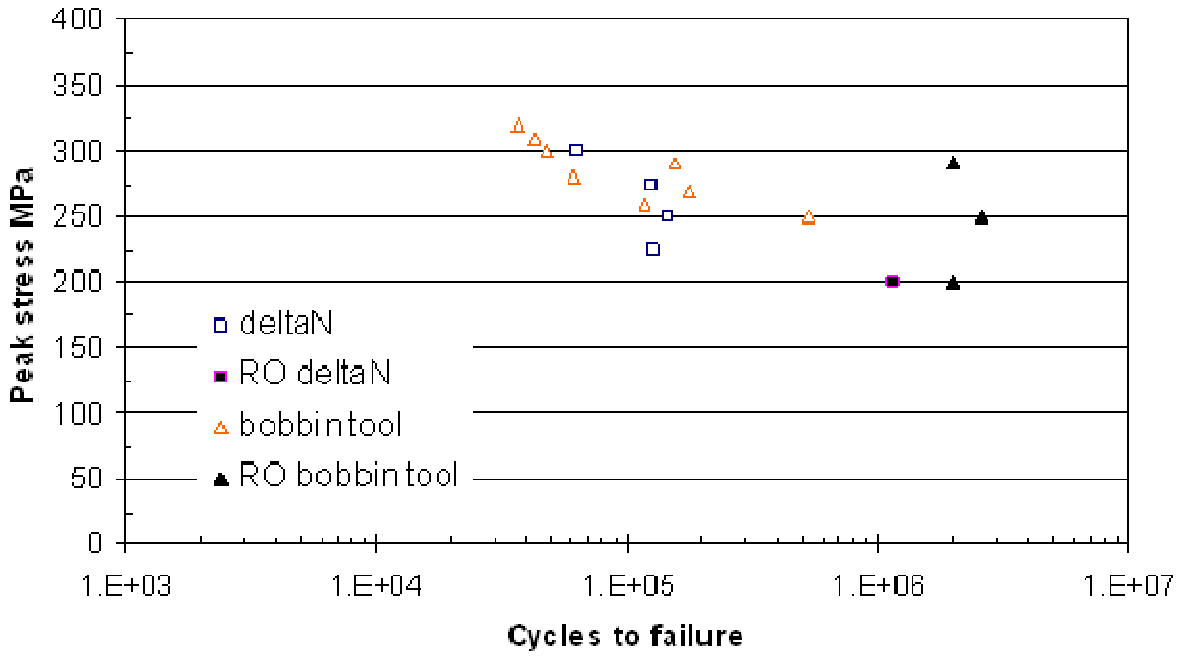

Figure 113: S-N data for Bobbin & DeltaN welding tools – 15mm thick 2050 alloy (Source: Cranfield Uni.)

3.5 Task 3.3 Development of FSW for New Dissimilar Alloys (Airbus Germany)

FSW of Al/Ti

The dissimilar combination of Aluminium alloy 6013 T4 and Titanium alloy Ti Ti6AL4V was successfully welded in a butt weld configuration using a cylindrical tool. The tool

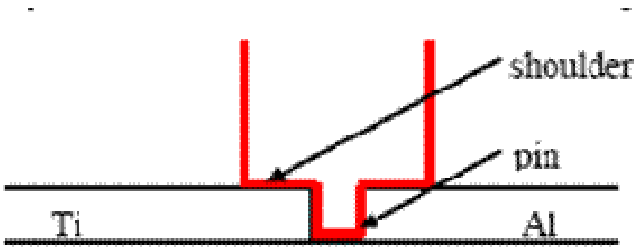

Figure 114: Cylindrical pin tool for the dissimilar Ti/A1 FSW

The titanium surface preparation before welding was investigated. To achieve a good material connection between Ti6A14V and 6013, the oxide layer of the titanium faying surface must be

removed. Moreover a rough surface is expected to improve the adhesion due to the increased surface area.

All aluminium sheets were pickled before welding.

The first approach was to use Steel Shot blasting resulting in a surface roughness : Ra ~ 5 µm. Figure 115 shows two microsections comparing the surface after milling and after milling and steel shot blasting.

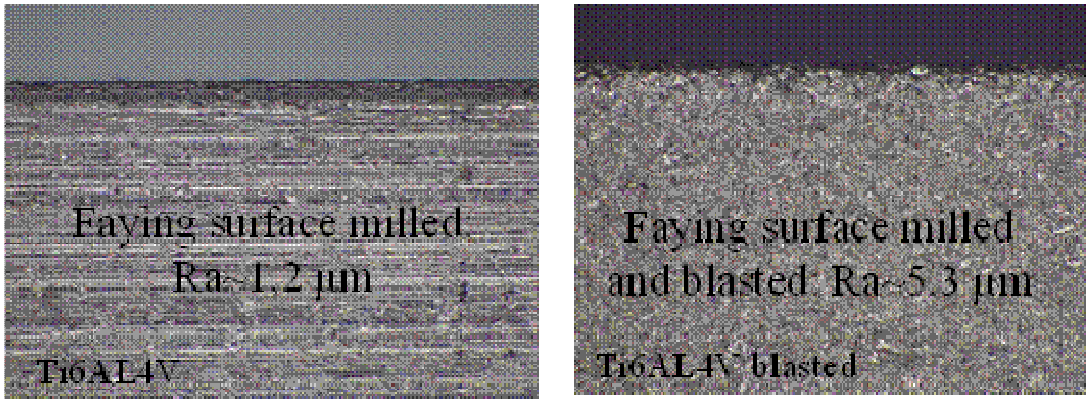

Figure 115: Surface preparation of Ti before welding: left milling; right milling and steel shot blasting

To remove oxide from the surfaces to be welded a pickling process is generally used. Figure 116 shows the resulting surface roughness after pickling of the simple milled surface and of the surface which has been steel shot blasted after milling.

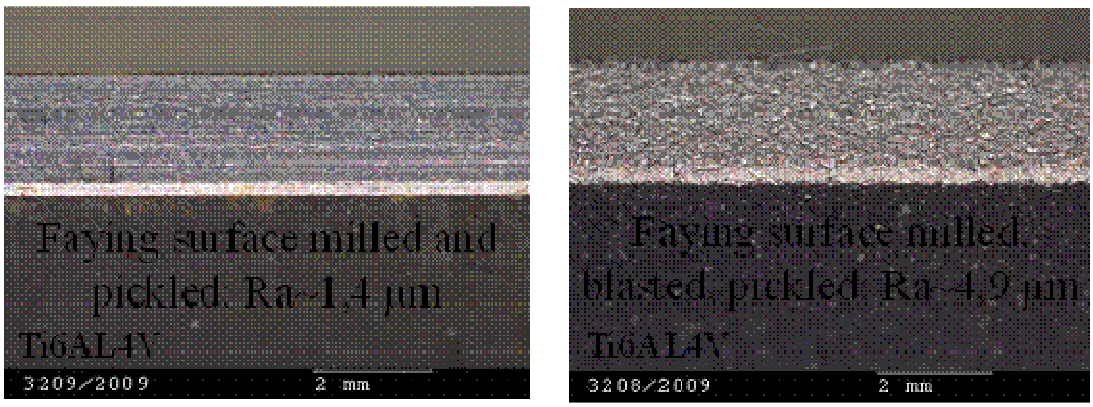

Figure 116: Surface preparation of Ti before welding: left milling and pickling; right milling, steel shot blasting and pickling

The aluminium and titanium parts were milled to the same thickness and welded using the following parameters:

	Weld travel speed [mm/min]	Tool rotation speed [rpm]	Tilt angle [°]	Down force [kN]	Spindle torque [Nm]
WPS 1	200	600	0	6	7

Table 20: Welding parameters for the 6013T4/Ti6A14V

Due to the need of having the pin tool parallel to the titanium high care was used to achieve a repeatable position of the joint line with an accuracy of 0.1mm. Figure 117 shows pictures taken during the welding process and Figure 118 shows the final welded plates.

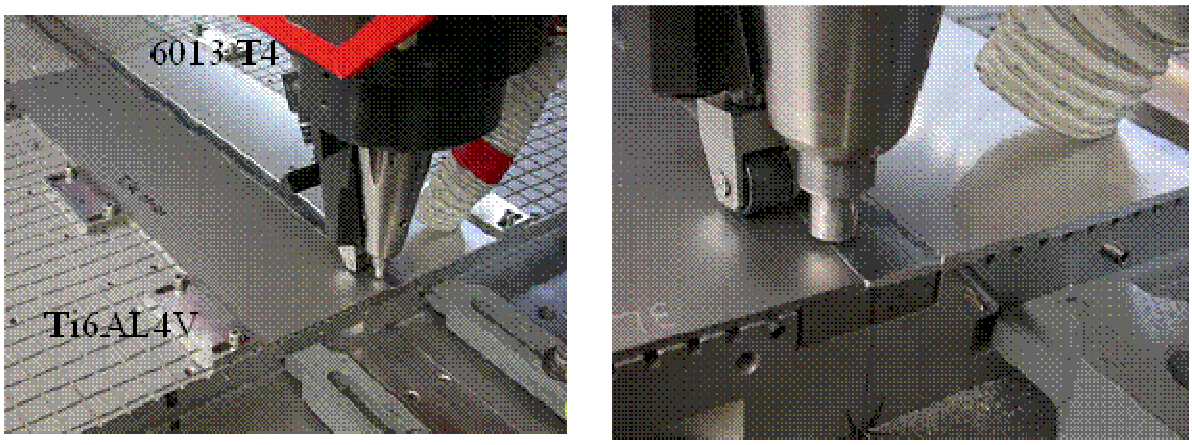

Figure 117: FSW of 6013 and Ti6Al4V

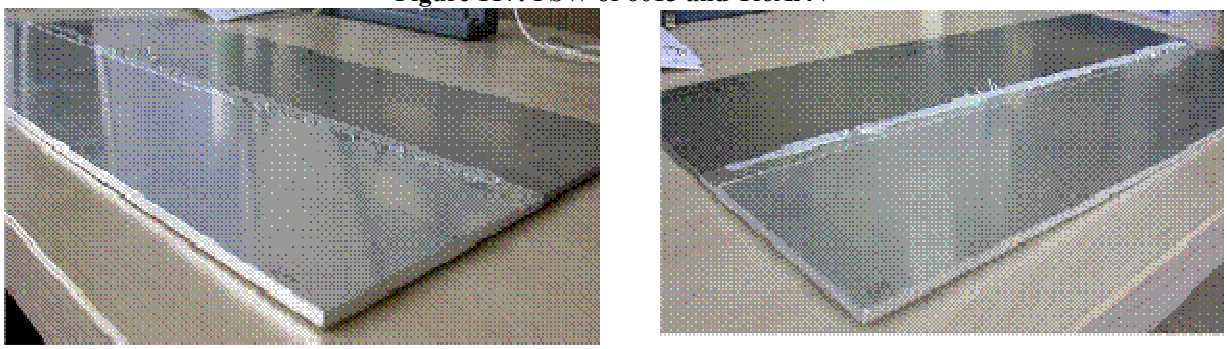

Figure 118: Final results of the dissimilar welds

The investigation has confirmed that dissimilar FSW of 6013 and Ti6Al4V is possible, however optimized weld parameters are needed.

Microsections from the first trials shown in Figure 119, shows presence of defects and Ti particles created by the contact of the tool pin with the titanium faying surface.

No assessment of the mechanical performance, e.g. tensile strength test, was performed. The corrosion behaviour is also a topic for future investigations.

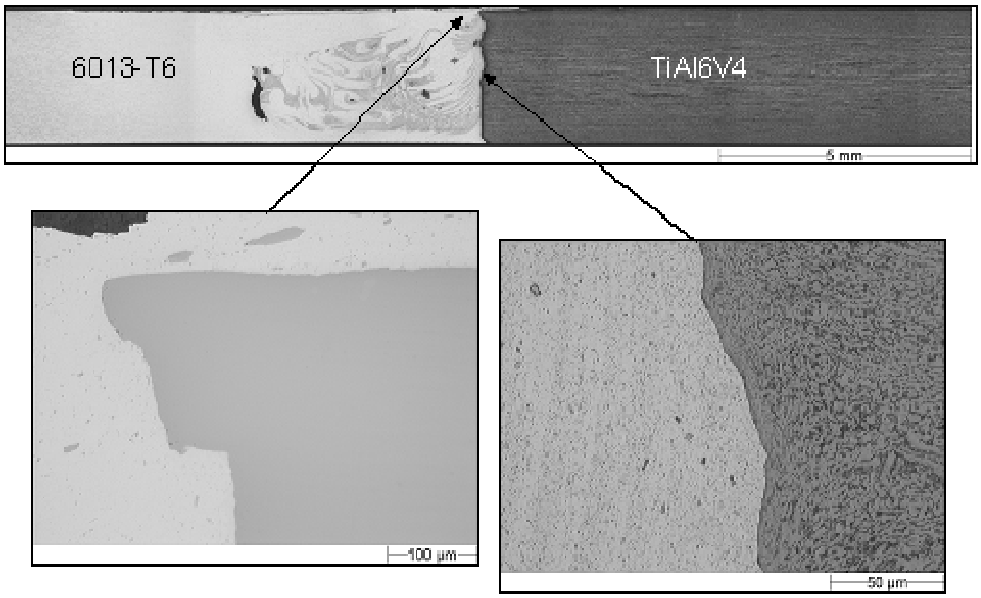

Figure 119: Micro-section of FS welded 6013 and TiAl6V4

3.6 Task 3.3 Development of FSW for New Dissimilar Alloys (EADS Germany)

Development of welding parameters for joints of 2050 with 7449 in thickness up to 20 mm by DeltaN tool concept.

It was not possible to perform dissimilar welds with a high weld quality by using the DeltaN tool concept. Only by using extremely low welding speed of 40 mm/min a stationary welding process appeared.

3.7 Task 3.4 Testing of new dissimilar alloys (EADS Germany)

Welded joints of 2050 with 7449 alloys by DeltaN tool concept will be tested, micro-structure and micro-hardness investigated and static, fatigue and tear strength tested.

The extremely low welding speed shall cause a high degradation of the mechanical properties of both alloys of this dissimilar joint configuration. Therefore a characterisation has not been performed. The use of the DeltaN welding tool will not lead to benefits for this specific welding application.

3.8 Task 3.5 New Geometries (BAE)

Joint geometry concepts were developed for FSW to replace GMAW counterparts in land vehicle fabrication; these were reviewed earlier in Workpackage 2. Selected solutions were scaled down to enable local manufacture and evaluation, and used a combination of plate material and extrusion in high-strength 7000 series aluminium alloys.

3.8.1 Weld Joint Geometries

The weld joint geometries selected for experimental evaluation would be used on the BAE Systems technology demonstrator, which represents a partial cross-section of a vehicle hull and incorporates

five new corner joint geometries, use of dissimilar alloys and extruded material. The demonstrator component is shown in Figure 81 (Workpackage 2), with the five corner joint geometries (identified as A through E) detailed in Figure 120.

All welds were produced using a Huron NU5 milling machine that had previously been adapted for FSW. The FSW tools used were of scrolled shoulder design with a tapered, tri-flat pin and were selected depending on the weld depth requirements for the particular joint geometry. The particular welding parameters, tool rotation speed and linear welding speed were selected based on the tool and the material to be joined. In all cases the welding procedure was the same. The rotating tool was slowly plunged into the adjoining plates until the shoulder made contact with the material surface, where it was briefly allowed to dwell before traversing along the joint line to complete the weld.

3.8.1.1 Joint A

The main feature of Joint A was the AA7449 extruded corner section. This was joined to 'thin' section plates of AA7020 and AA7056 at either side using full penetration square edge butt welds. Although a relatively simple configuration, it included a dissimilar alloy weld between the AA7020 plate and the AA7449 extrusion. The AA7020 is a fusion weldable alloy, similar to that used on existing land platforms, and AA7449/AA7056 are (non-fusion weldable) higher strength alternatives. Whilst with correct planning it is anticipated most joints on a vehicle could be achieved using FSW, there may be some area where GMAW would still be required. One solution that still allows higher strength alloys to be selected for the primary build would be to join a strip of fusion weldable alloy to the high-strength material, as demonstrated in this joint.

The development of dissimilar alloy welding of this type has been reported in previous activity reports and is detailed in COINS deliverable reports D4.1 & D4.2. In summary, the joint adopts the tensile properties of the weaker alloy and, when welding, the higher strength alloy must be placed on the advancing side of the weld (i.e. the tool rotation is in the direction of welding) for the process to be successful. A cross-section of a dissimilar alloy weld is shown in Figure 121, and was free from visible defects.

3.8.1.2 Joint B

Like Joint A, Joint B also uses an AA7449 extruded corner section though in this configuration there are both 'thin' and 'thick' section joins. The latter was achieved using a rebated joint where welds from opposing sides are offset as shown in Figure 122.

Both welds were again free of visible defects; however a separation of approximately 0.5mm is notable along the internal interface of the joint. This was attributed to insufficient side clamping, as when the plates were turned over for the second weld, a slight mismatch was observed. This problem may in the future be overcome through addition of overhead clamping.

3.8.1.3 Joint C

For Joint C, a tailored blank configuration was used for joint 'thick' to 'thin' section material, and Figure 123 shows the three different approached that were investigated to achieve this type of joint. In the first, a simple squared-edged anvil was used as illustrated in Figure 123a. This produced a reasonable joint, but closer inspection showed the presence of a small crack (Figure 124) at the root of

the weld that could impact on fatigue performance, particularly since its location was at a natural stress concentration point.

With the second approach, the edge of the anvil was machined with a 2mm radius. The intention was to forge the material at the weld root to create a rounded internal corner that would reduce any concentration of stresses in that region. The result is show in Figure 125, and although some forging of material did occur, it failed to create a bond with the other side of the joint. The result again was a root flaw.

The final generation of tailored blank welding is shown in Figure 123c and used a disposable or 'sacrificial' bar of the same alloy as the weld material to produce a fully consolidated welded joint with an internal rounded profile. The rear anvil had a 6x6mm notch removed from its outer edge to accept a disposable insert of the same cross-sectional dimensions. A FSW tool was selected with a pin length of 7.8mm and thus over-penetrated the 6mm thickness plate into the disposable insert. To finish the joint, a bull nosed milling cutter was used to machine away the disposable bar leaving a radius profile on the inside of the joint. On inspection, the joint was found to be defect free, with the insert fully consolidated into the weld as shown in Figure 126. This demonstrated the ability to select any desired internal profile to add strength to a joint.

3.8.1.4 Joint D

Joint D is another example of a 'thick' to 'thin' section joint. In this example, a double sided weld in the 'thick' section has been used to create a full thickness weld without leaving the internal joint line as with a rebated joint. The corner section was produced from extruded section, and there is a standard single-pass, fully penetrating weld to the 'thin' section plate. The corner profile demonstrates an advantage of extrusion or pre-machined sections; in this example the large internal radius has the potential for blast deflection.

The double sided joint was made in 16mm thickness 7056. After completion of the first weld any minor flash or burrs were removed using a belt sander before inverting the joint and repeating the welding process to complete the joint. No problems were encountered when producing these welds, other than ensuring sufficient side clamping was applied. Figure 127 shows a cross-section of the joint, which was free from defects.

3.8.1.5 Joint E

The final joint is an interlocking configuration that could be adapted to join a variety of material thicknesses. In this example, shown in Figure 123, both sections of material would require pre-machining, though the interlocking nature of the joint would aid location and may improve the mechanical performance after welding.

The sequence for produced this joint is shown in Figure 128. The pre-machined material was held in the tooling using side clamping only. The first weld was fully penetrating and the second was added to further consolidate the material within the joint, improving the joint integrity and potentially the overall mechanical performance. Between the welds the part was rotated through 90° in the tooling and re-clamped. For this weld it was important to apply adequate side clamping all the way to edge of the corner due to the close proximity of the weld to the edge. Not only did this clamping nullify separation of the plates during welding but also any sideways forging of hot material during the weld.

Figure 129 shows a cross-section through an interlocking joint. The joint can be seen to be free of defects.

3.8.2 Conclusions and Recommendations

- The conceptual joint design study identified numerous alternative joint configurations, utilising friction stir welding, that have the potential to be applied to the manufacture of land vehicles.
- Scaled down examples of novel corner joint design have been successfully produced on specifically designed tooling blocks, demonstrating alternatives to more common fusion welded joints.
- It is essential that during the production of the welds and corner joints the individual weld pieces are clamped very securely into the tooling blocks either by side clamping, overhead clamping or a combination of both methods to negate separation of the joint during the welding process.
- Friction stir tacking was successfully demonstrated during the manufacture of joints. Further studies into the suitability of the tacking process and the adaptation of small diameter shoulder/short pin tools to tack longer lengths of welds prior to final welding is recommended.

The logical continuation of the work would be to produce the new joint configurations to actual size and demonstrate examples on a suitable scale. Impact or blast testing of the new joints would prove any benefit in joint strength and integrity compared to similar fusions welded joints.

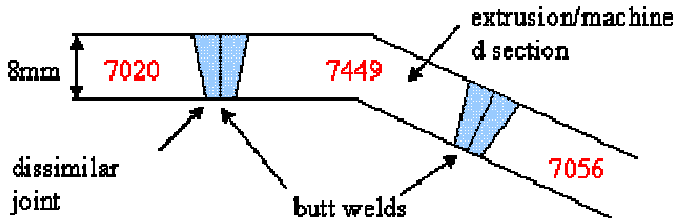

Joint 'A' – Dissimilar Weld

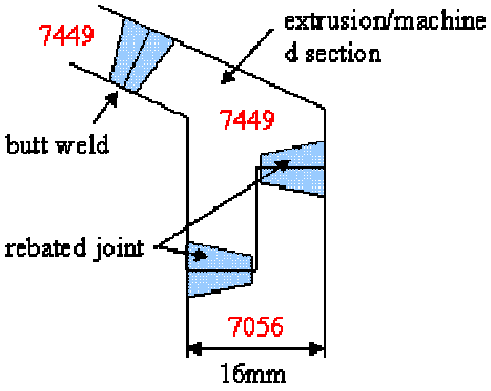

Joint 'B' – Rebated Joint

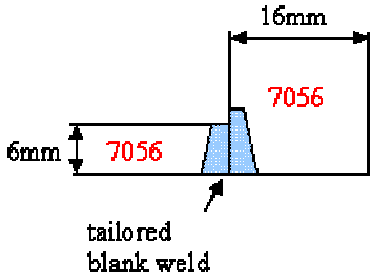

Joint 'C' – Tailored Blank Weld

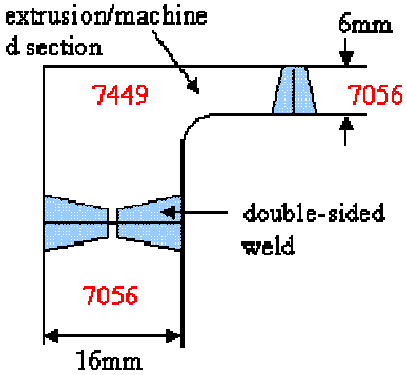

Joint 'D' – Double-Sided Weld

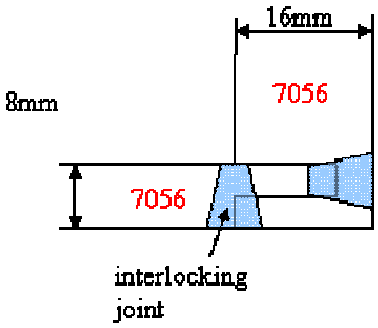

Joint 'E' – Interlocking Joint

Figure 120: Selected corner joint geometries

Figure 121: Photograph of typical dissimilar 7020/7056 weld

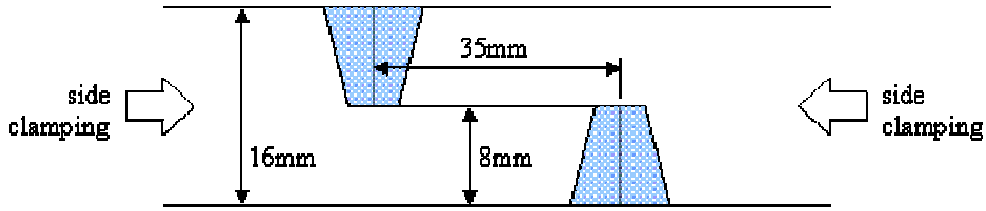

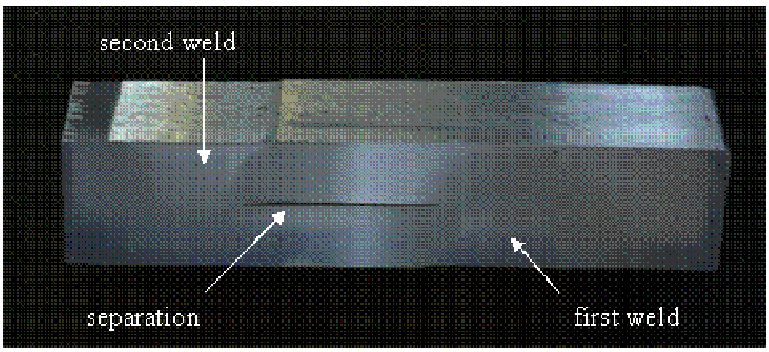

Figure 122: Rebated joint schematic and polished cross-section

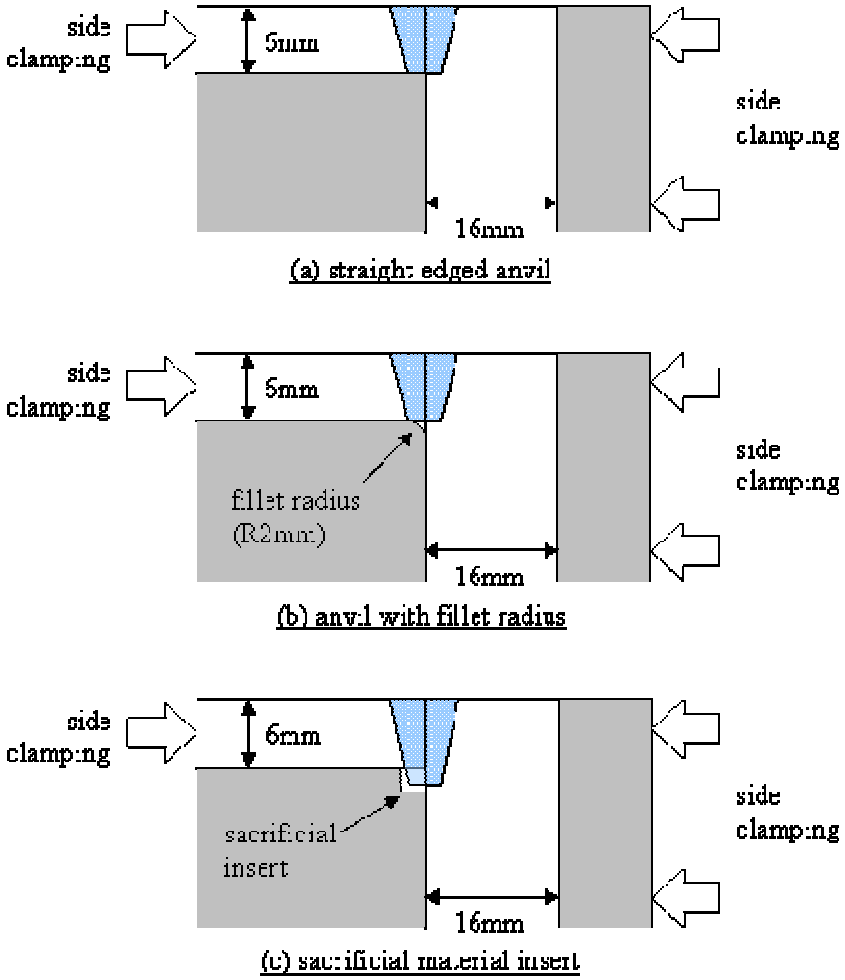

Figure 123: Approaches investigated for tailored blank joint configuration

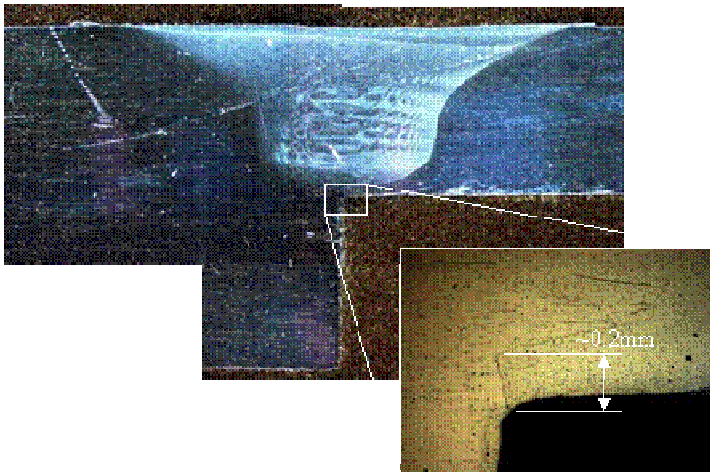

Figure 124: Cross-section of tailored-blank weld produced using square-edged anvil

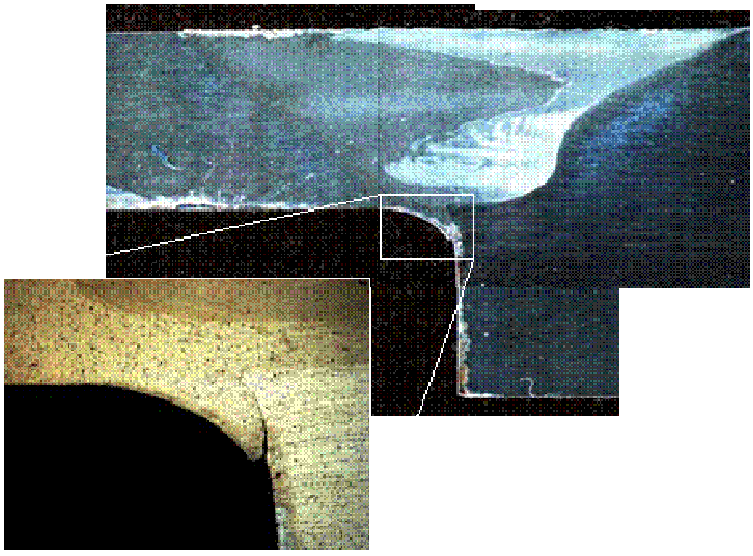

Figure 125: Cross-section of tailored-blank weld produced using anvil with fillet radius

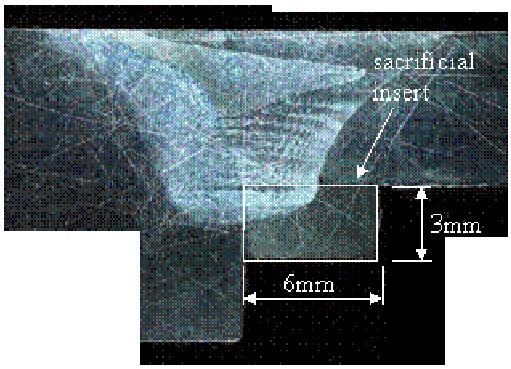

(a) cross-section of weld prior to machining of insert material

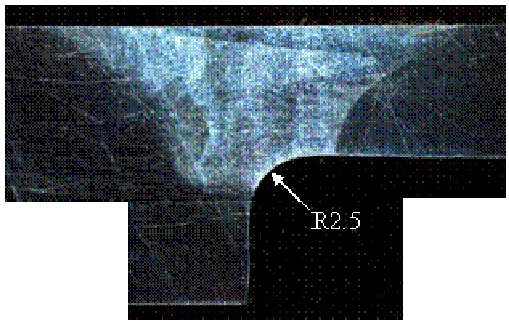

(b) cross-section of weld after machining of insert material

Figure 126: Cross-sections of tailored-blank weld produced using sacrificial insert material

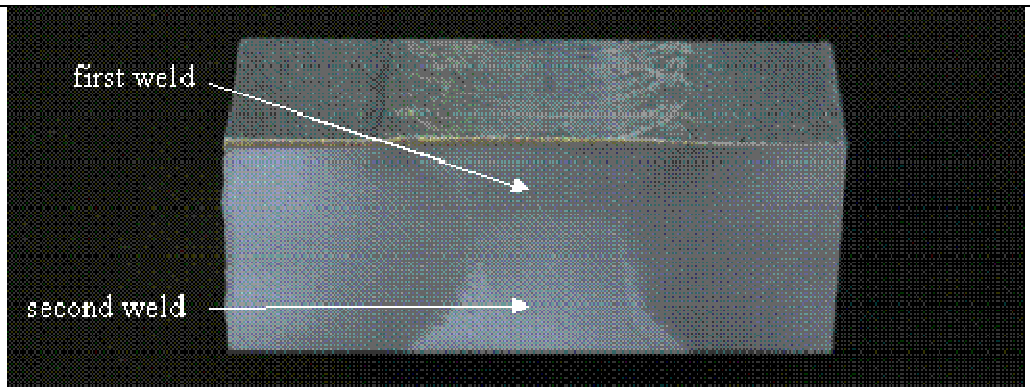

Figure 127: Cross-section of double-sided weld

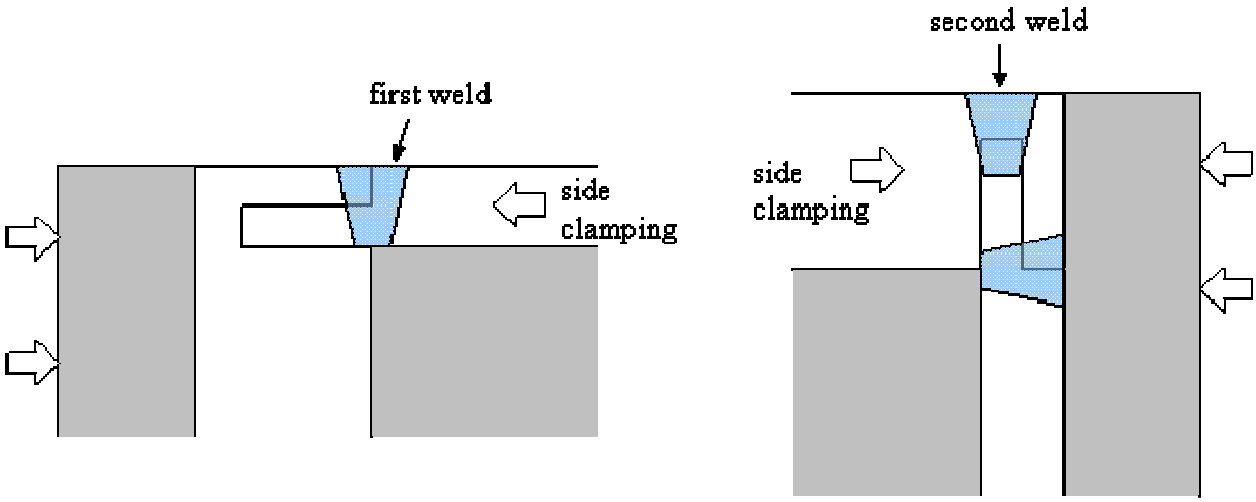

Figure 128: Interlocking joint welding sequence

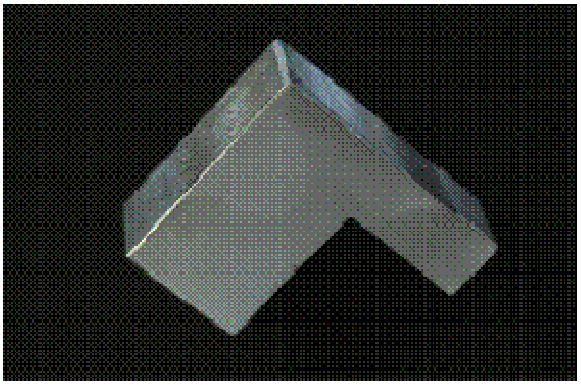

Figure 129: Section through interlocking joint

3.9 Task 3.5 New Geometries (Airbus Germany)

Investigation of mechanical performances of overlap welding

For a better understanding of the stress field around the overlap joint a finite element model with a single lap joint was made. The model was composed by parabolic shell elements with 8 nodes and with 6 degrees of freedom per node. The total elements of the models are about 2000 for a total of 7010 nodes. The geometry of the specimen is 2 mm thick, 50 mm of overlap, 12.5 mm width and welded in 12 mm of the all overlap joined length. The geometry of the FE model is representative of the specimen geometry welded at EADS-IW and tested at LTSM (Patras University).

Figure 130 presents the geometry of the model and the mesh applied in this study.

a) Specimen geometry

b) Finite element mesh

Figure 130: Finite element model of a generic welded overlap joint

Figure 131 shows the stress field results when a remote load equivalent to 50 MPa is applied in *x* direction. The stress fields are presented under the deformed shape of the specimen with a magnification of 15 times. These results display the stress field for the 3 directions (11, 22, 12 corresponding to the directions *xx*, *yy* and *xy* respectively) as well as the stress field using the von Mises criteria. The Cartesian coordinate system presented in Figure 130.

A detailed view of the different stress fields, in the joined area are given in Figure 131. From these figures it is noticed that the higher stresses are in *xx* direction, as expected. If the hooking tip defect is oriented at 90°, the joint strength will decrease considerably and fatigue loading will induce a rapid crack propagation of the hooking tip. The ideal condition for the interface shape is to be aligned with the load (with lowest vertical movement of the material during the weld).

The shear stress is not predominant, although its intensity peak at the interface tips of the joint can be enough to promote a rupture by shear when the materials in the joint area are not completely mixed.

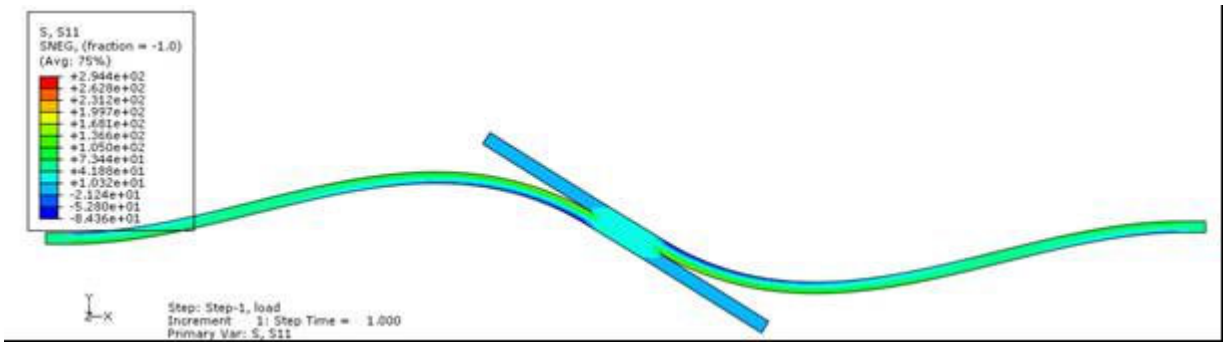

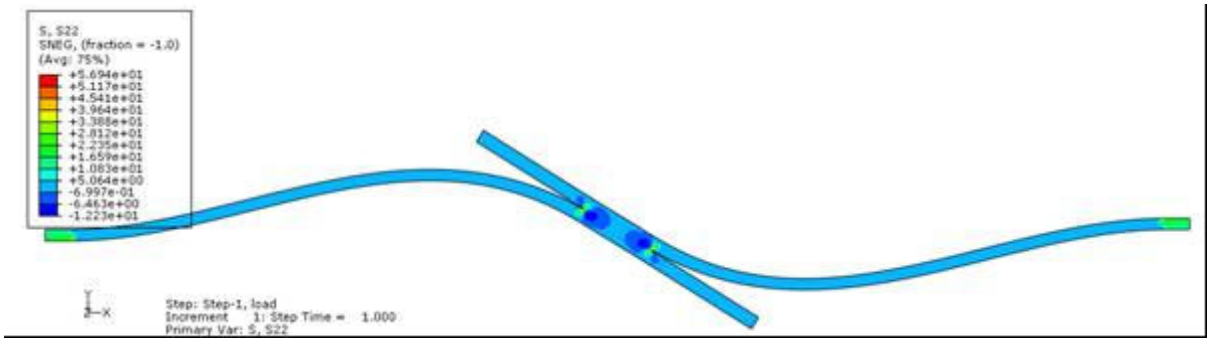

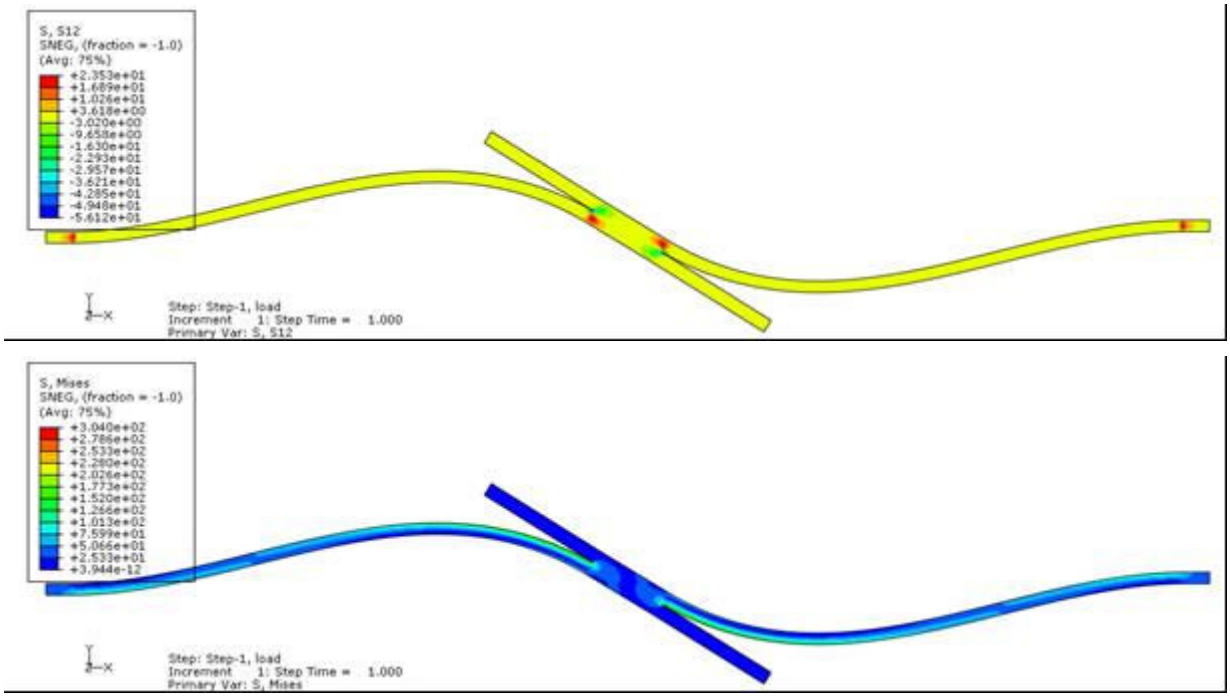

Figure 131: Finite element overall results of the overlap joint for the different directions, deformation magnified 15X

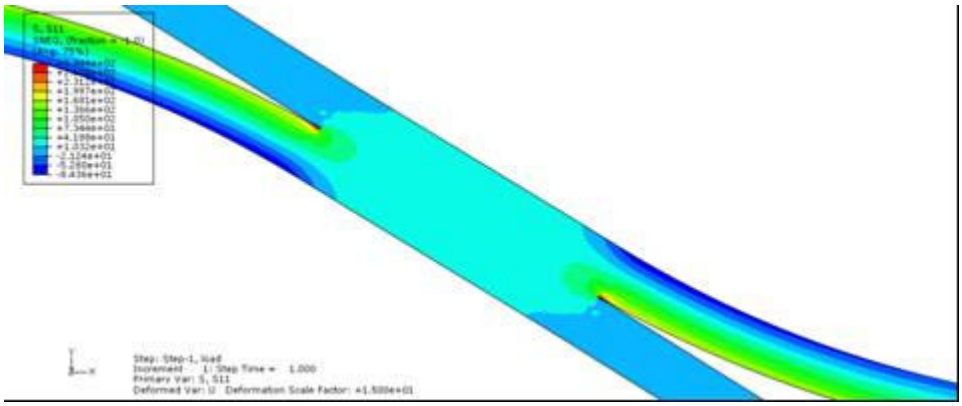

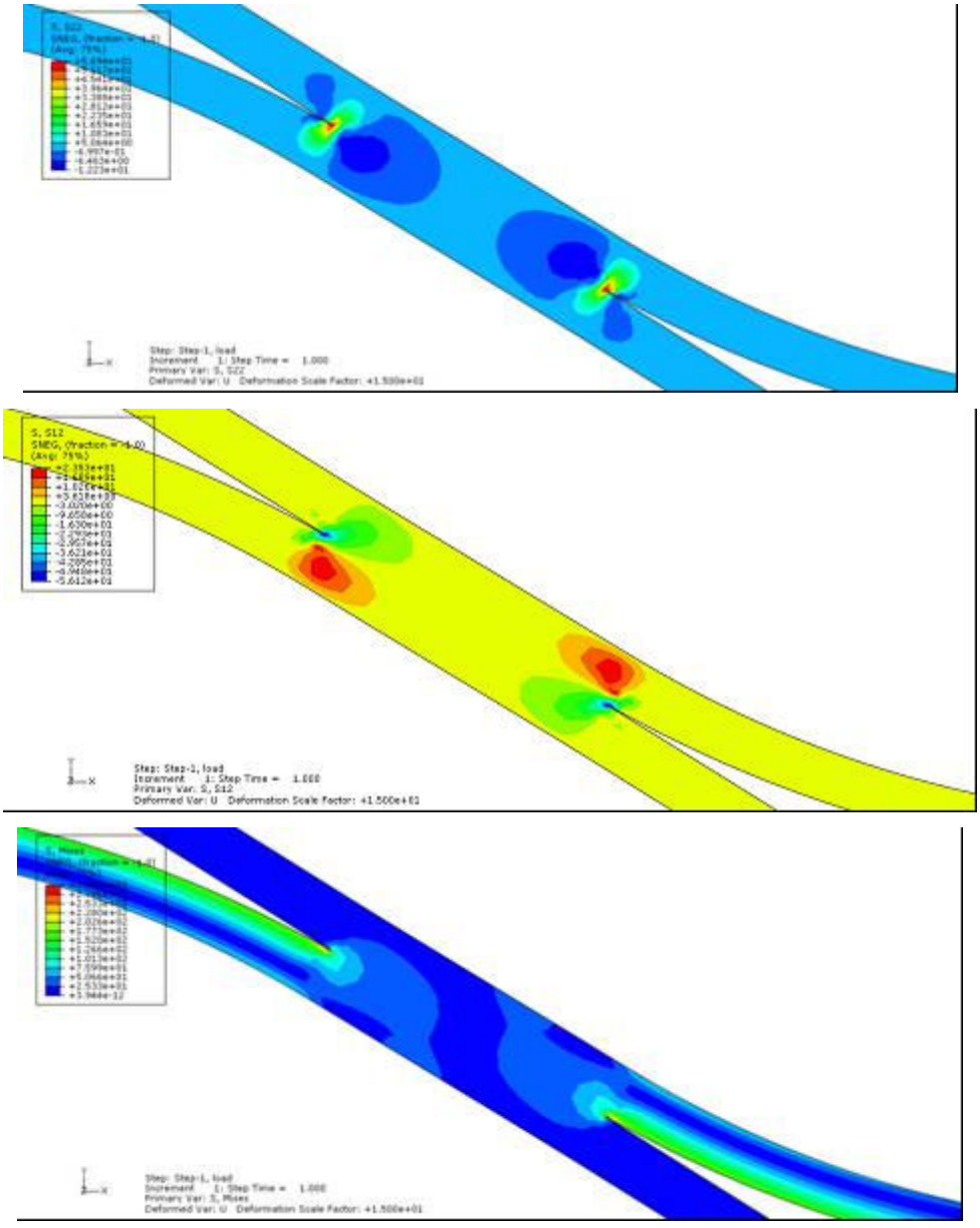

Figure 132: Detailed stress distributions around the joined area (S11, S22, S12 and S von Mises respectively)

The stress along the overlap joining line are plotted in Figure 133. As described above, the S11 stresses are predominant in the joining area and the limits of the joined line are the areas with stress concentration, which is as well, where are located the interface defects.

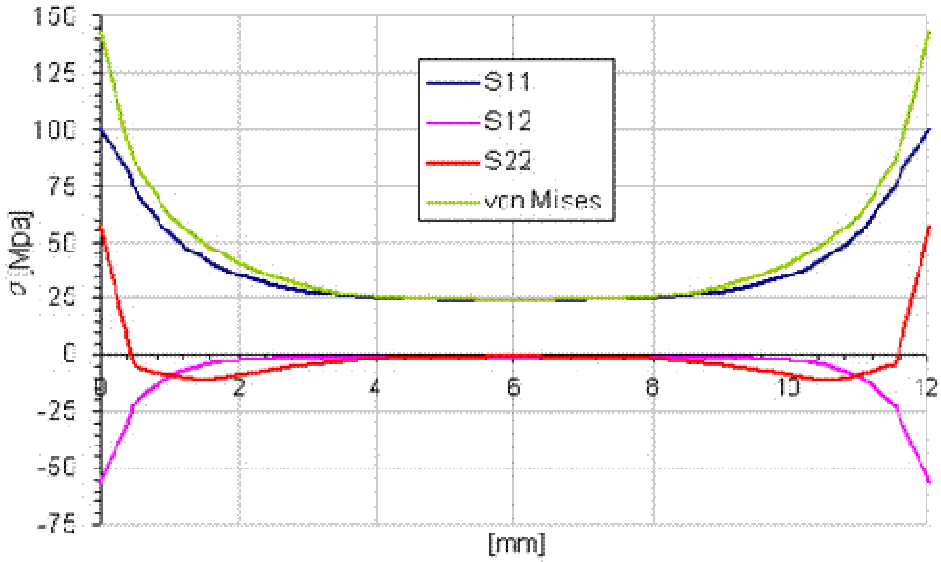

Figure 133: Stress distributions along the overlap joint line

The experimental plan comprises two pin lengths Figure 134, single and multiple weld passages, different distances between the welding passages and different surface conditions (anodising - TSA, primer and adhesive in the welding area).

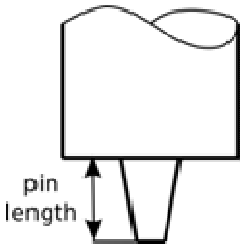

Figure 134: Pin length

The plate positioning, weld directions and the path for the double and triple passage are shown in Figure 135. For the single passage the welding path was centred in the overlap area and with the same direction of the first path in double passage configuration. The 3 different configurations for the overlap double passage used the same path configuration presented in Figure 135, with different distances between the paths. This path configuration should allow to remove the hooking defect of the advancing side that is usually more critical than the retreating side. The path 25-25 means that the two paths were done in the centre of the overlap without translation of the tool, the 20-30 path indicates that the first path was done at 20 mm from the boundary of the joint and the second one at 30 mm. For the triple passage, the last path was done in the middle of the joint as pointed out in Figure 135.

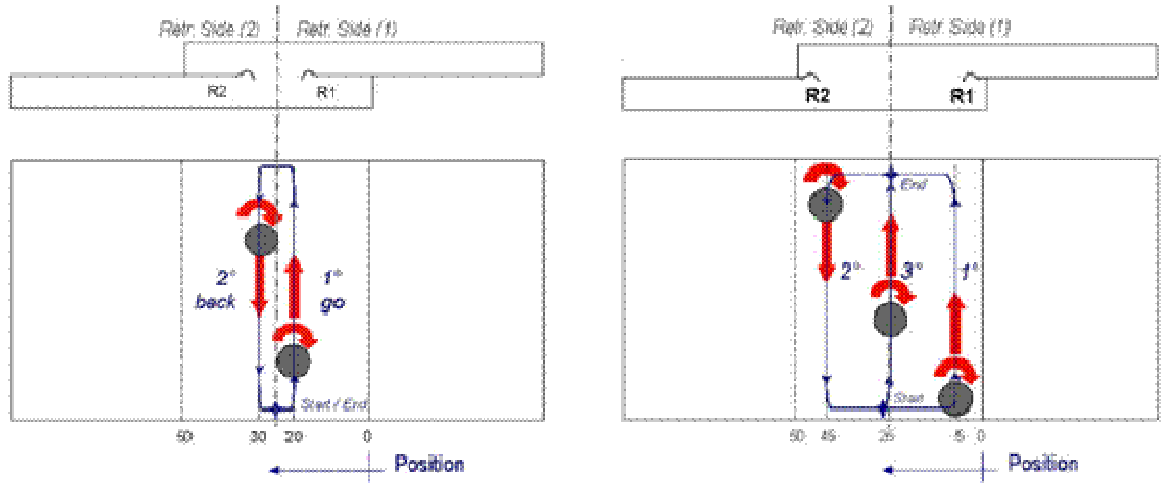

Figure 135: Overlap welds, double passage 20-30 configuration and tripe passage 5-25-45 configuration

Table 21 lists the different configuration for the overlap welds that were manufactured. Only configurations in the green lines were tested and the result discussed in the following.

Weld Label	Pin Length	N° of Passages	Passage Position(s) [mm]	Surface Treatment
KL6-2	2,6	1	25	-
KL7-3	3,4	1	25	-
KL10-6	3,4	2	25 - 25	-
KL14-9	3,4	2	23 - 27	-
KL15-11	3,4	2	20 - 30	-
KL18-14	3,4	3	5 - 25 - 45	-

Table 21: COINS, overlap joints, test matrix with the different conditions tested

Fatigue results

Fatigue tests were performed on specimens 12 mm wide using a load ratio of R=0.1 (σmin/σmax). The stress amplitude, equation (1), was adjusted in order to achieve fatigue life's between 10.000 and 2.000.000 cycles. When the specimens reached 2.000.000 cycles the test was stopped.

The results are compiled in Figure 136 for all specimens. The stress amplitude, Δσ, in the fatigue chart means:

$$\Delta\sigma = \frac{\sigma_{max} - \sigma_{min}}{2} \qquad (1)$$

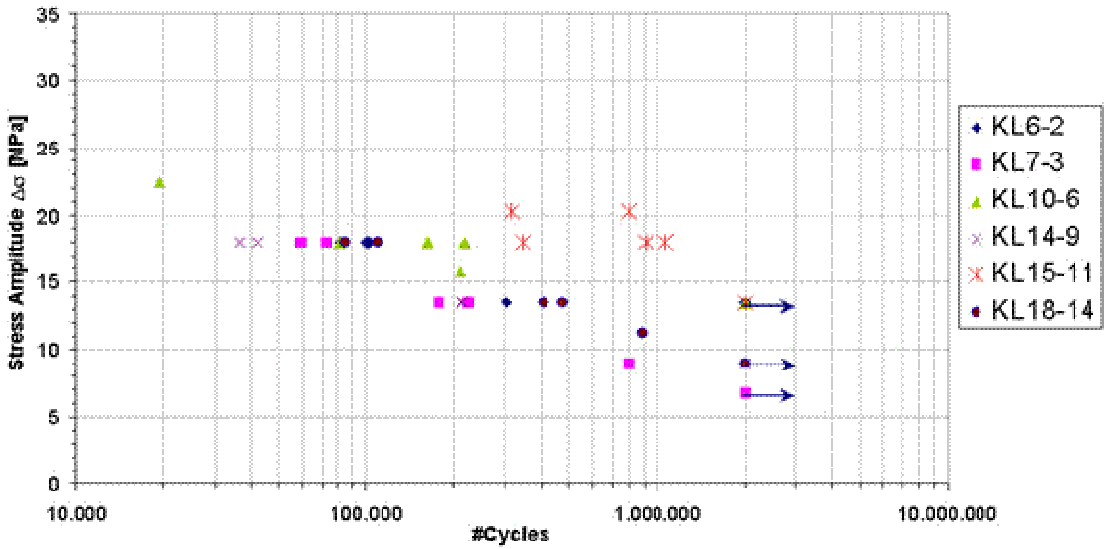

Figure 136: Overview of the fatigue results

Results assessment

A comparison between the different configurations was done using trend lines with the results of each configuration. For some configurations was just acquired 5 points (as KL 14-9) for the Wöhler curve, nevertheless the purpose of this study is not to provide SN curves for design but a straightforward comparison between different overlap concepts.

The pin length effect on fatigue life is shown in Figure 137, the best results were obtained for the lower pin length. As reported below, the pin length should be the short as necessary just to promote the mix in the interface and produce the lower thermo-mechanical affected zone. Due the preliminary static tests, prepared to check the weld quality, gave higher strength for the pin 3.4 mm length this configuration was used for the remaining welds. Although, the fatigue results pointed up that the pin length 2.6 mm may gives slightly better results.

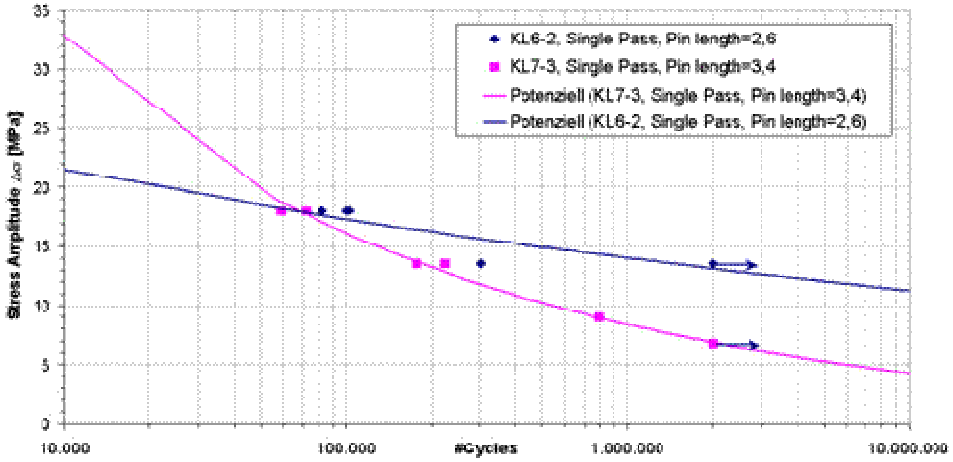

Figure 137 : Fatigue comparison, effect of the pin length in single pass

Comparing the results of the single pass with double pass, Figure 138 and Figure 139, without tool translation and with 4 mm tool translation, respectively, the improvement obtained was not substantial. In the case of Figure 139, the improvement is negligible, unlike the expectation. Although, the analysis of the welds in order to identify if they are defect free was not done, and could be the reason for the low fatigue values.

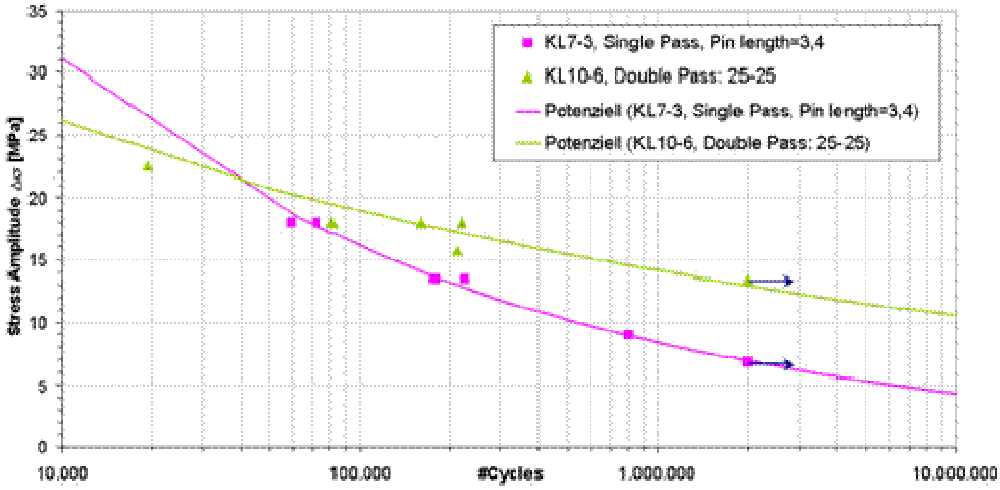

Figure 138: Fatigue comparison, single pass with double pass without translation

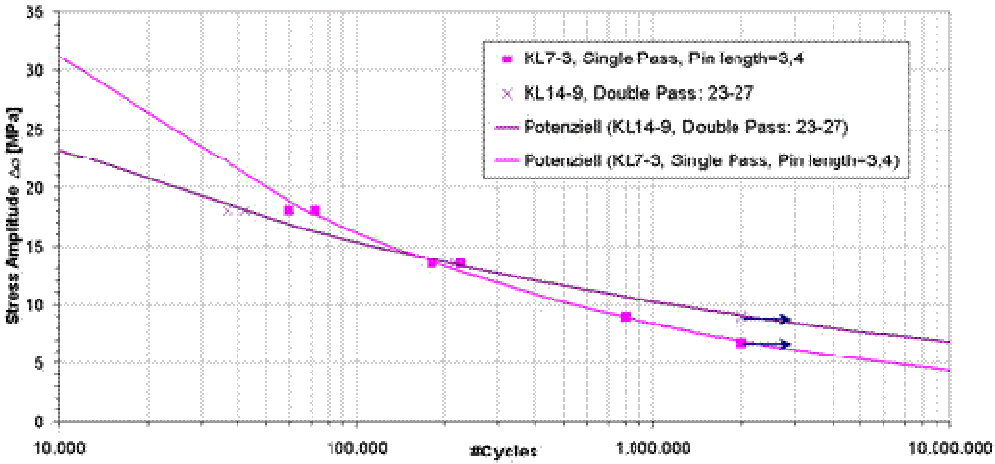

Figure 139: Fatigue comparison, single pass with double pass with 4mm translation

Figure 140 shows the results for the 3 different double pass configuration, where the translation of the tool was incrementally increased. The best results, as expected, were given by the configuration with the higher translation (10 mm). Putting side by side the two best single pass results with the triple pass, Figure 140, the results are also unexpected, because the triple pass didn't give a real benefit. One possible reason is the trade off between the increase of welding area and the distance of the hooking defects to the bending centre, that increases the interface forces in the hooking tips, reducing the joint strength.

The best results using the single, double and triple pass configurations are presented in Figure 141. As detailed above, the best results were obtained with the single pass configuration with 20 mm of tool translation.

The results achieved have some inconsistency, that may be justified by the small amount of fatigue specimens. Nevertheless, the important point to retain is that any result gave a reasonable fatigue value in order to this type of joint to be considered for primary structures.

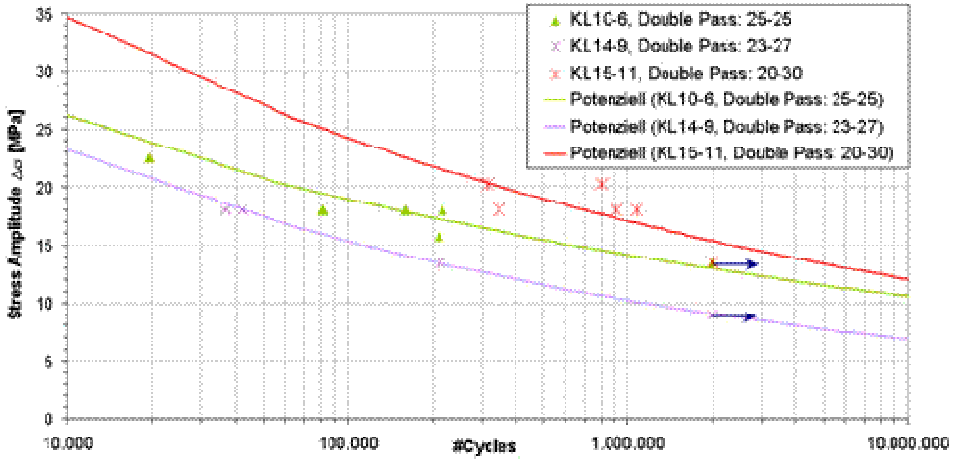

Figure 140: Fatigue comparison, double pass configurations

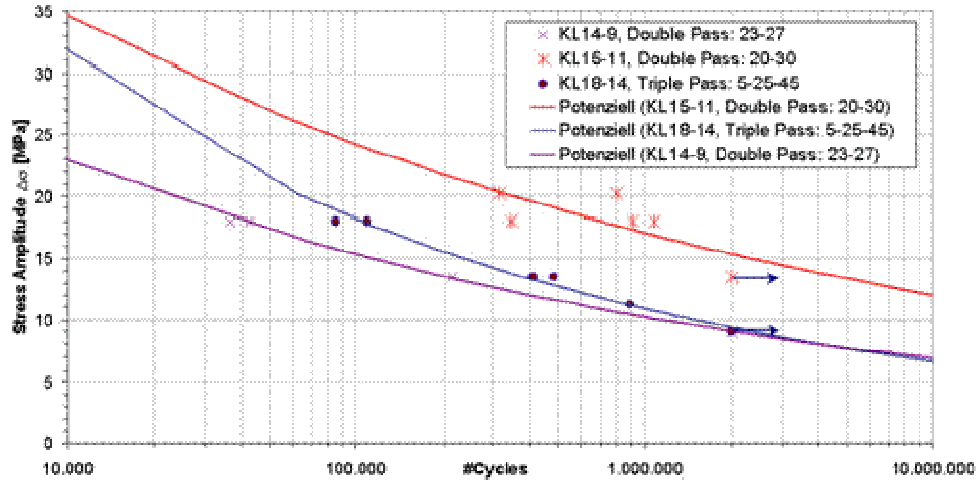

Figure 141: Fatigue comparison, double pass 23-27 and 20-30 with triple pass configuration

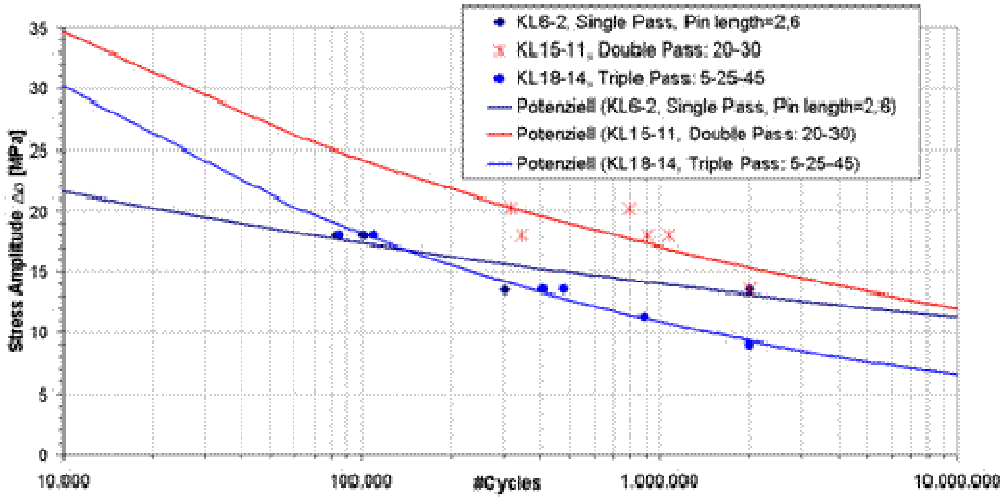

Figure 142: Fatigue comparison, single, double and triple pass configuration, best results

The fatigue results for the different configurations were summarized using the fatigue strength for two number of cycles (1E5 and 1E6 cycles) and are presented in Table 22. The strength was determined from the power regressions to the experimental points.

	Δσ [MPa]	
	1E+05 Cycles	**1E+06 Cycles**
KL6-2, Single Pass, Pin length=2,6	17,4	14,0
KL7-3, Single Pass, Pin length=3,4	16,1	8,4
KL10-6, Double Pass: 25-25	19,0	14,1
KL14-9, Double Pass: 23-27	15,3	10,2
KL15-11, Double Pass: 20-30	24,2	17,1
KL18-14, Triple Pass: 5-25-45	18,1	10,9

Table 22: COINS Fatigue results condensation of overlap joints

3.10 Task 3.5 New Applications, Geometries, fixtures, realisation, testing (Sabca)

Task 3.5 : designed: box beam feasibility structure, with weld inspection capability and post-milling practicability in the inside of the box ; design of potential dedicated raw material form (e.g. specific extrusion) for the box

Task 3.6 : designed: specific fixture and tooling for the welding of a closed box section

Task 3.7 : samples, mock-up and beam components manufactured (2050 T8). Tooling fixtures manufactured (Steel and Stainless Steel)

Task 3.8 : testing plan of samples updated and finalised

3.11 Task 3.5 New Geometries (Piaggio Aero)

PAI has defined with Alenia a large demonstrator of FSWelding application: “Shear Beam”

Material of central web is aluminium Al 2056 thickness t= 2,5 mm, upr, lower cap and central vertical stiffener are extruded Al 2024 constant thickness t = 2,5 mm:

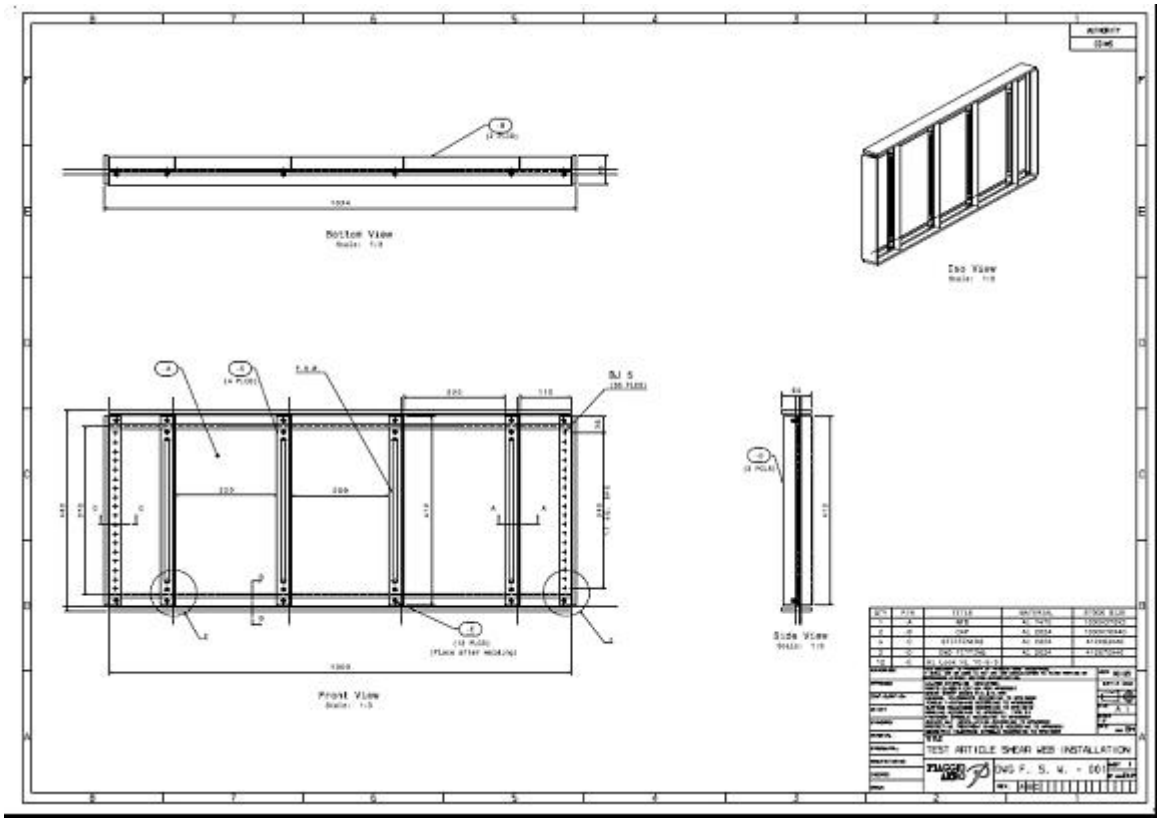

Figure 143: Shear beam

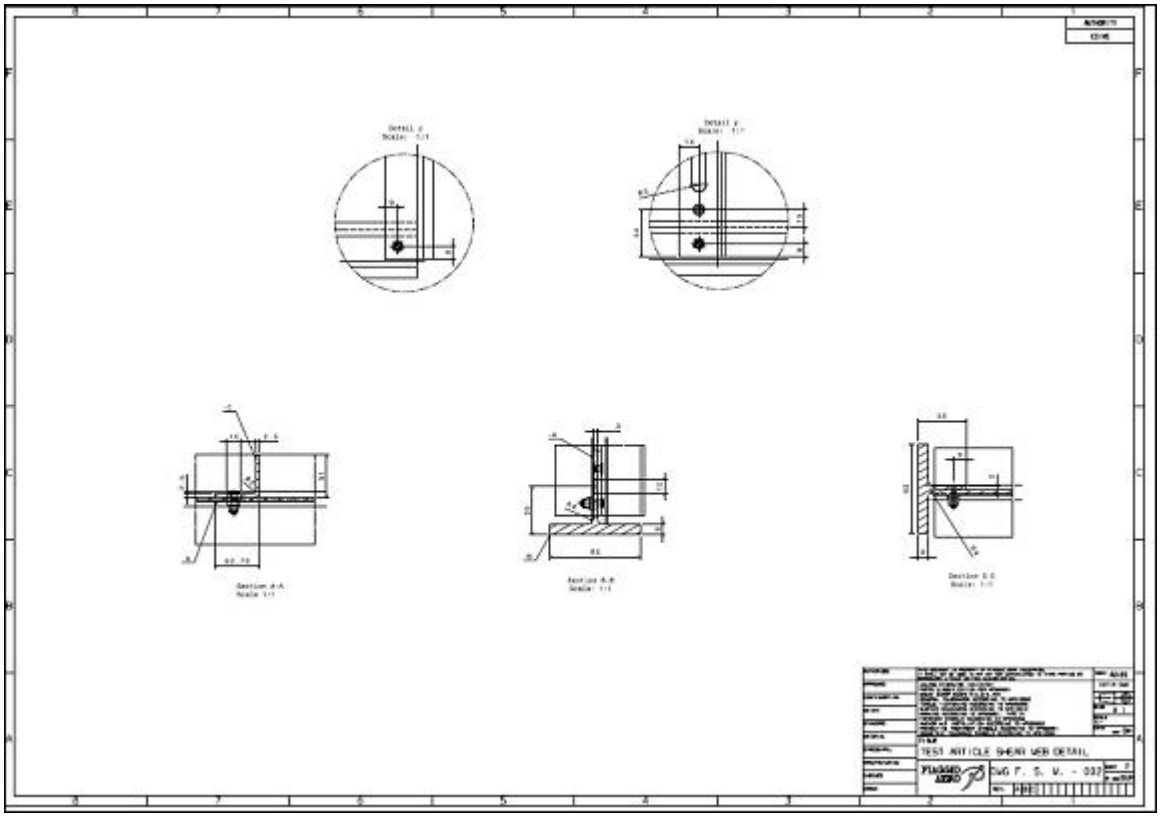

Figure 144: Shear beam detail

Upr and lower cap are butt-welded to central web, vertical stiffeners are lap-welded to central web. At extremities each vertical stiffener is fixed to web by two Hi-Lok

3.12 Task 3.5 New geometries (EADS Germany)

Welds on new geometries will be performed by the new DeltaN tool concept. The advantage of process force reduction will greatly benefit welds on hollow structures and stiffeners.

Partner SABCA designed a beam track out 2050 plates material and delivered the parts to be welded and further some of the clamping devices to EADS G. The beam track shows a hollow box design. EADS G began the welding scenario by tack welding of the 4 parts inside the clamping jig arrangement and afterwards DeltaN full penetration welding. The demonstration was successful, see Figure 145 and Figure 146.

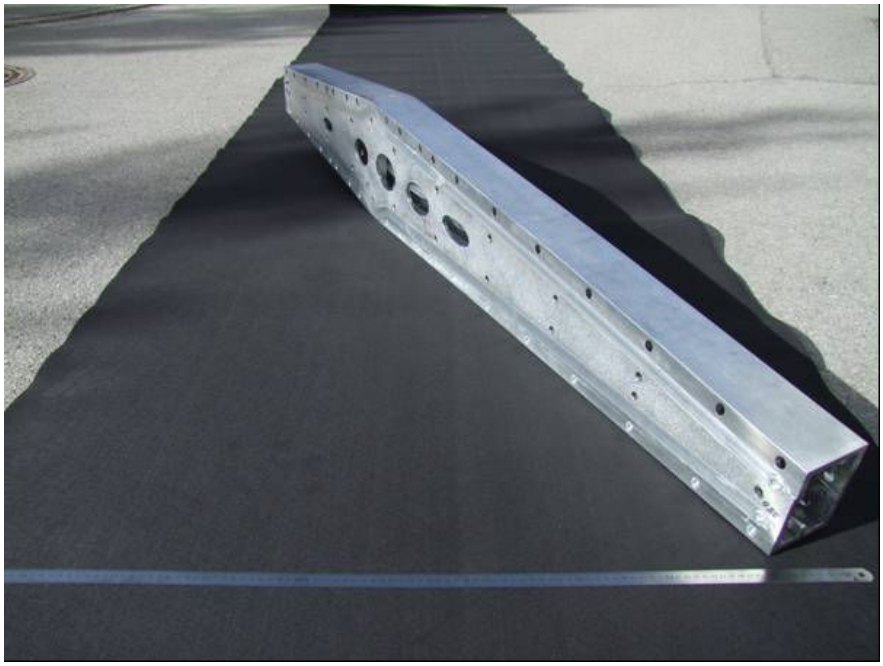

Figure 145: Total view of the DeltaN tool welded 2050 alloy beam track

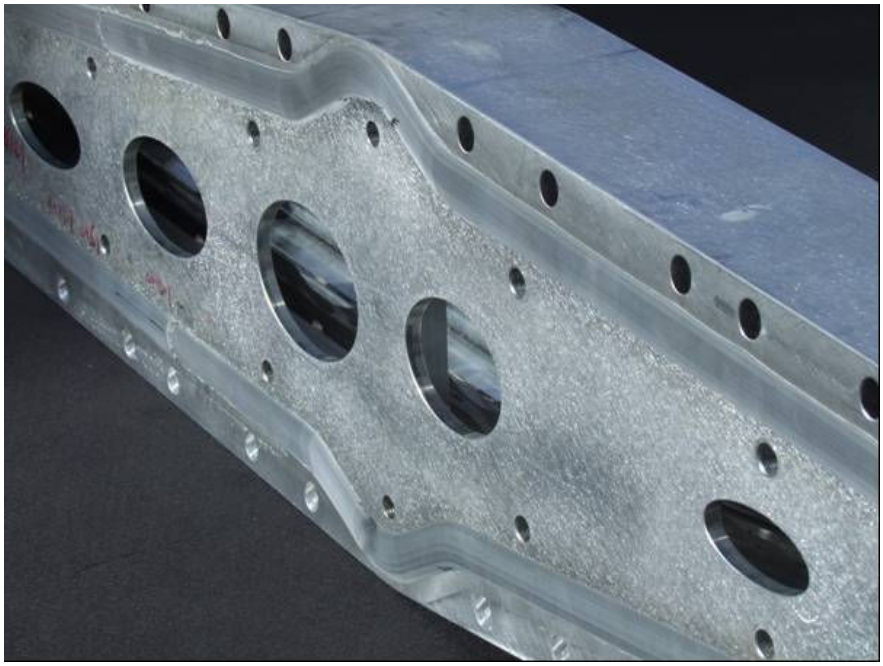

Figure 146: Detail view of the DeltaN tool weld top surface and its superb surface finish

The beam track shows no visible distortion despite the intense welding impact, the surface appearance after DeltaN tool use is superb as expected and the welded component has been delivered to the SABCA Brussels facility.

3.13 Task 3.5 New geometries (University of Patras)

3.13.1 Fatigue Testing of 2050 T3 T-Type samples

During the reporting period, the fatigue behavior of 2050 T3 aluminum alloy with two different weld configurations was assessed. The two different specimen types which are compared can be seen in the figures below (lines indicate the rolling direction).

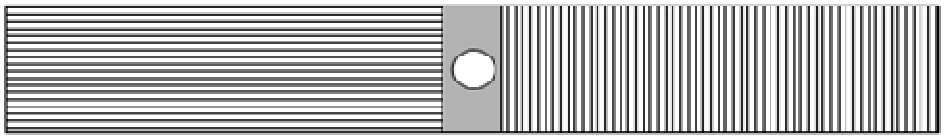

T type Sample LT

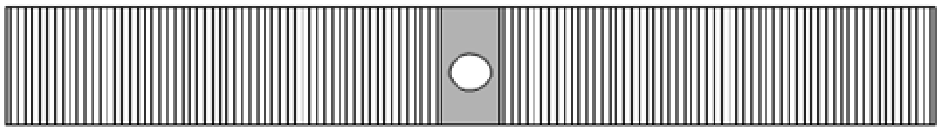

T type Sample TT

Figure 147: Fatigue testing specimen types

The specimens were prepared according to the prEN 6072 specification. The dimensions of the specimens was 150x30x12mm and the hole was of 10mm diameter. A total of 18 fatigue tests were performed, nine for each configuration.

Fatigue test results

The test results are presented in the figure below.

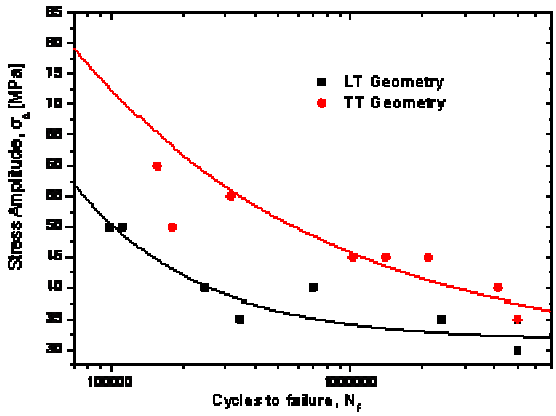

Figure 148: Comparative plot of the LT and the TT welded sample

Main findings

- From the graph above, it is noticed that the fatigue behaviour of TT welded plates is superior to the respective behavior of the LT welded plates.
- The difference is more intense for higher stress levels and diminishes when approaching the fatigue limit.
- A metallographic analysis of the specimens is required to explain the differences observed.

3.13.2 Fatigue testing of pre-corroded 2198 T8 FSW aluminum alloy with and without LoP defect

During the reporting period, the effect of corrosion on the fatigue behaviour of 2198T8 FSW alloy, with and without the presence of a Lack of Penetration defect was assessed. Mechanical testing on the corroded specimens were completed. The respective tests on non-corroded specimens have been completed during the previous reporting period.

In this test series, a total of 24 fatigue tests were performed on corroded specimens. The test matrix is summarized in the table below.

Test sample	Test content	No of samples
As welded	Salt spray testing + fatigue	12
As welded + artificial LoP defect	Salt spray testing + fatigue	12

Table 23: Fatigue test matrix on pre-corroded 2198 T8

For corroding the alloys, the salt spray chamber test method has been used according to the ASTM B117 specification.

Corrosion characteristics

- Neutral salt spray testing
- Duration : 30 days
- 5% NaCl
- Temperature : 35° C
- 6,5 – 7,2 pH
- 10 – 25 psi

Test specimens were prepared according to the Airbus Industry Test Method 1-0011-96 (replaced by prEN 6072) with a reduced section of 50mm.

Test results

The test results are summarized in the figure below.

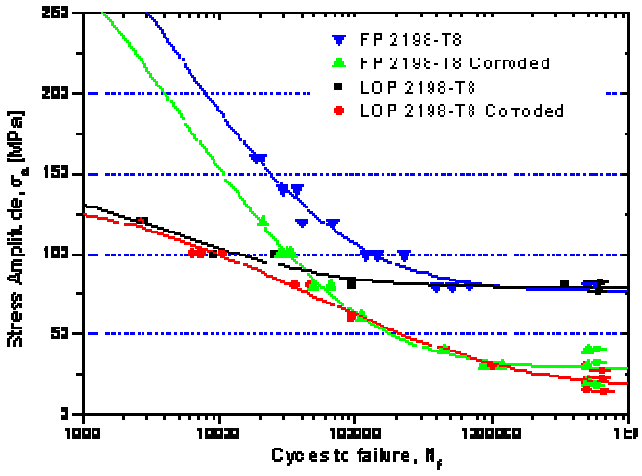

Figure 149: Comparison of the S-N curves derived for all test series performed

All the above plots have been fitted by a non-linear analysis (Weibull 4 point function), which is defined as: $S = P_1 + \frac{P_2 - P_1}{\exp\left(\frac{\log N_f}{P_3}\right)^{P_4}}$

The coefficients derived by the non-linear analysis of the fatigue strength data are summarized in the table below.

Coefficient	Uncorroded		30 days SSC	
	FP	LOP	FP	LOP
P_1	76.91336	79.41143	28.82068	17.53932
P_2	424.12796	150.85319	360.69723	137.80291
P_3	3.86067	3.92474	4.01589	5.00537
P_4	3.5147	4.13928	3.75035	4.2456

Specimens fracture types

Three different fracture types were observed:

i) Fracture in the weld joint line: This type of fracture was mostly observed in the case of specimens with LoP defect.

ii) Fracture on the weld interface: This type of fracture was mostly observed for the full penetrations specimens

iii) Fracture out of the heat affected zone: This type of fracture was mostly observed for the corroded specimens

Fracture in the weld joint line

Fracture on the weld interface

Fracture out of the heat affected zone (weld zone)

Figure 150: Specimen Fracture Types

Main findings

- The lack of penetration defect significantly reduces the fatigue life of the material. This effect diminishes as the stress levels reduce and the fatigue limit remains practically unaffected by the LoP defect. An estimate of the fatigue limit can be taken as the value of the P1 coefficient of the Weibull-4 curve fitting function.
- Corrosion attack also reduces significantly the fatigue behavior in both, the full penetration specimens and the specimens with the LoP defect.
- For high stress levels, corrosion does not affect the fracture mode of the specimens. For lower stress levels, however, corroded specimens failed from cracks which originated from corrosion pits.

3.14 Workpackage 3: Development of New Applications for FSW (Airbus UK)

Determined mean stresses and alternating stresses for coupon testing of 2195 specimens.

NDI of laminated blank assemblies (post bonding).

Manufacture and NDI of laminated test specimens (post machining).

Test request produced for testing of laminated specimens and single ply tensile specimens.

Test definition produced for testing of laminated specimens

Tensile testing of 1.6mm 2198 sheet completed

Fatigue testing of laminated 2198 sheet assembly specimens completed

Production of drawings and manufacturing instruction sheet for the manufacture of the sub-element demonstrator.

Sub-element demonstrator produced, demonstrator consisted of a dissimilar FSW consisting of a 2196 extrusion to 2198 sheet and additional 2198 sheet bonded on to produce a laminated structure (see Figure 151 below).

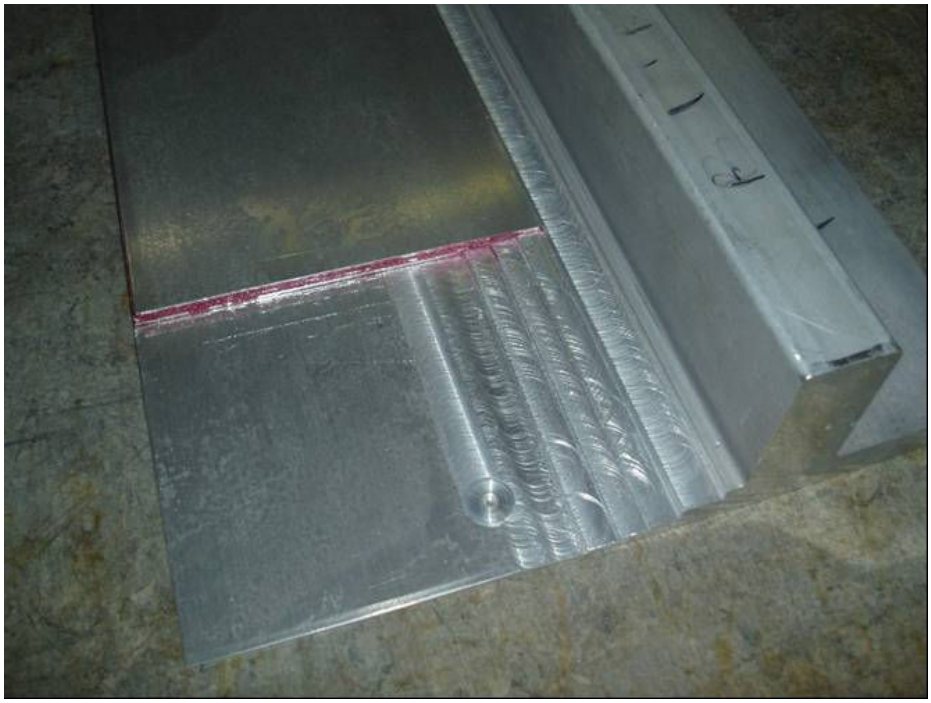

Figure 151: Welded Laminated demonstrator

3.15 Task 3.6 Development of Fixtures for New Applications (BAE)

To exhibit the potential of FSW for application in land vehicle fabrication, a scaled technology demonstrator was produced. This component was a generalised cross-section of a hull based on current land vehicle platforms and incorporated the five new and different joint designs as discussed in preceding sections.

To produce the welds, tooling was developed to secure each joint configuration during the welding process. The tooling block was developed to be reconfigurable, and took into account the clearances and access requirements of the Huron NU5 milling machine that was used to produce the welds. The result was a modular system consisting of several anvil blocks and add-on parts for edge and overhead clamping. The tooling blocks are the welding sequence is shown in Figure 152.

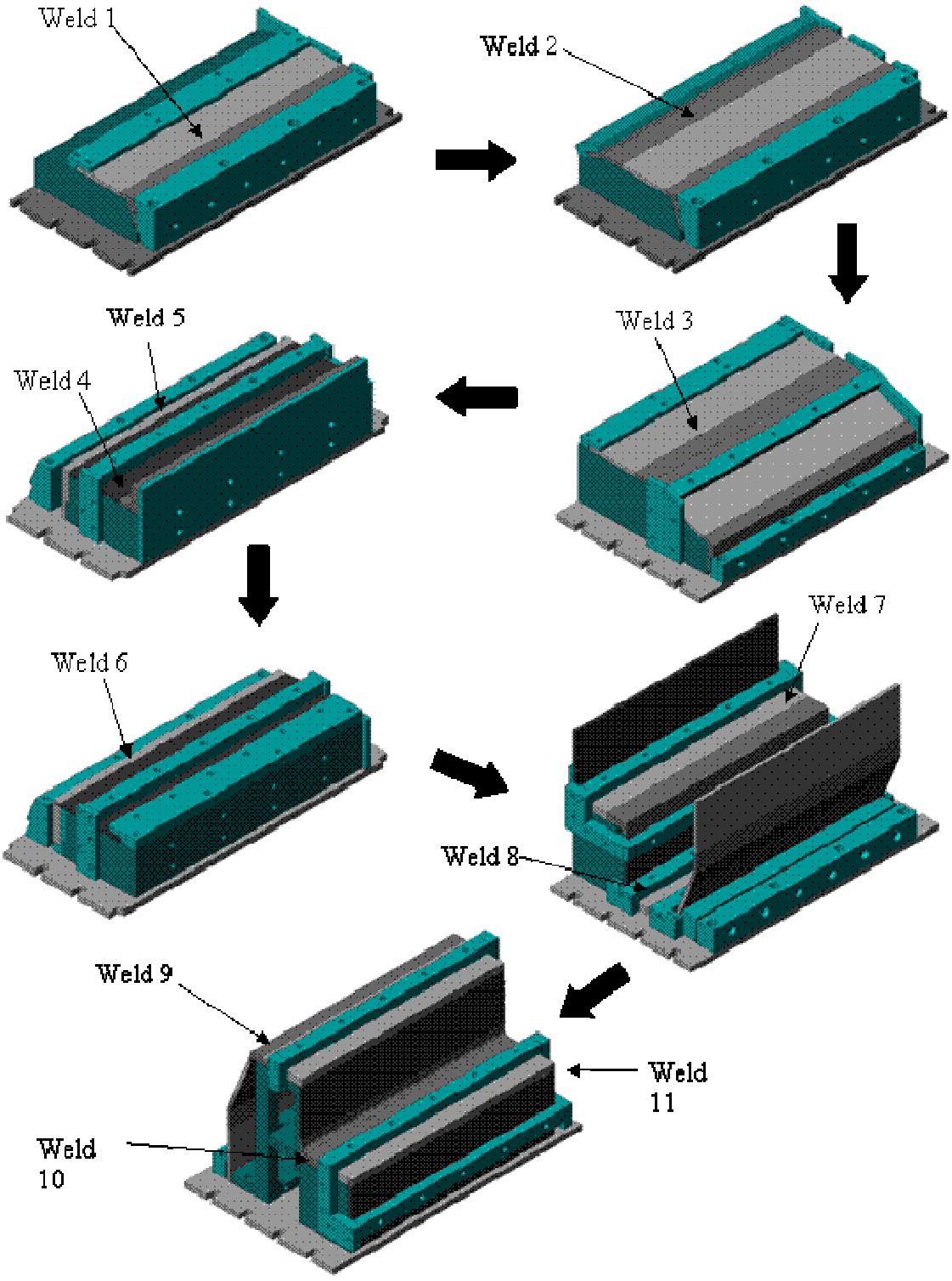

Figure 152: Tooling blocks and welding sequence

3.16 Task 3.7 Realisation of New Applications using Existing/New Data and New Geometries (BAE)

The BAE Systems technology demonstrator was designed to be made from three separate sub-assemblies not only to reduce distortion, but for ease of manufacture. The weld sequence and the subassemblies are shown in Figure 153. Welds 1, 2 and 3 made up subassembly A (red). Welds 4 and 5 made subassembly B (blue) and a single weld, weld 6 made subassembly C (yellow). The three subassemblies were then fully assembled using welds 7, 8, 9, 10 and 11 to complete the component.

To address any potential difficulties or engineering issues that occurred during manufacture, such as insufficient clamping or incorrect welding parameters i.e. speed, feed or vertical tool load, four-off of each sub-assembly were made in parallel. Manufacturing problems encountered during production were addressed and corrected prior to moving on to subsequent sub-assemblies.

3.16.1 Fabrication of Subassembly A

Subassembly A was comprised of three full penetration square edge butt joints that combined welding of dissimilar aluminium alloys in both plate and extruded forms.

The first weld was a dissimilar alloy joint comprising 7056 plate with a 7449 machined corner section that had been extracted from extrusion. Prior to welding some minor bowing was noted along the length of the corner section, which was attributed to the machining operation.

The sections were rigidly secured in the tooling block, and all distortion and misalignment was mitigated by the combination of edge and overhead clamping. Friction Stir Tacking (FST) was applied to prevent any separation or lifting of the sections during the welding process. FST was conducted using a short pin tool (in this instance, 3mm) to produce 5-10mm partial-penetration tack weld at the beginning and end of the joint. Unless stated otherwise, this process was applied to all joints during the assembly of the technology demonstrator.

The full penetration weld was successfully completed. No visual defects were observed in the finished weld, although some minor distortion was seen after the clamping was removed.

Weld 2 was also a dissimilar weld and added a 45° angled 7449 corner section to the 7056 plate edge of the preceding assembly. The corner section was again made from extruded bar in which some minor distortion due to the machining operation was observed. The tooling fixtures were reconfigured to accept the added section then welded.

The final weld (3) in the first subassembly was another demonstration of welding dissimilar alloys. However, in this instance there was a significant difference in the mechanical properties of each alloy. Whilst the 7449 and 7056 alloys used in the previous joints are mechanically similar in terms of yield strength, Weld 3 joins 7449 to 7020 which has a yield strength that is 62.5% of the 7449. To produce a successful weld is essential the higher strength alloy (7449) is on the advancing side of the weld and the lower strength alloy (7020) is on the retreating side.

As observed in the previous weld there was some minor distortion in the corner section due to machining, which again was mitigated by the clamping. A full penetration weld was successfully

completed, although some minor distortion was noted in the subassembly after the clamping had been removed.

3.16.2 Fabrication of Subassembly B

Subassembly B comprised two welds; a dissimilar alloy square edge butt joint with 7056 plate and 7449 extrusion and a tailored blank joint.

Weld 4 was a dissimilar weld made from 7056 plate and a 7449 corner section. The corner piece was machined to shape from extruded material. No distortion was observed in the corner section in this instance, which made clamping and alignment in the tooling relatively straight-forward. Only edge clamping was possible for this joint due to the size and shape of the corner section.

Weld 5 demonstrates a method for manufacturing a defect free tailored blank weld (described earlier under Task 3.5) that uses a sacrificial insert of the same alloy as the weld material, which is inserted in to a recess in the tooling block along the edge of the thinner of the two sections. The joint is illustrated in Figure 126. Figure 126a shows the welded joint prior to machining; Figure 126b after machining.

Weld 5 was produced using the method described without any difficulty. However, minor post weld distortion meant careful machining of the radius profile was required to complete this subassembly.

3.16.3 Fabrication of Subassembly C

Subassembly C consisted of a single weld (6) that formed the first of two welds that made up a 90° interlocking joint detailed in Figure 128 and Figure 129. The interlocking joint was essentially a simple tongue and groove joint machined from flat 7056 plate. A sliding interference fit between the tongue and the groove ensured easy fit up that did not require FST when clamped into the tooling.

A full penetration weld was successfully carried out without any visible post weld distortion.

3.16.4 Fabrication of Half-Section Assembly

To complete the half-section geometry, subassemblies A, B & C were joined by the subsequent welds described below.

Weld 7 was a 10mm depth, partial penetration weld and was the first of two the completed a full penetration double-sided 7056-7056 joint. The two welds forming this joint were both deeper than the material thickness resulting in an overlap in the centre of the plate. A metallographic cross-section of a double-side weld is shown in Figure 127. The weld was successfully completed with no visible distortion.

Weld 8 was the first weld of a two weld rebated joint. A FSW tool with a pin length greater than half the material thickness was used to create this joint. One consideration when making this joint was FSW tool access issues. A tool with an extended body length was designed to reach to the bottom of the tooling block without the machine head fouling the assembly. Welding traverse speed was reduced for this weld to reduce transverse welding forces and counter any anticipated bending of the tool due to its length. Weld 9 was the second weld to complete the rebated joint. The weld was carried out successfully using the same tool that made the first part of the joint.

Weld 10 was the second weld to complete the double sided joint. The extended tool was again used due to access issues. The welding speed was reduced to successfully complete the weld.

Weld 11 completed the interlocking joint configuration and was again successfully carried out using the extended tool with reduced traverse speed.

3.16.5 Full-Section Assembly

Production of the half component progressed without any major manufacturing challenges. To demonstrate a fully enclosed part, the four half sections produced were welded together to produce two full assemblies as shown in Figure 154. An I-beam was inserted inside the two components which were held together using side clamping and secured to the FSW machine bed.

Welds 23 and 24 were full penetration butt welds. On completion of weld 23 the component was turned over to allow weld 24 be carried out to complete the full component assembly. The welds were carried out successfully with no visible defects.

3.16.6 Post Assembly Procedures and Surface Treatments

On completion of the welding phase the fully assembled final component was removed from the machine bed for post weld treatment. Each weld showed a minor amount of flash and the 'onion ring' welding marks associated with the process. An angle grinder with a sanding disk attachment was used to take out these surface imperfections over approximately three quarters of the length of the component. This prepared area was then masked up and given three layers of primer followed by three layers of top coat to give a final component that highlighted an as welded region, a post weld sanded region plus regions of primer and top coat as shown in Figure 155.

3.16.7 Results

A technology demonstrator component was successfully manufactured demonstrating the production by the use of simple tooling blocks, of an enclosed structure utilising novel joint design. Figure 155 shows the final component and the areas of post weld treatment.

By manufacturing multiples of each sub-assembly, any difficulties or engineering issues were addressed and corrected prior to moving on to subsequent assemblies. Engineering issues addressed were in the form of insufficient clamping or incorrect welding parameters i.e. speed, feed or vertical tool load and were easily rectified. The fact that the four half assemblies were manufactured without any major difficulties was largely attributed to good tooling design, sufficient side and overhead clamping and the production of separate, realistic sized sub-assemblies prior to manufacture of the final enclosed component.

3.16.8 Conclusions and Recommendations

FSW has been demonstrated as a suitable process for the production of enclosed structures however careful considerations must be given to the following.

- Alternative joint designs to those made by more conventional arc welding processes must be applied to allow FSW to be carried out in the horizontal position.

- To allow for alternative to conventional joint configurations such as double sided, rebated joints and tailored blanks to be made, design of sub-assemblies and correct weld sequencing is essential. Not only does sub-assembly design assist with ease of build but minimises accumulative distortion.
- Sub-assemblies and final assembly can be carried out on relatively simple, modular tooling blocks. It is however essential that sufficient side and overhead clamping is applied when carrying out each weld to eliminate weld plate separation and lifting that could lead to weld defects.
- Friction stir tack welding was demonstrated as a highly successful procedure for assisting in alignment and fit-up of weld pieces prior to the actual weld being made and assisted in the production of consistent, repeatable welds.
- It is recommended that further work is carried out to scale up the demonstrator part. This work would identify engineering challenges associated with large scale tooling design and welding challenges associated in manufacture of thick section parts by FSW.

A test study is also recommended comparing the strengths and weaknesses of a FSW enclosed structure against one made by conventional methods.

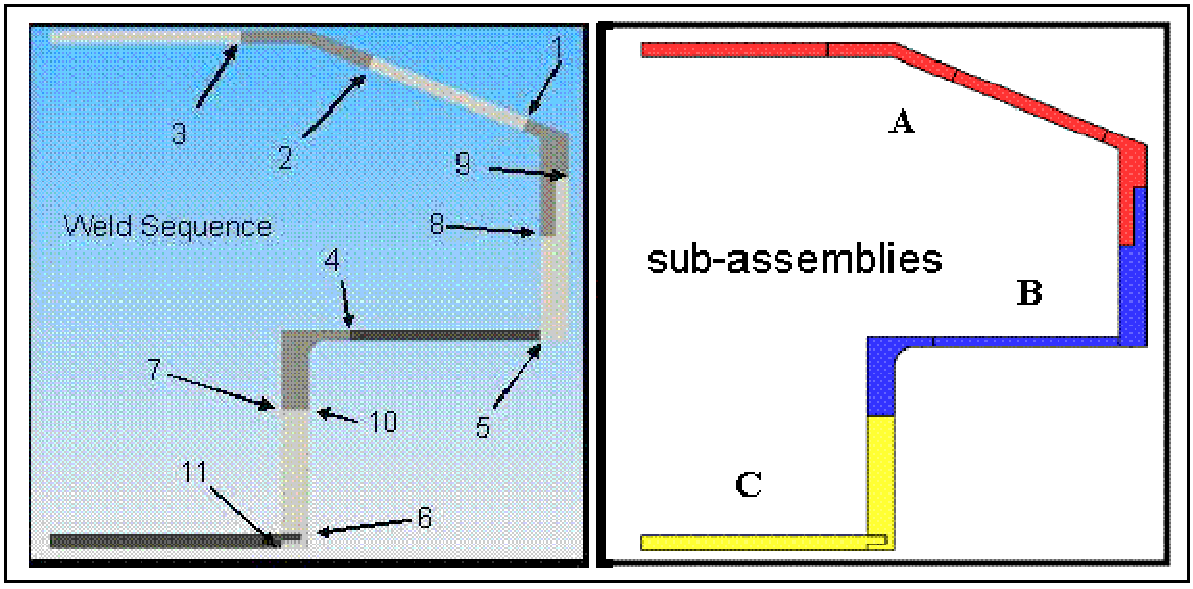

Figure 153: Demonstrator weld sequence and subassemblies

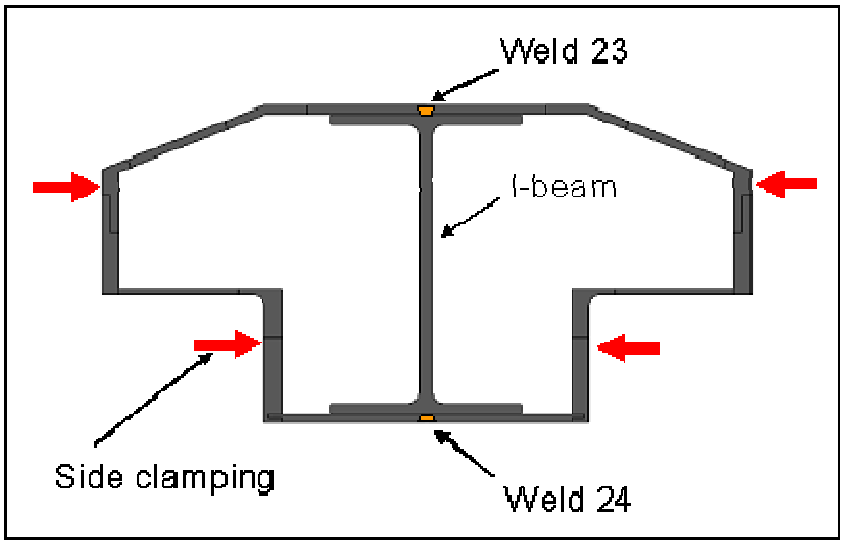

Figure 154: Schematic of the full assembly

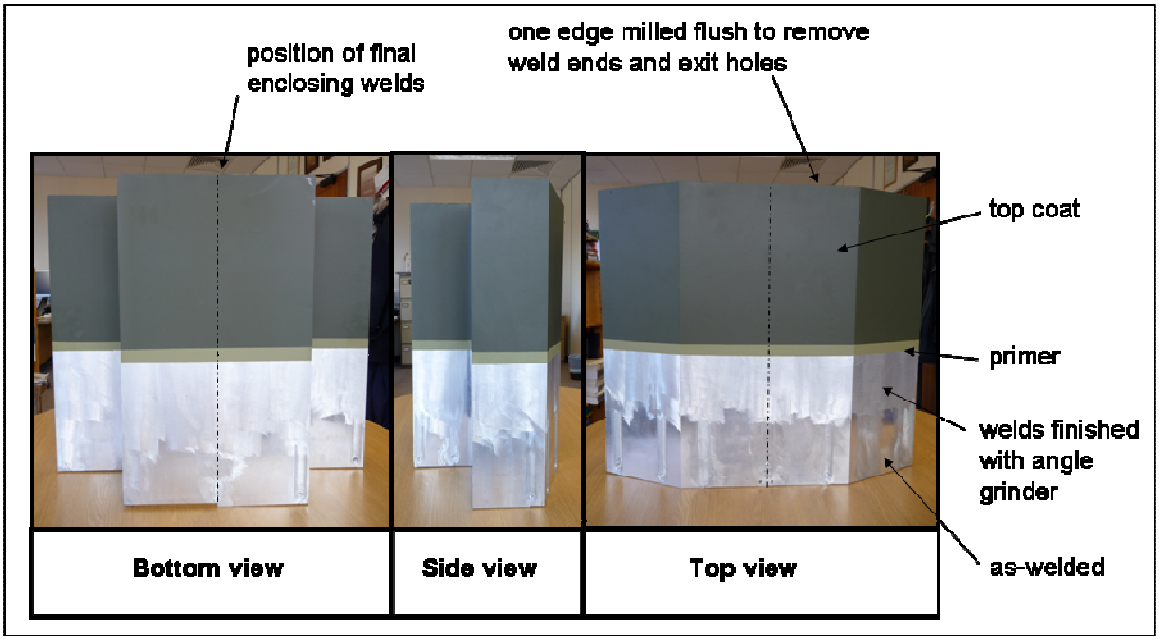

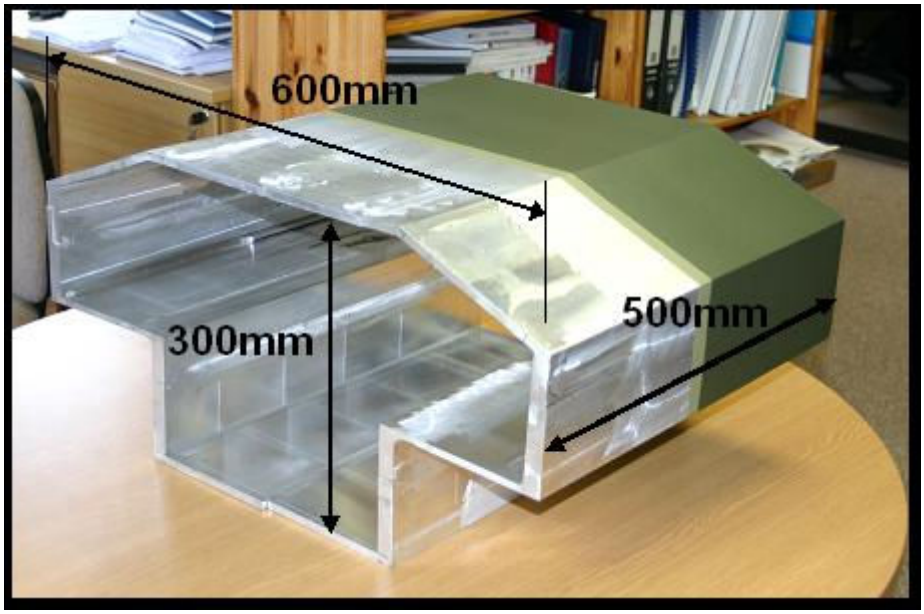

Figure 155: Fully assembled and post weld treated final component

3.17 Task 3.8 Testing and Evaluation of New Applications (Piaggio Aero)

Test activity of 2T test coupons was concluded.

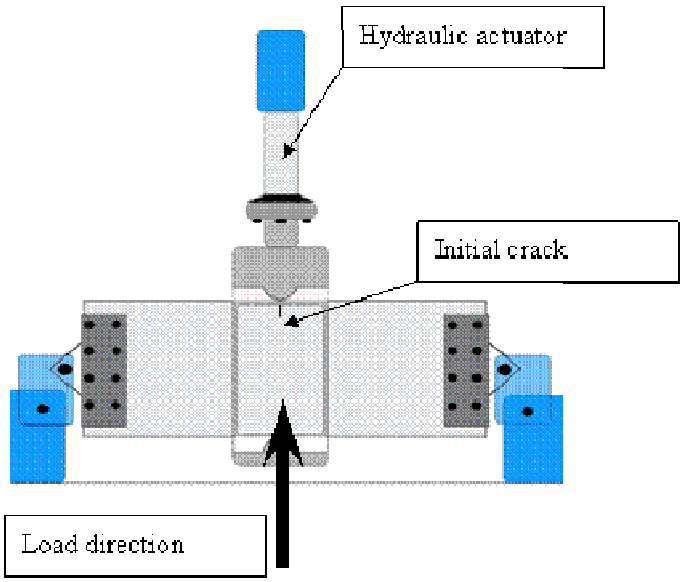

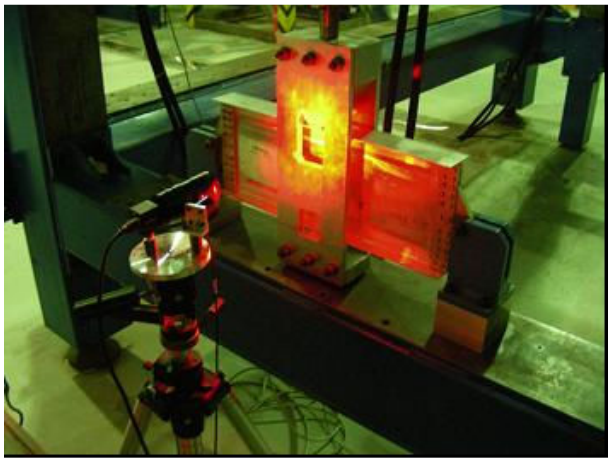

Figure 156: Welded wing spar test coupon

Summary of test is reported below:

COUPON			COUPON		
A	Lega	2198/2196	H	Lega	7075/2024
	RPM g/min	1000		RPM g/min	
	Avanzam. mm/min	300		Avanzam. mm/min	
	Tilt deg.	1		Tilt deg.	
	Cicli eseguiti	30500		Cicli eseguiti	150000
	Carico applicato	1500 Kg		Carico applicato	2400 Kg
	Tipo di prova	Crack grow		Tipo di prova	ciclica
	Note	-----		Note	
B	Lega	7075/2024	**I**	Lega	7075/2024
	RPM g/min	800		RPM g/min	1000
	Avanzam. mm/min	250		Avanzam. mm/min	350
	Tilt deg.	1.5		Tilt deg.	1.5
	Cicli eseguiti	175000		Cicli eseguiti	65000
	Carico applicato	1500 Kg		Carico applicato	1500 Kg
	Tipo di prova	Crack grow		Tipo di prova	Crack grow
	Note	-----		Note	
C	Lega	7075/2024	**L**	Lega	7075/2024
	RPM g/min	900		RPM g/min	1000
	Avanzam. mm/min	300		Avanzam. mm/min	400
	Tilt deg.	1.5		Tilt deg.	1.5

	Cicli eseguiti	280000		Cicli eseguiti	1500 Kg
	Carico applicato	2400 Kg		Carico applicato	91000
	Tipo di prova	Ciclica		Tipo di prova	Crack grow
	Note	-----		Note	
D	Lega	7075/2024	**O**	Lega	2198/2196
	RPM g/min	900		RPM g/min	1000
	Avanzam. mm/min	400		Avanzam. mm/min	300
	Tilt deg.	1.5		Tilt deg.	1.5
	Cicli eseguiti	60000		Cicli eseguiti	--------
	Carico applicato	1500 Kg		Carico applicato	--------
	Tipo di prova	Crack grow		Tipo di prova	--------
	Note	-----		Note	Non testabile*
F	Lega	7075/2024	**P**	Lega	2198/2196
	RPM g/min			RPM g/min	1000
	Avanzam. mm/min			Avanzam. mm/min	250
	Tilt deg.			Tilt deg.	1.5
	Cicli eseguiti	42000		Cicli eseguiti	-----
	Carico applicato	1500 Kg		Carico applicato	-----
	Tipo di prova	Crack grow		Tipo di prova	-----
	Note	-----		Note	Non testabile*
G	Lega	7075/2024	**Q**	Lega	2198/2196
	RPM g/min	1000		RPM g/min	950
	Avanzam. mm/min	250		Avanzam. mm/min	250
	Tilt deg.	1.5		Tilt deg.	1.5
	Cicli eseguiti	300000		Cicli eseguiti	-----
	Carico applicato	**		Carico applicato	-----
	Tipo di prova	ciclica		Tipo di prova	-----
	Note	-----		Note	Non testabile*
R	Lega	2198/2196	*** Provino R non testato a causa di run in /run out presente nella zona interessata dalla prova (saldatura) ** Provino G : testato a 3 carichi differenti. 100000 cicli a 1500 Kg,100000 a 1800 Kg e 100000 a 2100 Kg * Provini O,P e Q non testabili perché di misura troppo ridotta per essere inseriti nella struttura di prova		

Test activity of bulkhead test coupons was concluded.

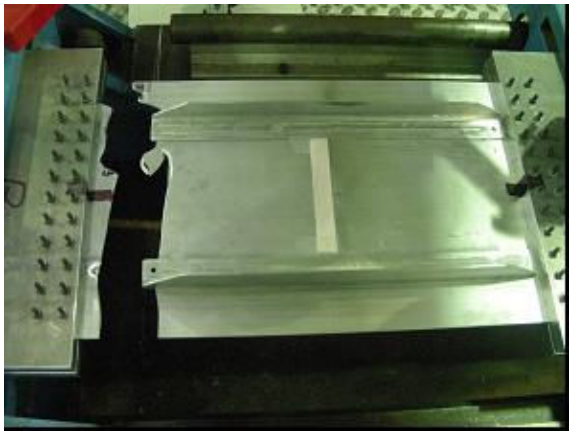

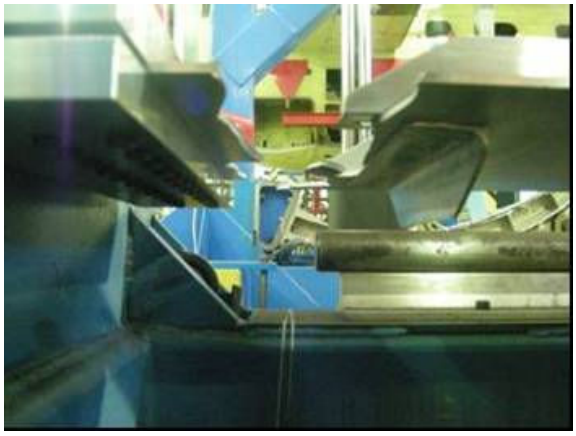

Figure 157: Failed shear beam test specimen

Cracks started not in correspondence of initial damage but in correspondence of run-out after 300,000 cycles.

Full scale shear beam fatigue and crack propagation tests have been perfomed. Alenia delivered to Piaggio four Shear beam large demonstrators. In order to perform a detailed analysis of the shear beam a finite element model has also been made.

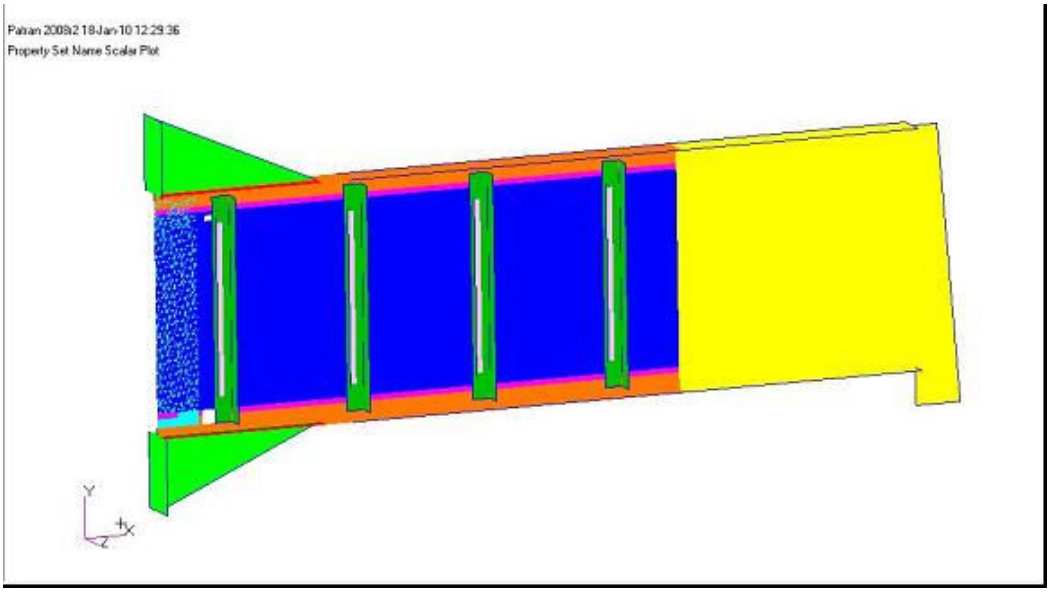

Figure 158: Modelled shear beam

A dedicated fixture assembly has been designed in order to fix the cantilevered shear beam and apply the vertical load at one extremity.

Straps and support have been sized for durability to prevent non-representative failures.

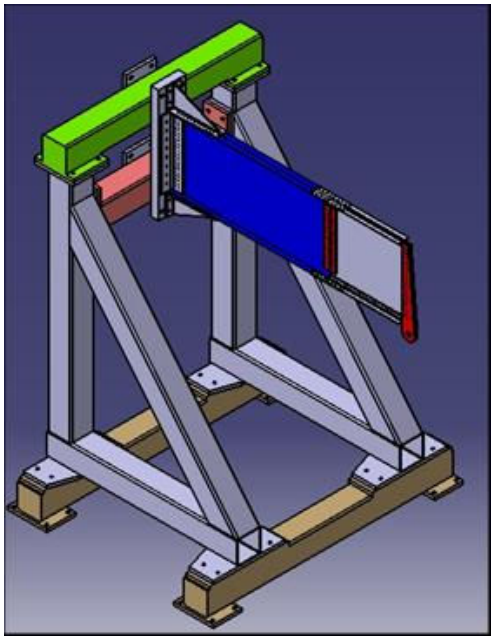

Figure 159: Testing arrangements

Test articles were instrumented with rosettes and strain gauges.

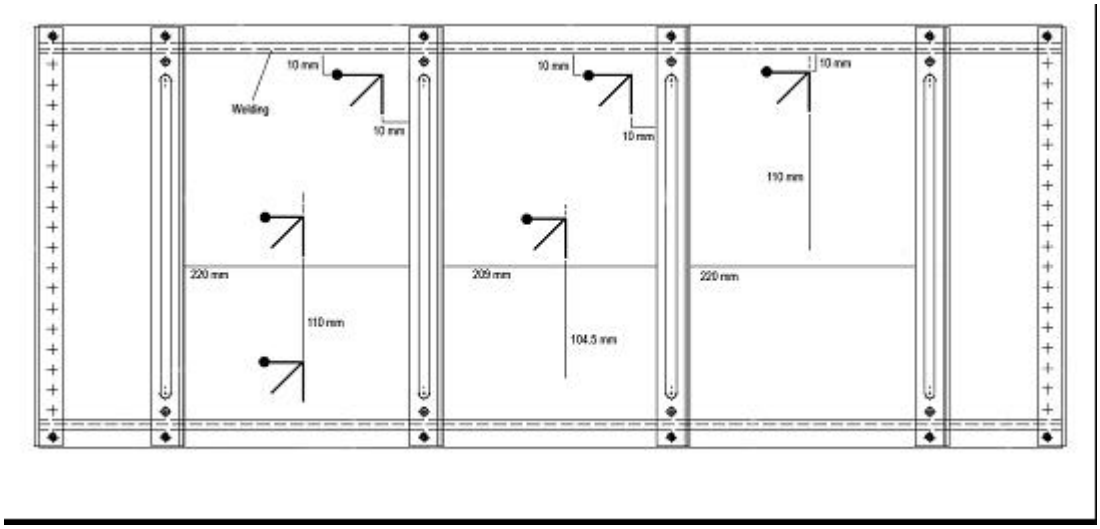

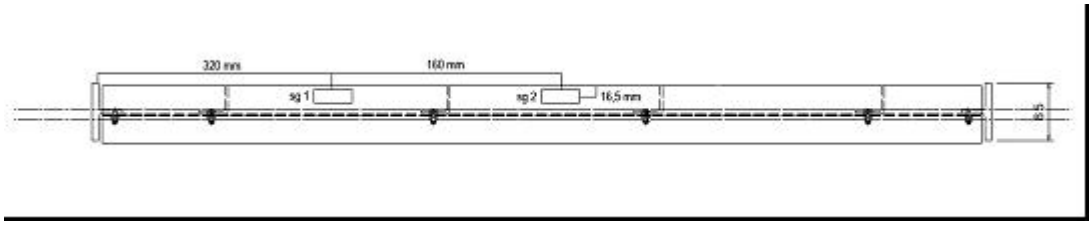

Figure 160: Detail drawing of shear beam test specimen

Fatigue loads under post-buckling field were:
Maximum load: Pmax = 13700 N
Minimum load: Pmin – 1370N
R = 0.1

In the welded shear beam the fatigue cracks appeared in correspondence of first Hi-Lok at extremity of welding line.

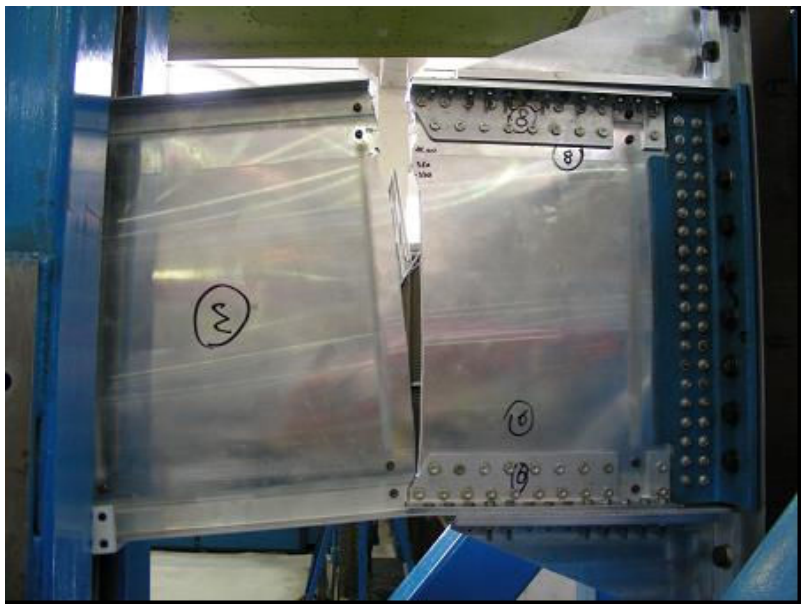

Figure 161 :The fatigue crack started at Hi-Lok hole at 250,000 cycles

Numerical results are in agreement with experimental ones.

3.18 Task 3.8 Testing and Evaluation of New Applications (EADS Germany)

Welds produced in hollow structures like boxes and stiffeners with the DeltaN tool will be tested by micro-section, micro hardness. Also static strength, impact and corrosion tests will be performed.

Before welding the SABCA beam track in total 4 DeltaN tools welds have been performed in advance. The DeltaN gen4 tool has been used and the plate thickness was 10 mm. The welds have been characterised according to the SABCA requirements by University of Patras.

3.19 Workpackage 3: ALCAN

- The results of welds' characterization were assessed and included in the contribution to deliverable D4.1 and D4.2. The FSW process of 2050 on 7449 20mm thick according to different heat treatments was also detailed. The microstructures of these joints were characterized versus the different heat treatments by tensile tests and SEM observations. Special pulsed FSW process was used for 2050/7449 dissimilar joint to improve the stirring in the nugget and obtain better static properties.

- The contribution to deliverable D5 for similar welding and testing the extruded panels in 7449 and in 2196 was written. FSW process, microhardness, corrosion of the joints were detailed, and flow stress were evaluated by the model described in the deliverable D7.
- The static behaviour of the joints and more particularly the ultimate tensile strengths are similar at about 440 MPa. The open hole fatigue behaviour of the 2196 FSW joints is similar in L and LT direction and also similar to the base material tested in L direction. The fatigue crack propagation in L-T direction of the weld tested with CCT specimen is lower than that of the base material.

4 Work Package 4: Repair Applications

4.1 WP 4.1 In-Production Repair Including Dissimilar Welds (University of Patras)

4.1.1 Testing of welded Joints

During the reporting period, a total of 12 tensile and 36 fatigue tests we performed. A total of 6 discrete cases were tested, as summarized in the table below.

Weld Type	Numbering	Pin Diameter [mm]	Pin length [mm]	No of passages	Position(s) [mm]
A	KL6-2	4	3.0	1	25
A	KL7-3	4	3.0	1	25
B	KL10-6	4	3.0	2	25-25
C	KL14-9	4	3.0	2	23-27
D	KL15-11	4	3.0	2	20-30
E	KL18-14	4	3.0	3	5-25-45

The figure below explains the various weld types tested as well as the position of the passages

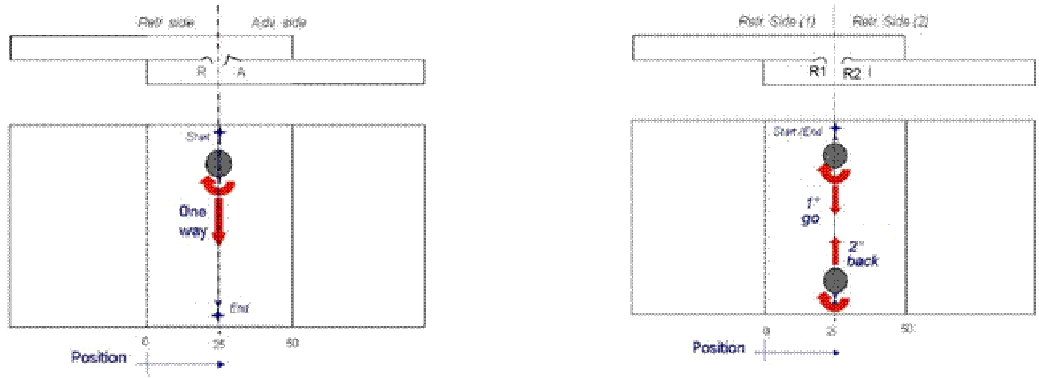

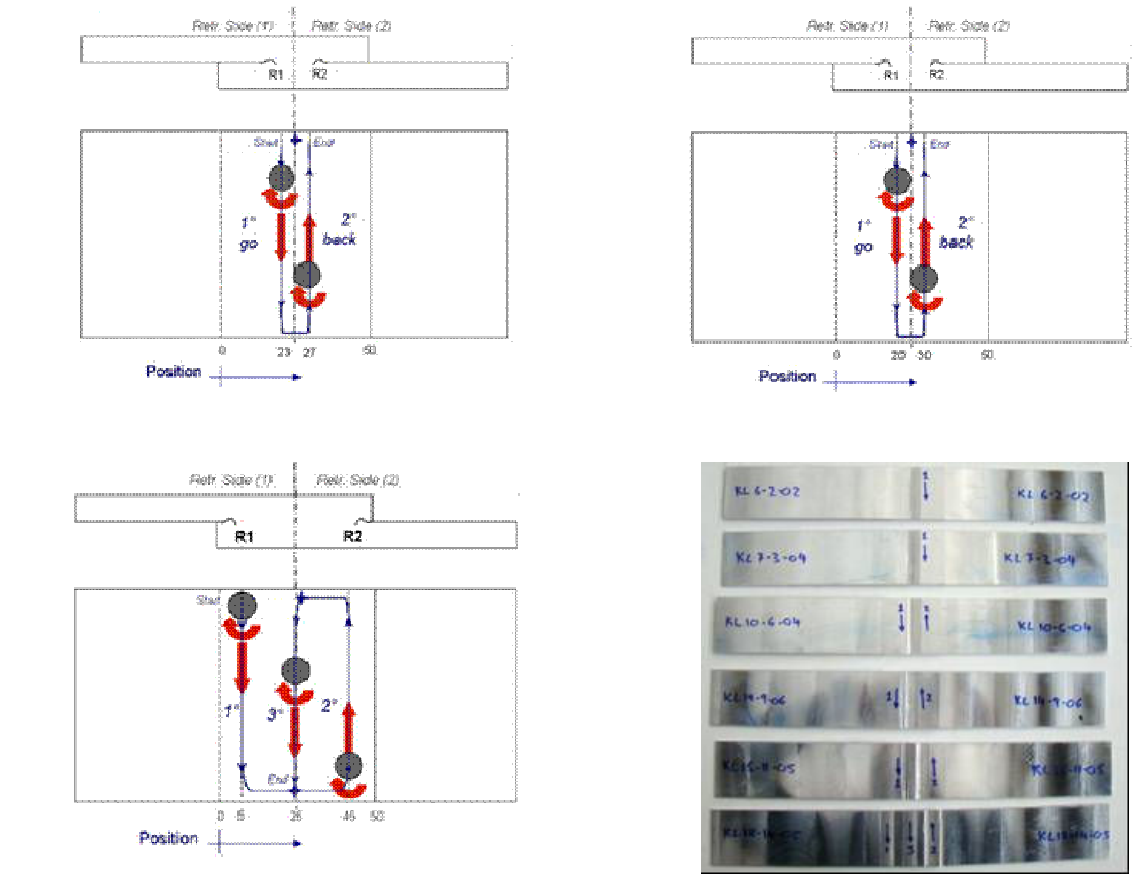

Figure 162: Weld types tested in WP4.1 by University of Patras

4.1.2 Tensile test results

The tensile test results are summarized in the table below and indicative stress-displacement curves are presented in the figure below.

Weld Type	Numbering	Tensile strength [MPa]
A	KL6-2	188.5
A	KL7-3	226.4
B	KL10-6	149.5
C	KL14-9	256.8
C	KL15-11	303.5
E	KL18-14	300.5

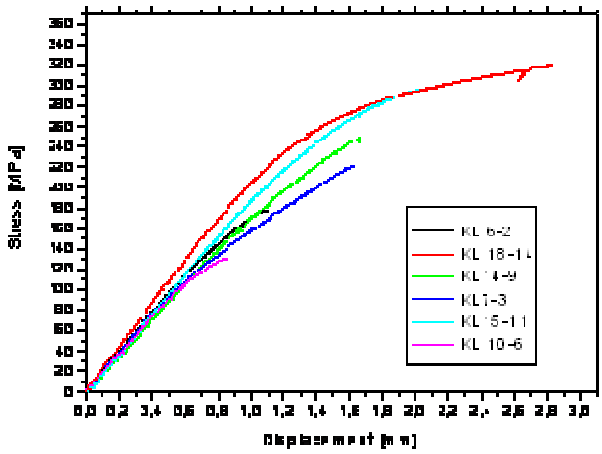

Figure 163: Indicative Stress displacement curves

Note that Stress-displacement (machine displacement) plots are shown instead of the usual stress-strain curves. As the specimens deformed out-of-plane during testing, strain measurements by the use of an extensometer would be misleading. Strain measurements with the use of markings on the specimens gave practically zero strain in the fracture zone.

All tensile specimens failed in the top sheet (top side of the weld) and failure was located on the outmost weld and in the nugget interface. Significant bending was observed on all specimens, even though tabs were used to correctly align the specimens. Only specimens 18-14 did not exhibit any bending, as both sides of the overlapping plates were welded.

4.1.3 Fatigue test results

The fatigue test results are summarized in the plot below.

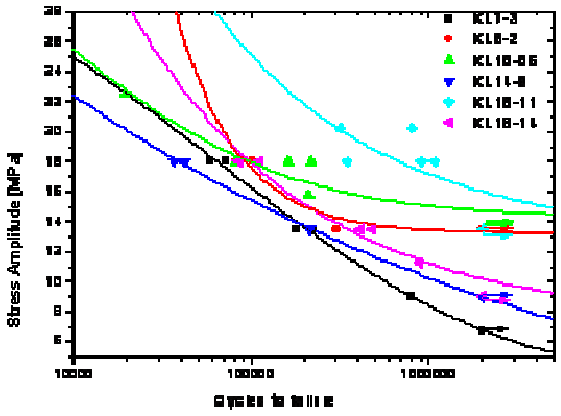

Figure 164: Comparative S-N curves

All the above plots have been fitted by a non-linear analysis (Weibull 4 point function), which is defined as: $S = P_1 + \frac{P_2 - P_1}{\exp\left(\frac{\log N_f}{P_3}\right)^{P_4}}$

The coefficients derived by the non-linear analysis of the fatigue strength data are summarized in the table below.

Test series	P_1	P_2	P_3	P_4
KL 6-2	13.21158	7658165.71	0.35	1
KL7-3	3.57	33.82	5.17	4.10
KL 10-6	14.41055	50.32	3.79	3.04
KL14-9	-3.8667	86	3.25	1.008
KL15-11	12.81	2147.93	0.97	1
KL18-14	7.246	1439.62	1.03	1

Discussion

All fatigue specimens failed in the top sheet (top side of the weld) and failure was located on the outmost weld and in the nugget interface. Exception was specimen type KL 18-14 which failed on the bottom sheet and on the interface with the top sheet.

4.2 Task 4.2 In Service (Airbus Germany)

In Task 4.2 have been produced specimens for testing fatigue performances of in service riveted repairs of fuselage shells containing FSW joints.

The background is that during service of the aircraft damages may occur to fuselage panels due to accidental cause (e.g. impact, see Figure 165 below) or by fatigue crack nucleation. Whatever the reason standard in-service repair approach consist of installing a riveted repair on the damaged area. An example is shown in Figure 166: the repair consist of an aluminum patch installed in the damage area; to achieve the required fatigue life requirements it is usually necessary to use 3 rows of fasteners.

Figure 165: Example of in-service damage of a fuselage due to impact with ground equipment

Figure 166: Example of repair of a fuselage panel with a riveted path. View from inside showing circumferential and horizontal stiffeners

In a fuselage panel incorporating FSW joints it is necessary to assume that defect (scratches, dents, etc.) or damages (impact damages, natural fatigue cracks) will occur in the weld or close to the weld. In developing a new aircraft design to meet airline repairability requirements, consideration of the type of damage that operator experience in the early design stage might results in an aircraft that has better dispatch reliability. The standard repair approach need to install riveted patches and there will be cases where rivets needs to be installed in the weld or close to it.

Specimens representative of the repair approach have been produced with the weld located in correspondence with the fasteners having the highest load transfer. Moreover, the fasteners are in the weakest part of the welded joint: which is typically the weld TMAZ, retreating side.

Purpose of the investigation is to quantify the fatigue life of such repair and to prove the feasibility of a standard repair approach on FSW panels. Would be a concern for airlines if the repair of a welded panel would need special technical solutions leading to a greater time to repair or higher costs.

The investigation was performed on 2198 alloy welded in the T8 conditions and without post weld treatments. This material is a good candidate for the skin of future metallic fuselages of civil transport aircrafts.

The test matrix is given in Table 24 specimen's geometry was single shear with 3 rows of rivets in two parallel lines. Figure 167 shows the location of fasteners (pitch and edge margins) with reference to the 3rd series of coupons.

As reference were produced similar coupons without any weld.

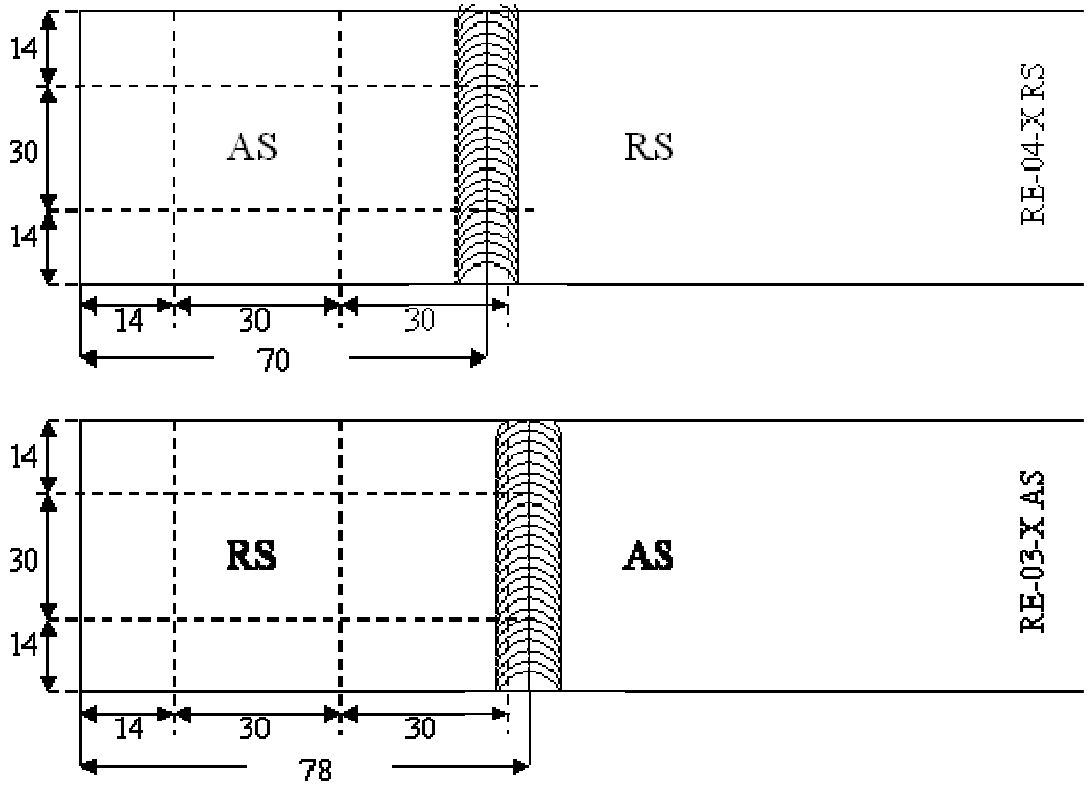

Figure 167: Rivets distribution

Notation		Description	Number of specimens
Baseline		no FSW Joint	6
I.	N RE-01	Rivets in Nugget (FSW joint only in the external plate)	5
II.	RE-02	Rivets in TMAZ (FSW joint only in the external plate)	5
III.	RE-03-1…9 AS + RE-04-1…9 RS	Rivets in TMAZ (2 FSW Joints, 1 on each sheet) AS = Advancing Side at outer end, rivets in retreating side RS = Retreating Side at outer end, rivets in advancing side	9

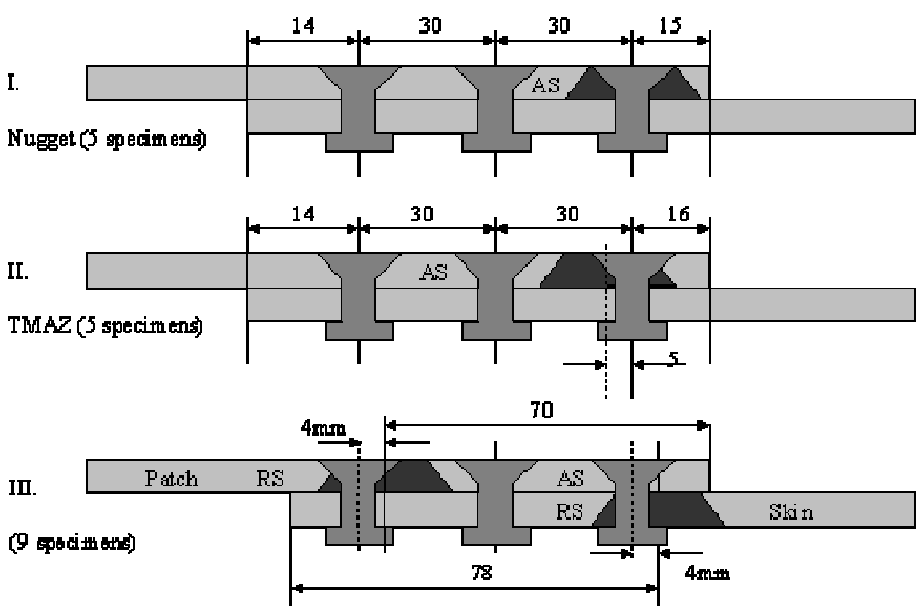

N RE-01

RE-02

RE-03-1…9 AS
(countersunk)
+
RE-04-1…9 RS

Table 24: Test Matrix and sketch of the specimen geometry

Specimens manufacturing (welding and riveting) was performed at Airbus Germany (Bremen site). The parts were surface treated with TSA (Tartaric-Sulfuric-Anodization); washprimer and sealant (Naftoseal MC650) was applied before riveting.

Countersunk aluminum rivets were according to EN6080 (100° normal flush head): EN 6080, diameter 5,56mm.

Specimens in the Ist and 2nd series of Table 24 had the weld in correspondence of the head of the 3rd row of rivets: the less loaded location as shown in Figure 168. This configuration assumes a riveted repair concept performed installing the fatigue critical fasteners (1st row) in base material and the less loaded fasteners in or close to the weld line.

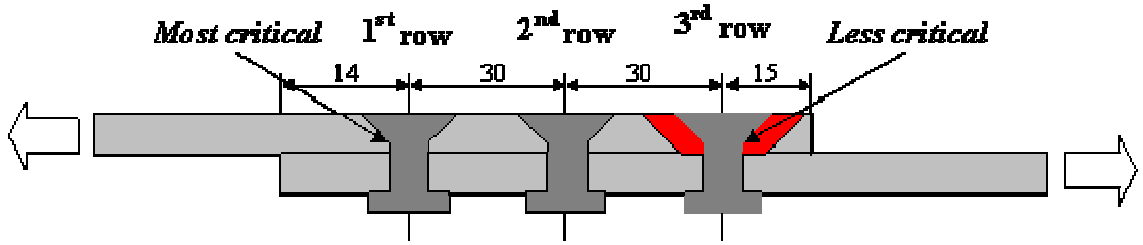

Figure 168: Repair with friction stir weld in the less critical location

The most severe repair configuration was tested with the IIIrd series of fasteners, see Figure 169. Two friction stir welds were introduced in correspondence of the countersunk head of the 1st row of rivets, as well as in correspondence of the tail of the 3rd row of rivets: both positions represent the most critical fatigue locations of the joint due to the highest stress. To be conservative the rivet were centred in the TMAZ of the weld, on the retreating side.

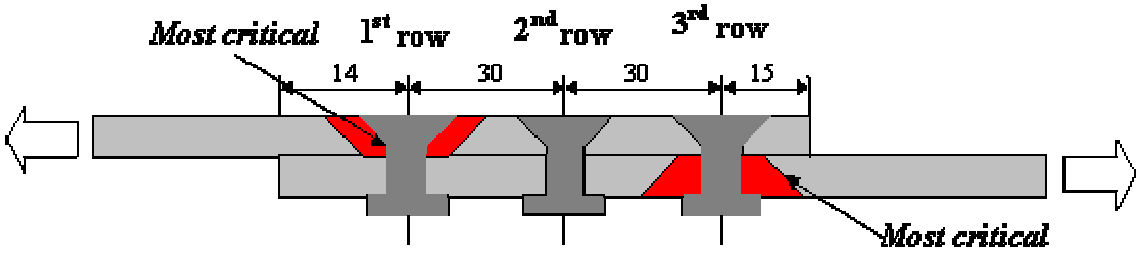

Figure 169: Repair with friction stir welds in the most critical locations

Specimens have been delivered to LTSM for fatigue life characterization. The fatigue test performed under a load ratio R = 0.1 are shown in Figure 170.

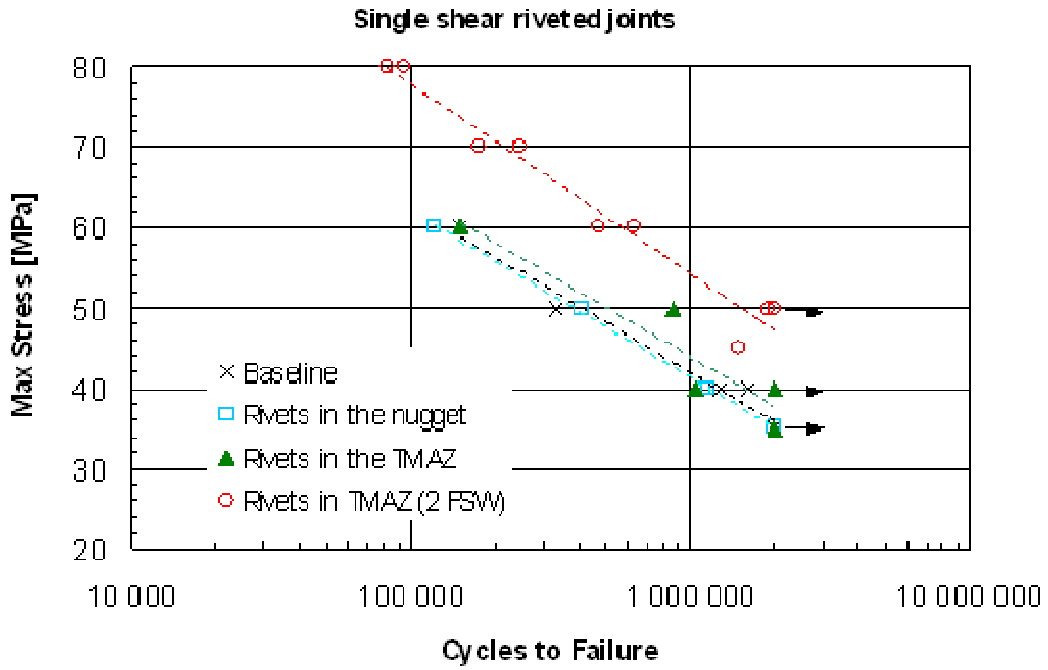

Figure 170: Fatigue test results on the riveted coupons performed at LTSM

Conclusions:

On all specimens, fracture took place in the first rows of rivets, on the countersunk side;

The presence of a FSW Nugget in the 3rd row does not change the fatigue failure location. No difference exists in fatigue life between the rivets of the 3rd row installed in the TMAZ and in the centre of the Nugget;

Very limited scatter between the reference and the specimen with the FSW in the 3rd row;

The presence of a FSW Nugget in the 1st row (critical row) has improved the fatigue life. No change of failure location took place.

4.3 Task 4.2 In service repair (Piaggio Aero)

Piaggio and Eads-Germany were involved in the repair of cracks present inside Pax door of A/C "P 180" tested mock-up .

Several short cracks were found after N = 33000 fatigue cycles on the web frame of door, close the pin holes.

- Door was removed from P180 and was shipped to EADS.

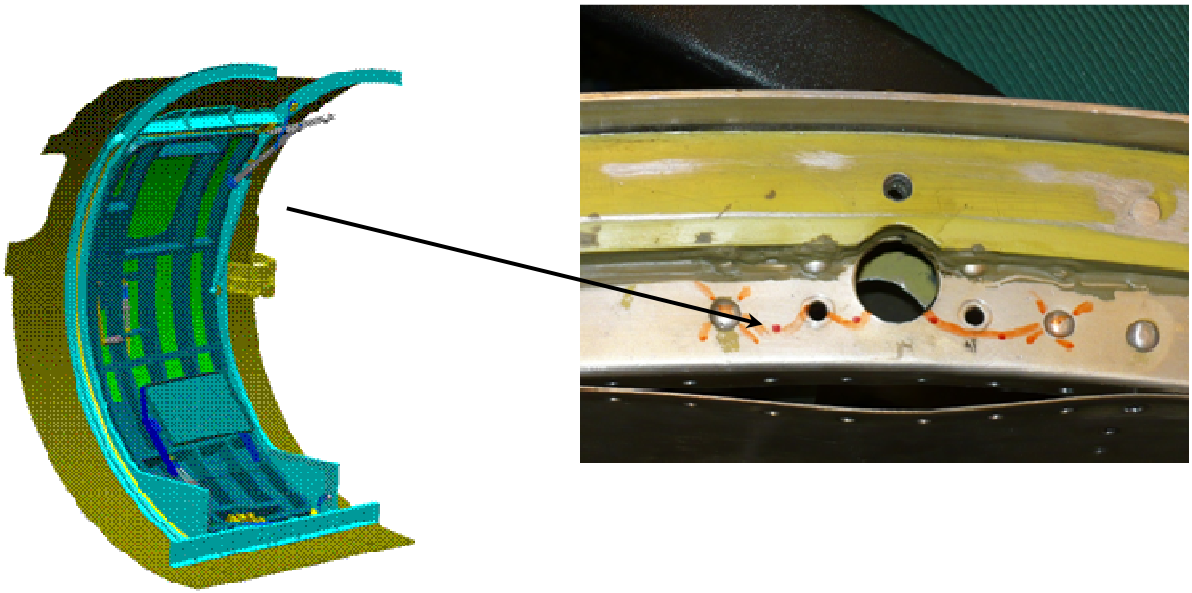

Figure 171: An economical and rapid repair in service requires the Pax Door isn't disassembled so Pai and Eads-G decided to use Bobbin Tool

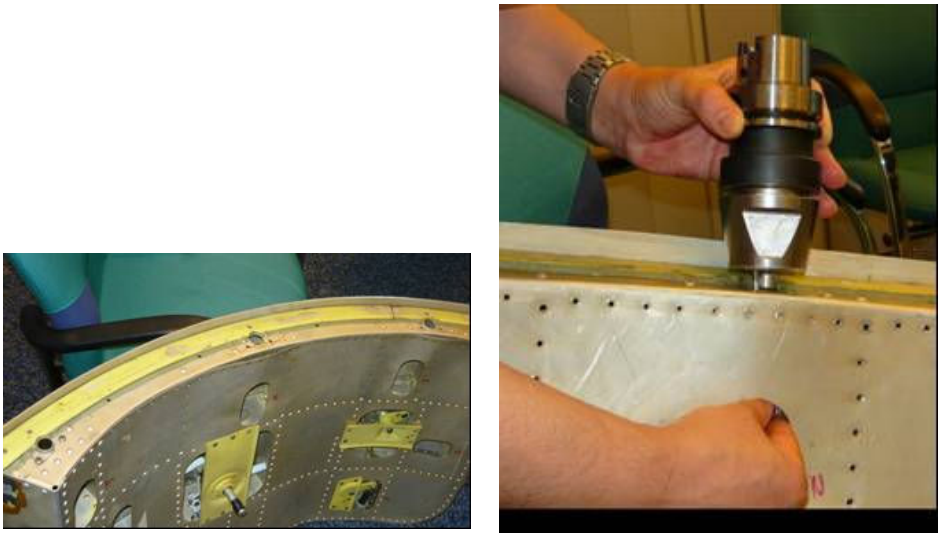

Figure 172: After repair the Pax Door repaired zone should be checked with a non destructive inspection (Liquid penetrant) and reinstalled

4.4 Task 4.2 In service repair (University of Patras)

Fatigue testing of riveted Joints

During the reporting period, 4 configurations of riveted specimens were tested in order to assess and compare their fatigue behaviour. Six to eight fatigue tests for each configuration were performed. Tests were performed at room temperature with a frequency of 30Hz. See Table 24: Test Matrix and sketch of the specimen geometry.

Test results

The fatigue test results are summarized in the figure below.

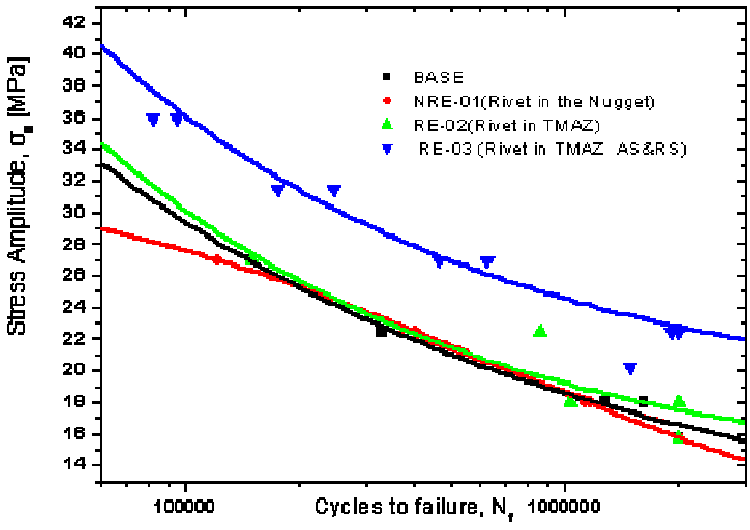

Figure 173: Fatigue Test Results

Discussion

All the above plots have been fitted by a non-linear analysis (Weibull 4 point function), which is defined as: $S = P_1 + \frac{P_2 - P_1}{\exp\left(\frac{\log N_f}{P_3}\right)^{P_4}}$

The coefficients derived by the non-linear analysis of the fatigue strength data are summarized in the table below.

Coefficient	Base	NRE-01	RE-02	RE-03
P_1	17.62269	10.32513	12.54269	17.62269
P_2	1429.80585	33.1989	2393.0666	1429.80585
P_3	1.34455	5.98496	1.0051	1.34455
P_4	1.11687	7.0652	0.99143	1.11687

Main findings

- On all specimens, fracture occurred on the first row of rivets on the countersunk side.
- All riveted specimens, irrespective of the welding configuration failed at the first row of rivets (leftmost as shown in the sketches). The presence of a FSW nugget in the 3rd row does not change the fatigue failure location. No difference exists in fatigue life between the rivets of the 3rd row installed in the TMAZ and in the centre of the Nugget;
- As failure occurred on the same site for all specimens, for the base material as well as the two configurations where the weld was not in the failure site, the fatigue behaviour is practically identical.

The presence of a FSW Nugget in the 1st row (critical row) has improved the fatigue life. No change of failure location took place. However, as the specimens were produced in two different batches, possible modifications to the surface treatment could also have a small effect on the observed differences. Therefore, any conclusions regarding the effect on the fatigue life should be making qualitative and not quantitative.

4.5 Task 4.2 In service repair (Airbus UK)

Visit to GKSS for Bobbin tool knowledge day.

Production of engineering drawings for bobbin tool jig and bobbin tool.

Manufacture of bobbin tool jig and bobbin tool.

Weld preparation of 2024 material.

Development of welding parameters for 2024 T3 material.

Provided information about portable FSW machine development and performance to Fatronik.

Second batch of bobbin tool development trials completed.

Drawings for new bobbin tool produced (shoulder changes for improved surface finish).

Servicing of portable FSW machine and prepare modification to bobbin tool.

Produce drawing for portable machine bobbin tool and machine modification

3rd set of Bobbin tools weld completed.

Preparation and skin replacement on dummy wing-box for portable machine trials.

Welding trials carried out using portable machine on a dummy wing-box skin.

Figure 174 below show a typical bobbin tool welded produced on a dummy wing-box.

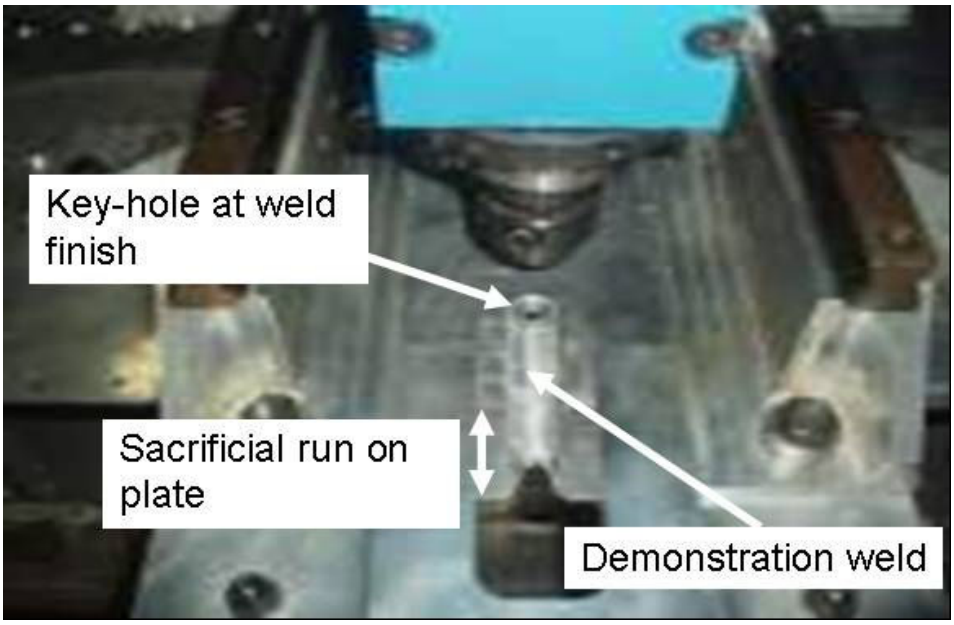

Figure 174: Repair weld over an in-service crack using a bobbin tool

4.6 Task 4.3 FSW as a Repair Tool (BAE)

Repair applications on current land vehicles are potentially a more immediate application of FSW when compared to primary vehicle fabrication. A total three repair scenarios were identified for investigation.

Non-Penetrating Surface Damage

Spalling or gouging may result from a variety of mechanisms including impact, collision and environmental effects such as corrosion and weathering. For the purpose of this work, the damage is considered to be non-penetrating with little or no secondary deformation of the structure. Potentially, this type of repair could be undertaken at a field base.

Planar Delamination in Thick-Section Plate

Delamination in thick-section plates have been observed in vehicles following a period of in-service operation. This mode of failure has been attributed to variation in through-thickness mechanical

properties that allow planar cracks initiating in the end grain to propagate through the plate. This type of failure is generally identified during refits and consequently repairs would be expected to be conducted at a home base.

Cracks

Cracks can occur within the weld or parent metal due to a combination of residual weld stresses, presence of manufacturing defects and in-service loading. Depending on the severity of the crack, repair could be instigated at a field base.

In addition to the specific repair investigation, an evaluation of unsupported FSW has also been conducted. For full thickness welds FSW requires that the underside of the weld is mechanically supported to react the substantial processing loads generated during welding. For an external repair this would require complete access to the inside of the vehicle and specialised tooling, which make it impractical for field base repairs. For repair of non-penetrating surface damage in particular, full thickness welds would not be necessary and the purpose of this work was to evaluate the extent to which the vehicle structure would be self-supporting – and thus amenable to a field base repair solution.

4.6.1 Non-Penetrating Surface Damage Repair

The concept for repairing non-penetrating surface damage is to machine out the damage region, creating a pocket in the parent plate. This is then filled by a repair insert of the same material and dimensions then welded around its edge. Depending on the size of the damaged area, additional strengthening welds could be added as required.

Three variations of this type of repair were investigated, which are individually addressed in the following.

4.6.1.1 Insert Repair with Singular Edge Welds

For this repair case, single pockets were machined to various a depths simulating removal of surface damage of different severity. Inserts, made from the same alloy as the parent plate, were matched to the geometry of the machine out and circumferentially welded in position.

Using the same tool for each repair depth produced similar welds with a constant depth that allowed the assessment of three weld situations; an over-penetrating weld repair, a full-penetration weld repair and an under-penetrating weld repair as illustrated in Figure 175.

To evaluate the repairs, three sections were extracted for each weld case and subjected to a 3-point bend test. Figure 176 plots the averaged load-displacement curves obtained for the three repair cases; the parent material is also included for comparison. It can be seen difference in terms of ultimate failure load for the three repair cases is marginal, with all failing around 50kN. This is approximately 70% of the parent material failure load. It is notable the displacement at failure for the thickest insert repair was approximately 50% of that achieved for both the 6 and 10mm repairs.

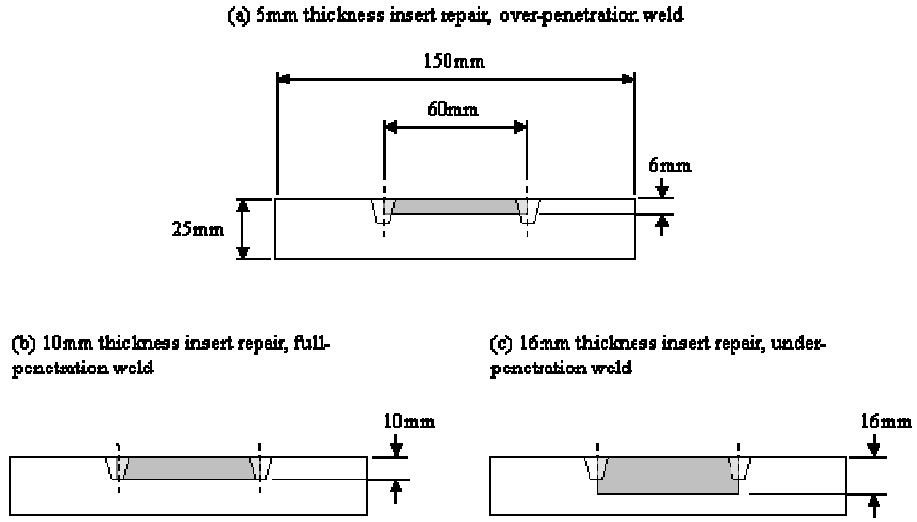

Figure 175: Cross-sections of insert repair cases

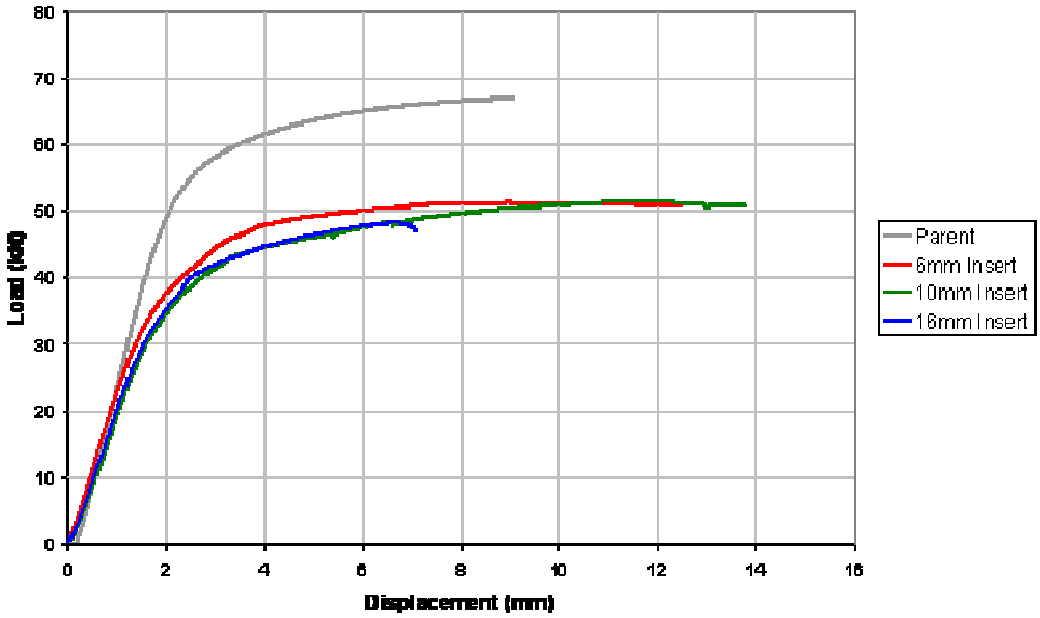

Figure 176: Load displacement behaviour of insert repair with a singular edge weld

4.6.1.2 Insert Repair with Strengthening Welds

In the second stage of the surface damage repair investigation additional welds were added to the edge welds with the intention of improving the strength of the repair. It is envisioned this would be used for larger area repairs and correspondingly the machined pocket width was increased.

Figure 177 shows the dimensions and weld positions for the samples produced. Three specimens were cut from each repair and subjected to a 3-point bend test.

Figure 178 shows the load-displacement curved obtained for the 3 weld insert repairs (results from individual samples within a specimen set are identified as A, B and C). Similar trends were observed for the 2 and 5 weld insert repairs and in each instance the failure loads were all similar (around 20kN) although an increase in the stability of the failure mechanism (less susceptibility to buckling) was observed with increasing number of welds. This was exemplified by the consistency of the load-displacements behaviour observed for the 5-weld repair. All three and five weld repairs failed in tension in the centre of the specimen on the underside.

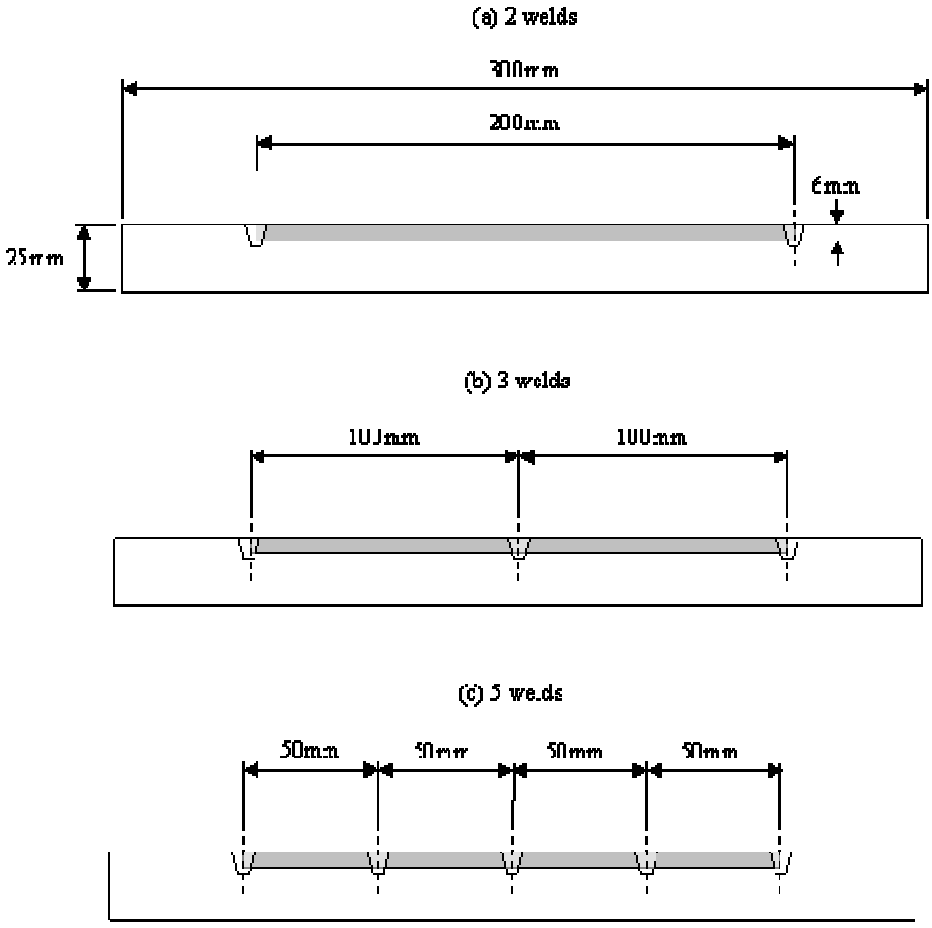

Figure 177: Cross-sections of strengthened weld repairs

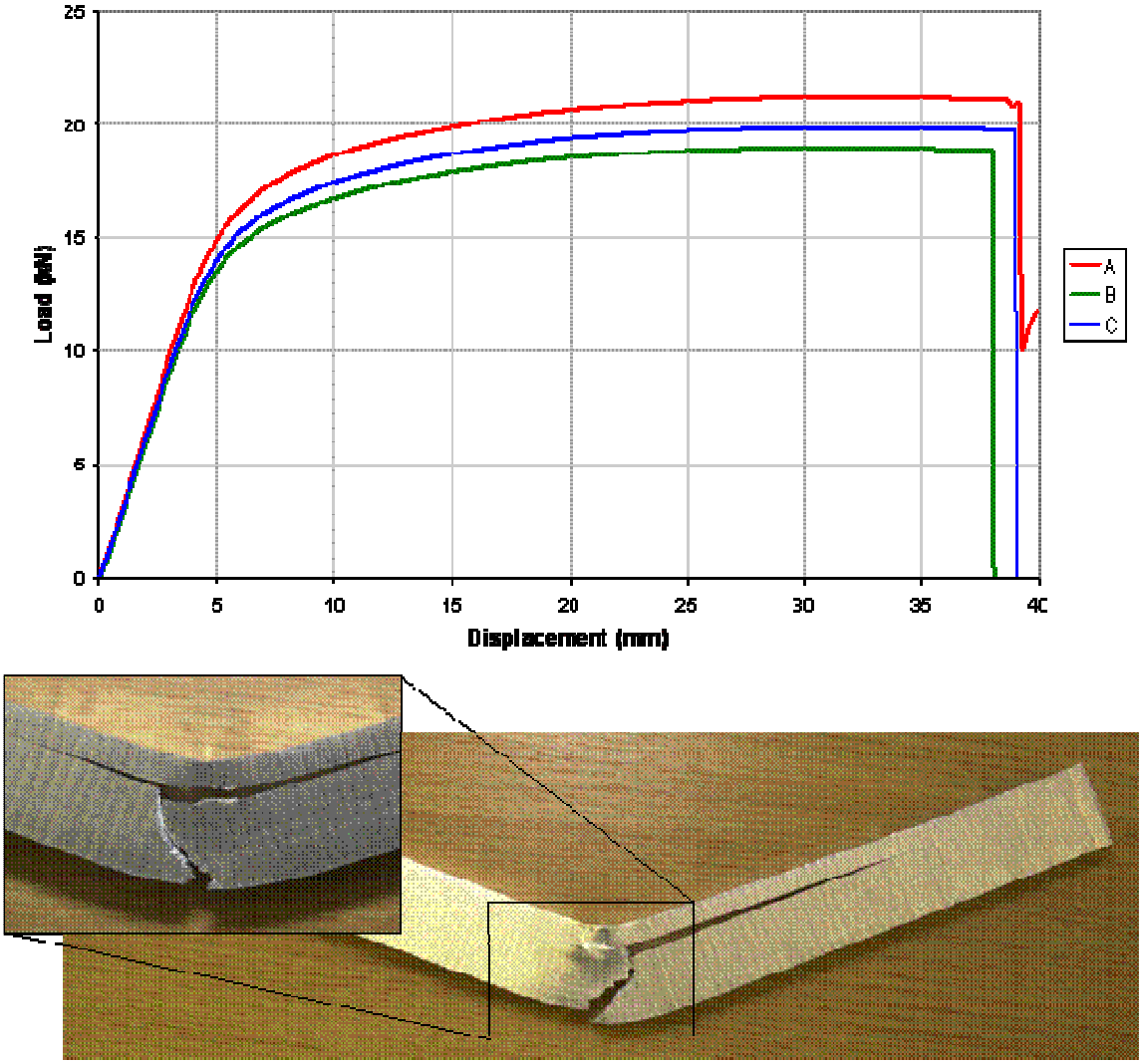

Figure 178: Load displacement behaviour of insert repair with a three welds

4.6.1.3 Laminated Insert Repair

The final topic investigated under surface damage repair was laminated inserts. This is seen as a potential solution for dealing with deeper damage and a means of overcoming the half-thickness rule of thumb limitation for self-supporting welds. Unsupported FSW is discussed later in this workpackage report, but in essence welds greater than half the material thickness require additional tooling to support the rear of the weld and as such are considered impractical for a field base repair. The use of laminations could overcome this problem by effectively changing the ratio between the weld depth and material thickness. Figure 179 shows two laminated insert repair cases; in the first, singular edge welds are used for both plates, whilst the second case makes use of additional strengthening welds. For either case, the inner insert was welded in position first, followed by the outer insert.

For the repair case with the singular edge welds, the load displacement behaviour is shown in Figure 180. This repair was observed to lose some degree of strength after approximately 30mm of displacement likely due to yielding in one of the laminate layers and subsequently failed just beyond 40mm of displacement. The peak loads were observed to be slightly reduced compared to the single insert repairs but this was expected due to the depth of the repair and subsequent reduced thickness of the remaining parent material. Failure was similar to the two-weld, single insert repair with bucking of the insert and failure at one of the outer insert edge welds.

The load displacement plot for the laminate repair with strengthening welds is shown in Figure 181. Under loading, buckling of the outer insert was observed, but was inhibited by the additional welds until these welds failed (identifiable in Figure 181 by the dip in load). The maximum load achieved and displacement at failure were however similar to the singular edge welded case.

In summary, non-penetrating repair of surface damage can be achieved by machining out the damaged section and inserting a repair plate which is welded in position. It has been shown that such repairs can achieve up to 70% of parent material strength and weld depths equal or greater than the insert thickness allow greater deformation before ultimate failure. For larger area repair, additional welds can be added to stabilise the failure mechanism and avoid buckling the insert, although there appears to be no increase in the strength of the repair. Repairs greater than half the material thickness can be achieved through the use of laminated repairs.

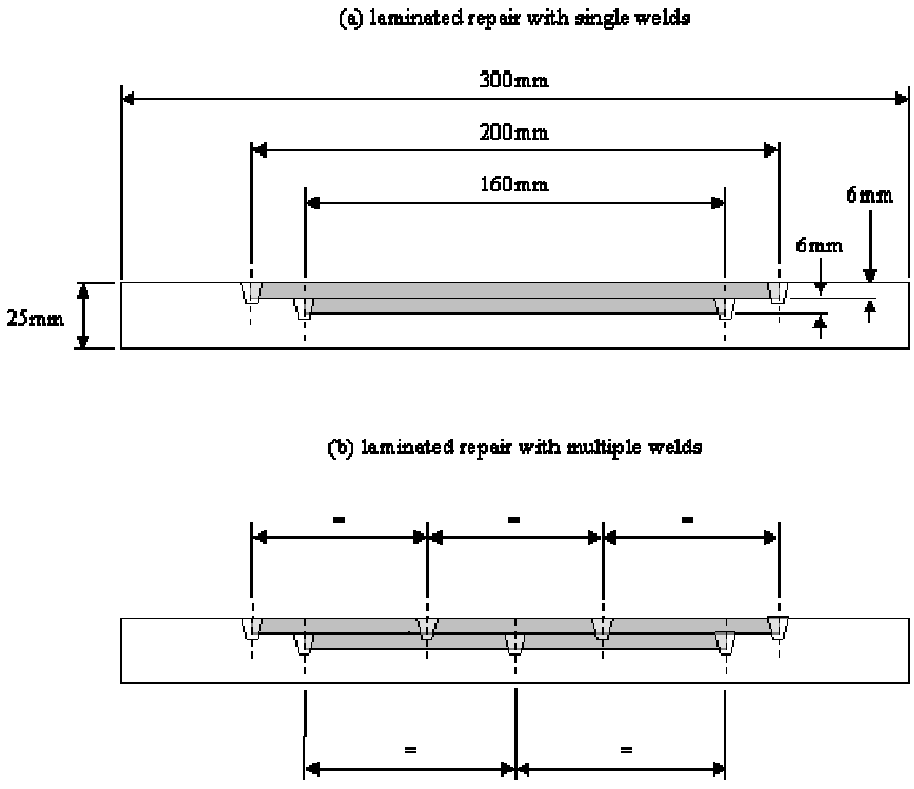

Figure 179: Laminated insert repair

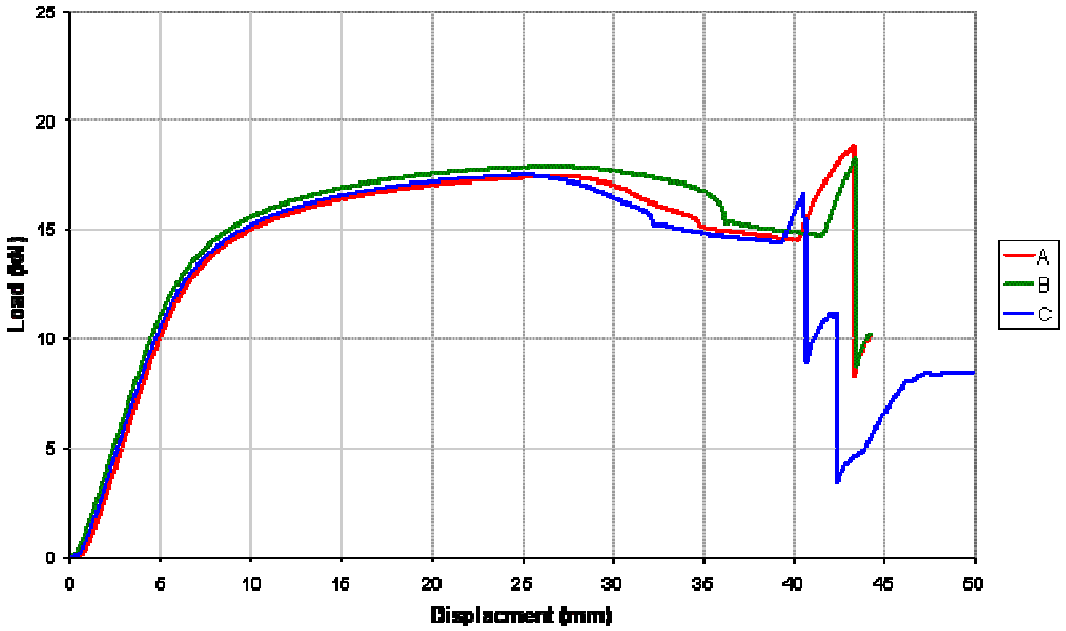

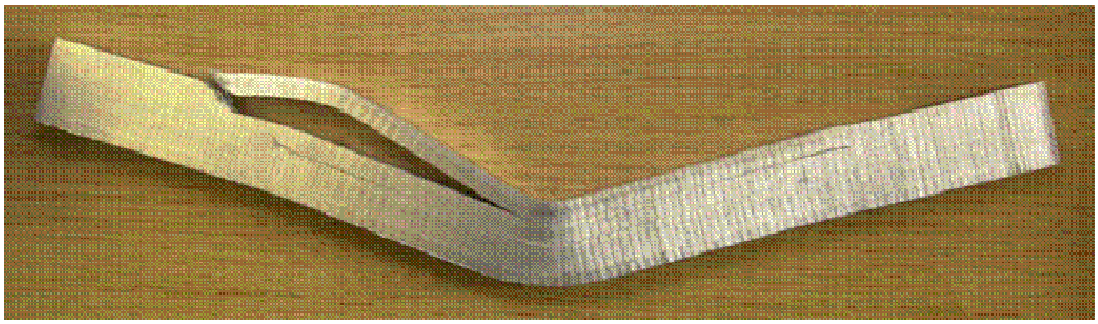

Figure 180: Load displacement behaviour of laminate insert repair

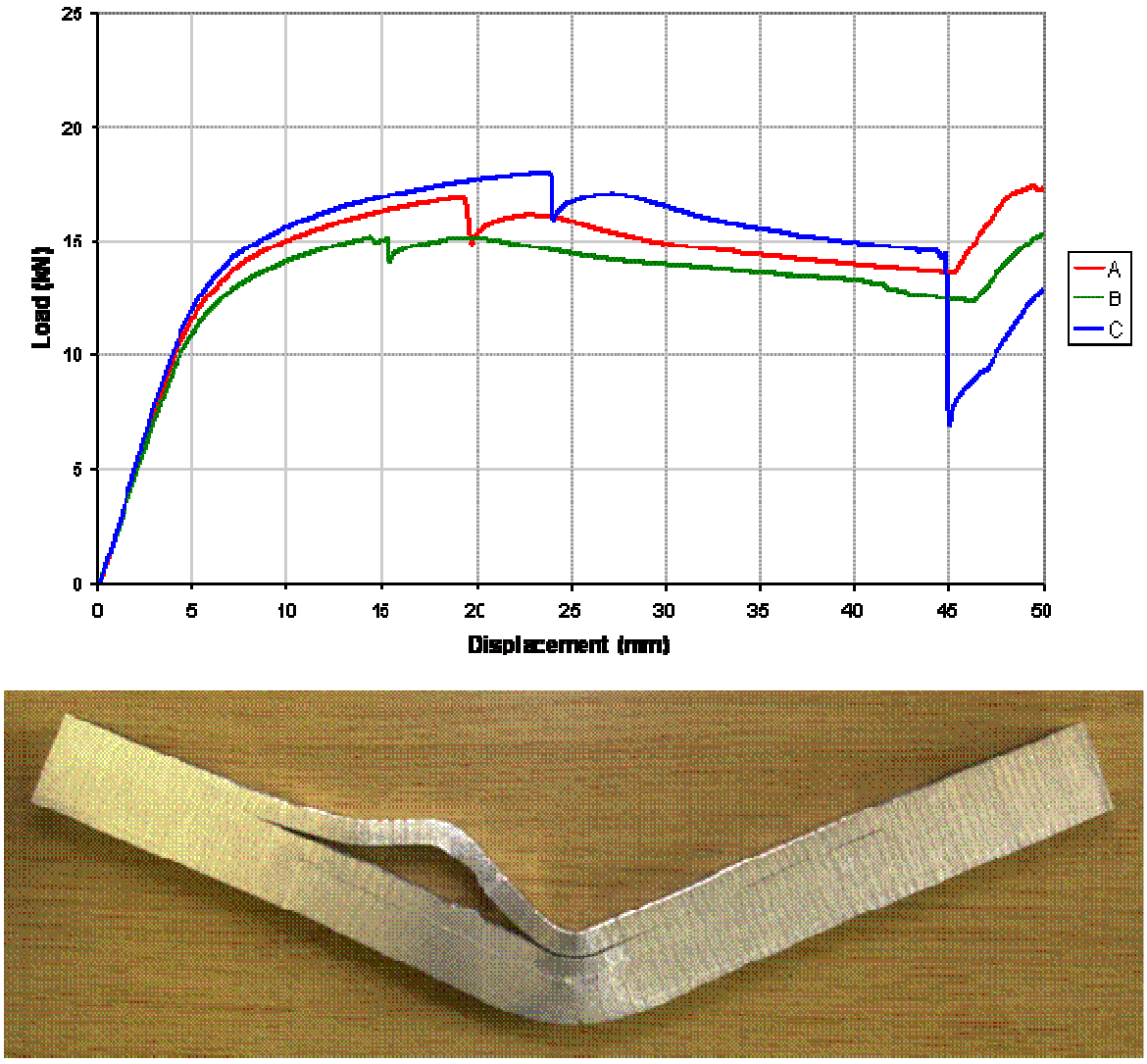

Figure 181: Load displacement behaviour of laminate insert repair with strengthening welds

4.6.2 Planar Delamination in Thick Section Plate Repair

Planar delamination in thick-section plates was simulated by using wire erosion to produce a 100µm slit in parent material with the dimensions shown in Figure 182. Samples were prepared with combinations of the three weld positions identified in Figure 182 as W1, W2 and W3. Weld W1 seals the end grain, closing the initiation site for the defect; weld W3 closes the toe of the defect and prevents the delamination continuing and weld W2 would be added depending on the extent of the damage to tie the material together.

To conduct the repair welds, samples were mounted in tooling that was rigid enough to prevent the slit from being forced open during application of the W1 weld. Run-on and run-off blocks were also added to allow welds to be produced across the full width of the sample.

Welds were produced with combinations of W1, W2 and W3 welds to assess relative performance when the joint was subjected to a pull test.

4.6.2.1 Repairs using Welds W1 & W3

During the pull test, the specimens failed catastrophically within the Thermal Mechanically Affected Zone (TMAZ) of weld W1. Upon reaching the maximum load, the terminating weld W3 also began to fail in the TMAZ with a crack propagating through the plate towards the surface. This result demonstrates planar delamination can be arrested by the termination weld.

4.6.2.2 Repairs using Welds W1, W2 & W3

The addition of the middle weld W2 improved the performance of the repair considerably. During the tests there was no initial failure at W1 as seen in the previous tests, although cracks were beginning to form here and at weld W3. However, before catastrophic failure in the sample occurred, the steel fixture began to fail and the test was halted at a load of 57kN.

In summary, a potential repair solution has been demonstrated on simulated planar delamination in test samples. The delamination can be arrested by using a terminating weld (W3) with less concentration of stresses than that that would result from using multiple bolts (the only other practical method for pinning the delamination together). Significant strengthening can be achieved by using supplemental pinning welds such as weld W2.

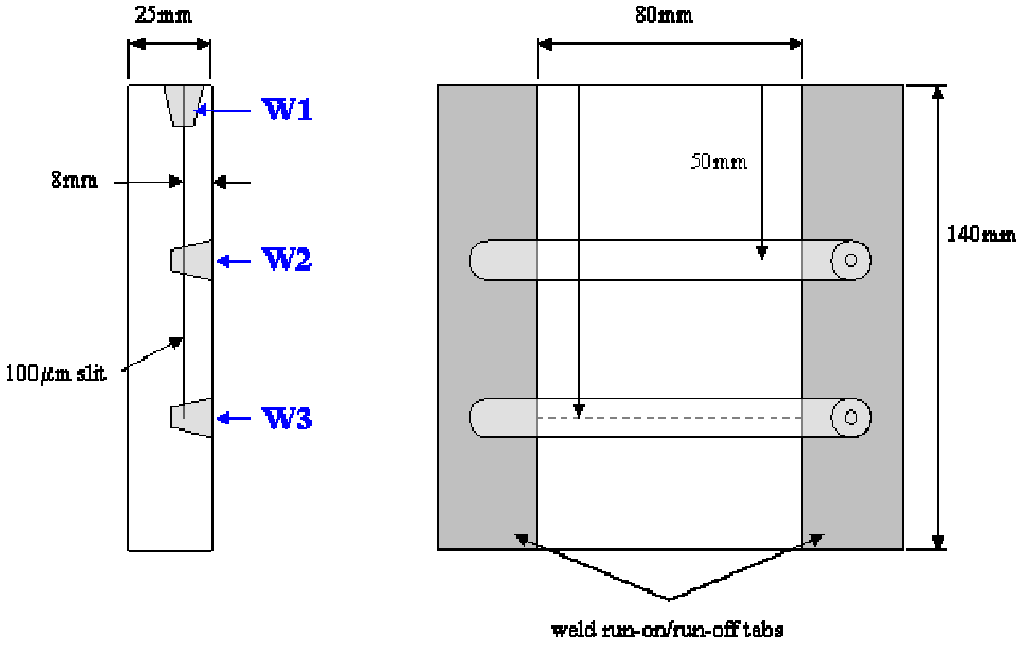

Figure 182: Geometry used to simulate planar delamination

4.6.3 Weld Crack Repair

Two weld crack scenarios were considered. In the first, the crack width would be sufficiently narrow such that a repair could be realised with a simple over-weld. The most important aspect of this was determining the maximum crack width that could be over-welded while remaining defect-free. The second scenario addressed the situation where the crack width is too large for an over-weld to be an effective repair. The investigated solution was to machine out the crack and replace with a solid insert of the same alloy, then weld. The width of the insert would be narrower than the FSW tool pin diameter and would thus be fully consolidated into the repair weld. This solution would also be effective for repairing cracks contaminated with corrosion products (for example).

4.6.3.1 Weld Crack Repair without Material Insert

To assess the maximum crack width that could be repaired while maintaining the quality of the repair weld, a tapered crack was simulated by using a machined taper. Crucially, the taper was machined to half thickness in 16mm thickness 7056 aluminium alloy in one plate forming a square-edged butt joint. This is illustrated in Figure 183.

The onset of weld defect formation is clearly visible in Figure 184 and was found to occur at a gap width of 1.2mm. This was also confirmed by a subsequent longitudinal section of the weld.

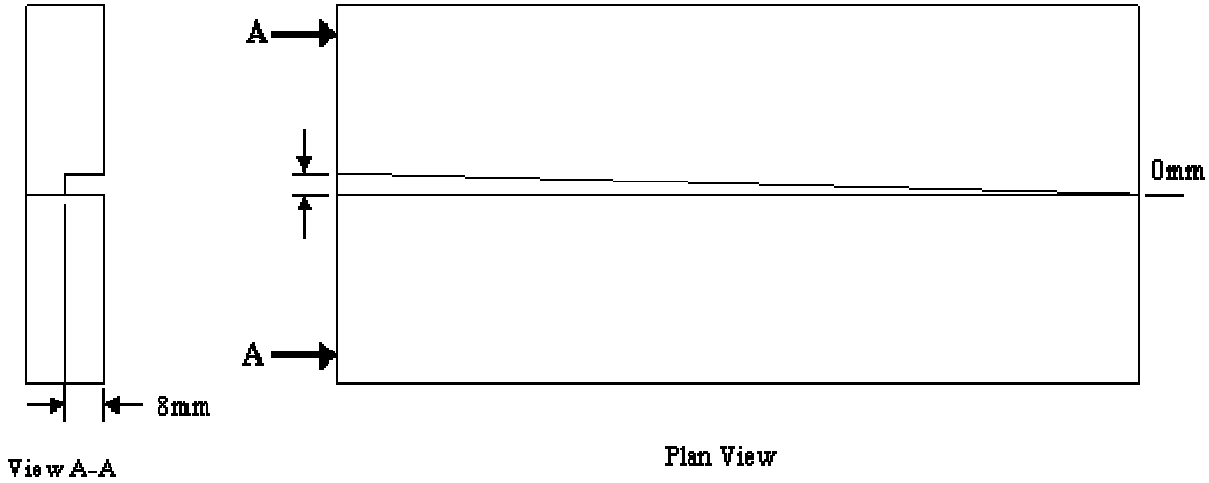

Figure 183: Simulation of tapered crack using partial thickness machined edge

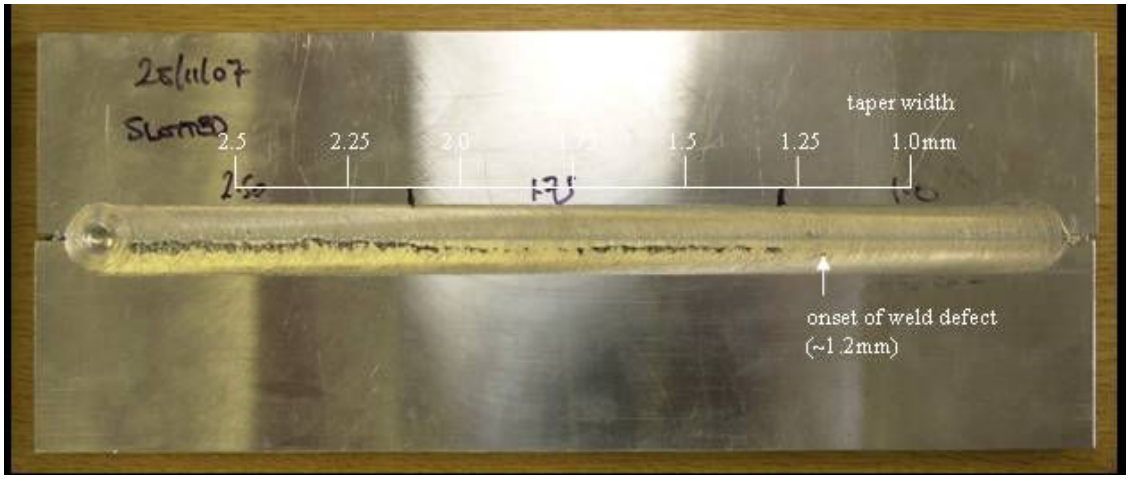

Figure 184: Tapered crack repair indicating onset of weld defect

4.6.3.2 Weld Crack Repair with Material Insert

To simulate crack repair using an insert an existing FSW joint was used where it was assumed a crack existed between the nugget and the Thermal Mechanically Affected Zone (TMAZ). The repair sequence is illustrated in Figure 185. First, a standard milling tool was used to machine out the 'crack' and a matched insert was used to replace the removed material (Figure 185b). Finally, a repair weld was used to consolidate the insert into the joint. Importantly, the cross-section of the insert needs to be smaller than the FSW tool dimensions.

In summary, two crack repair scenarios have been examined and proofs of principle results have been obtained in both cases. Cracks up to 1.2mm in width can be repaired without using an insert provided they are free from debris. For wider cracks, the material can be machined out and an insert used that is then consolidated into the repair weld. In either instance, if the existing weld was a fusion weld then the weld reinforcement would need to be machined back.

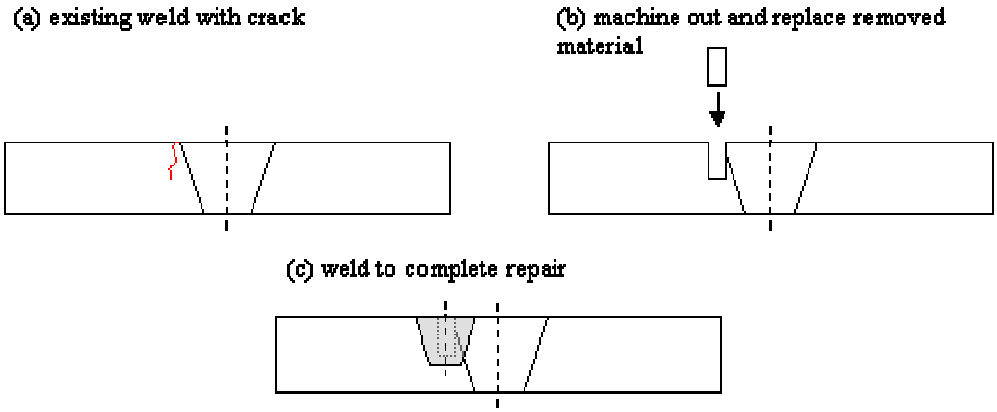

Figure 185: Crack repair sequence with insert

4.6.4 Unsupported Friction Stir Welding

Full thickness welds require the underside of the weld to be mechanically supported to react the substantial processing loads that are generated during welding. For repairs that only require partial penetration welds, such as non-penetrating surface damage the structure itself may provide sufficient support for the repair operation. This is particularly advantageous for enclosed structures such as land vehicles that would otherwise require stripping of internal components and insertion of possibly complex tooling to support the underside of the weld. If this could be avoided then potential field base repair solutions could be envisioned. Thus, the purpose of this investigation was to investigate the extent to which a partial-penetration weld could be self-supporting.

One of the principal factors governing the quality of a weld is the axial tool load, which following the tool plunge phase is largely transferred to the material through the shoulder. If the tool axial load is tool low, insufficient heat and compaction can result in weld defects. Too high a load can lead to excessive heat input and reduced mechanical properties in the resulting weld. The axial load can vary from 10kN for thin section material to 50kN for thick-section, but it is important to note a 0.5kN variation can produce notable changes in the weld quality. For unsupported FSW the absence of rear support makes the influence of the axial tool load very important. If the material is insufficiently stiff the axial tool load and subsequent deflection of the workpiece will be detrimental the welding process.

4.6.4.1 Theory

An appreciation for the reaction of the workpiece under load can be gained by using simple bending theory. Figure 186 plots the resulting maximum bending stress and deflection for a simple plate, which generally indicate both bending stress and deflection increase (in magnitude) with decreasing material thickness. Taking 25mm thickness as an example, the corresponding bending stress is 48kN and the deflection is 65μm. However, whilst the bending stress is an order of magnitude below the material yield stress, it should be noted the model does not take into account the variation in yield strength due to local temperature gradients during welding and would need to included in a more complete analysis. Similarly, Figure 187 plots the minimum bending stress and deflection as a function of the plate length.

4.6.4.2 Experimental Investigation

Unsupported FSW was investigated experimentally in 16mm thickness 7056 aluminium alloy. An initial process parameter investigation was conducted to establish suitable welding conditions. Having established suitable welding conditions, unsupported FSW trials were conducted by suspending the 300x150x16mm weld material along its edges using 6mm square inserts, as illustrated in Figure 188. Bead-on-plate welds were then produced; Table 25 summarises the pin length as a percentage of the plate thickness.

Tool ID	**A**	**B**	**C**	**D**
Pin Length [mm]	9.8	7.8	6.2	3.8
% Plate Depth	60%	50%	40%	25%

Table 25: Pin length as a percentage of the plate thickness

On inspection, the only weld exhibiting permanent plastic deformation on the rear side of the weld was the weld produced using tool A as is shown in Figure 189. No deformation was seen in any of the remaining welds.

In summary, unsupported FSW has been successfully demonstrated. Although, only basic study was conducted it can be concluded repair welds up to approximately 50% of the material thickness may be possible and offers the potential of field repair of land vehicles with not penetrating (surface) damage. An extended investigation is recommended.

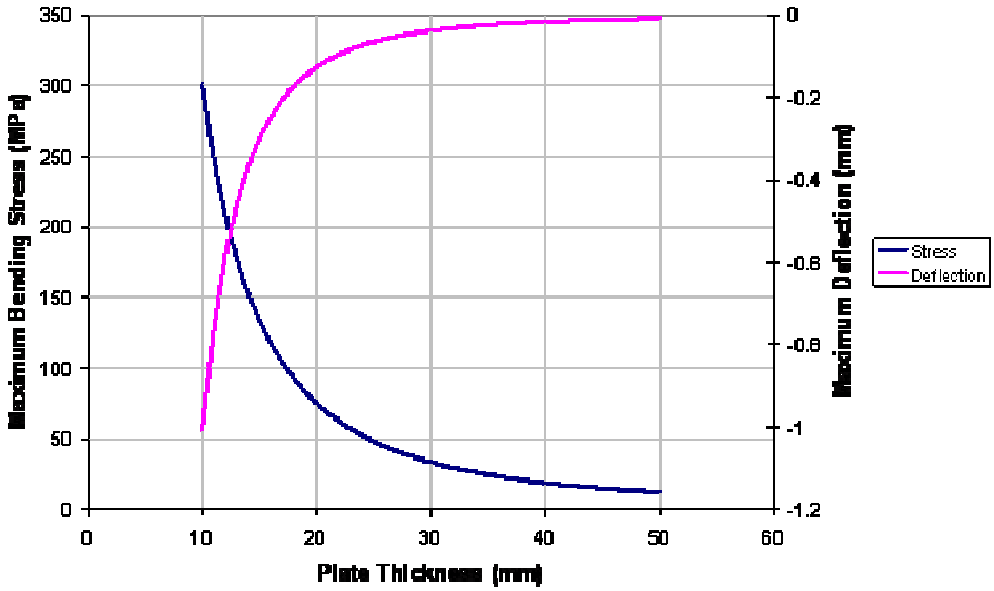

Figure 186: Maximum bending stress and deflection as functions of plate thickness (t)

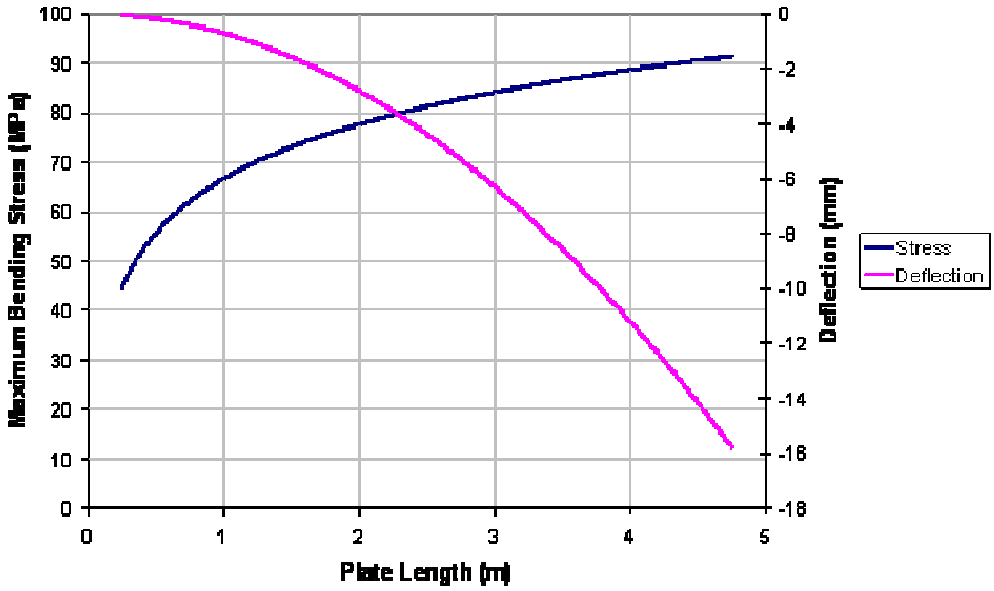

Figure 187: Minimum bending stress and deflection as functions of plate length

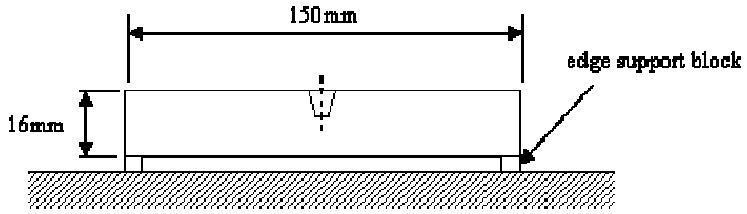

Figure 188: Unsupported FSW showing suspension of material using edge support blocks

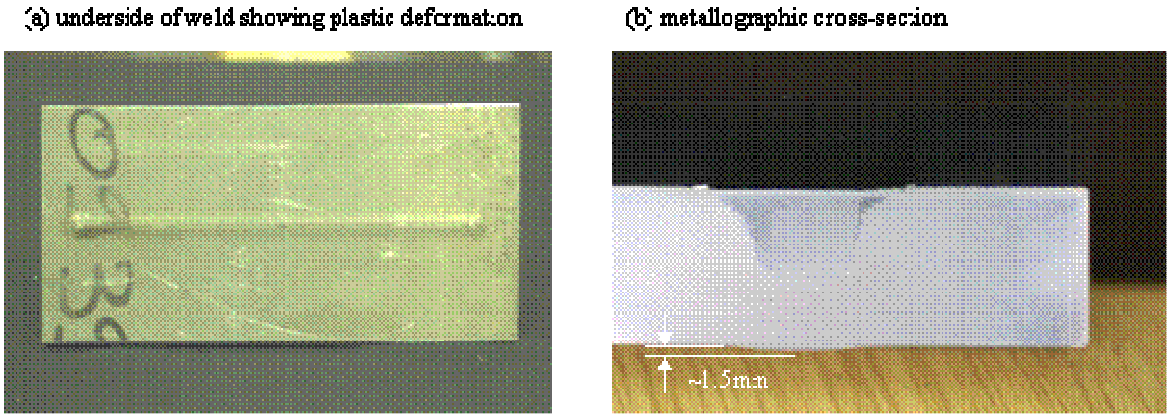

Figure 189: Weld produced using tool A indicating plastic deformation of rear face

4.6.5 Conclusions

- Non-penetrating repair of surface damage has been demonstrated by machining out the damaged section and inserting a repair plate that is welding in position.
- Surface damage repairs can achieve up to 70% of parent material strength and weld depths equal or greater to the insert thickness allow greater deformation before ultimate failure.
- For large area surface damage, additional welds can be added to stabilise the failure mechanism and avoid the insert buckling; no additional increase in the strength or the repair was observed.
- Deep surface damage (greater than 50% material thickness) can be achieved by using laminated repairs.
- Planar delamination repair has been demonstrated using FSW by using a combination of welds to close the end grain, pin and terminate the crack growth.
- FSW is the only welding process that is capable of pinning and terminating delaminated material.
- The strength of planar delamination repairs is significantly improved by using pinning welds to 'tie' the laminations together.
- Weld cracks up to 1.2mm in width can be repaired by simply over-welding the existing weld.
- For weld cracks greater than 1.2mm, or where the crack is contaminated by corrosion products for example, the crack can be machined out and an insert added.
- Unsupported FSW welding has been shown to be possible with repair welds up to 50% of the material thickness, offering the potential of field repair of land vehicles with non-penetrating (surface) damage.

4.7 Task 4.3 FSW as a repair tool (EADS Germany)

Repair welds will be performed by using DeltaN tool concept.

Object of interest is a PAX door and this door shows some cracks after a specific time in service, image Figure 190 and Figure 191 and YY.

Figure 190: View of the location of cracking next to rivet holes

Figure 191: Detailed view of a crack next to a rivet hole

Motivation for a repair by welding scenario is to avoid the manufacturing of spare parts but to use the existing components.

Caused by the geometrical restrictions the DeltaN FSW tool process cannot be applied. The necessary backing part must be positioned below the location of welding tool but a fixation of this backing for carrying the tools vertical downwards force is not possible.

This geometrical restriction could theoretically be overcome by using a bobbin tool instead of the DeltaN tool. The bobbin tool is free of vertical loads but shows nevertheless significant lateral loads. This fact causes severe problems for the door repair scenario because also because of the given geometry grippers or clamps cannot be applied near the welding zone.

5 Work Package 5: Combination of FSW with other Production Processes

5.1 Task 5.1 Welding of large prefabricated part (Airbus Germany)

The design of advanced welded joint for pressurized fuselage has been performed in WP2 with the rationale described in D3.1. The 6 concepts developed show that it is possible to combine a FSW joint of the fuselage skin with all the 3 existing assembly techniques for stiffened panels: mechanical fastening, adhesive bonding and laser welding. Moreover, the different design explores the use of FSW as assembly process (joining of large stiffened panel) as well as manufacturing process for creating large unstiffened skins (so called supershell) to be assembled at a later stage with stiffeners.

The proposed design solutions have been manufactured in the form of large test articles (panels 2 meter long with two stiffeners) in order to validate the proposed concepts and to identify any potential manufacturing issue. In addition, the performance of the joints have been assessed by a partner (CU) testing the specimens listed in Figure 204. The specimens have been extracted from the large test articles.

The manufacturing activity of the test articles was started with the definition of statements of works and work packages for the Airbus plant in Nordenham (today Premium Aerotec GmbH). Due to the innovations introduced in the manufacturing approach discussions with manufacturing plants were necessary and feedback from manufacturing was used to improve the design proposals. The manufacturing results are presented.

Large test articles

The detailed design with drivers and rationales is discussed in Deliverable D3.1; a sketch of the 6 different concepts developed is given in Figure 192.

Concept 1: Welded skin joint next to a riveted stringer (assembly process)

Concept 2: Welded skin joint next to bonded stringer (assembly process)

Concept 3: Welded skin joint under a bonded stringer (large skin for supershell)

Concept 4: Welded skin joint next to a welded stringer (assembly process)

Concept 5: Welded skin joint under a riveted stringer (large skin for supershell)

Concept 6: Welded skin joint under a bonded doubler with stringer (large skin for supershell)

Three design solutions are based on the latest state of the art (concepts 1,2 and 4) and 3 of them (concepts 3, 5 and 6) are based on innovative manufacturing concepts.
Four configurations (concepts 1 to 4) are with local skin pad-up, it means that a local increase of the material is introduced in the area of the joint to compensate the detrimental effect of the weld. Since pad-up is a weight penalty and often a cost issue because increase the thickness of the original material two configurations developed are “pad-up free”. The necessary local reinforcing of the weld is achieved bonding or riveting a structural part on top of the weld.

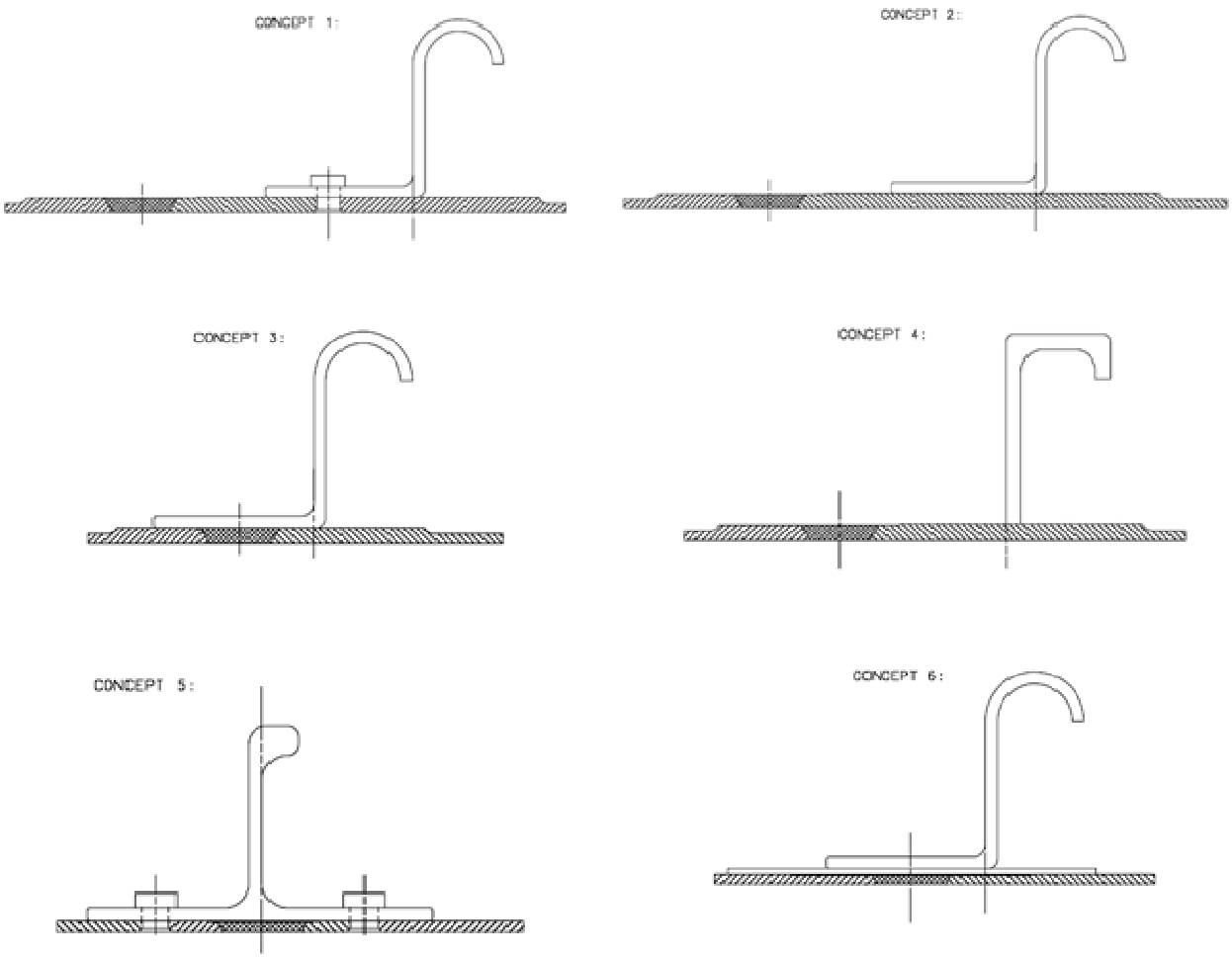

Figure 192: Overview of the 6 different designs for the large test article

Manufacturing innovations are introduced in concepts 3, 5 and 6, in particular related to the creation of a redundant load path from a combination of FSW of the skin and bonding or riveting a second structural member (stringer, doubler) on top of the weld. Innovative is also the surface preparation process necessary for the bonding process on top of the FSW.

The design concept developed cover 2 different manufacturing approaches for the fuselage panels. The concepts 1, 2 and 4 can be applied to the assembly of stiffened shells to create larger panels or even fuselage barrels. The design concepts 3, 5 and 6 require the installation of the stringers (by adhesive bonding or riveting) on top of the weld. These concepts could be implemented in manufacturing with the creation first of a very wide unstiffened skin panel and then installing all the stiffeners to create a super-shell.

The test articles to be manufactured to validate the design have a length of about 2000 mm and a width of about 500 mm; they include the fuselage skin, two stringers each and doublers. The weld is

positioned always in the centre of the specimen. The test articles are flat to reduce manufacturing cost and testing efforts, anyhow the design is applicable to curved shells having diameter of typical civil transport aircrafts.

Manufacturing

The manufacturing of the large test articles took place between the Airbus-Bremen plant (FSW or the original sheets) and the former Airbus-Nordenham plant (shell manufacturing and assembly).

Investigation of deformations

A typical issue of the welding process is the risk of creating deformations of the welded parts outside of the acceptable limits.

The panels have already deformations before friction stir welding. An example of typical status is given in the photos in Figure 193 taken before welding the skin for the design concept 3. The maximum vertical distance between the parts and the backing plate was about 5 mm. The source for this deformation is mainly the machining operation to optimise the skin thickness to the local strength requirements, in the case of the Figure 193 to create the weld pad-up. The large test articles are flat panels, the effect of forming processes like rolling or stretch-forming is here not present.

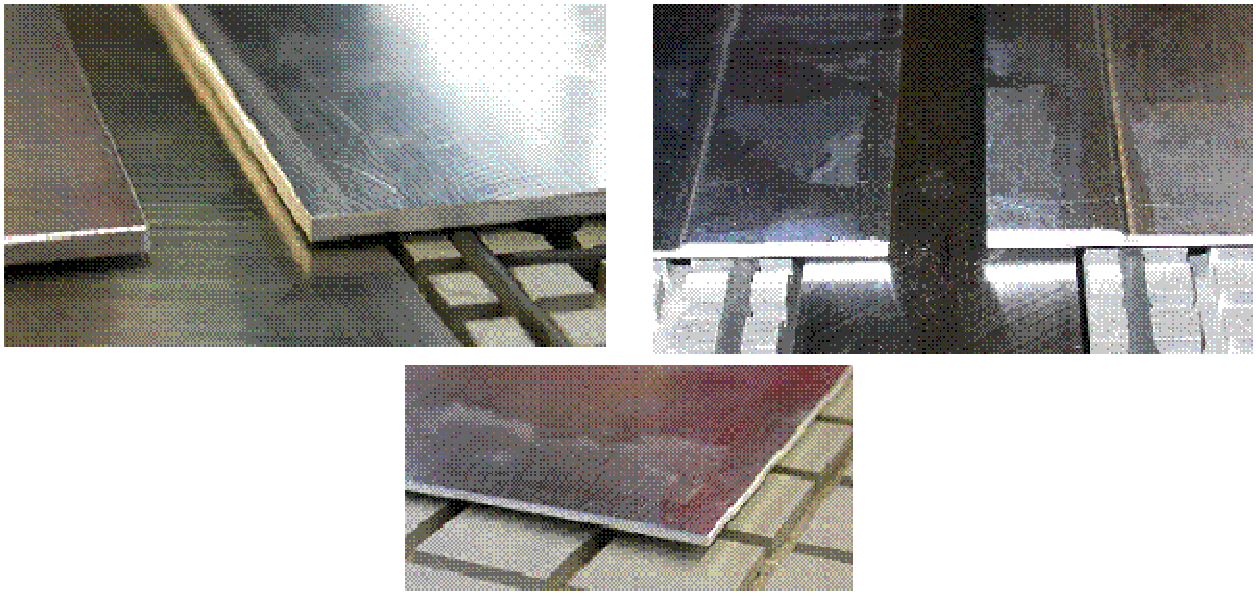

Figure 193: Examples of deformations of the unstiffened panel before welding design concept 3

After friction stir welding the deformations are always significantly higher. Differences exist if the panels are stiffened or not. A visual example of the deformations after welding of a panel without stringer is given in Figure 194.

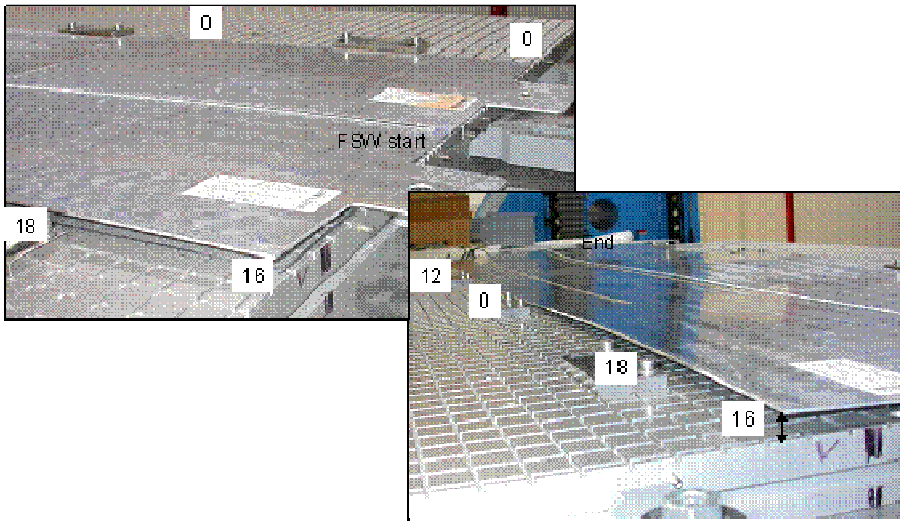

Figure 194: Distortion of a flat panel after FSW (concept 3)

For a stiffened panel the deformations created by the FSW are generally lower compared to un-stiffened plates, Figure 195 shows the distortion in the test article for concept 1 having riveted stringers.

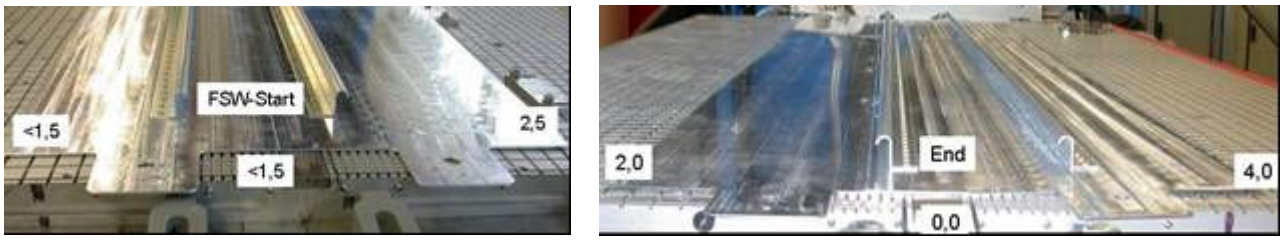

Figure 195: Distortion of a stiffened panel after FSW (concept 1)

Figure 196 shows the welding of panel concept 3 having bonded stiffeners located next to the weld. Important to notice the roller in front of the welding head used to press the panels against the backing bar.

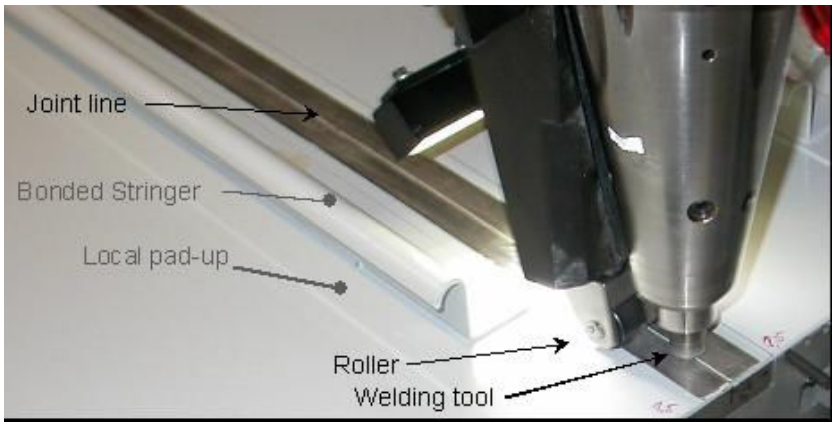

Figure 196: Welding of panel with bonded stiffeners (concept 2)

Other assembly/manufacturing processes may introduce larger deformations and shall be investigated in combination with the deformations created by the FSW process. Figure 197 shows a limit case from concept 4 where the Laser beam welded (LBW) stringer has introduced a significant deformation. Due to the limited stiffness of the panel it was possible (but was not easy) to clamp the part on the working table. Current production use shot peening to reduce the deformation caused by the LBW process. In the manufacturing of the concept 4 it was decided not to use shot peening to reduce deformations from LBW.

Figure 197: Example of large deformation caused from Laser welding of a stringer. In addition, in this particular case, the presence of gap between stringer and panel has led to a bad quality of LBW

Regardless of the high initial deformations FSW process was successful and the resulting assembly is shown in Figure 198. The final assembly is highly distorted and to achieve the required tolerances would be necessary to shot peen.

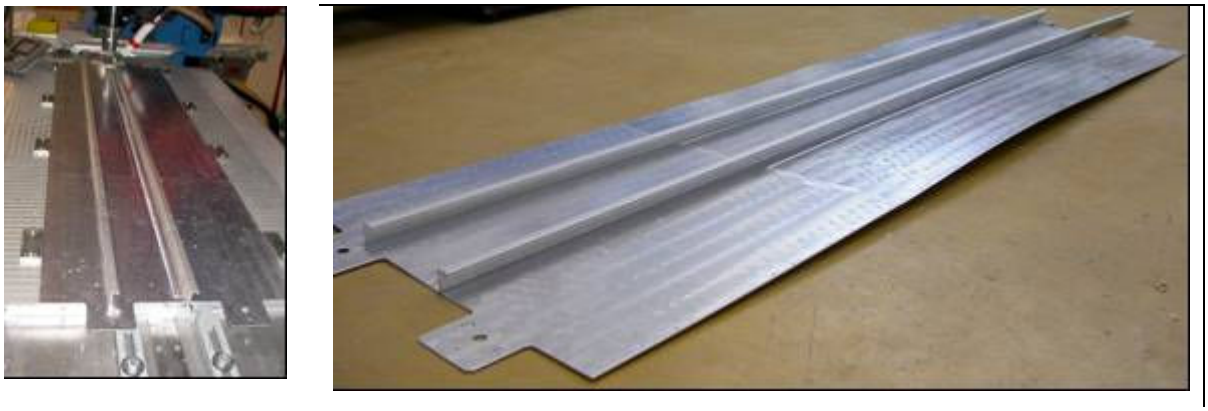

Figure 198: Friction Stir Welding of concept 4 having LBW stringers (V534-H1504-006)

In the next figures are given more detailed information about the major deformations measured on different design concepts. The distortions are always measured in terms of vertical distance from the backing plate.

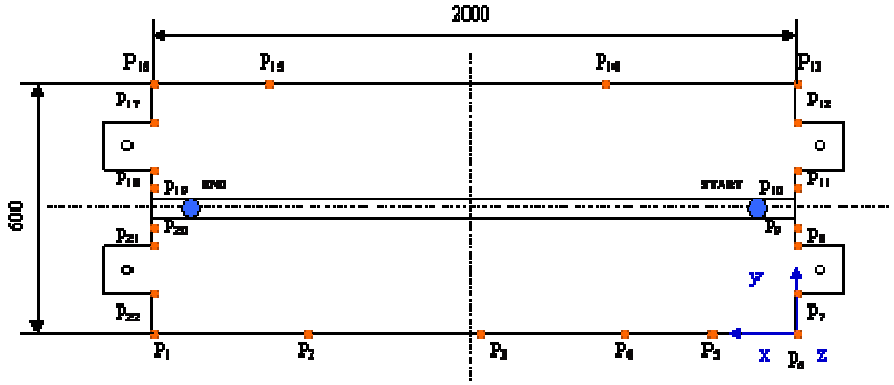

- The coordinates of the points are:

P1 = [2000,0,24] P2 = [1400,0,7] P3 = [900,0 ,2] P4 = [490,0,1] P5 = [180,0,1] P6 = [0,0, 1]

P7 = [0,100,0] P8 = [0,210,2] P9 = [0,270 ,1] P10 = [0,320,0] P11 = [0 ,390,2] P12 = [0,500,8]

P13 = [0, 600, 13] P14 = [600,600 ,5] P15 = [1600,600 ,0] P16 = [2000, 600, 2] P17 = [2000, 500, 2] P18 = [2000,390,1]

P19 = [2000,320,0] P20 = [2000,270,4] P21 = [2000,210 ,10] P22 = [2000, 100, 20]

Figure 199: Distortions after FSW of the skin for the design concept 2

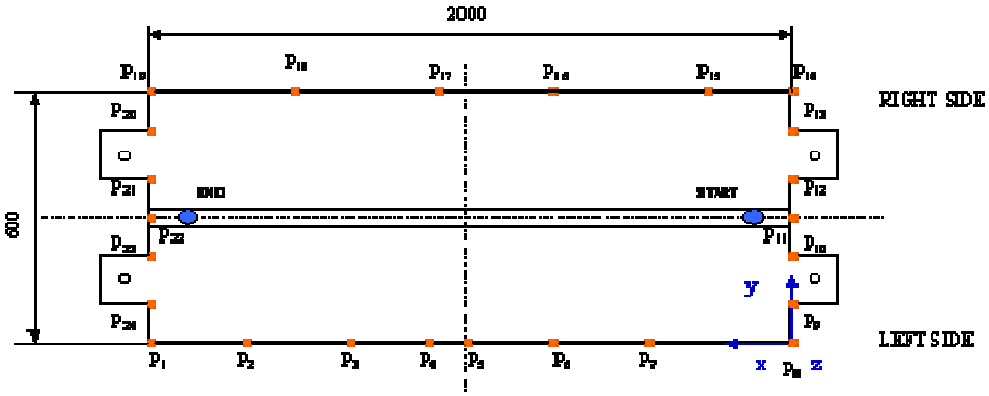

- The coordinates of the points are:

P1 = [2000,0,,15] P8 = [0,0,7] P15 = [350,600 ,15] P22 = [2000,300,0]
P2 = [1770,0,,12] P9 = [0,100 ,4] P16 = [740,600,,31] P23 = [2000,200,6]
P3 = [1380,0 ,0] P10 = [0,,200,,1] P17 = [1100,600,,40] P24 = [2000,,100,,11]
P4 = [1130,0,,6] P11 = [0,,300,,0] P18 = [1540,600,,17]
P5 = [1000,0,,0] P12 = [0,,400,,1] P19 = [2000,300,,9]
P6 = [780,0,,4] P13 = [0,,500,,3] P20 = [2000,,500,,5]
P7 = [580,0,,0] P14 = [0,,600,,6] P21 = [2000,400 ,1]

Figure 200: Distortions after FSW of the skin for the design concept 4

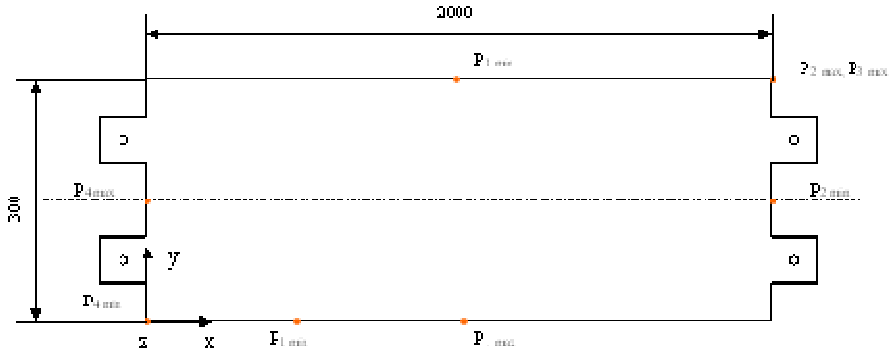

- The coordinates of the points are:

P1 min = [500, 0, 0]	P1 max = [1100, 0, 15]
P2 min = [2000, 150, 0]	P2 max = [2000, 300, 19]
P3 min = [1000, 300, 0]	P3 max = [2000, 300, 19]
P4 min = [0, 0, 5]	P4 max = [0, 150, 15]

Figure 201: Distortions after FSW of the skin for the design concept 5 (dwg: V534-H1506-008)

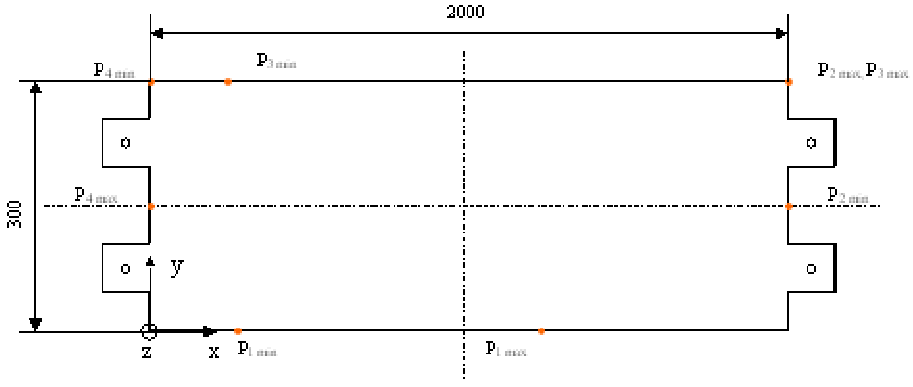

- The coordinates of the points are:

P1 min = [300, 0, 0]	P1 max = [1300, 0, 18]
P2 min = [2000, 150, 0]	P2 max = [2000, 300, 20]
P3 min = [300, 300, 1]	P3 max = [2000, 300, 20]
P4 min = [0, 300, 7]	P4 max = [0, 150, 15]

Figure 202: Distortions after FSW of the skin for the design concept 6 (dwg: V534-H1506-010)

Redundant joint design

An innovation introduced with design concepts 3, 5 and 6 is the creation of a redundant load path from a combination of FSW of the skin and bonding or riveting a second structural member (stringer, doubler) on top of the weld. This innovation requires preparing the surface of the weld for the additional assembly processes: mechanical fastening and adhesive bonding. For both processes the preparation consists of mechanical milling of the surface and subsequent surface treatment. For the adhesive bonding process the high quality of surface treatment is of critical importance to avoid any risk or corrosion or reduced mechanical strength. For the 3 bonded concepts where bonding is performed on top of the weld the surface is anodyzed after performing FSW and surface machining in order to prepare it for adhesive bonding. Anodyzation is performed with a bath process, for this reason shall be performed before assembly of stringers. After anodyzation a bonding primer is applied. For concept 2, where FSW is used as an assembly process of bonded shells the surface treatment consist in a conversion coating applied locally on the weld surface.

Assessment of joint performances

Ultrasound NDT investigation of the panels have identified two manufacturing defects created during the bonding process of the stiffeners for the panel concept 6. Due to the small size of the defects the panel was considered suitable for the rest of the investigation.

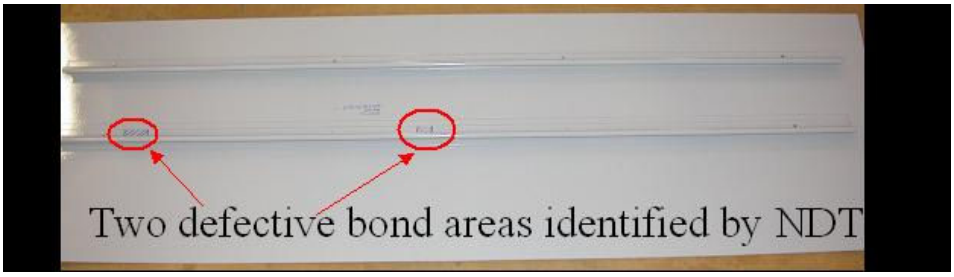

Figure 203: Picture showing the area of the defects identified in panel concept 6

Specimens	mm	
Microsection	80	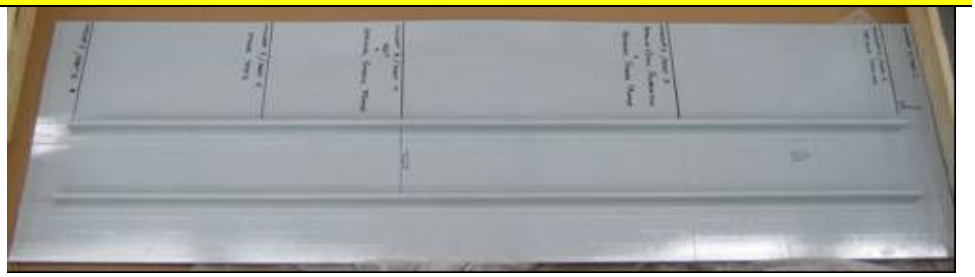
Bend test	80	
da/dN	600	
fatigue	500	
NDT	300	
Other	1	

Figure 204: Specimens extracted from test articles for weld assessment

Conclusions

It is feasible to manufacture redundant joint concepts exploiting a combination of FSW and bonding or mechanical fastening process.

FSW of flat shell was always possible regardless of the initial deformations created by other manufacturing processes.

Significant distortion created by process like LBW used to join stringers and skin can be tolerated by the FSW process if a suitable clamping concept is used. Anyhow the distortion caused by LBW needs to be corrected by means of shot peening otherwise would results in unacceptable deformations.

5.2 Task 5.1 Welding of large prefabricated part (Alenia Aeronautica)

The Alenia contribution to WP5 consisted in studying the effect of pre-welding operation and the external finishing of edge before welding. It is been developed through past theoretical studies and experiments.

The study was divided in two parts: the first will concern the pre-welding operations, the second the post-welding operations. In the first part will be concentrate about external operations of edge before the welding and about the necessity to remove or not the clad.

In the second part have been illustrated the external operations of edge after the welding and the machining operations to have the standard superficial finishing, request to ASTM specifications.

External finishing of edge

In past it is been observed that the sheets' edges to weld must be manufactured on purpose. In particular they must be milled to have the perfect mating. The perfect weld in absence of this characteristic is impossible: the lack of material transforms itself in presence of tunnel into nugget zone or defects after welding. The data testing of specimens with milling operation are lower of those milled with same parameter.

For the same reason, is required a further operation to eliminate the burrs produced with milling. This operation is very delicate because if removing the burrs the 90° edge is broken, a risk for new defect will arise.

Another important operation pre-weld is the clad removing. This operation can be effected trough mechanical or chemical manufacture and is used to eliminate a ultrapure superficial aluminium coating (Clad). It is necessary for the success of welding: it is tested that the present of this protection (clad is used to shield the aluminium to oxidization) during weld, lowers the mechanical characteristic.

Post welding Operations

In order to finish the edge post-welding for specimens manufacture, are been studied sawing and sharing operations. The results of static tension are been processed developing two same sets of specimens for also evaluate the repeatability: T1 and T2. The comparison is been good.

In the case of surface preparation of parts, mechanical specimens for fatigue test may require a roughness Ra=0,8 in according to ASTM specifics. In this case different combinations of surface preparation has been tested (with milling, sanding and treatment with scotch brite) to study the effect on surface. The goal is to have a lower roughness in order to improve the fatigue performance possibly with an economic process.

5.3 Task 5.1 Combination with other production processes – prefabricated parts (Sabca)

- Other manufacturing process involved CNC milling.
- Designed: milled parts displaying a geometry that is favourable for welding, trying to limit the complexity of fixtures; for a production definition, specific extruded profiles for top and bottom panels would be used design enabling possible inner inspection after welding, and seam milling, if necessary

Further a comprehensive dissemination plan, building on this demonstration, has been proposed by SABCA. This might prove beneficial for the consortium partners to prove that FSW is a fully competitive joining technique.

5.4 Task 5.2 Combination of FSW with Stretch Forming (University of Patras)

In the reporting period University of Patras:

a) Developed a methodology for the determination of the formability of metal blanks.
b) Developed and validated a stretch forming model of welded and unwelded coupons based on the experiments carried out by SHORTS.
c) Developed a pre-test simulation model of the tri-axial stretch forming experiments performed by GKSS.

In order to determine the formability of metal sheets, a ductile fracture criterion based on the strain energy density has been applied. Sih [J. Theor. Appl. Fract. Mech., 1980, pp. 157 -173] proposed a failure criterion based on the accumulation of the strain energy density, which has generally been applied in the prediction of crack propagation in fracture mechanics. A modification of this criterion can be applied in metal forming processes:

$$\frac{dW}{dV} = C = \int_0^{\varepsilon_{ij}} \sigma_{ij} d\varepsilon_{ij} \tag{9.1}$$

In equation (9.1) dW/dV is the strain energy density C the metal strain energy density, σ_{ij} the equivalent stress and ε_{ij} the equivalent strain.

5.4.1 FLD Coupons

Formability experiments are carried out by SHORT Brothers PLC with the aim of determining the Forming Limit Diagrams (FLD) of welded and unwelded A2024 T3 coupons.

The formability experimental set up is schematically illustrated in Fig. 9.1.

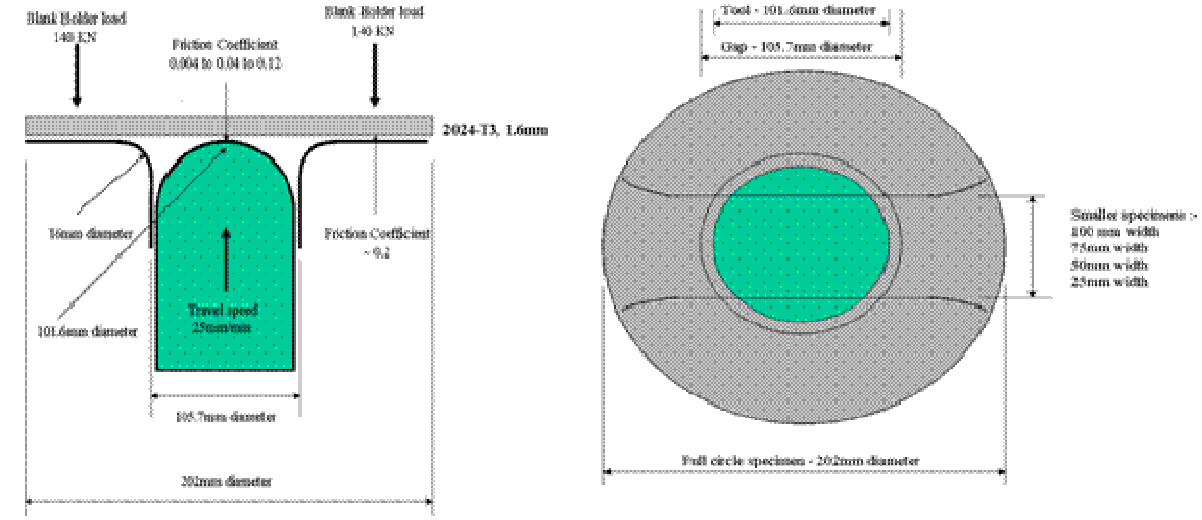

Figure 205: Formability experimental set up, (a) Side view and (b) Top view

Finite Element code ANSYS has been used for the development of a numerical simulation model of the stretch forming experiments. The metal blank has been modelled using the four-node element type 'SOLID45' which is suitable for analyzing 3D solid structures. The punch and the blank holder have been modelled using element type 'TARGE170', which is used to represent 3-D deformable bodies and is paired with associated 'CONTA175'contact elements on the metal blank surface. In order to minimize the CPU time, only one quarter of the model is used. The developed FE model is shown in Figure 206.

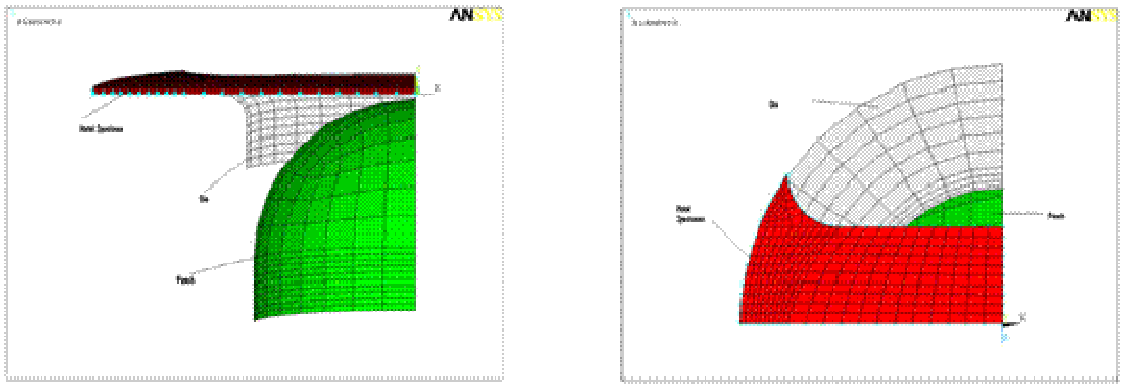

Figure 206: Developed FE model (a) Side view and (b) Top view

The initial verification process is the comparison of the deformed shapes of the FE model with the experiment, Figure 207.

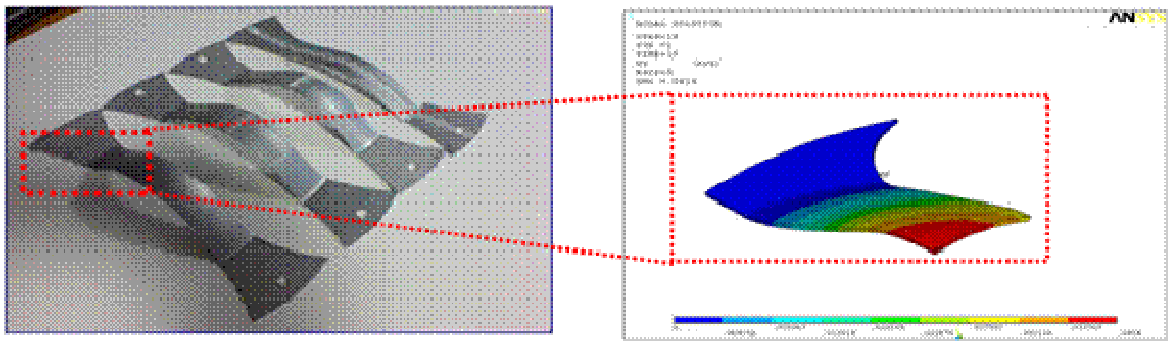

(a) (b)

Figure 207: Deformed shape, (a) From the experiments and (b) from the mode

From Figure 207 it can be observed that the deformation trend of the FE model is the same as the experimental. The next step is the determination of the fracture points, which are used for the determination of the forming limits. Herein the criterion based on strain energy proposed is applied.

The FLD is constructed by calculating the major strain, ε_1 and the minor strain ε_2 when fracture is initiated along the strain path. The different strain paths - biaxial tension, plane strain, pure shear and uniaxial compression are achieved by varying the width of the metal blank, in this case between 25 mm – 100 mm. Fracture begins when elements along the strain path attain the critical strain energy density as the deformation proceeds. The predicted FLD for the parent material and a FSW panel are compared in Figure 208.

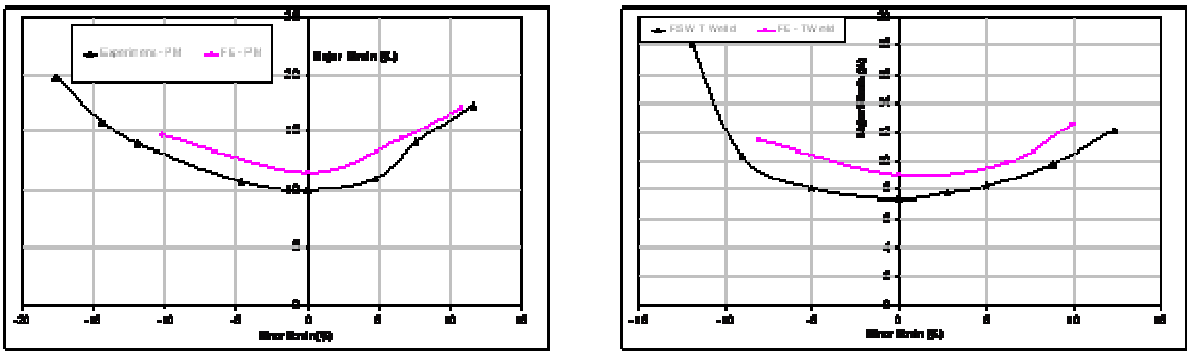

(a) (b)

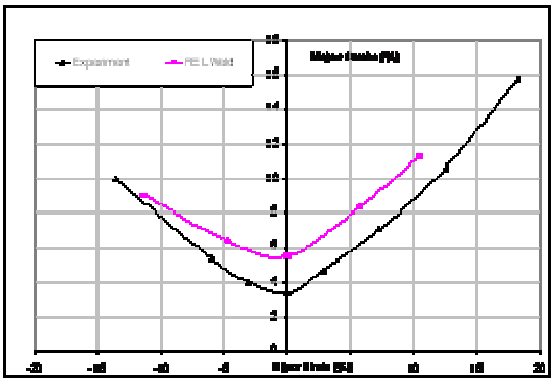

Figure 208: Predicted FLD curves, (a) For Parent Material, (b) For Transverse welded panel and (c) For lengthwise welded panel

From Figure 208, it can be observed that based on the specific strain paths, the experimental and numerical FLD for both the welded and un welded panels are in good agreement. The slight differences can be attributed to the fact that in the numerical model the residual stresses are not taken into consideration.

5.4.2 Biaxial stretch forming model

Having successfully predicted the FLD's using the small coupons, the methodology is applied in the formability analysis in a stretch forming situation. A biaxial stretch forming model is developed, Figure 209. The stretching process is carried out in two steps: The first step involves an in-plane stretching process where a tensile force is applied at the edges of the metal blank. This force is gradually applied until the strain at the edges is about 2.5-3%.

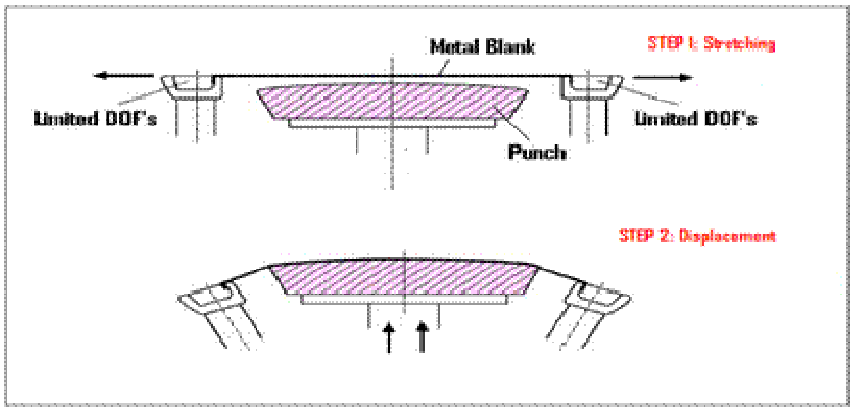

Figure 209: Illustration of the stretch forming process

In the second step, the punch deflects the blank to a radius of curvature of 1000 mm. This radius of curvature corresponds to a vertical displacement of 90 mm. The preliminary tool proposed is a double curvature punch with two radii of curvature R_1 = 1000mm and R_2 = 2000mm, Figure 210.

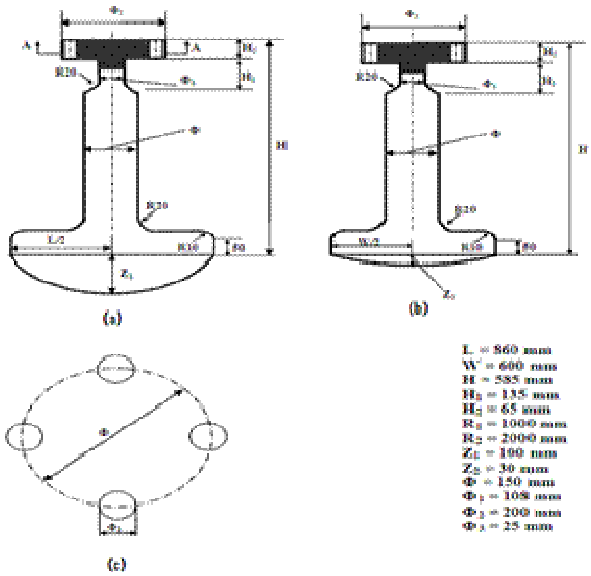

Figure 210: Technical drawings of the tool used (a) Front view, (b) Side view and (c) Top view

Initially a lengthwise weld with a width of 15 mm is considered and the dimensions of the blank used are:

- Blank length 860 mm
- Blank width 600mm
- Blank thickness 3.2 mm

For the modelling of the metal blank, element type ‘Solid 45’ is used. The interface phenomenon due to the contact between the punch and the metal blank is simulated using element type ‘Conta175’. For the modelling of punch element type ‘Targe170’ is used. The developed FE model is schematically shown in Figure 211.

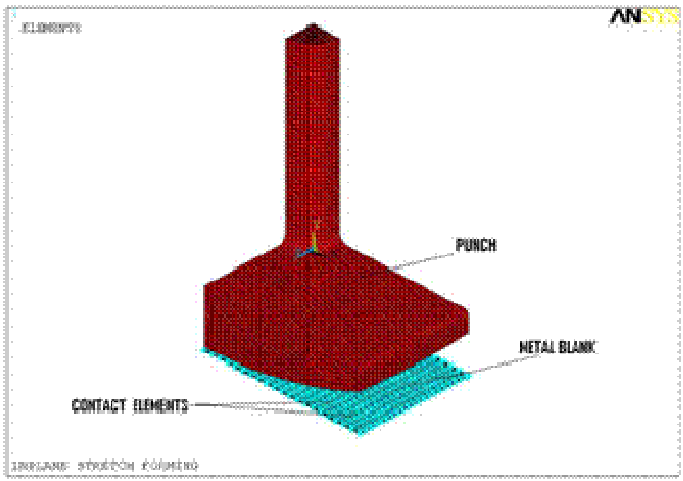

Figure 211: FE model for the stretch forming process

Only a quarter of the real structure is modelled, due to the two - axes symmetry of the problem. The material used in the initial model is Al 2198 – T8. Local to the weld-line material properties were introduced based on micro tensile tests carried out at GKSS, Figure 212. The friction coefficient between the punch and the metal blank is varied between 0.1 – 0.3.

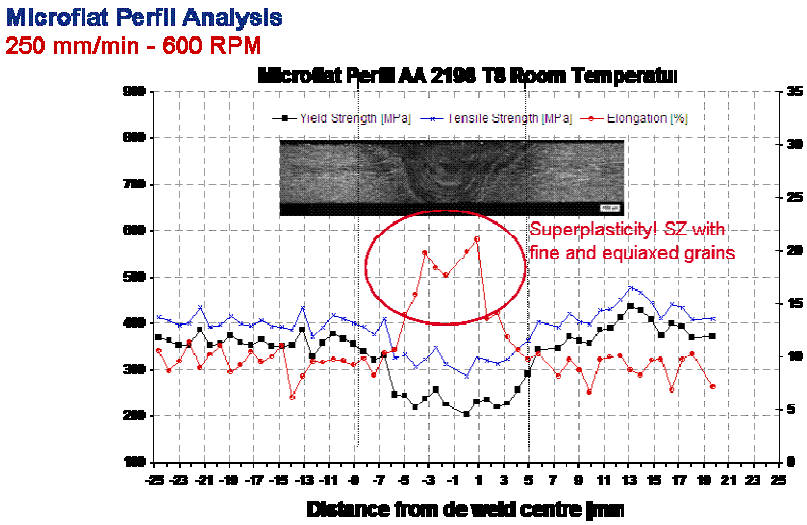

Figure 212: Local material properties

In Figure 213, the predicted deformed shapes of the metal blank during the forming process are shown.

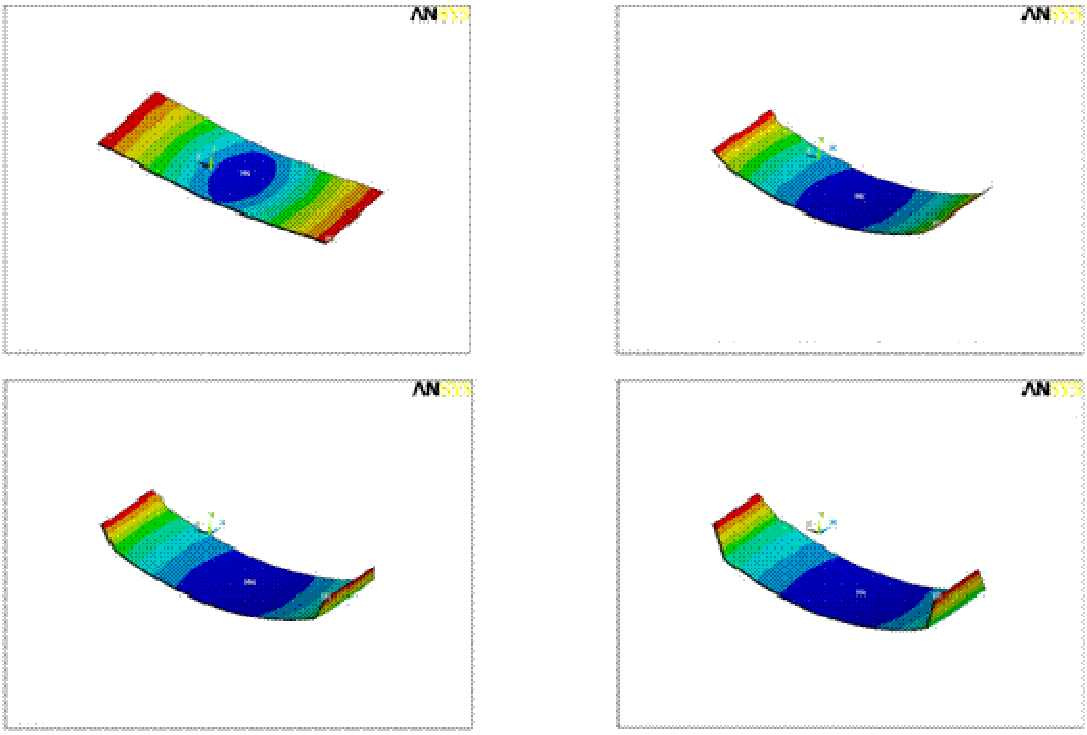

Figure 213: Deformed shapes of the metal sheet

From Figure 213 it can be observed that in order to achieve the desired curvature, the punch displacement should be at the level of 150 mm. Larger radii of curvature on the blank (without local failure) can be achieved if the dimensions of the punch are changed.

In Figure 214, the force displacement diagram of the punch is presented.

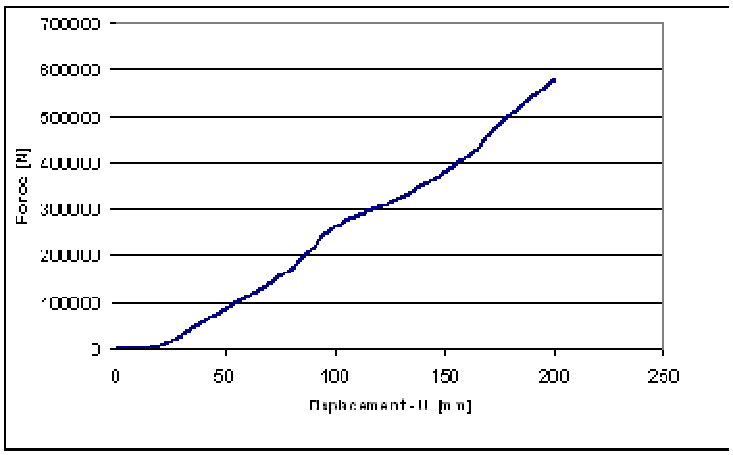

Figure 214: Force displacement diagram

After the model validation, its application to parametric studies will become possible, in order to investigate the effect of the blank width (W), blank length (L), punch radius (R), stretch height and weld orientation on the formability.

5.5 Task 5.3 Creep-age forming (Dassault Aviation)

Based on the experience in previous European program AGEFORM, the feasibility of creep-age forming after FSW has been studied on mid-size (500x500 mm2) single and double curvature specimens as presented in Figure 215. The results analysis is presented in Figure 216.

The test plan for welded materials characterisation (mechanical properties and corrosion) is reminded in Table 26.

The tests (hot temperature elongation, crack propagation, residual stress and corrosion) were completed (see the results in Figure 220, Figure 221, Figure 222, Figure 223 and Figure 224).

The D11 and D18-2 deliverables have been done.

This task is completed.

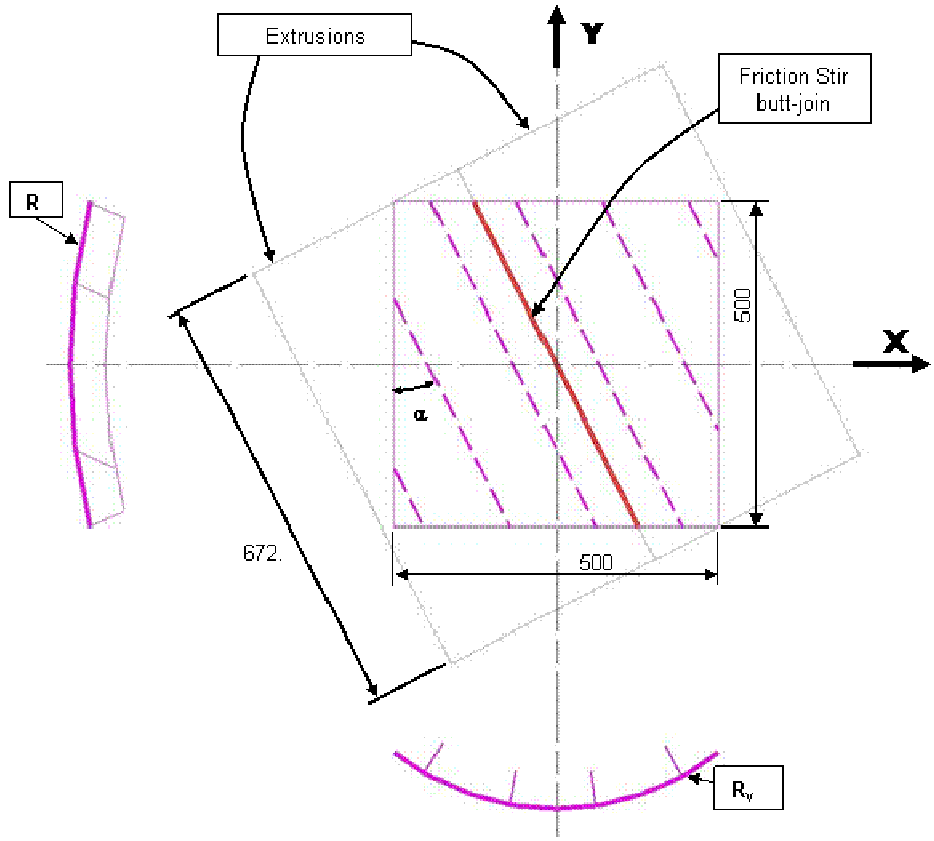

Material	α (°)	R_x (mm)	R_y (mm)	Number of specimens
7449	0	0	500	2
	0	0	1 200	2
	0	3 000	500	2
2196	0	0	500	2
	0	0	1 200	2
	0	3 000	500	2

Figure 215: Creep-age forming testing matrix

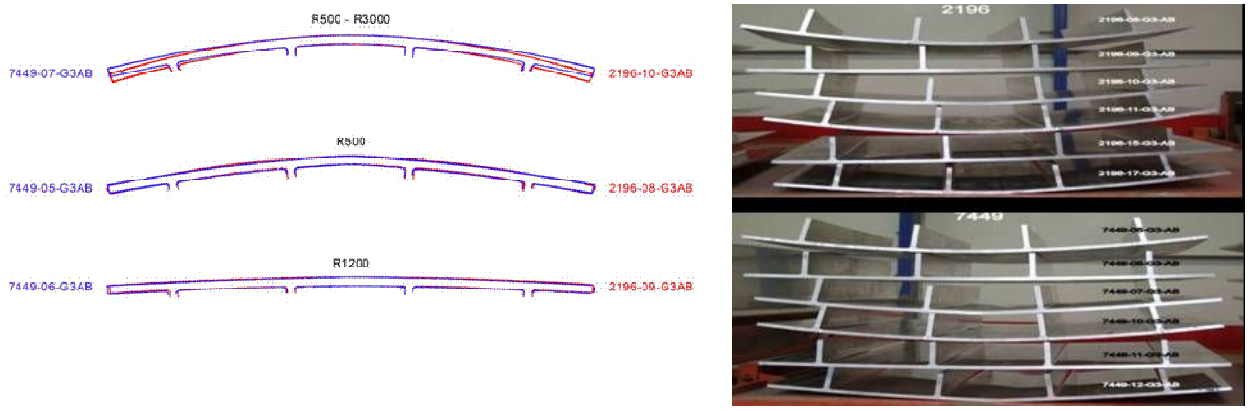

Figure 216: Creep-age forming tests results

Material	Aging cycle	Property	Elongation during Age-Forming (⊥ to FSW joint)	Cutting direction	Coupon type	Number of coupons
7449 T79	12h@ 120°C + 17h@ 150°C	**Static** (Rm; Rp0.2; A%)	0%	LT	"Alcan" type	5
			0.5%		"Alcan" type	6
			0%	**L**	**TP XXL**	**2**
			Base metal	**L**	**TP 10**	**3**
		Corrosion	0%	LT-L	60x120	1+1

		Intergranular corrosion	0%	LT-L	60x120	1
		da/dN after ST	0%	LT-L	CCT 200x600x7	3
2196 T8	30h@ 152°C	**Static** (Rm; Rp0.2; A%)	0%	LT	"Alcan" type	5
			0.5%		"Alcan" type	6
			0%		**TP XXL**	**2**
			Base metal		**TP 10**	**3**
		Fatigue	**0%**	**L-LT**	Tϕ10 Type 1	7
			Base metal	**L-LT**	Tϕ10 Type 1	7
			0%	LT-L	Tϕ10 Type 2	7
			0%		Tϕ10 Type 1	2 x 7
		da/dN (R=0.1)	0%	LT-L	CCT 100x300x4	1
		Fracture Toughness	0%	LT-L	CCT 100x300x5	1
					CCT 300x900x5	1
		Corrosion	0%	LT-L	60x120	1+1
		Intergranular corrosion	0%	LT-L	60x120	1

Table 26: FS Welded material characterisation testing matrix

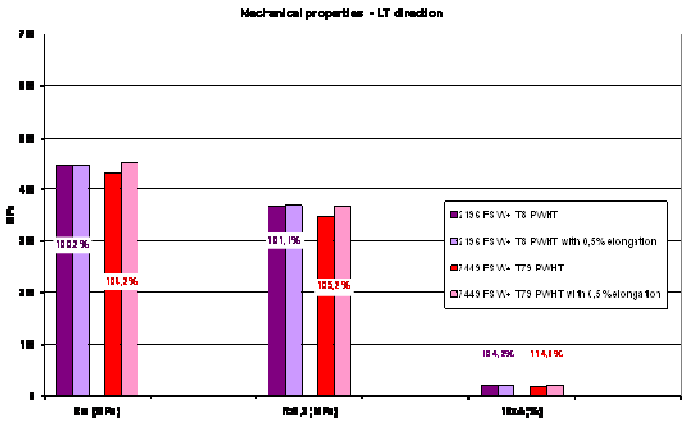

Figure 217: Mechanical properties after hot temperature elongation

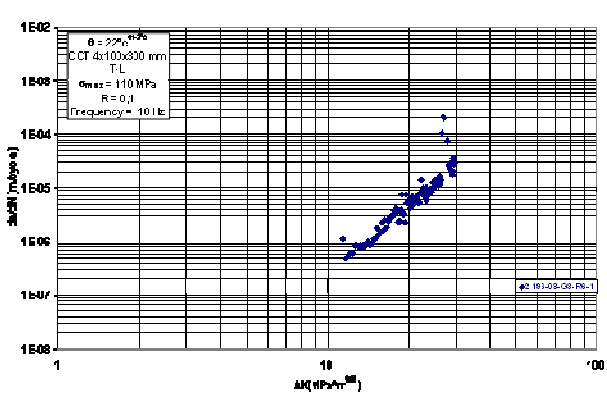

Figure 218: Fatigue crack growth rate of 2196 T8 as welded condition

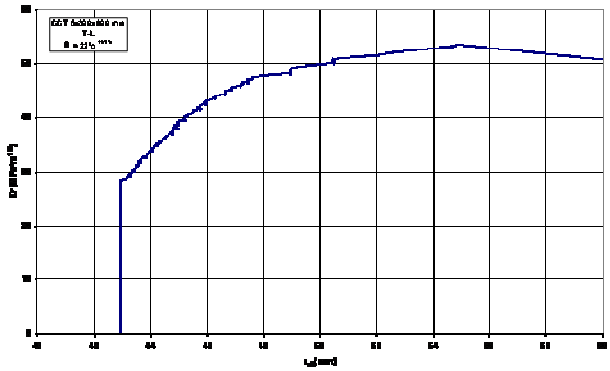

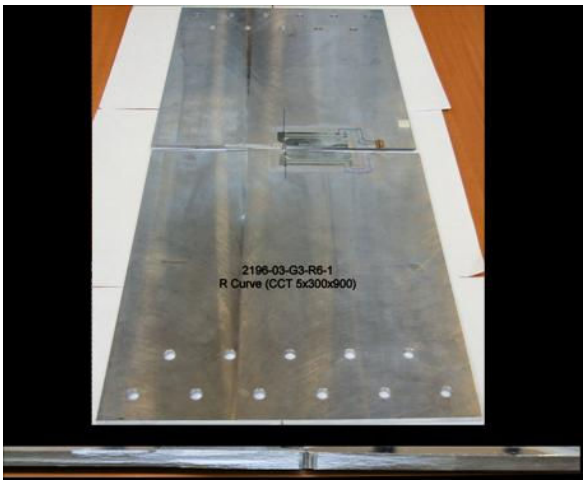

Figure 219: Fracture toughness of 2196 T8 in as welded condition

2196 T8 PWHT after 3000 hours of salt spray exposure

7449 T79 PWHT after 3000 hours of salt spray exposure

More than 3 pits on non sealed area
Nothing on sealed area

More than 3 pits on non sealed area
Nothing on sealed area

Figure 220: In salt spray exposure

Coupon reference	Sensitivity	Macrograph
2196-05-G3-BS-4	P	
7449-05-G3-BS-4	ED	

Figure 221: Intergranular corrosion – according to ASTM G34 Standard (EXCO)

2196 T8 PWHT

7449 T79 PWHT

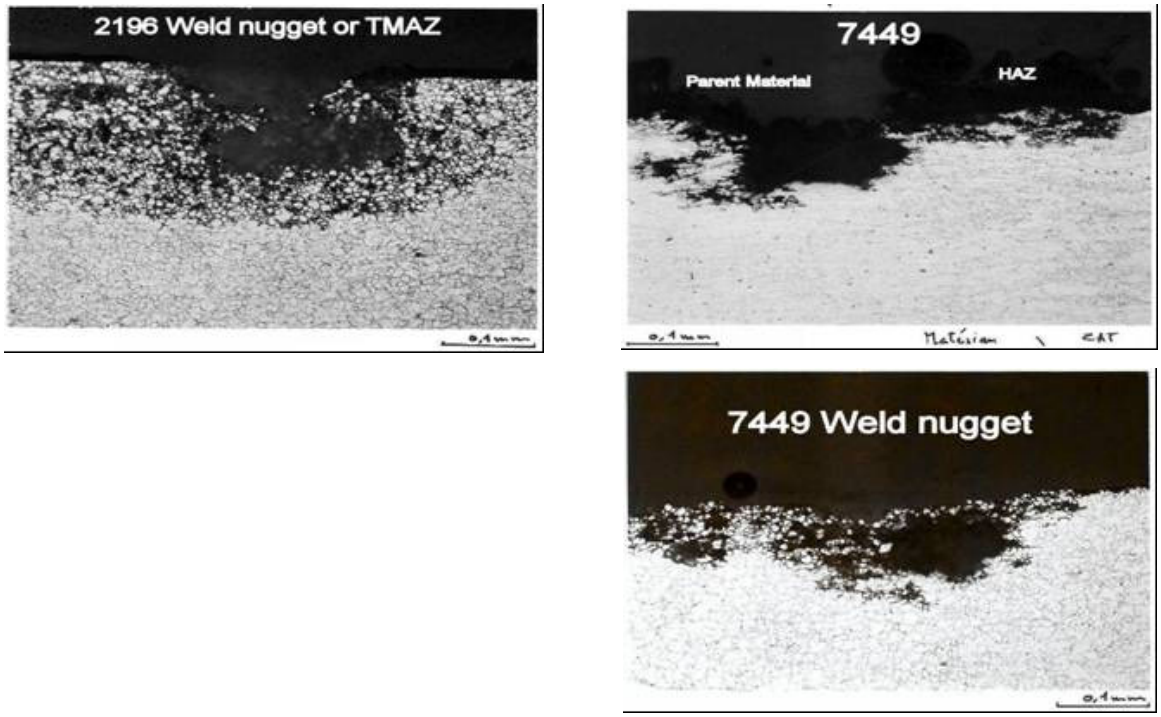

Figure 222: Intergranular corosion – according to AIR 9048 (Annex D Standard Method 1)

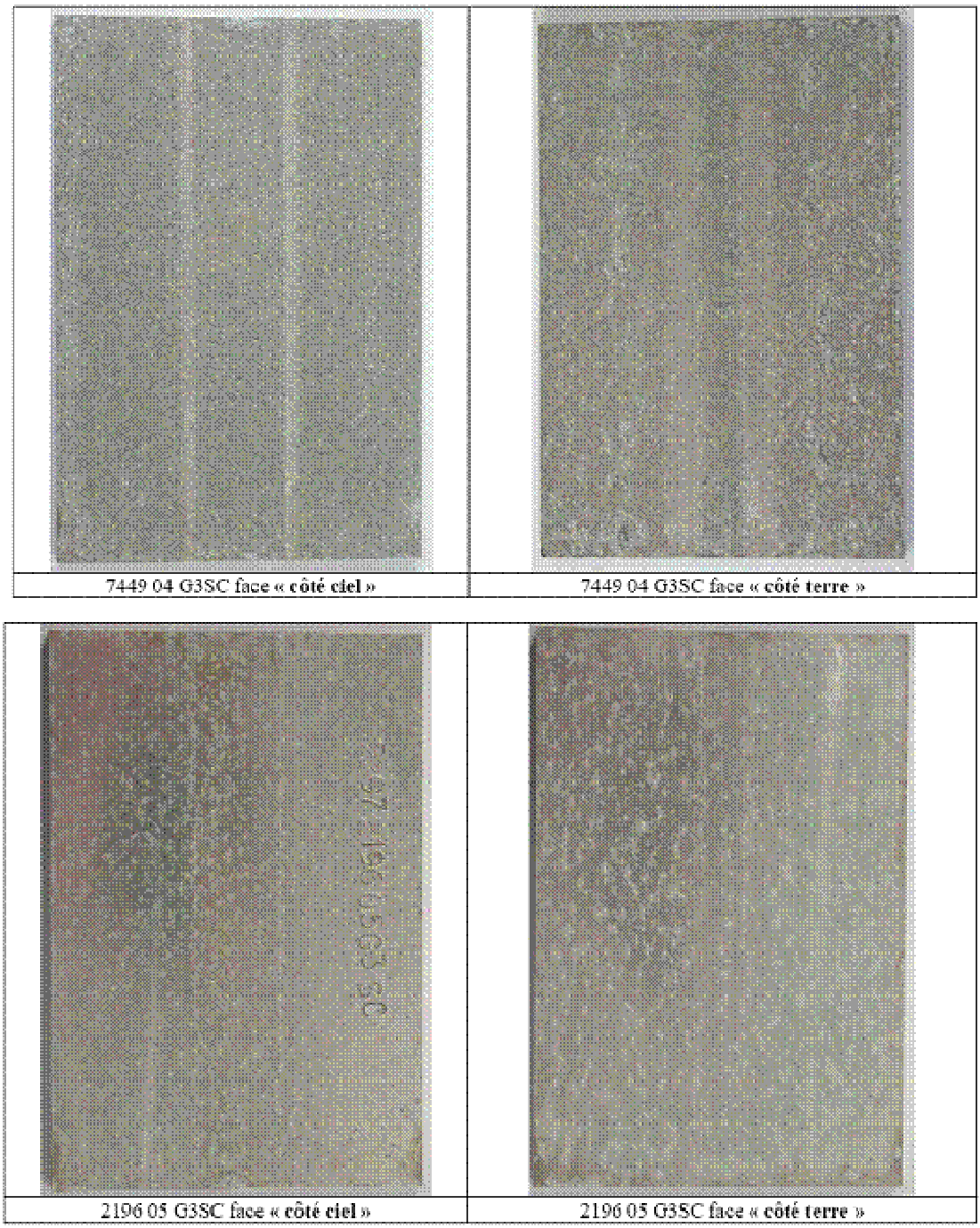

Figure 223: In sea cost atmosphere exposure.
As reported in the following table and as shown here below, for each FSW + PWHT alloys, any corrosion appears after one year of exposure in sea costs atmostphere

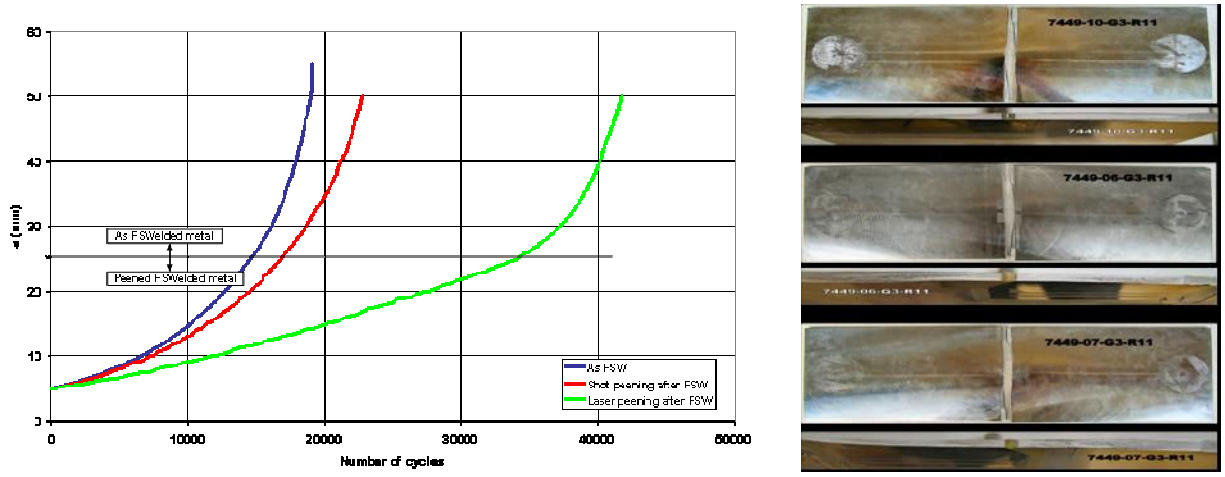

Figure 224: Impact of peening processes on Fatigue Crack Growth rate of 2196 T8 FS Welded

5.6 Workpackage 5: FSW with other production processes (Airbus UK)

Complete manufacture of tensile and fatigue specimens for time delay specimens. This was carried out to establish if unnecessary joint preparation work was been done. This would reduce time and cost. See time delays and finishes in the table below.

1 hour	Time between machining the mating face and FSW
1 week	Time between machining the mating face and FSW
16 weeks	Time between machining the mating face and FSW
16 weeks	Slit saw mating face, no finish machining

Specimens tested by Bombardier Shorts.

All tested specimen failed in the TMAZ and all failed at about the same number of cycles.

6 Work Package 6: Improvements to the FSW Process

6.1 Overview

The technical content of this work package is about new welding tools, improved existing welding tools and about improved welding scenarios to avoid welding features and to improve the weld quality.

All activities have reached the intended results:

1. The influence of FSW tool probe coatings in their influence on the weld quality has been evaluated.
2. The bobbin tool welding concept has been extended to thickness sections up to 23 mm.

3. It has been shown that by performing a specific weld edge preparation the risk of the lack-of-penetration welding feature can be reduced significantly.
4. The DeltaN tool FSW concept has been brought to a higher maturity level by definition and built-up of a robust tool design and the realisation and characterisation of real component, e.g. A380 wing flap rib, and real size demonstrator part, e.g. SABCA wing flap beam track, welds.

All generated results are suitable to increase the attraction of the FSW process for its use in aerospace applications.

The former existing number of concerns about that joining process is much smaller by taking the achieved results into account.

In conclusion a chamfer of the weld edges has shown a positive effect regarding avoidance of LOP defects in case of errors in the control of the distance between tool tip and backing bar. The size of the chamfer should be not smaller than 0.4mm.

The welding tool probe coatings for modifying the friction coefficient do make a difference. The biggest difference was seen in the quality of the weld nugget. The next most significant difference was in thermal measurements, up to 17°C at the tip of the tool pin when considering each group of welds (identical parameters) and 51°C when considering all welds. Finally a small change was seen in the loads placed on the tools (tool loads also influenced by the tool depth in the material). No differences between tools could be detected when observing the torque feedback readings.

Main conclusions of the bead-on-plate testing campaign can be summarized as followed.

The Diabolo pin type, associated with a 23 mm flat upper shoulder and a 20/26 mm stepped lower shoulder was selected for the continuation of FSW development on butt joint.

Travel speeds higher than 50 mm/min produced too high forces in the welding direction (about 20 kN), so that the tool could not be maintained perpendicular to the workpiece due to the welding head gimbal (limited stiffness). This resulted in a lack of consolidation of welds under shoulders or pin breakages. Rotation speeds higher than 300 rpm led to insufficient material stirring (too much slipping between tool and material) that resulted in pin breakages as well. Rotation speeds lower than 250 rpm did not generate enough heat and also caused tool failures. A narrow processing window was found: $v < 50$ mm/min; $250 < \omega < 300$ rpm.

The use of a DeltaN tool does no longer mean a high complexity to be dealt with. The tool design became simple and robust and the extra-amount of adjustments is not much higher compared to a standard tool. Depending on the welding application DeltaN allows a reduction of the vertical downwards force of up to 50%. The remaining distortion after welding can be reduced significantly depending on the welding application. For the real component weld on the A380 wing flap rib the distortion has been reduced by factor of 8 compared to the use of a standard welding tool.

6.2 Task 6.1 Process Modelling (BAE)

A study was conducted using numerical modelling to investigate the application of thermal assistants during thick-section FSW for the purpose of improving the through-thickness thermal profile. Since heat is generated during FSW primarily by friction between the top surface of the workpiece and the tool shoulder, there can be problems maintaining a sufficiently high temperature at the base of the

weld which is necessary to avoid the formation of defects. Three different configurations of thermal assistants were investigated, each having the purpose of redistributing heat towards the base of the weld. The configurations are:

1. Cooling applied to the FSW tool body
2. Cooling applied to the workpiece around the FSW tool
3. Internal heating of the FSW tool

6.2.1 The Thermal Model

Thermal modelling of the FSW welding process was completed using COMSOL Multiphysics 3.4 utilising the heat transfer module. The geometry for the model was based on experimental arrangement that had been used in previous work conducted at BAE Systems ATC, and from which temperature histories were readily available. The thermal measurements from this were used to calibrate the model and establish a reference condition for a baseline weld.

For the model developed, only conductive and convective heating were considered, and for simplicity stirring effects and material transport due to the rotation of the tool were neglected. As a consequence, the thermal fields would be symmetric about the welding line, and it was thus sufficient to model only one half of the welding process. The model was further simplified by assuming the weld material had infinite length in the welding direction and the coordinate system was fixed on the weld tool. This allowed relative movement between the tool and the workpiece to be simulated using a convective flux that flowed through the work-piece (including the anvil) in the welding direction.

The basic geometry used in the model is shown in Figure 225 (welding direction into page), and consisted of three components; the tool, workpiece and anvil. The tool comprised the FSW tool itself and a sufficient volume of the chuck to provide a representative heat sink. The workpiece is self-explanatory, and the anvil served as a representative heat sink below the workpiece. Convective heat transfer coefficients were assigned to the free surfaces of the model geometry. For none moving surfaces (i.e. the workpiece and the anvil) a convective heat transfer coefficient of 10 W/m^2K was used, which is typical for natural convection in air. Since the tool would – in the real world - be rotating and subject to forced convection, a higher value of 50 W/m^2K was applied to its free surfaces.

Cryogenic cooling of the tool body was simulated with a uniform negative heat flux applied to the free surface of the tool between heights of +5mm and +25mm measured from the workpiece surface.

Cryogenic cooling of the workpiece was simulated by a uniform negative heat flux applied to an annular area centred on the tool axis with inner and outer radii of 22 and 37 mm respectively.

Heating of the tool pin was simulated with a uniform heat flux applied to a 2.5 mm radius spot, located +2.5 mm above the tip of the pin.

6.2.2 Results and Discussions

Prior to investigating the relative effects of additional thermal assistants to the FSW process, it was important to establish representative baseline conditions for a standard weld. This was achieved by comparing and adjusting model parameters to achieve a reasonable match with experimentally recorded values. A reasonable alignment with experimental measurements was achieved by using a

total input power of 4kW, which was split 1400W and 2600W respectively for the shoulder and the pin.

The objective of this work was to investigate the application of thermal assistants (both cooling and heating) with the purpose of improving the through-thickness temperature distribution during FSW. The approach used to assess any changes was to compare the temperature differential 10mm from the weld line, taken between 2mm (CH0) and 19mm (CH3) depth as measured from the surface of the workpiece, with the baseline weld. However, with the addition of thermal sources (or any other significant changes in heat sinking for that matter) there will be an affect on the overall process temperatures. To compensate for this, and enable a meaningful comparison, for the thermally assisted welds the tool rotation speed was adjusted until the CH0 peak temperature matched that of the baseline weld. Input torque was assumed constant for both the baseline and thermally assisted welds, thus changing the tool rotation speed had a linear affect on the tool input power and could be calculated using the equations presented earlier. The ratio of power distribution between the shoulder and the pin was also assumed to be constant. Assuming a constant torque should be valid for small changes in rotation speed, since, at the shoulder at least, the workpiece temperature and hence material resistance, were similar. Taken from the baseline welding conditions, the torque value used throughout was 298Nm.

Using other work conducted at BAE Systems ATC as a reference[1,2], cryogenic liquid CO_2 is the most efficient, and practical cooling medium to use. Achievable cooling powers are of the order of approximately -300W. For the modelled assistants, a higher cooling power of -500W was selected for both cooling cases. Whilst still within the realm of experimental capabilities, using the higher power would also magnify any effect on changes in the temperature distribution between the top and bottom of the weld. For the internal heating case, a power of 500W was used. This is perhaps the highest power that could be used in practice, as increasing the input power further would significantly affect the structural integrity of tool pin, up to and including melting.

6.2.2.1 Cryogenic Cooling of the Tool Body

Figure 226 compares the through-thickness temperature differential for the baseline weld and the weld produced using the thermal assistant. For the latter, tool rotation speed was increased from 120rpm to 132rpm to match the CH0 peak temperature. This equates to a tool input power of 4.4kW. As is apparent from Figure 226, the addition of cooling applied to the tool body had very little effect on the through-thickness temperature differential. The change was a decrease of 5.9K or 3.5%.

6.2.2.2 Cryogenic Cooling of the Workpiece Surrounding the Tool

Figure 226 compares the through-thickness temperature differential for the baseline weld and the weld produced using the thermal assistant. For the latter, tool rotation speed was increased from 120rpm to 126rpm to match the CH0 peak temperature. This equates to a tool input power of 4.2kW. As is apparent from Figure 226, the addition of the cooling applied to the workpiece area surrounding the

[1] Price, D., Harrison, C., Williams, S. and Wescott, A. The Performance of Active Tensioning Techniques for Stress Control in Welding. Internal Report JS15232, 2004.

[2] Morgan, S., Wescott, A. and Colegrove, P D1.1M Development and Feasibility of Unproven SE Tools. Internal Report TES101379, 2007

tool had very little effect on the through-thickness temperature differential, and was in fact slightly detrimental (i.e. the temperature differential was increased). The change was an increase of 4.4K or 2.7%.

6.2.2.3 Internal Heating of the Tool Pin

Figure 227 compares the through-thickness temperature differential for the baseline weld and the weld produced using the thermal assistant. For the latter, tool rotation speed was decreased from 120rpm to 112rpm to match the CH0 peak temperature. This equates to a tool input power of 3.75kW. The effect of the heating source on the through-thickness temperature differential is more apparent than for the cooling sources. The change was a decrease of 23.1K or 14%.

From the results obtained from this modelling study, adding cryogenic sources to the welding process in the configurations suggested would have negligible effect on the through-thickness temperature differential. Of the techniques examined, internal heating of the tool pin would have the greatest benefit, though the improvement of 14% was only achieved by heating the pin to 1275°C. This temperature is approaching the melting point of most steels (approximately 1500°C) and it is questionable that the tool would retain sufficient mechanical strength to cope with the stresses of the FSW process under these circumstances. Furthermore, the practical implementation of internal tool heating would be extremely problematic. For thin-section material (<6mm) internal tool heating has been attempted by BAE Systems ATC using a laser to heat a hollow tool. The results indicated no effect from the heating process, although the weld thickness was probably insufficient to exhibit any through thickness changes. Scaling this work up to thicker section material is impractical due to the nature of the FSW equipment that would be involved, and uncertainty of the benefits that would be gained.

6.2.3 Conclusions and Recommendations

The following conclusions are drawn from this investigation:

1. For the configurations examined, and under practically achievable cooling conditions, cryogenics would provide no benefit to the through-thickness temperature differential during FSW.
2. Whilst there was some improvement in the through-thickness temperature differential using internal heating of the tool pin, the mechanical performance of the tool at these elevated temperatures would be unlikely to survive the stresses of the FSW process. Furthermore, the technical challenges for practical implementation of internal heating during thick-section FSW are not insignificant and beyond the scope of the COINS project.

The results obtained suggest there is little mileage in pursing further the application of thermal assistants for modifying the through-thickness thermal profile during FSW. Future efforts would be better directed to improving in FSW tool design in this respect.

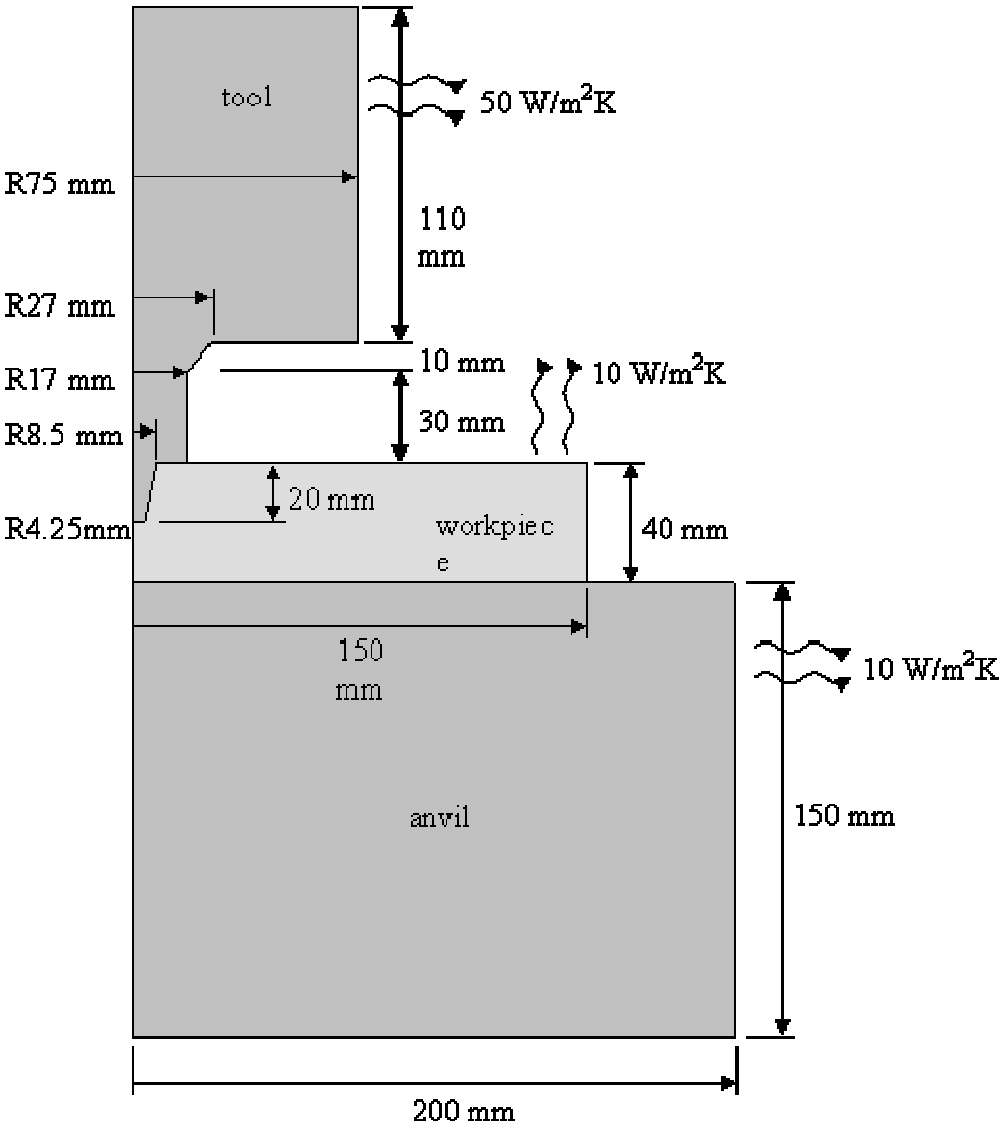

Figure 225: Model geometry

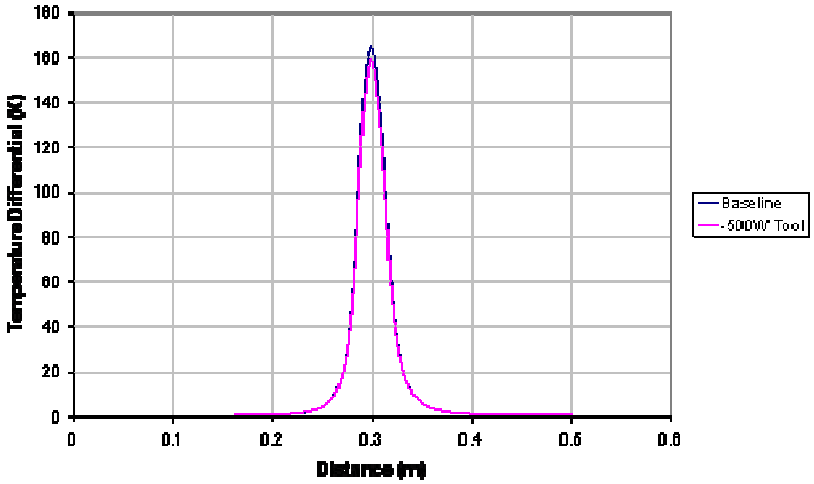

Figure 226: Comparison of the through-thickness temperature differential for baseline weld and the weld with cooling applied to the tool body

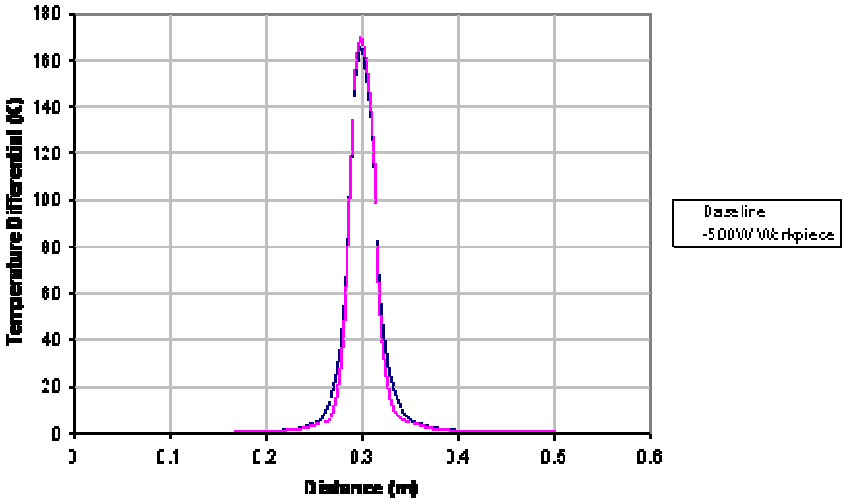

Figure 227: Comparison of the through-thickness temperature differential for baseline weld and the weld with heating applied internally to the tool pin

6.3 WP6: Process Modelling (ALA)

Alenia has presented the application of the FSW process to weld aluminum alloy in lap joints to be used in aeronautic industries. A wide experimental and numerical investigation on the lap joining of 2198-T4 aluminum alloy was carried out at the varying of the tool geometry and of the main process parameters. The obtained parts were accurately analyzed and the consequent observations together with the numerical results permitted to highlight the effects of the process parameters on the process mechanics and joint microstructure, allowing the set up of a few design rules for metallurgical and mechanical joints efficiency.

6.4 Task 6.1 Process Modelling (SHORTS)

Given the delays in both receipt of the Alcan sheet material and the subsequent manufacture of the required butt joints at GKSS, Shorts launched formability testing on 1.6mm, thick, 2024-T3 FSW weldments manufactured during a previous project with The Welding Institute (TWI), in Cambridge. The Forming Limit Diagrams (FLD's) were supplied to the University of Patras for initial verification of their modelling process. The specimen geometries, tool shape, boundary conditions and raw data were all included in the information package, supplied to Patras.

After this initial work was completed, the 2198-T3 and 2139-T3 FSW butt joint weldments were subsequently received from GKSS. Based on the preliminary 2024 testing results, Shorts limited the test programme on the advanced alloys to special uniaxial tension testing for the measurement of the plastic strain ratio, or r-value. The r-value is a parameter that indicates the ability of a sheet metal to resist thinning or thickening when subjected to either tensile or compressive forces in the plane of the sheet. Measurement of uniaxial yield strength was also recorded. Both sets of parameters provide inputs that can be used for the calibration of the Hill (1990) Yield Criterion or its subsequent proposed modification by Leacock.

For both of the parent materials, specimens were extracted at 0°, 15°, 30°, 45°, 60°, 75° and 90° to the rolling direction. Similarly for both of the welded joints, specimens were extracted at 0°, 15°, 30°, 45°, 60°, 75° and 90° to the direction of the weld. In all cases 3 specimens were extracted for each orientation i.e. 21 specimens per set, making 84 specimens in total. The testing was performed in accordance with ASTM E 517, with the exception that the specimens remained loaded during the r-value determination. The r-values were calculated using strain data taken at ε_L of 4% and 8% determined from the individual stress strain curves. The uniaxial tensile tests were performed on an Instron 8500 hydraulic testing machine at a constant cross-head speed of 0.075"/min. The longitudinal and transverse strains were recorded throughout the test using Instron extensometers.

The 2198 parent material exhibited considerable anisotropy with a difference of 150MPa between the 30°/45° samples and the 90° (L) direction samples. In comparison the difference in the FSW specimens was not as severe with a delta of only 55MPa between the 45° and 90° orientations. The 2139 material exhibited much more consistent yield strength properties with only a 50 MPa increase in strength as the orientation moved from 45° to 90°. The welded samples were even more consistent, with only a 12MPa delta between maximum and minimum. Weld efficiency ranged from 85% in the 90° orientation, to 99% as the specimens rotated from 30° to 45° to 60°.

In general a higher r-value indicates material with better formability. Consistency of the r-value with respect to the rolling direction of the material, however, is possibly of even higher significance, as it indicates the material is isotropic and tends to allow a uniform and predictable performance of the material during the forming process. It should be noted that the changes in the texture of the material during tensile straining may also have an effect on the r-value, effectively either increasing or decreasing it. Any changes in texture due to the welding process may therefore lead to variations in the strain effects across the test specimen width compared to parent material. Although the 2139 samples were consistent with respect to the rolling and welding direction they were also consistently below the 2024 baseline. The 2198 parent material displayed a much more variable performance with respect to the rolling direction with a r-value as high as 1.47 at 30° and as low as 0.37 at 75°. This degree of variation may have some impact on the consistency of the stretch forming operation in the T3 temper. FSW the 2198 material had the effect of limiting the highest r-value to 1.14.

Shorts have supplied a summary report to EAS-IW-Germany, for inclusion in Deliverable D7 - Process Modelling and Data for FSW.

6.5 Task 6.1 Process Modelling (Alcan)

- The contribution of flow stress modelling was reported in the deliverable D 7.
- A simple model called “flow stress predictor” based on the previously obtained flow stress-strain curves evaluates the threshold flow stress versus chemical composition. These final data give us a comparison of the flow stress data between different alloys and could be further introduced in a FSW model.

6.6 Task 6.1 Process Modelling (EADS France)

BT FSW experiments with process data monitoring were carried out on 23 mm thick 7449 TAF alloy, so that University of Patras validate their thermal modelling.
The welding conditions and parameters were those developed in Task 6.2: 23/15/20-26 type bobbin tool, full force control (F_{pin}=9kN, resulting F_z=0), 260 rpm rotation speed, 40 mm/min travel speed.
The spindle torque and 3D welding forces were measured thanks to delta pressure sensors in the fully hydraulic welding head.
Temperatures were measured using 0.5 mm diameter K type sheathed thermocouples inserted in 0.6 mm diameter holes with thermal compound.
The thermocouples locations are reported in Figure 228

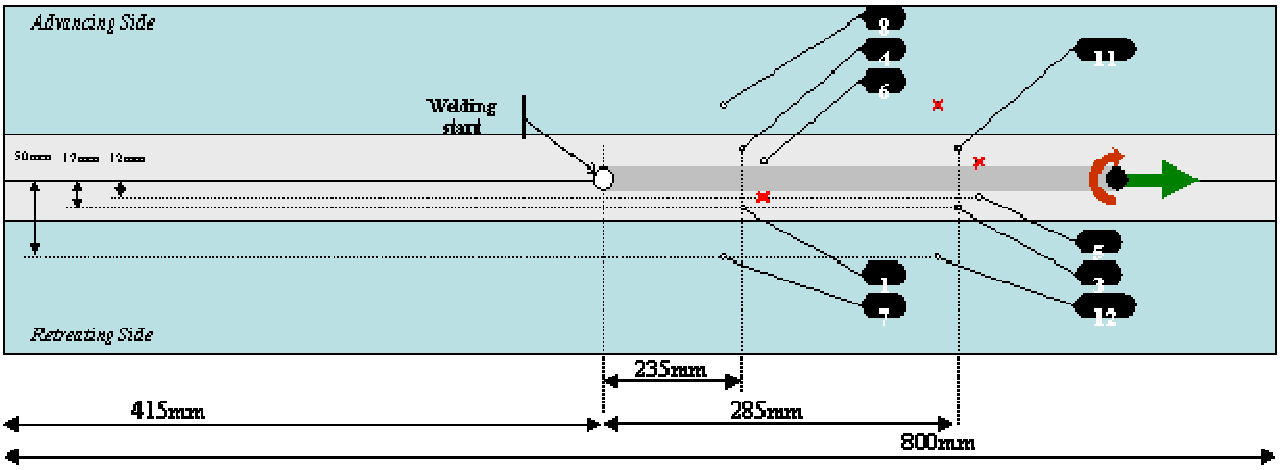

Figure 228: Thermocouples location in 7449 plates

Forces - torque and temperature measurements during Bobbin Tool FSW of 23 mm thick 7449 TAF alloy are plot versus time respectively in Figure 229 and Figure 230.

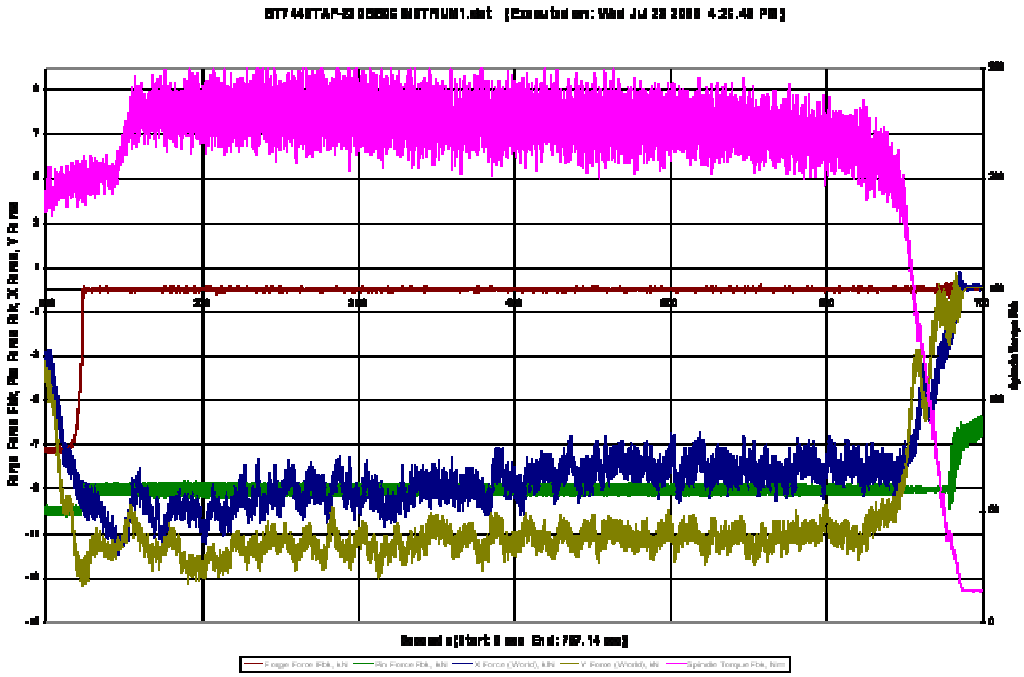

Figure 229: Forces and torque versus time during FSW of 23 mm thick 7449 TAF plates

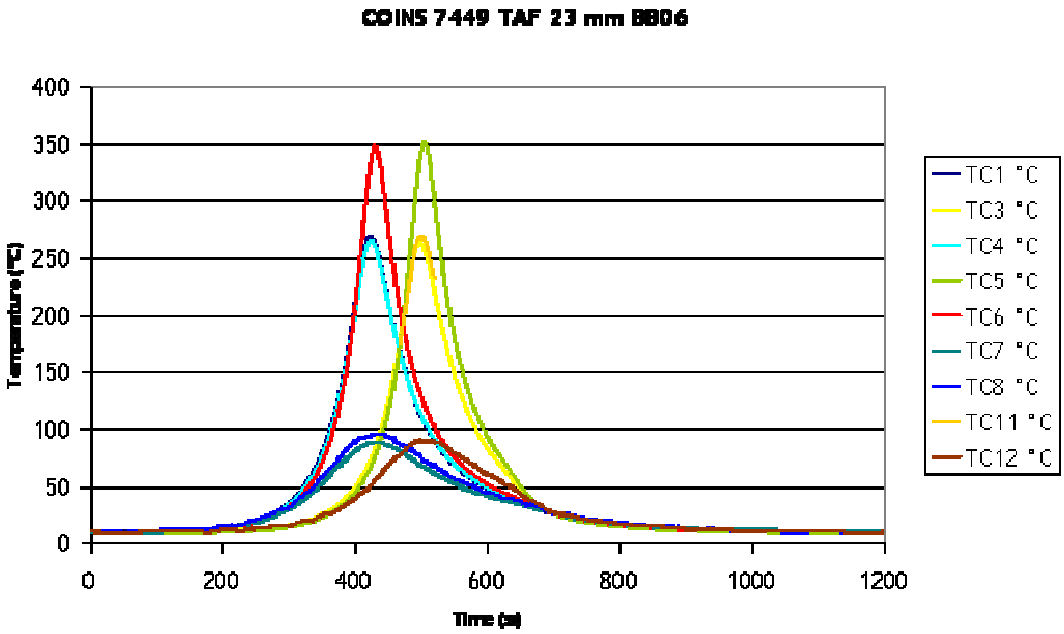

Figure 230: Temperature versus time during FSW of 23 mm thick 2050 TAF plate

The full force controlled welding test showed a very high and noisy spindle torque, about 230 N.m. Temperature measurements were satisfactory: temperatures were very reproducible; there was no significant difference between advancing and retreating sides.
The results were sent to the modelling Partner University of Patras.

6.7 WP 6.1 Process Modelling, Data and Fundamental Understanding (University of Patras)

Following to the studies concerning the Bobbin tool and the non-rotating shoulder in the case of Delta-N tool, in the presently reported period FSW using the Diabolo-pin tool (Figure 231), designed by EADS-IW, has been simulated. Thermal analysis of the procedure has been performed and the results have been compared to respective experimental temperature measurements in the frame of a “blind” simulation, for the validation of the proposed methodology.

Figure 231: Diabolo-pin tool design

In order to simulate the effect of this new tool in the development of temperature distributions and RS, the FE simulation methodology is applied. Global three-dimensional finite element models of the entire weld configuration are developed to simulate the friction stir welding process for butt joining two Aluminum 7449 plates 800x140x23mm The welding parameters and the geometry of the tool, as provided by EADS-IW, are shown in table 10.1.

	Diabolo-pin-tool (7449)
Pin radius – R_{pin}	12-15 mm
Pin height – H_{pin}	23 mm
Upper Shoulder Radius- R_{Shup}	11.5 mm
Lower Shoulder Radius- R_{shdn}	11.5 mm
Tool rotational speed-ω	260 RPM
Welding velocity-v_w	40 $^{mm}/_{min}$
Normal toll force-P_N	About 9 kN
Horizontal tool force-P_H	About 7.5 kN

Table 27: Geometry and welding parameters of the studied case, as provided by EADS-IW

A very dense mesh is used in the area along and nearby the weld line, in order to simulate the complex physical phenomena that take place in the area, while a coarser mesh is used for the rest of

the structure. The utilization of symmetric boundary conditions leads to the significant reduction of the total element number in about 78000 ‘Solid70’ elements. Over and under the welded plates there are Copper cooling bars. Furthermore, a water flow system for quick and effective cooling of the welded plates is used Figure 232).

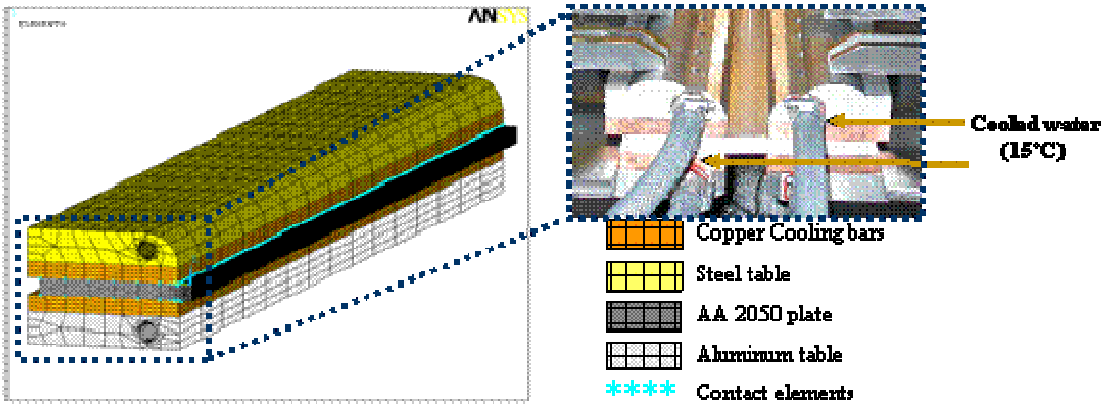

Figure 232: FSW FE model configuration for the Diabolo-pin tool case

In order to take into account the heat transfer between the welded plates and the auxiliary devices (such as copper bars and steel table) thermal contact elements ‘TARGE170’ and ‘CONTA175’ are used. The selection of the boundary conditions, mentioned above, is based on the experimental conditions that take place during the respective experiments, implemented in EADS-IW-France.

A transient thermal analysis is conducted using temperature dependent thermal material properties, such as conductivity, convection coefficient and specific heat. Experimental temperature measurements from EADS-IW-F have been used for the validation of the numerical simulations. In Figure 233, the points where temperature has been measured are shown.

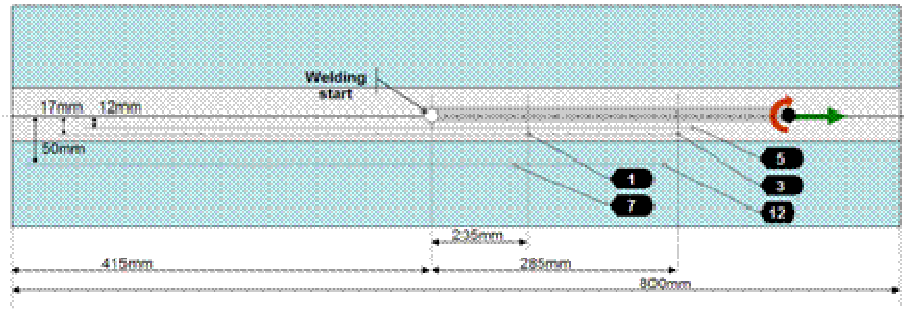

Figure 233: Temperature measurement points for the case of Diabolo-pin tool

For Diabolo-pin tool, due to the lack of experimental data, which are required in order to define the undetermined parameters δ and μ_F and thermal model to be calibrated, ranges of these parameters were used, i.e. $0.4 \leq \delta \leq 0.8$ and $0.3 \leq \mu_F \leq 0.5$. and primarily, temperature history predictions, which have been arisen from two thermal analysis using the minimum and maximum δ and μ_F values, are presented in form of ranges and not as single diagrams. After the experimental measurements were

been available, a comparison between prediction and experiment was performed (Figure 234). As it can be observed from Figure 234c for the material nearby the weld line the prediction comprises a very good and reliable approach of the experimental measurement. On the other hand, as the distance from the weld line rises (i.e. Figure 234 (b) and Figure 234 (a), it can be observed that the model underestimates the developed temperatures. This underestimation may be occurred due to the complex cooling system which leads to an inaccurate simulation of the entire cooling process.

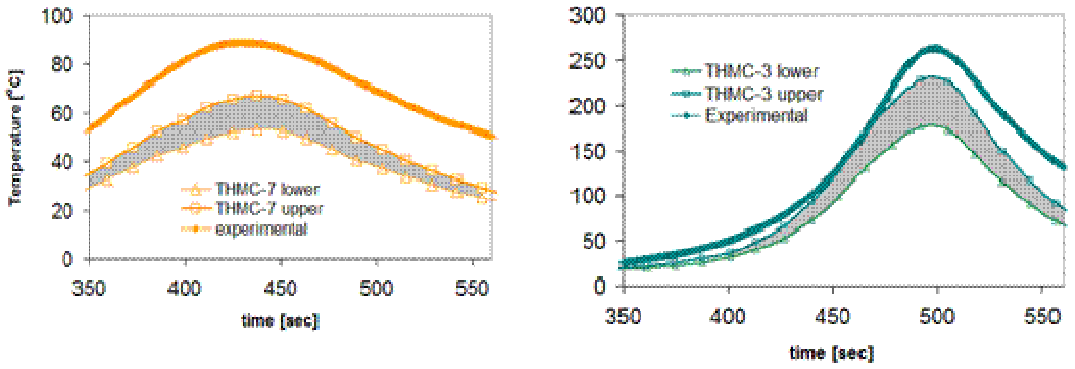

(a) **(b)**

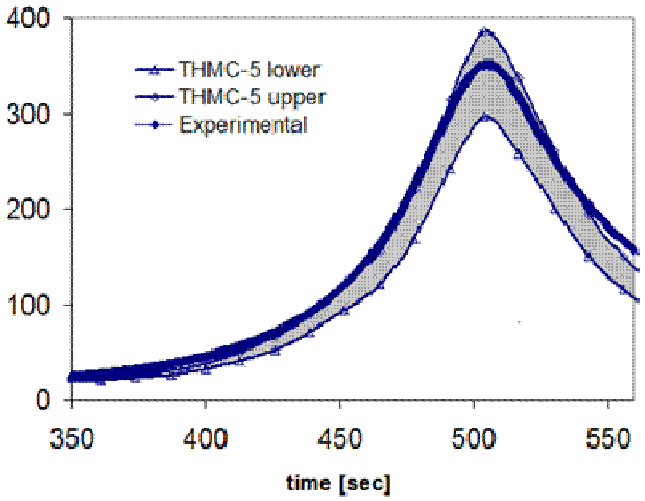

(c)

Figure 234: Comparison between temperature experimental measurements and FEA results – Diabolo-pin-tool (EADS-F)

6.8 Task 6.2 Primary processing improvements (BAES)

6.9 Task 6.2 Primary processing improvements (AD)

6.10 Task 6.2 Primary processing improvements (EADS France)

EADS F contribution to task 6.2 (Development of the Bobbin Tool technique for 23 mm thick 7449 alloy) was completed during the previous reporting period.

6.11 Task 6.2 Primary processing improvements (EADS Germany)

The new DeltaN tool will be built up, assessed and improved.

These activities origins are in the invention and patent application DE102005030800.7 of 7.7.2005 titled “Reibrührwerkzeug sowie Verfahren und Vorrichtung zum Reibrühren”. .
The Delta N welding tool concept is the consequence of the assumption that the simplification of the heat generation leads too advantages in the weld performance.

The simplification is being achieved by decoupling the two tool components pin and shoulder and further by completely avoiding shoulder revolutions. As a consequence the only rotating component is the tool pin.

1. Reduction of distortion because of homogeneous heat generation only and around the tool pin.

2. Reduction of the total amount of heat because of the avoidance of the rotating shoulder heat generation which does not benefit the welding process. Therefore the heat affected zone should be smaller compared to welds performed by tools using rotating shoulders as standard and bobbin tool.

3. Reduction of the vertical down force during welding. The DeltaN tool shoulder contact is a slide of solid shoulder on solid weld component surface. Using a standard tool the shoulder contact is solid on softened because of the shoulder revolutions the components surface is heating up and softening. The welding parameter have to be adjusted to this fact and therefore the shoulder conditions dominated the welding process although the weld itself does not happen in this area.

The two main emphasise of the DeltaN tool development activities in this task where the design and built-up of in total 3 generation of DeltaN tools. Each tool generation has been assessed and improved.

Generation 1 has been designed and built-up in the very early phase directly after the invention about the DeltaN concept has been made.

The de-coupling of the two components shaft/shoulder on one side and the pin on the other side has been realised with only one single bearing, Figure 235 and Figure 236.

The motivation for this layout was just to verify that the DeltaN concept in principle works.

The advantage of the simplicity came together with a consequent overloading of the single bearing and therefore a very limited lifetime of that component. Important to mention is that in all 4 DeltaN tool generations only standard bearings with a acceptable cost and performance ratio have been used.

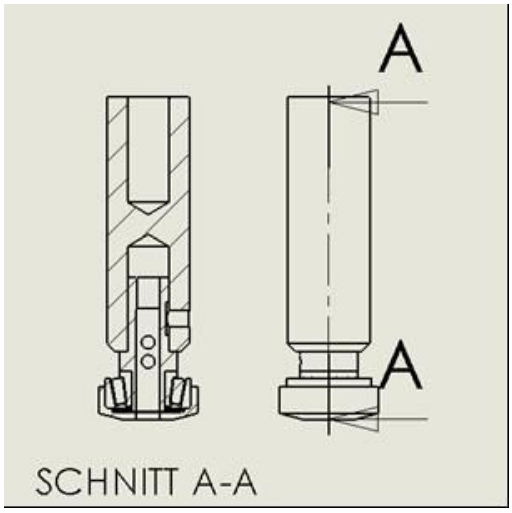

Figure 235: Cut section and side view of DeltaN Tool gen1

Figure 236: Shoulder cup, shaft and bearing as the three main components of the DeltaN tool concept

The experiences that have been made with generation lead to the DeltaN tool layout of generation 2. To split the complex loads during welding here 3 bearings instead of 1 have been implemented: One is taking the axial loads and two take the radial loads resulting from the lateral forces and their induced bending loads, Figure 237 and Figure 238.

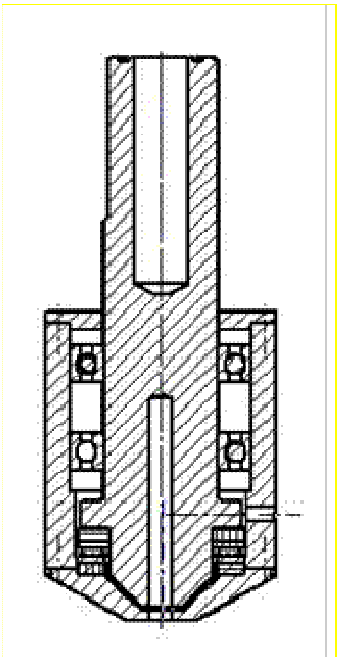

Figure 237: DeltaN tool cross-section

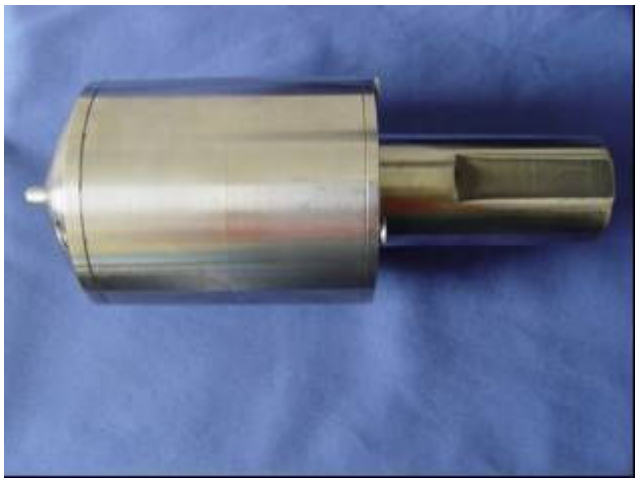

Figure 238: DeltaN tool

With this generation 2 DeltaN tool successful welds on 15 mm plate material have been performed. Although it is much stronger than generation 1 the limitation of this tool are still severe:

The vertical downforce must be kept above 25KN. Otherwise the shoulder components starts begins to rotate because of the high friction inside the bearings.

The temperature of the tool becomes critical for the bearings when using revolutions higher than 600 1/min. Cooling with accelerated air brings benefit and is suitable but is not a professional solution.

The outer dimension of the tool case are diameter 140 mm. Therefore the risk to collide with the clamping equipment is high.

To abolish the last mentioned disadvantage of the former generation the generation 3 has been realised. The layout is similar with 3 bearings but the benefit is the change of the bearings positions and the consequence that for this reason the outer diameter could be reduced down to 80 mm, Figure 239 and Figure 240.

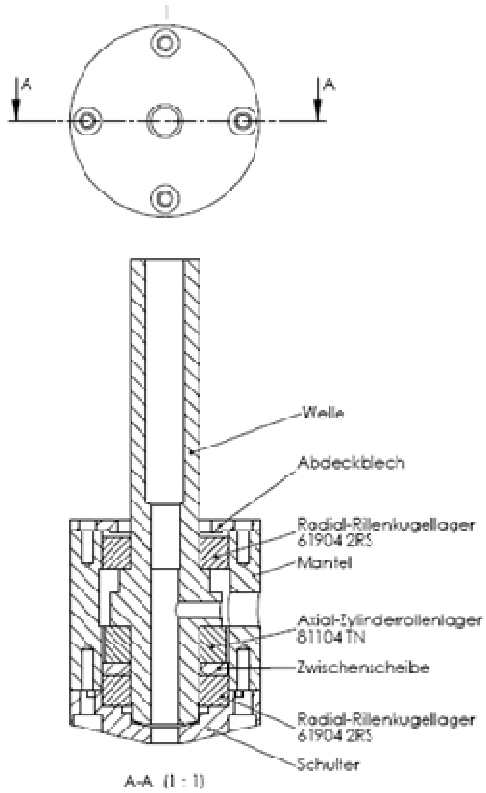

Figure 239: Cut section view of Delta N tool generation 3

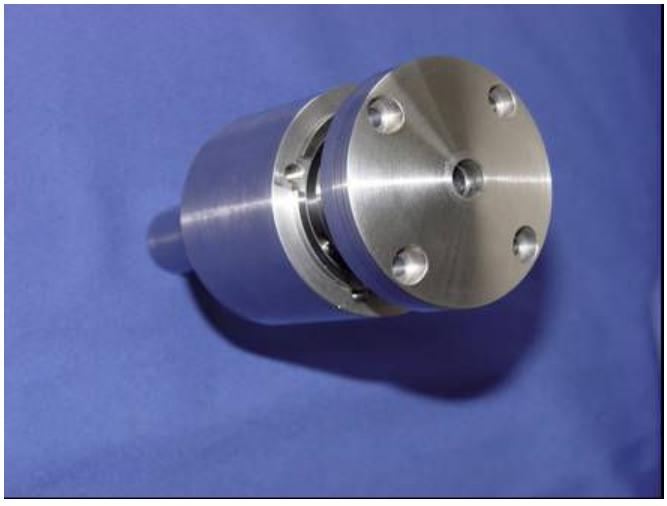

Figure 240: Top view of DeltaN tool generation 3 shoulder cup and tool case

Welds of up to thickness 10 mm have been realised successfully but with the same restrictions as with generation 2.

The DeltaN tool generation 4 summarises all experiences which have been made with the former generation 1 to 3.
The limited lifetime of the bearings lead to the conclusion that it should be beneficial to avoid bearings.
This decision brings a completely different layout of the tool. The DeltaN generation 1 to 3 where stand-alone tools which could be used on all machines or welding heads which have spindle and tool holder. Generation 4 is individually designed for the ESAB Superstir because the tools case is directly fixed to the machines welding head and not to the spindle, Figure 241 and Figure 242.

Figure 241: DeltaN tool generation 4 tool case fixed at the lower end of the ESAB Superstir welding head

Figure 242: DeltaN tool generation 4

The DeltaN generation 4 tool case consists of three parts which increase the flexibility of the tool: On the upper end there is a flange part that is fixed to the ESAB machine by screws. The dimensions of the mid part of the tool case are defined by the ESAB spindle in length and diameter. The spindle and its tool holder are now inside the DeltaN tool case and are directly holding the pin. The pin comes out through a hole in the lower shoulder part of the tool case. That design is extremely robust because it is

simple.
At the lower end of the tool there is a shoulder part that can be adjusted to the given welding application in length and diameter in a limited range.
All disadvantages of the DeltaN toll generations 1 to 3 have been eliminated by changing the tools layout in that significant way.
The limitation in revolutions does not exist any more.
The lifetime limitation now is defined by the pin.
Next to the symmetrical weld nugget shape and the resulting reduction of distortion the second argument for the development and use of the DeltaN tool concept is the possible reduction of the vertical down force compared to the use of a standard FSW tool. The necessary vertical down force for DeltaN welding has been determined on a butt joint weld of alloy 2050T3, thickness 15 mm. On one single weld the vertical down force has been varied between 10 and 25 KN. Visually tight welds without internal features have been realised on alloy 2050T3 with 15 KN vertical down force using feed of 200 mm/min and revolutions of 500 1/min. This result has been confirmed by horizontal bending tests: Because it is not recommended to bend test a 15 mm plate weld a slice of thickness 3 mm has been cut along the plate section. This slice has been bend tested as a horizontal bend specimen. The bending test results confirm the visual test results: The 10 KN weld bend specimens fail after 40°. The 15, 20 and 25KN weld specimens fail after 110°.
Metallographic investigation by macro and micro sections has shown that it is possible to weld 15 mm sections with DeltaN tools gen4. Increasing the vertical down force from 10 to 25 KN the macro and micro sections confirm the result of the bend test.
The potential of the DeltaN tool in reduction of vertical down force is significant. A comparable standard tool weld has been performed with vertical down force of 32KN. Using this as reference the potential for vertical down force reduction is approximately 50%.
The use of a DeltaN tool does no longer mean a high complexity to be dealt with. The tool design became simple and robust and the extra-amount of adjustments is not much higher compared to a standard tool. Depending on the welding application DeltaN allows a reduction of the vertical downwards force of up to 50%. The remaining distortion after welding can be reduced significantly depending on the welding application. For the real component weld on the A380 wing flap rib the distortion has been reduced by factor of 8 compared to the use of a standard welding tool.

6.12 Task 6.2 Primary processing improvements (GKSS)

6.13 Task 6.2 Primary processing improvements (Airbus UK)

6.14 Task 6.3: Post Weld Treatments (BAE Systems)

In addition to the developing FSW, complementary processes such as corrosion protection of welds have also been addressed within COINS. ATC activity on this topic has be an evaluation of High-Power Beam Surface Melting (HPBSM). This process uses a laser or electron beam to induce rapid solidification processes that have been shown to increase the surface chemical and microstructure homogeneity leading to an increase in corrosion resistance. Such a process would be considered complementary to any existing treatments such as painting. Included is a concept design for mobile electron-beam system for treatment of large areas or components.

6.14.1 High-Power Beam Surface Melting

Surface engineering involves the modification of the properties of only the surface of a material, leaving the bulk properties unchanged. This is advantageous as properties such as wear or corrosion resistance can be modified without a loss in strength or ductility. HPBSM, with lasers or electron beams, can be used to induce rapid solidification processes that have been shown to increase the surface chemical and microstructure homogeneity leading to an increase in corrosion resistance.

Laser Surface Melting (LSM) can improve the corrosion resistance of bulk material and also FSW joints. However, this technique has possible problems: there are concerns with the application of LSM including the limitations of laser processing parameters that may affect the melt layer thickness as in many cases only relatively a thin modified layer have be produced.

Modelling has shown that a key parameter for increasing the LSM layer thickness is the pulse duration, which is an inherent property of the laser. Electron Beam Surface Melting (EBSM) is an alternative rapid solidification technique to LSM, which has a greater degree of flexibility in the processing parameters, including pulse duration.

6.14.2 Laser Surface Melting

Laser Surface Melting (LSM) is an HPBSM technique which is used to alter material surface properties through rapid solidification. LSM can be performed using many different lasers each of which has its own characteristics and processing capabilities. As a variety of lasers can be used for LSM, there is a wide range of processing parameters available which are selected to suit the material being processed and the material property being modified.

In LSM, radiation is absorbed into a thin surface region and the thermal energy is then conducted away from the surface into the material bulk in all directions. In LSM the heating rates used are high enough to melt the surface region and a fusion interface then propagates down into the substrate. Further increases in the surface heating will result in vaporisation of material. Once the laser radiation is removed from the material surface, rapid cooling occurs, which freezes the material to form non-equilibrium structures and compositions as there is insufficient time for diffusion or precipitation.

Investigations into LSM have been based on commonly used alloys such as aluminium alloy AA2024. Figure 243 shows a typical surface microstructure and cross-section from excimer LSM and Figure 244 shows the micro-electrochemical characteristics of the surface produced from this LSM process. The corrosion resistance of the material is improved as there is a decrease in both the anodic and cathodic activity. The anodic activity shows a plateau region where there is no corrosion occurring and the pitting resistance has been greatly improved. The decrease in cathodic activity means that there is a decrease in the rate of corrosion.

This increase in the corrosion resistance is due to alterations in the microstructure. For many materials, precipitates have been linked to the initiation and propagation of corrosion; in aluminium alloys it is the constituent precipitates that act as cathodic sites and have been associated with the initiation of pitting and Inter-Granular Corrosion (IGC). The removal of precipitates from a surface region has been highlighted as a key factor to improving a material's corrosion resistance. LSM can remove surface precipitates by dissolution into the matrix solid solution. In most LSM studies complete removal of precipitates and surface homogenisation has not been achieved. LSM does however reduce the number of precipitates in the surface region and modifies the structure.

Newer generation 2xxx series aluminium alloys with increased lithium content such as AA2198 have much better corrosion resistance than AA2024. An investigation to ascertain whether the application of a LSM treatment would be beneficial in such alloys found the corrosion of AA2198 was localised and tended to penetrate preferentially along the grain boundaries aligned with the material rolling direction. The main intermetallic particles in AA2198 were found to contain iron and copper and some of these particles were cathodically active. This cathodic activity meant that the untreated parent material showed the highest cathodic current density in micro-electrochemistry measurements when compared to that of an LSM AA2198 surface. Micro-electrochemistry measurements showed that the LSM treatment on AA2198 reduced the cathodic reactivity, but there was minimal change in the anodic reactivity compared to the parent material.

The corrosion resistance of the material was investigated further by long term immersion tests. In these tests the surfaces of the untreated AA2198, both in the as-received and milled-surface condition showed uniform corrosion over the entire surface. In contrast, however there was non-uniform corrosion in the form of large pits on the LSM samples particularly along a scratched area, where the modified layer is damaged to expose the underlying substrate. The LSM treatment does not therefore sacrificially protect the AA2198 substrate once the layer is damaged. The LSM layer did provide protection though when it remained intact.

The LSM treatment was applied to a FSW of AA2198, to ascertain whether it offered any corrosion protection. An un-machined AA2198 FSW showed when tested in immersion tests that there was preferential corrosion in the weld zone and heat affected zone. LSM treatment of an un-machined weld changed the corrosion morphology to that of a more uniform attack across the surface. However an LSM treatment on a weld that had been machined before LSM exhibited a uniform attack only when the layer was undamaged. A scratch through the layer localised the attack in the scratch which penetrated into the substrate.

6.14.3 Laser Surface Alloying

Laser Surface Alloying (LSA) is similar to LSM except for the addition of extra alloying elements into the final modified layer. For the case of aluminium alloys, this can be achieved by alloying with powder, sputtering metal layers or formation of a chemical conversion coating on the layer. The incorporated elements in LSA can change the electrochemical reactivity of the laser treated layer and further increase the corrosion resistance. This benefit has been shown in excimer laser treatments of AA2024 where the LSA layer had a higher corrosion resistance than the LSM layer that was produced using the same processing parameters.

During LSA of AA2024, elements that have been shown to provide an increase in corrosion resistance include; chromium, manganese, molybdenum, tantalum, tungsten, vanadium and zirconium. The effectiveness of an alloying element on the corrosion resistance depends on the stability and solubility of the oxidised species that the alloying element forms on the material being treated, as a stable insoluble oxide will provide high corrosion resistance.

The effect on corrosion resistance from excimer LSA of a wide variety of elements deposited by chemical dipping on AA2024-T351 has been investigated with the highest corrosion resistance achieved by alloying with manganese. In this chemical dipping process a conversion coating containing the required element in the oxidised form was deposited on the surface and upon melting the element was incorporated in the metallic form into the modified layer. The increase in corrosion

resistance from LSA of manganese was due to an overall decrease in the surface passivity from a decrease in the cathodic activity.

Excimer LSA of AA2024 with sputtered layers of a range of elements was performed to further understand the effect of different elements on the corrosion improvement. It was found that the elements with a lower melting point such as manganese and chromium were more effective at increasing the breakdown potential with chromium achieving the highest. The less successful elements investigated with higher melting points were tungsten, tantalum and molybdenum. The corrosion attack that was observed on these LSA layers was similar to that of LSM layers with general attack occurring before de-lamination of the layers.

To increase the corrosion resistance of the surface by LSA there must be high element incorporation into the modified layer which is achieved more easily through sputtering deposition than by dip coating. The thickness of the sputtered layers has also been shown to influence the degree of element incorporation with sputtered layers of 0.1µm producing higher element concentrations compared with thicker sputtered layers. The higher element incorporation provides the increase in corrosion resistance.

LSM has been applied to 2024 and other 2xxx series alloys which contain lithium and provided an increase in the corrosion resistance. LSM has other benefits which include the absence of damage to the bulk material properties, non-contact processing, and the fact that there are few restrictions on component shape or treatment area. However, lasers have disadvantages which include the high initial investment cost, and the limitation that only a small volume of material can be treated at one time.

LSM has also been successfully applied to surfaces of FSW joints and there has been shown an improvement in the corrosion resistance by homogenising the surface. FSW tends to produce welds of poor corrosion resistance owing to sensitisation of the microstructure from precipitation and increased anodic activity across the weld.

Excimer LSM has been applied to weld surfaces produced by the FSW of AA2024, AA2198, AA7010 and AA7449 aluminium alloys. The LSM treatment suppressed corrosion over the welds by decreasing both the number and depth of corrosion attack sites. The corrosion resistance increase from LSM remains whilst the layer is intact, however investigations into LSM of FSW on AA2024 and AA7449 have shown that once the layer is scratched there can be significant substrate attack in the weld's HAZ region.

Ideally the LSM layer, to improve the corrosion resistance, would be smooth, crack free, protective barrier with complete precipitate removal with a uniform surface oxide and contain no regions of sensitisation from processing.

6.14.4 Electron Beam Surface Melting

Electron Beam Surface Melting (EBSM) is a HPBSM technique that uses a high energy beam of electrons to interact and modify a surface. The aim of EBSM is to melt and re-solidify the surface to form through planar solidification a homogeneous layer of well controlled thickness. This layer would have improved corrosion resistance by the removal of reactive precipitates from the surface and retaining the elements in a solid solution. For such a modified layer to be achieved requires a careful understanding of the electron beam interaction and the affect of different processing parameters.

BAE Systems has developed an electron beam system using a basic design taken from a system developed at The Institute of High Current Electronics at the Russian Academy of Sciences. The Russian design provided the key system features for processing which are shown in the schematic outline in Figure 245 and in a system photograph shown in Figure 246. Although the key features were taken from the Russian design, the BAE Systems design was built to generate lower powers and have more flexible electronics.

Key features include; the cathode, the vacuum gases, the sample fixings and variable pulse duration. The basic design of the system involves the movement of the sample surface underneath the pulsing electron beam. The design allows for movement of the sample in three directions to provide focusing and treatment over an area. Focusing is also aided by mounting the sample at an angle to the beam as shown in Figure 245.

Figure 245 also illustrates the shape of the system cathode which is a critical component and has been developed from previous work. The cathode of the system is important as its electrical resistance affects the electron discharge stability and its shape controls the beam focusing of this system. The system used a circular aluminium cathode with a radius of curvature on the side that faced down into the processing chamber. The concave shape was designed to increase the ability for the beam to self-focus and this would achieve high energy densities for processing at low cathode separations within a simple system. An aluminium cathode was used and it produced stable electron discharges until the cathode started to degrade by loss of oxide uniformity. Alternative cathodes could have been used with higher resistivity that did not degrade but the advantage of using an aluminium cathode was that the discharge performance could be easily regenerated by simple mechanical processing. The cathode stability was further increased as the system used a gas flow of helium with 5% oxygen mixture. The addition of oxygen was critical to maintaining the cathode stability and there was the added bonus that it also increased the electron discharge yield.

Once a stable electron discharge was produced, EBSM could be performed by passing samples through the beam as shown in Figure 245. To pass the samples through the beam they were mounted on a platform either at an angle or flat. Samples were mounted at an angle to vary the cathode to sample separation as it moved through the beam. The variation in separation meant that there was also a change in the beam focus and energy density at the surface during treatment at set processing parameters such as energy, pulse duration or number of pulses per unit area. This variation in separation also aided experimental set-up with identification of the focus. The system was designed to have changeable pulse duration so that the modified treatment depth could be varied and this would identify the optimum treatment that produced a thick, crack free, homogeneous layer.

Previous EBSM work has been on a variety of materials using a range of electron beam systems. Figure 247 shows typical surface and microstructure modification using the BAE Systems electron beam on AA2024.

The main bulk of the EBSM work has been for the improvement in wear or corrosion resistance of many different materials including pure metals, steels, aluminium bronzes, titanium alloys and aluminium alloys. The increase in wear resistance is achieved from microstructural refinement providing an increase in the surface hardness. Some problems have been encountered with improving the wear resistance due to poor surface finish, non-uniformity of treatment depth, and the presence of both pores and cracks within the modified layer. The microstructure refinement that increases the wear resistance can also increase the corrosion resistance due to changes in the precipitate

distribution. The dissolution of reactive particles can also increase the corrosion resistance with the production of a homogeneous surface.

6.14.5 EBSM Concept Design

The electron beam is generated and propagated in a low pressure environment, typically 0.2 torr. If the technique is to be used in an industrial environment for the treatment of metal workpieces much larger than the low pressure chamber that houses the e-beam, a means must be devised to maintain this pressure during treatment. The incorporation of a sliding seal between the e-beam chamber and workpiece should permit this. In addition, some method of scanning the beam within the chamber and, also of moving the chamber with respect to the workpiece, must be implemented. Finally, consideration has been given to the type of vacuum pumps that would be necessary.

The following features of the mobile processor have been considered:

1. Beam scanning
2. Processor translation
3. Sliding seals
4. Chamber evacuation

These will now be discussed in turn.

6.14.5.1 Beam Scanning

In the event of the mobile processor treating a FSW joint, the e-beam will have to traverse a distance of ~25mm to either side of the centre line of the weld (in order to cover the heat affected zone), i.e. a total scan of ~50mm. It is likely that the weld line will be many metres long and so the most straightforward operation would have the vacuum chamber moving in this direction with a transverse scan to cover the weld and heat affected zone. In the present laboratory set-up the e-beam is generated from a concave cathode with a focussing distance of ~10cm (the precise distance is current dependent). These dimensions are shown in Figure 248, where x is the beam path length to the centre point of the weld, y is the path length when the beam is at the outermost point of the transverse scan. x is nominally 10cm, y is then given by,

$$y = \sqrt{(1002 + 252)} = 103$$

If the beam is set to focus at 101.5mm from the cathode centre, then at any point in the scan it will never be more than 1.5mm out from this. Initial tests indicate that the subsequent effect on spot size and surface melting variation across the traverse would be acceptable but this would probably need to be verified for each set of operating parameters (workpiece material, required melt depth etc). Otherwise the current could be adjusted so as to maintain a constant focus condition.

The scanning could be achieved by means of a motorised gimbal mounting on the cathode holder with bellows between the cathode holder and the rest of the vacuum chamber. Such an arrangement is sketched in Figure 249. The underside of the processor with some provisional dimensions is shown in Figure 250. The aperture is shown as a 15mm x 60mm rectangular aperture – this allows the beam to scan to 25mm either side of a weld centre line.

6.14.5.2 Processor Translation

The e-beam processor may have to treat relatively long objects (wings, fuselages). In consequence, it is proposed to fit a remotely controlled, motorised drive. An alternative would be to suspend the processor from a gantry.

6.14.5.3 Sliding Seals

The design of the sliding seal(s), which is located between the underside of the chamber and the upper surface of the workpiece, is probably the most demanding aspect of this study.

In order to reduce the frictional load on the seal the mounting of a set of wheels or ball bearings on the underside of the processor is recommended. These allow only a partial compression of the seal and prevent the processor being forced into contact with the workpiece when the chamber is evacuated.

Three seal companies and the Welding Institute were contacted for advice. The companies identified were:

- FTL Seals Technology Ltd, Leeds UK
- Freudenberg Simrit LP, Lutterworth UK
- Garlock, Eland, West Yorkshire UK

FTL recommended a moulded elastomer seal with the cross section shown in Figure 251 The seal would make a tight fit into the groove on the underside of the processor. The cost would be very low – perhaps less than £20 per seal. The seal could be coated with a low friction material such as PTFE.

Freudenberg-Simrit considered that ‘o’ rings would probably suffice. Garlock suggested an inflatable seal that would have to be deflated when the processor was in translation – some form of internal sliding seal would be required in the processor in order to prevent the e-beam chamber going to atmospheric pressure when the inflatable seal was deflated.

The Welding Institute advised that sliding seals have been an area of intermittent investigation since the 60s, that TWI carried out work for a local company, CVE (Cambridge Vacuum Engineering) on this topic and provided photos of such a seal (see Figure 252) but has proved unwilling to give further information (presumably without a commercial agreement in place). This photograph shows a double seal arrangement (as in our design) with internal rollers. The seals appear to be fabricated from a high density, felt-like material.

It is probable that the e-beam processor would have to treat curved surfaces. If we assume a curve in a single dimension and a minimum radius of curvature of 2m then the seals will have to accommodate this as shown in Figure 253.

The outer seal will have to be capable of the greatest variation in thickness and it is easily shown for the layout above that this will have to be ~ 0.5mm for a workpiece radius of 2m. This change in thickness should be feasible for the FTL design and also for an ‘O’ ring if it is > 4mm thick.

The seals will have to be capable of withstanding abrasion from the workpiece when the processor is in motion. Low friction coatings (e.g. PTFE) could be applied to the seals to assist in this.

6.14.5.4 Chamber Evacuation

The double seal arrangement permits the use of a differentially pumped system - for the e-beam zone and an intermediate one between the seals. The e-beam zone would be pumped down to the lowest pressure of ~10-2 torr whilst the zone between the seals was maintained at a pressure between this and atmospheric. Figure 250 and Figure 254 show the dispositions of the vacuum ports to the workpiece for the two zones and the configuration of the zones within the processor body.

The advantage of pumping the outer zone is that a leak from the outer to the inner zone across the inner seal will be of less consequence if the outer zone is at a pressure significantly lower than atmospheric.

Specification of the type of pumps required depends on the leak rate of the seals – probably highest when the processor is in motion. Until this can be quantified (and this will depend on the surface roughness and seal design) it is safest to allow a large margin of accommodation for the pumping capacity required. Discussions with Severn Science (a local vacuum equipment dealership, Bristol UK) have resulted in the following tentative recommendations:

1. Outer zone – Edwards XDD1 diaphragm pump, pumping rate 1.2m3 hr-1, ultimate vacuum ~2 torr. If the leak rate is higher then an Edwards scroll pump, XDS5 (5 m3 hr-1) or XDS10 (10 m3 hr-1) will be necessary.
2. e-beam zone - Edwards scroll pump, XDS5.

If these pumps can maintain a base pressure of ~10-2 torr in the e-beam zone then a helium-oxygen bleed can be used to provide the optimum plasma conditions for beam generation. In our laboratory facility this takes place in the pressure range 0.15 – 0.4 torr. An electronic pressure monitoring and control system would be devised and fitted to the processor head.

The salient features have been considered of a mobile, pulsed electron-beam processor for metal surface treatments. These include a scanning beam system, a method for translation across a workpiece surface, sliding seals and maintenance of the optimum pressure conditions within the processor head.

A beam scanning system could include a gimbal mounted, motorised cathode holder mounted on a bellows at the top of the processor. The beam would exit from a rectangular aperture on the processor underside. The processor could translate over a workpiece surface with the aid of computer controlled, motorised wheels on its sides. The most significant technical uncertainty is probably the design of the sliding seals that will be required to maintain adequate vacuum conditions in the e-beam zone when the processor is moving. Such seals would be subject to abrasion and would have to accommodate both local surface irregularities and larger scale curvatures. Advice has been sought from seal manufacturers and The Welding Institute. As a result a possible design has been identified – a custom elastomer seal that locates in a rectangular groove on the processor underside and has a projecting flexible tongue to seal against the workpiece. Two seals would be used with differential pumping for the zone between them and the inner, e-beam zone.

A prototype system in which the all the above could be demonstrated could thus be built with a reasonable degree of confidence.

6.14.6 Summary

HPBSM has shown to improve the corrosion resistance of certain materials. This is particularly the case with LSM of aerospace aluminium alloys, where there has been considerable research and development. However, there are limitations with the lasers parameters available. EBSM has a greater parameter flexibility then LSM but has not been as extensively researched in terms of improving materials corrosion resistance. The main concern for the application of EBSM is the processing requirement of a soft vacuum, however this document has shown how floating seals could be used to meet the vacuum requirements. Therefore both LSM and EBSM have the capability of being scaled-up into an industrial process and would be particularly suitable in the application of localised surface treatments.

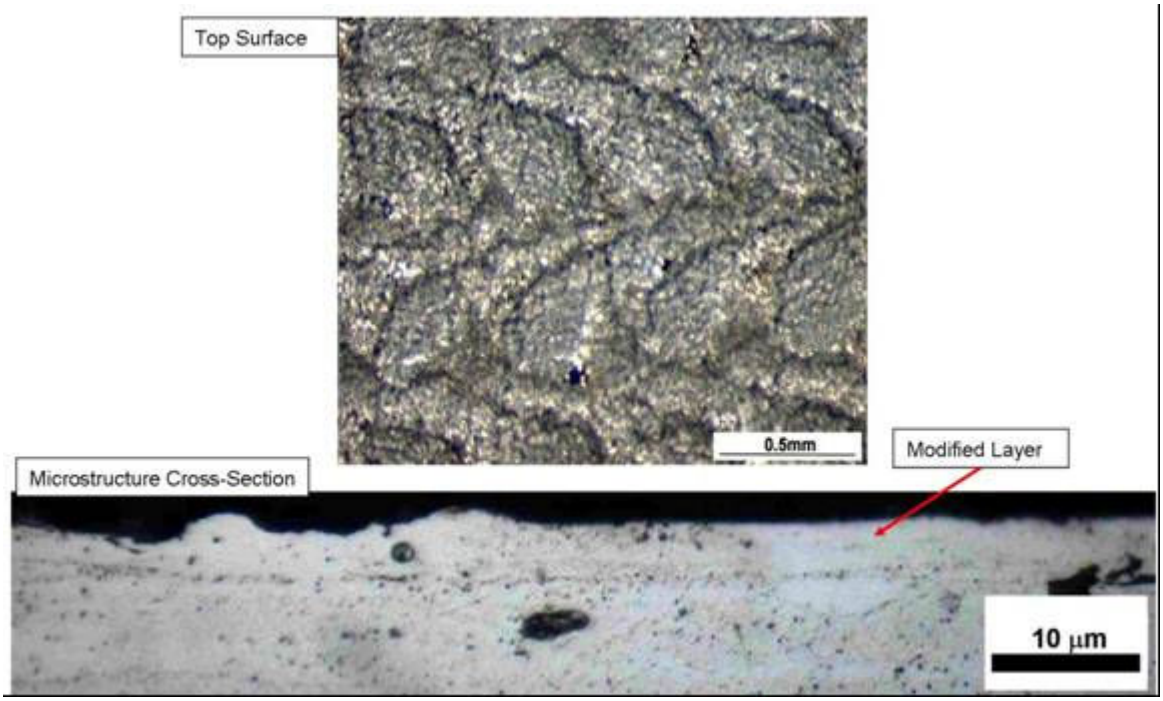

Figure 243: Surface appearance and cross-section of excimer laser surface melted AA2024 with treatment parameters of 10J/cm2, 9 pulses per unit area

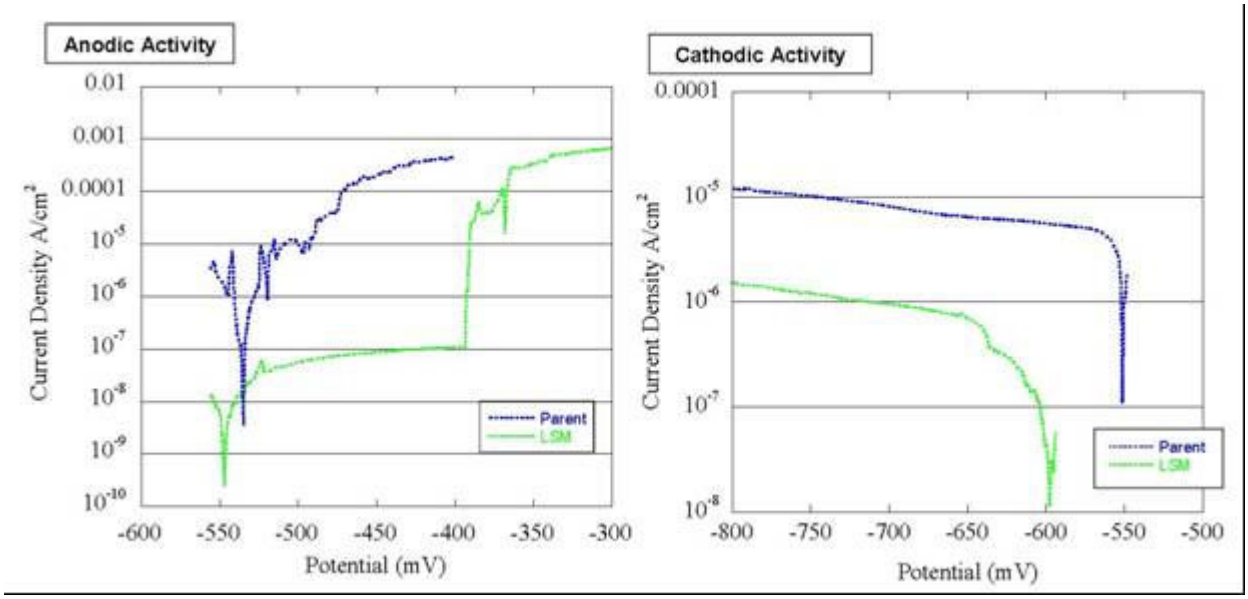

Figure 244: Electrochemical reactivity following excimer laser surface melting of AA2024 at 10J/cm2, 9 pulses per unit area compared with the parent alloy: (a) cathodic polarisation curve and (b) anodic polarisation curves measured with a microelectrochemical cell with 0.1M NaCl solution at a scan rate of 1mV/s scan rate (Ag/AgCl reference electrode)

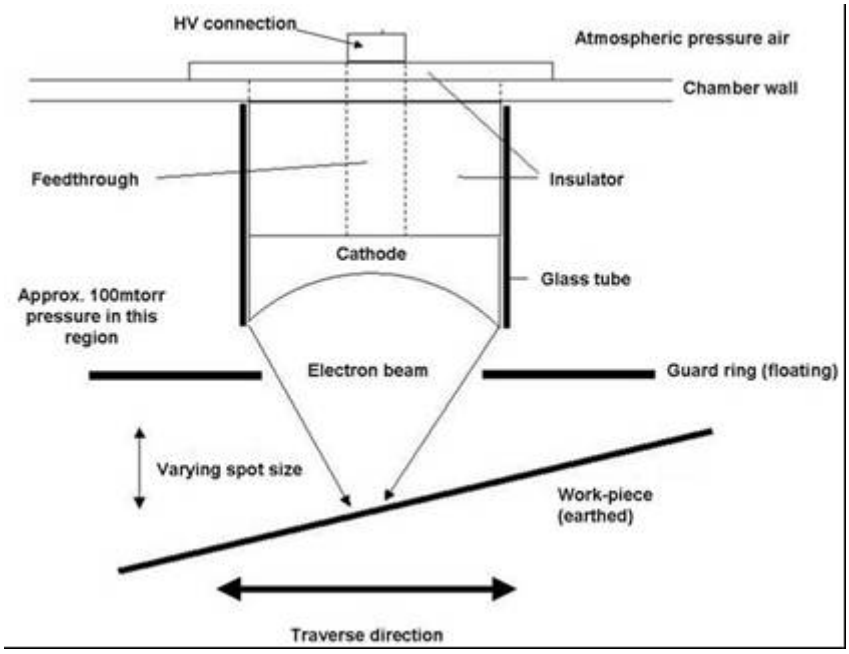

Figure 245: Schematic diagram of the pulsed, high power electron beam setup used for the treatment of specimens

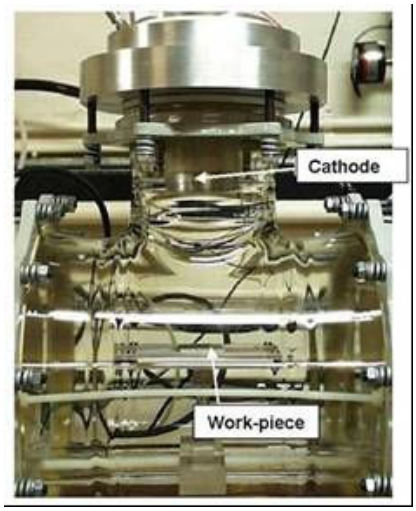

Figure 246: The BAE Systems electron beam apparatus highlighting key components

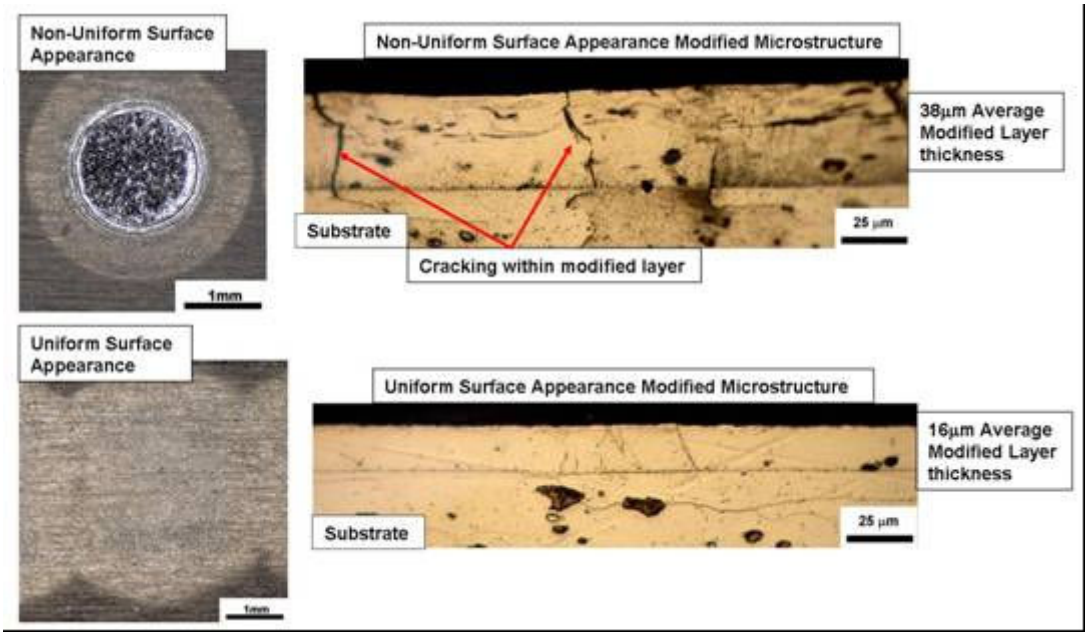

Figure 247: Examples of uniform and non-uniform melt zone surface appearances and their associated etched microstructure cross-sections produced in electron beam surface melting of AA2024 at 20µs pulse duration, 6J, 1 pulse per unit area

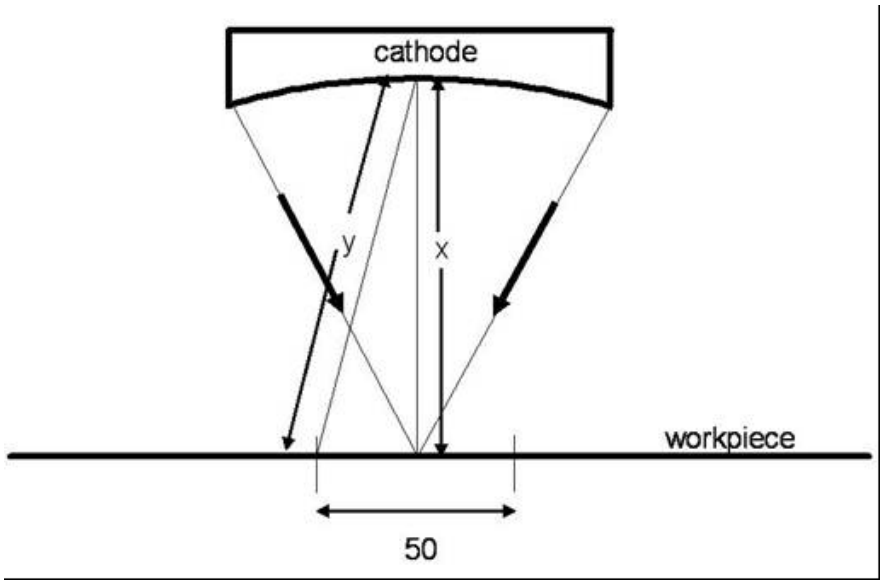

Figure 248: Effect of scanning on beam path length

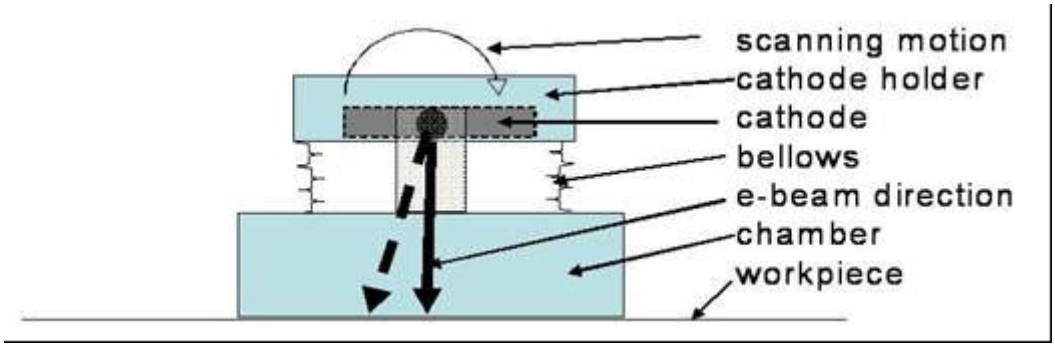

Figure 249: Set-up for scanning e-beam

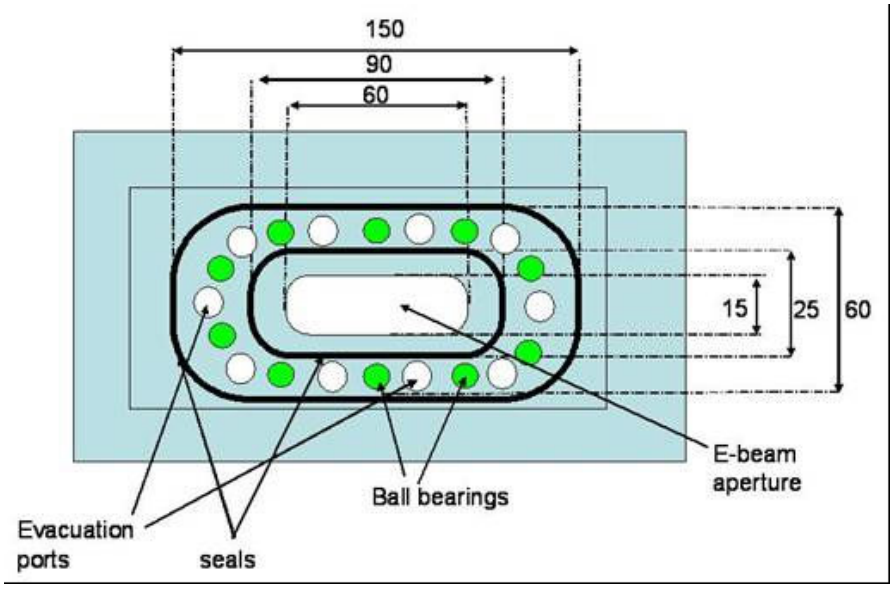

Figure 250: Underside of processor showing rectangular aperture for scanning e-beam

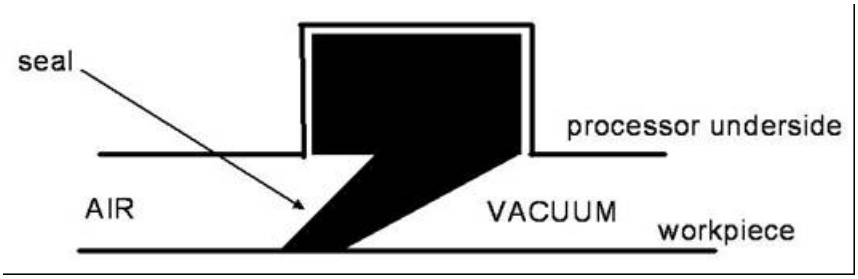

Figure 251 Cross-section of elastomeric seal proposed by FTL

Figure 252: TWI sliding seal for e- beam processor

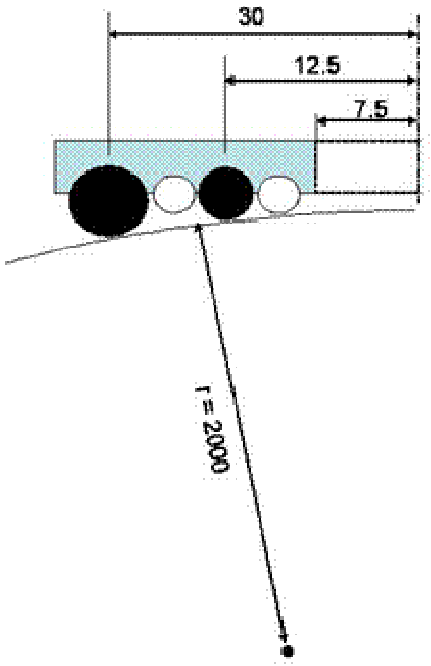

Figure 253: Cross-sectional view of curved workpiece and processor seals (half-view taken across narrow side of e-beam aperture)

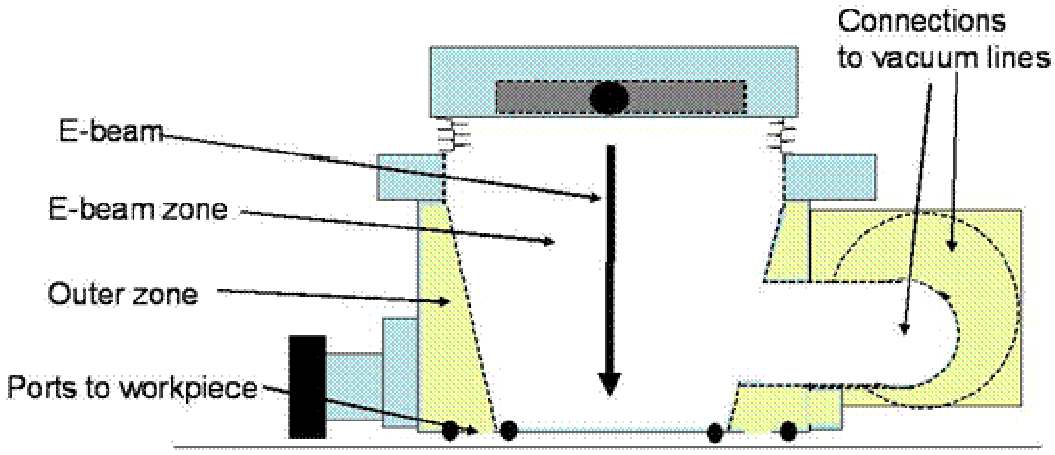

Figure 254: Cross section of processor showing vacuum zones

6.15 Task 6.3: Post Weld Treatments (Dassault)

The DASSAULT-AVIATION contribution concerned the 7449 T79 characterization after welding + surface treatment, including the definition of peened areas in partnership with Metal Improvement Company (subcontractor). Crack propagation tests were carried out after Shot Peening and Laser Shock Peening in comparison with as welded material (see the results in Figure 224).

The contribution for D9 deliverable has been done.This task is completed.

6.16 Task 6.3: Post Weld Treatments (ALCAN)

- The contribution was reported in the deliverable D14 : the influence of post weld heat treatments on corrosion tests was evaluated for different heat treatment of 2050/7449 dissimilar joints, for 2195 FSW joints performed by AUK.
- For 7449/2050 joints, the impact of different ageing heat treatments has low effects on the static, the microstructure and on the corrosion properties. 2195 plate/plate and 2195 plate/profile friction stir welded in T3 and post heat treated in T8 have a good stress corrosion cracking resistance about 250 MPa.

6.17 Task 6.4 Process Monitoring Control (Airbus Germany)

Activity consisted in continuing the dialog with Fatronik to support their development.

6.18 Task 6.4 Process Monitoring Control (Fatronik)

Welding of long fuselage panels by friction stir (AD interest) requires the use of retractable pin tools in order to absorb sheet thickness variations and gaps in the abutting edges without damaging the backing bar. However, this kind of welding tools can lead to Lack of Penetration (LOP) defects. LOP defects appear since the pin-to-backing distance (PBD), see Figure 255, is at present difficult to control with the requested reliability (±50μm according to AD estimations). They cause a significant drop in the weld fatigue strength and are not fully detectable through NDT techniques.

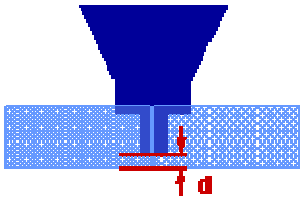

Figure 255: Pin-to-backing distance

In order to reduce/eliminate LOP defects, two research lines have been envisaged.

1. Measurement of the PBD

During the reporting period work has been focused on confirming the feasibility of measuring the PBD, see Figure 256, through magnetic principles as suggested by exploratory experimental measurements.

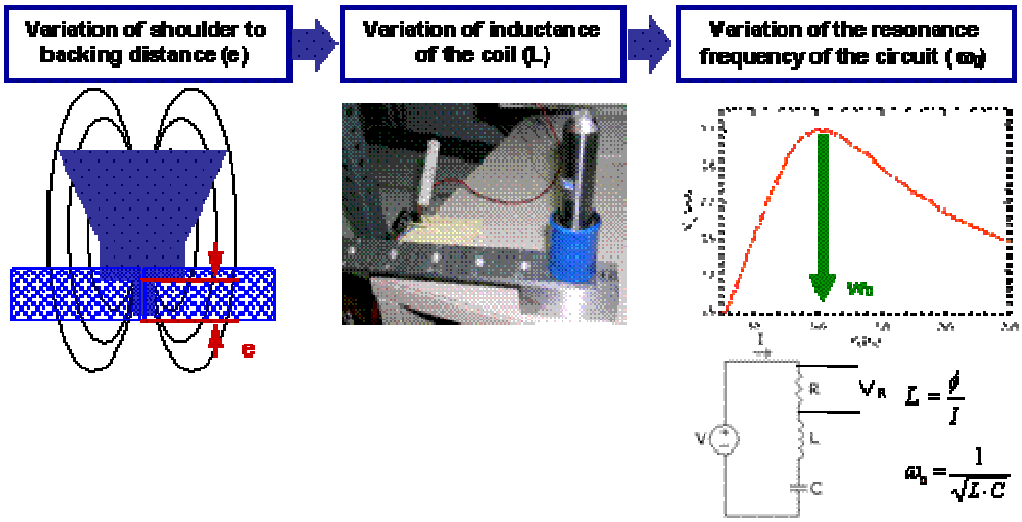

Figure 256: Concept for distance measurement using magnetic principles and exploratory results

Based on FE simulations, design parameters of a prototype device have been adjusted for an adequate performance. Figure 257 shows the obtained results. From the simulation outputs it can be seen that self-inductance (L) and resonance frequency sensitivity to distance (df/de) are high for the device closing cup relative permeability (250000) which benefit an effective measurement of the distance from the shoulder to the backing. Moreover, both variables appear as low sensitive to permeability variations expected with temperature increase during welding.

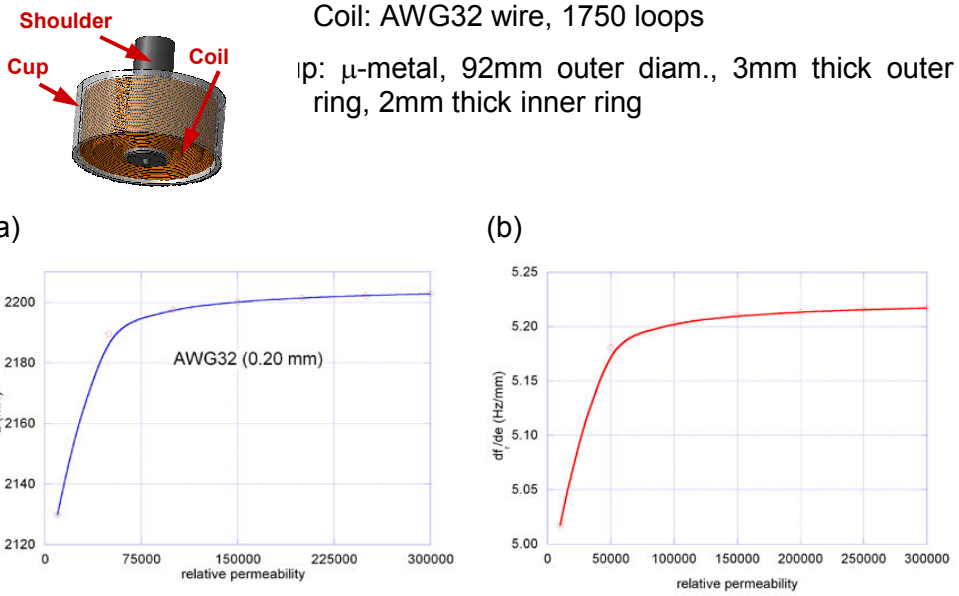

Figure 257: FE simulation outputs: (a) self-inductance of the coil, (b) sensitivity of the circuit resonance frequency to variation of the distance from the shoulder to the backing

According to the FE simulation results, the prototype device has been fabricated for experimental measuring. The obtained results have shown, see Figure 258, that the sensitivity of the resonance frequency increases with the circuit capacity (10 vs. 1µF) so 50µm distance variations (AD requirement) might be measurable. However, experimental results have also pointed out that the higher the resonance frequency the higher the output signal noise due to unexpected Eddy currents induced in the aluminium plate.

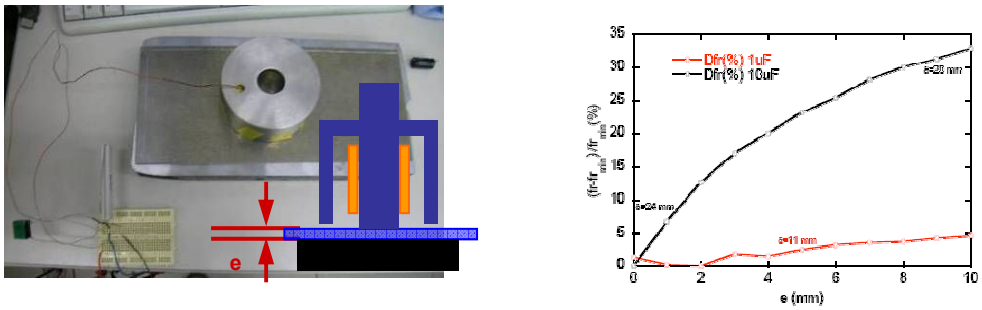

Figure 258: Experimental measurements obtained with the prototype device

Therefore, it can be concluded that the preliminary feasibility of the developed device to measure variations in the distance from the shoulder to the backing has been demonstrated. However, several issues remain unsolved to fully evaluate the device feasibility. Table 28 shows all the identified issues together with the proposed approach to solve them and the associated risk.

Issue	Proposed solution	Risk
Indirect measurement of the PBD	Include measurement of the pin length	L
Low permeability of the backing bar	Use a ferromagnetic backing bar	M
Unknown temperature effect on measurements	Determine the temperature effect	H
Coil temperature limited	Integrate a coil cooling system	M
Too big size of the closing cup	Run FEM & tests using smaller cup sizes	H
Need of circuit wires	Integrate bearings in the device design	L

L: Low; M=Medium; H=High

Table 28: Pending issues for fully evaluation of the feasibility of the developed measuring device

2. Pin vibration strategies to reduce/eliminate LOP defects

During the reporting period, the effectiveness of making the pin vibrate in order to reduce/eliminate LOP defects has been analysed.

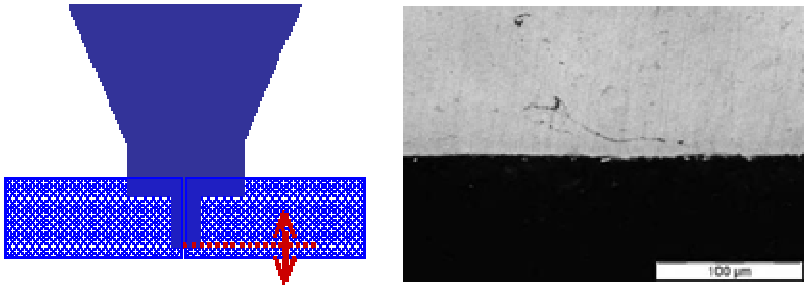

Figure 259: Tool pin vibration (left) in order to reduce LOP (right)

Firstly, the critical PBD (PBD*) where LOP starts appearing has been identified. Welding tests have been performed using AA2024-T3 210x120x3mm sheets and fixed welding parameters (1000rpm, 200mm/min, 13KN) which showed the feasibility to produce welds that withstand a 180º bending angle for a 0.1mm PBD. Regarding the welding tool, a 14mm diameter concave shoulder with a 3mm diameter, 2.8mm long and MX-Triflute shaped pin have been used. Welds have been produced, see Table 29, at different PBD values in order to identify the PBD*. As it can be seen, PBD* corresponds to 0.23mm where LOP has first been detected.

PBD (mm)	0.11	0.14	0.17	0.20	0.23	0.26
LOP	NO	NO	NO	NO	YES	YES

Table 29: Identification of the PBD*

Once the PBD* identified, a set of welding experiments have been performed at that distance in order to analyse the effectiveness of making the pin vibrate. Table 30 shows the selected conditions. A total of 5 different conditions have been tested and 4 iterations have been made per test condition. Regarding LOP evaluation, 3 measurements have been taken along the seam.

PBD* (mm)	Amplitude (mm)	Frequency (Hz)
0.23	±0/0.02/0.04	0/2.5/5

Table 30: Vibration conditions

Graphs of Figure 260 compare LOP values without and with pin vibration. As it can be seen, LOP value always decreases when the pin vibrates. Thus, graph on the left shows an average 20% decrease compared to non-vibrating welding. Moreover, graph on the left shows that pin vibration leads to a

higher repeatability of LOP value for identical conditions since higher scatter within measurements corresponds to non-vibrating and less exigent (2.5Hz; 0.02mm) conditions.

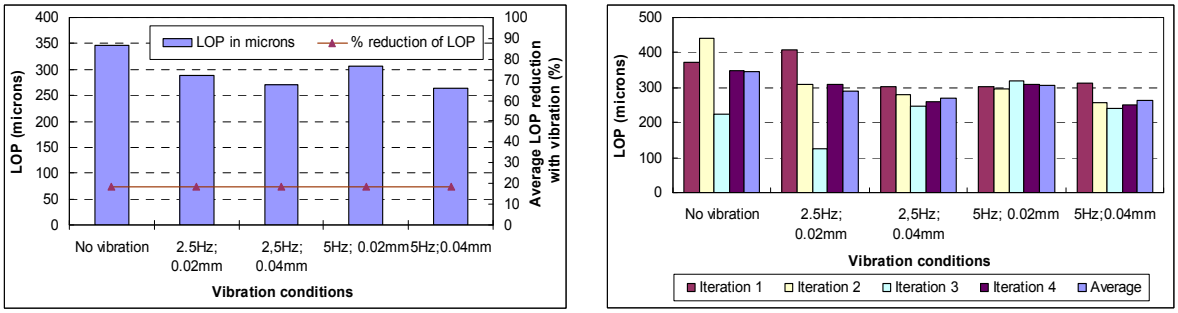

Figure 260: Effect of pin vibration on LOP

Regarding the effect of vibration parameters (amplitude and frequency of the vibration) on the results, Figure 261 on the left suggest a decrease of LOP with a higher frequency whereas the effect of frequency seems to be little significant. A closer analysis points out, as illustrated by Figure 261 on the right, that LOP decrease approximately equals twice the amplitude of the vibration.

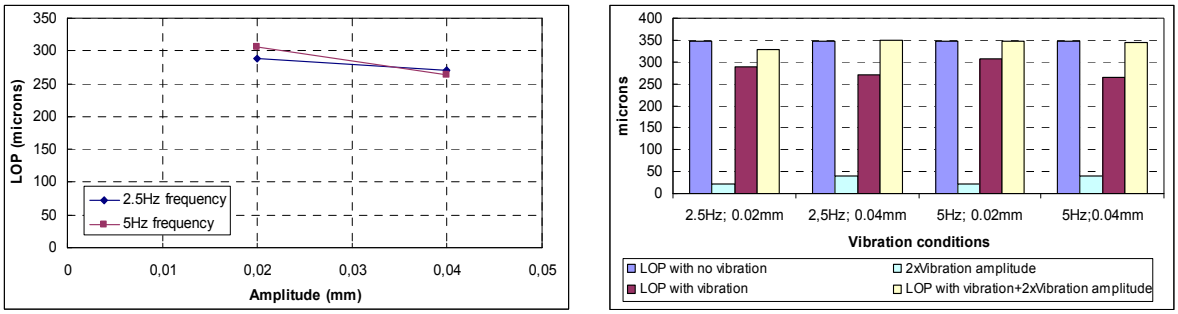

Figure 261: Effect of vibration parameters on LOP

However, the ANOVA analysis of the results, see Figure 262 (a), has shown a high scatter of LOP values within the selected parameter range. For this reason, a second analysis based on the highest measured LOP for each test condition (in order to skip the effect of scatter) has been carried out. As it can be seen in Figure 262 (b), maximum LOP values confirm the trend pointed out by average values of Figure 262 (a).

(a)

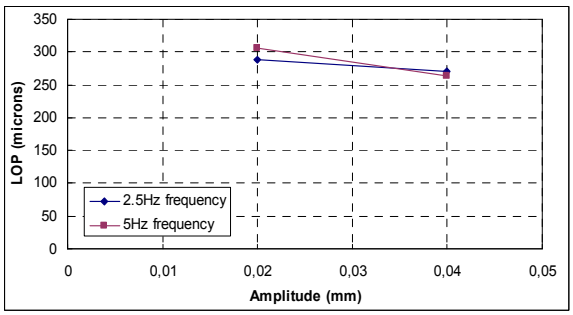

Factor	Sum of squares	df	Mean square	F value	p-value Prob>F
Model	4690,55	3	1563,52	0,38	0,7720
A-Freq	65,48	1	65,48	0,016	0,9022
B-Amp	3864,69	1	3864,69	0,93	0,3541
AB	760,38	1	760,38	0,18	0,6765
Pure Error	49902,42	12	4158,53		
Cor Total	54592,97	15			

(b)

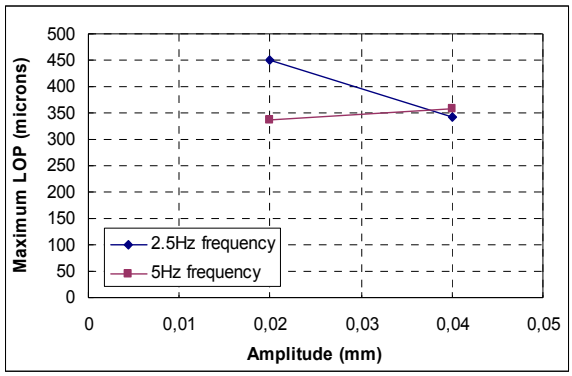

Figure 262: ANOVA (a) and maximum value (b) analysis of the effect of vibration parameters on LOP

Therefore, it can be concluded that pin vibration allows reducing LOP defects. Even though LOP measurements have shown a high scatter in the selected range of vibration parameters, it can be said that an amplitude increase makes the LOP decrease and that frequency shows little effect on LOP. Further experimentation over a wider range of vibration parameters is necessary in order to better evaluate the potential of the strategy to reduce/eliminate LOP defects.

6.19 WP6 Airbus Germany

Activity consisted in continuing the dialog with Fatronik to support their development.

7 Work Package 7

7.1 Task 7.3 Exploitation

At the conclusion of the COINS Project, most partners have concluded that the original opportunities identified for Exploitation remain in place. Dassault have also identified an opportunity to manufacture structural parts on the Falcon 7x Business Jet. In general the work performed within the project has heightened the level of technical readiness for both the Friction Stir Welding process itself and its introduction as a means of unitizing structural designs. More work will be required for most applications to be realised but the degree of risk has been minimised. For the OEM's or End Users the biggest challenge to the introduction of FSW is the on-going challenge that carbon fibre composites

present to the use of metallic designs on future primary structures. Although metallic structures remain more than competitive on weight and indeed cost, the reality is that technology decisions on new aircraft are not always driven solely by Engineering. Current in-house equipment resources, out sourcing to low cost suppliers, marketing strategies and political influences can have a major bearing on the final result. However, where a metallic solution is proposed it can be anticipated that FSW is likely to play a major role in reducing costs.

The dissemination activities within COINS have been numerous and varied, including 17 external papers and/or presentations as well as a dedicated Workshop, held by GKSS, in Hamburg at the end of the project. Dissemination of the results will continue beyond the end of the project, with several partners contributing to a Special Issue of the Journal of Aerospace Engineering, which is Part G of the Proceedings of the Institute of Mechanical Engineers. The Journal's Editorial Board approved this proposed special publication in March 2009 and appointed X. Zhang and S. Williams as the Guest Editors of this Special Issue. Publication is planned in late 2011 or early 2012 and is devoted to the research topics investigated in the COINS project.